



UNIwersYTET
IM. ADAMA MICKIEWICZA
W POZNANIU

Wydział Chemii

ROZPRAWA DOKTORSKA

mgr Dominika Przybylska

Up - konwersja w nanokrystalicznych fluorkach metali ziem alkalicznych i rzadkich, domieszkowanych jonami Yb^{3+} oraz Nd^{3+} , Ho^{3+} , Er^{3+} lub Tm^{3+} otrzymanych metodą hydrotermalną

Up - conversion in nanocrystalline alkaline and rare earth fluorides doped with Yb^{3+} and Nd^{3+} , Ho^{3+} , Er^{3+} or Tm^{3+} ions obtained by hydrothermal method

w formie spójnego tematycznie cyklu artykułów opublikowanych w czasopismach naukowych

Promotor dr hab. Tomasz Grzyb, prof. UAM

Poznań 2020

Podziękowania

Dla dr. hab. Tomasza Grzyba, prof. UAM za pomoc w rozwiązywaniu problemów naukowych, liczne dyskusje, dobre rady oraz wsparcie w prowadzeniu prac badawczych

Dla prof. dr. hab. Stefana Lisa za nieocenione wsparcie naukowe, wielką życzliwość oraz dobre rady udzielone w trakcie pisania pracy

Dla koleżanek i kolegów z laboratorium, za pomoc i wsparcie, prowadzenie dyskusji naukowych, cierpliwość i zawsze pozytywne nastawienie.

Najbliższym, za nieocenione wsparcie na każdym kroku mojego rozwoju naukowego, ogromne wsparcie i wyrozumiałość.

Spis treści

Cel rozprawy doktorskiej	7
Streszczenie rozprawy doktorskiej w języku polskim	8
Summary of the doctoral thesis in English.....	10
Życiorys naukowy.....	12
Lista publikacji wchodzących w skład rozprawy doktorskiej	14
Publikacje niewchodzące w skład rozprawy doktorskiej	15
Udział w konferencjach naukowych	16
Wstęp teoretyczny	19
Metody syntezy nanomateriałów użyte w pracy doktorskiej.....	35
Najważniejsze metody charakterystyki nanomateriałów użyte w pracy doktorskiej	36
Część eksperymentalna.....	39
Podsumowanie.....	44
Literatura.....	46
Kopie oświadczeń współautorów	51
Kopie publikacji stanowiących rozprawę doktorską	57

Cel rozprawy doktorskiej

Celem niniejszej pracy doktorskiej było otrzymanie nanomateriałów domieszkowanych jonami lantanowców (Ln^{3+}), wykazujących intensywną luminescencję pod wpływem promieniowania z zakresu bliskiej podczerwieni (NIR, ang. *near infrared radiation*), wykazując tym samym zjawisko up - konwersji (UC, ang. *up-conversion*). Zsyntetyzowane materiały przedstawione w pracy doktorskiej oparte są o matryce fluorkowe, a dokładniej metale ziem alkalicznych i rzadkich, powszechnie stosowane w badaniach dotyczących zjawiska up - konwersji. Przeprowadzona została ich charakterystyka morfologiczna oraz spektroskopowa.

Otrzymane nanomateriały w wyniku syntezy hydrotermalnej (zastosowanie wody jak rozpuszczalnika podczas reakcji), charakteryzują się niewielkim rozmiarem (do 560 nm), co ma istotne znaczenie w zastosowaniach biologicznych, np. w celu przenikania do komórek czy wydalania z organizmu. Otrzymane związki ze względu na zastosowaną metodę mają charakter hydrofilowy, dzięki czemu tworzą wodne koloidy, bez konieczności przeprowadzania dodatkowych etapów podczas syntezy czy późniejszej obróbki.

Wykonano również optymalizację stosowanej procedury syntezy nanomateriałów fluorkowych, w celu otrzymania pożądanej morfologii, a także wzmocnienia obserwowanej luminescencji. Istotnym aspektem była również funkcjonalizacja powierzchni nanocząstek up - konwersyjnych (UCNPs), umożliwiająca poprawienie stabilności wodnych koloidów zawierających otrzymane nanocząstki, a także zmniejszenie ich toksyczności. Ponadto, modyfikacja powierzchni nanocząstek zarówno w trakcie syntezy, jak i po niej, umożliwia ich dalszą biokoniugację.

W rozprawie doktorskiej przedstawiono syntezę nanomateriałów up - konwersyjnych, charakterystykę właściwości morfologicznych i spektroskopowych otrzymanych układów oraz badania cytotoksyczności dla wybranej grupy nanocząstek, celem określenia możliwości aplikacyjnych w naukach biologicznych czy medycznych.

Streszczenie rozprawy doktorskiej w języku polskim

Up - konwersja to zjawisko w wyniku którego po absorpcji minimum dwóch fotonów niskoenergetycznych następuje emisja fotonu o wyższej energii, tj. zachodzi konwersja energii „w górę”. UC nazywana jest również emisją anty-Stokesowską, ponieważ długość fali wzbudzenia jest większa od długości fali emisji.¹ Najczęściej wzbudzenie następuje w zakresie bliskiej podczerwieni, a emisja w zakresie spektrum światła widzialnego oraz ultrafioletowego. UC jest zjawiskiem charakterystycznym dla jonów lantanowców, ze względu na budowę ich poziomów energetycznych, wynikającą z przejść $f - f$ elektronowych, ale również jony metali przejściowych czy związki organiczne mogą konwertować energię „w górę”.^{2,3}

W niniejszej pracy doktorskiej materiałami, na podstawie których zbadana została UC, są fluorki nieorganiczne zawierające jony metali z drugiej grupy układu okresowego, tzw. metale ziem alkalicznych oraz jony pierwiastków ziem rzadkich. Matryce fluorkowe charakteryzują się niską energią fononów tj. drgań sieci krystalicznej, dzięki czemu wygaszanie wielofononowe, będące bezpromienistą depopulacją stanu wzbudzonego do niżej położonego poziomu wzbudzonego przy asyście fononu, jest zminimalizowane, zwiększając tym samym wydajność UC.⁴ Związki te wykazują również dużą stabilność chemiczną oraz fizyczną, stanowią dobry akceptor elektronów, a luminofory na ich bazie charakteryzują się wysoką wartością wydajności kwantowej luminescencji.^{5,6} Natomiast jony metali ziem alkalicznych mają podobny promień jonowy do jonów lantanowców, dzięki czemu możliwe jest wbudowywanie się jonów Ln^{3+} w ich miejsce, bez powodowania zniekształceń sieci krystalicznej.^{7,8}

Bardzo duży wpływ na właściwości otrzymanych struktur ma ich nanometryczny rozmiar, tzn. średnica w jednym wymiarze poniżej 100 nm. Dzięki temu możliwe jest uzyskanie nanocząstek (NPs) o właściwości innych od tych charakteryzujących ich odpowiedniki mikrokryształiczne. Istotny jest również duży stosunek powierzchni do objętości cząstki, niewielki rozmiar umożliwiający przenikanie przez membrany czy zmiana kolorów emisji zależna od wielkości, a także ich samoorganizacja.^{9,10}

Efektom przeprowadzonych prac badawczych są proste fluorki $\text{CaF}_2:\text{Yb}^{3+}$, Er^{3+} ; $\text{SrF}_2:\text{Yb}^{3+}$, Ln^{3+} ($\text{Ln} = \text{Ho}$, Er , Tm , Yb); struktury typu rdzeń/powłoka (ang. *core/shell*), $\text{SrF}_2:\text{Yb}^{3+}$, $\text{Er}^{3+}@\text{SrF}_2:\text{Yb}^{3+}$, Nd^{3+} oraz niestechiometryczne fluorki $\text{M}_x\text{RE}_y\text{F}_z:\text{Yb}^{3+}$, Er^{3+} ($\text{M} = \text{Ca}$, Sr , Ba ; $\text{RE} = \text{Y}$, La , Gd , Lu), otrzymane metodą hydrotermalną. Warunki syntezy jak i jej procedura (stężenia domieszek, zawartość źródła jonów fluoru, dodatek związków kompleksowych, pH) zostały zoptymalizowane dla wszystkich otrzymanych układów, w celu uzyskania efektywnej emisji pod wpływem promieniowania NIR cząstek o rozmiarze nanometrycznym.

Dla fluorków wapnia przeprowadzono analizę wpływu warunków syntezy oraz związku kompleksującego na obserwowaną luminescencję. Zbadano wpływ kompensacji ładunku na strukturę otrzymanych nanocząstek, a tym samym ich emisję. Na podstawie wykonanych pomiarów oraz ich analizy, ustalono występowanie jonów Yb^{3+} o różnej symetrii otoczenia w jednej próbce.

Optymalizacja układu $\text{SrF}_2:\text{Yb}^{3+}$, Ln^{3+} pozwoliła na otrzymanie stabilnych, wodnych koloidów, charakteryzujących się efektywną emisją pod wpływem promieniowania z zakresu bliskiej podczerwieni. Ponadto, NPs dla których przeprowadzono modyfikację powierzchni w roztworze soli fizjologicznej, wykorzystując do tego polimery amfifilowe, zbadano pod kątem ich cytotoksyczności.

Dzięki zsyntetyzowaniu struktur typu rdzeń/powłoka, możliwe było wprowadzenie do powłoki jonów Nd^{3+} , co umożliwiło otrzymanie up - konwersji pod wpływem wzbudzenia 975 oraz 808 nm. Ze względu na homogeniczną strukturę otrzymanych związków, potwierdzenie otrzymania próbek typu rdzeń/powłoka przeprowadzono poprzez dokładną analizę spektroskopową, wykorzystując do tego różne długości fali wzbudzenia (808, 975 oraz 1532 nm), obserwując przy tym zjawisko up - konwersji oraz down - konwersji (DC).

Dla niestechiometrycznych fluorków nieorganicznych $\text{M}_x\text{RE}_y\text{F}_z:\text{Yb}^{3+}$, Er^{3+} przeprowadzono dokładną analizę składu pierwiastkowego, na podstawie którego przedstawiono mechanizm formowania się otrzymanych związków, w którym duże znaczenie odgrywa trwałość kompleksów przejściowych jonów metali tworzonych z kwasem etylenodiaminotetraoctowym (EDTA). Dla związków o dużej intensywności emisji została również wyznaczona wydajność kwantowa.

Dla wszystkich związków wykonano dyfraktogramy proszkowe (XRD), analizę ilościową (ICP-OES/MS, EDS), zdjęcia mikroskopii elektronowej (TEM), analizę wielkości cząstek i ładunku na ich powierzchni (DLS, potencjał zeta) spektroskopię w podczerwieni (FT - IR) oraz spektroskopię laserową.

Poprzez badania nad wspomnianymi UCNPs charakteryzującymi się intensywną emisją, również w środowisku wodnym, możliwe jest otrzymanie struktur alternatywnych dla obecnie stosowanych znaczników biologicznych. Ponadto otrzymane nanocząstki mogą służyć do transportu leków, umożliwiając śledzenie szlaków metabolicznych, a uzyskane rezultaty wzbogacą obecny stan wiedzy odnośnie zjawiska up - konwersji.

Summary of the doctoral thesis in English

The upconversion UC is the phenomenon in which absorption of at least two low energy photons leads to emission of one high energy photon. UC is also called anti-Stokes emission, as the excitation wavelength is longer than the emission wavelength.¹ Usually, the excitation occurs in near-infrared range and emission in the visible and UV spectrum. UC is a phenomenon characteristic of lanthanide ions, which is related to the system of their energy levels, however, it is also observed for transition metals as well as organic compounds.^{2,3}

In the presented doctoral thesis, the UC process in inorganic fluorides containing metal ions from the second group of the periodic table, the so-called alkaline earth metals and rare earth elements ions, is examined. The fluoride matrices have a crystal lattice of low phonon energy, i.e. the low-energy crystal lattice vibration, which minimizes multiphonon quenching, due to phonon-assisted non-radiative depopulation of excited energy level to lower-lying energy level, and as a result, increasing UC efficiency.⁴ Moreover, these compounds exhibit high chemical and physical stability, they are good electron acceptors, and phosphors based on them have high quantum yield.^{5,6} On the other hand, alkaline earth metals ions have similar ionic radii to lanthanide ions, so incorporation of Ln^{3+} in their place occurs without distortion to the crystal lattice.^{7,8}

The properties of the obtained compounds are to a significant degree determined by their nanometric size (diameter in one direction is smaller than 100 nm). Thanks to this, nanoparticles (NPs) exhibit different properties than their bulk counterparts. Significant impact on NPs properties have also high surface to volume ratio, small size allowing penetration through membranes or change in nanoparticle's color depending on the size as well as the NPs ability to self-organization.^{9,10}

The study was performed on simple fluorides $\text{CaF}_2:\text{Yb}^{3+}$, Er^{3+} ; $\text{SrF}_2:\text{Yb}^{3+}$, Ln^{3+} ($\text{Ln} = \text{Ho}, \text{Er}, \text{Tm}, \text{Yb}$); core/shell structure $\text{SrF}_2:\text{Yb}^{3+}$, $\text{Er}^{3+}@\text{SrF}_2:\text{Yb}^{3+}$, Nd^{3+} and non-stoichiometric fluoride $\text{M}_x\text{RE}_y\text{F}_z:\text{Yb}^{3+}$, Er^{3+} ($\text{M} = \text{Ca}, \text{Sr}, \text{Ba}$; $\text{RE} = \text{Y}, \text{La}, \text{Gd}, \text{Lu}$), obtained by hydrothermal method.

The synthesis conditions, as well as the synthesis procedure (dopants concentration, amount of fluorine ions source, the addition of complexation compounds, pH), were optimized for all of the obtained nanometric structures, to observe effective emission under excitation from near-infrared range. For calcium fluorides, the impact of synthesis conditions as well as complexation agents on observed luminescence was analyzed. The effect of charge compensation on the structure of the obtained nanoparticles, and thus their emission, was thoroughly studied. On the basis of the measurements and their analysis, the presence of Yb^{3+} at different symmetry sites in one sample was determined.

The optimization of $\text{SrF}_2: \text{Yb}^{3+}, \text{Ln}^{3+}$ structure allowed obtaining stable water colloids, characterized by effective emission under excitation from the near-infrared range. Moreover, cytotoxicity of NPs whose surface had been modified by amphiphilic polymers, dispersed in PBS medium, was investigated.

The synthesis of core/shell structure, with Nd^{3+} ions in the shell, allowed UC emission under 975 and 808 nm excitation wavelengths. Due to the homogeneity of the prepared compounds, the presence of a core/shell structure was confirmed through detailed spectroscopic measurements, using for this purpose different excitation wavelength (808, 975 and 1532 nm), with UC and DC as an effect.

For inorganic fluorides $\text{M}_x\text{RE}_y\text{F}_z: \text{Yb}^{3+}, \text{Er}^{3+}$ the formation mechanism, based on elemental analysis and consideration of transition complex stability of metal ions with ethylenediaminetetraacetic acid (EDTA) was established. Moreover, for the compounds with the highest luminescence, the quantum yield was determined.

All obtained compounds were characterized by X-ray diffractograms (XRD), quantitative analysis (ICP - OES/MS, EDS), electron microscopy imaging (TEM), analysis of nanoparticles size and surface charge (DLS, zeta potential), infrared spectroscopy (FT-IR) and laser spectroscopy.

The studies of the above-described UCNPs, showing intense emission, also in a water environment, have proved that it is possible to obtain the structures alternative to those currently used as biomarkers. Moreover, the prepared compounds can be applied as drug delivery systems or for tracking of metabolic pathways. The presented results have contributed to the current knowledge about the up - conversion phenomenon.

Życiorys naukowy

Mgr Dominika Przybylska

Zakład Ziem Rzadkich

Wydział Chemii

Uniwersytet im. Adama Mickiewicza w Poznaniu

Wykształcenie

- 2015 – obecnie Studia doktoranckie III stopnia Uniwersytet im. Adama Mickiewicza w Poznaniu, Wydział Chemii, Zakład Ziem Rzadkich,
- 2013-2015 Studia Magisterskie uzupełniające na Uniwersytecie im. Adama Mickiewicza w Poznaniu; kierunek chemia, specjalność- chemia kosmetyczna,
- 2010-2013 Studia Licencjackie na Uniwersytecie im. Adama Mickiewicza w Poznaniu; kierunek chemia, specjalność- chemia kosmetyczna

Stáže naukowe:

05.09.2016-17.02.2017, Uniwersytet Osnabrück, Instytut Nowych Materiałów, Niemcy, w ramach projektu COST-STSM-CM1403, *The European upconversion network - from the design of photon-upconverting nanomaterials to biomedical applications*).

Projekty badawcze:

- kierownik projektu Preludium, NCN (grant Nr UMO-2017/27/N/ST5/02149), 2018-2021
- wykonawca w projektach:
 - SONATA-BIS, NCN (grant Nr UMO-2016/22/E/ST5/00016), 09.2017 – obecnie
 - LIDER, NCBiR (grant Nr LIDER/39/0141/L-9/17/NCBR/2018), 01.2019- obecnie
 - luventus Plus MNiSW, (grant ID IP2014 014573), 09.2015- 09. 2016
 - SONATA, NCN, (grant Nr UMO-2011/03/D/ST5/05701), 2012 – 2016

Osiągnięcia i nagrody

- stypendium naukowe dla najlepszych doktorantów oraz stypendium pro jakościowe rok akademicki 2018/2019
- nagroda zespołowa Rektora II stopnia za osiągnięcia naukowe w roku akademickim 2018/2019
- stypendium rektora drugiego stopnia dla najlepszych studentów chemii studiów magisterskich uzupełniających w roku akademickim 2013/2014 oraz 2014/2015 (1 oraz 2 rok studiów magisterskich uzupełniających DU)
- stypendium motywacyjne z projektu POKL „Poczuj chemię do chemii- zwiększenie liczby absolwentów kierunku CHEMIA na Uniwersytecie im. Adama Mickiewicza w Poznaniu, w latach 2011-2013 oraz 2013-2015
- III miejsce na XIII Ogólnopolskim Sympozjum Naukowego Koła Chemików Uniwersytetu im. Adama Mickiewicza w Poznaniu 2013 za prezentację ustną pt. „Synteza i badanie właściwości fizykochemicznych nanocząstek wykazujących up - konwersję, opartych o BaYF₅ domieszkowany jonami Yb³⁺ i Tm³⁺, Ho³⁺, Er³⁺”

Lista publikacji wchodzących w skład rozprawy doktorskiej

Zgodnie z art. 13 ust. 1 ustawy z dn. 14 marca 2003 r. O stopniach i tytułach naukowych oraz o stopniach i tytułach w zakresie sztuki (tekst jednolity Dz. U. z 2017 r. poz. 1789) oraz § 5 ust. 1 Rozporządzenia Ministra Nauki i Szkolnictwa Wyższego z dn. 19 stycznia 2018 r. w sprawie szczegółowego trybu i warunków przeprowadzania czynności w przewodzie doktorskim, w postępowaniu habilitacyjnym o raz w postępowaniu o nadanie tytułu profesora (Dz. U. z 2018 r. poz. 261); na podstawie art. 179 ust. 1 ustawy z dn. 3 lipca 2018 r. Przepisy wprowadzające ustawę – Prawo o szkolnictwie wyższym i nauce (Dz. U. z 2018 r. poz. 1669).

P1. Dominika Przybylska, Tomasz Grzyb,

Tailoring structure, morphology and up - conversion properties of CaF₂:Yb³⁺,Er³⁺ nanoparticles by the route of synthesis

Journal of Materials Science, **2020**, DOI: 10.1007/s10853-020-05049-9

IF₂₀₁₉ 3.553 IF5-₂₀₁₉ 3.282 Cytowania 0 (0)

P2. Dominika Przybylska, Anna Ekner-Grzyb, Bartosz F. Grześkowiak, Tomasz Grzyb,

Upconverting SrF₂ nanoparticles doped with Yb³⁺/Ho³⁺, Yb³⁺/Er³⁺ and Yb³⁺/Tm³⁺ ions – optimisation of synthesis method, structural, spectroscopic and cytotoxicity studies,

Scientific Reports, 9 **2019**, 8669, DOI: 10.1038/s41598-019-45025-1

IF₂₀₁₉ 4.011 IF5-₂₀₁₉ 4.576 Cytowania 5 (5)

P3. Dominika Przybylska, Tomasz Grzyb,

Synthesis and up - conversion of core/shell SrF₂:Yb³⁺,Er³⁺@SrF₂:Yb³⁺,Nd³⁺ nanoparticles under 808, 975, and 1532 nm excitation wavelengths,

Journal of Alloys and Compounds, 831, **2020**, 154797, DOI: 10.1016/j.jallcom.2020.154797

IF₂₀₁₉ 4.65 IF5-₂₀₁₉ 4.082 Cytowania 0 (0)

P4. Tomasz Grzyb, Dominika Przybylska,

Formation Mechanism, Structural, and Upconversion Properties of Alkaline Rare-Earth Fluoride Nanocrystals Doped with Yb³⁺/Er³⁺Ions,

Inorganic Chemistry, 57, **2018**, 6410–6420, DOI: 10.1021/acs.inorgchem.8b0048

IF₂₀₁₉ 4.825 IF5-₂₀₁₉ 4.559 Cytowania 11 (10)

Publikacje niewchodzące w skład rozprawy doktorskiej

1. Tomasz Grzyb, Sangeetha Balabhadra, Dominika Przybylska, Mariusz Węclawiak,
Upconversion luminescence in BaYF₅, BaGdF₅ and BaLuF₅ nanocrystals doped with Yb³⁺/Ho³⁺, Yb³⁺/Er³⁺ or Yb³⁺/Tm³⁺ ions,
Journal of Alloys and Compounds, 649, **2015**, 606–616, DOI: 10.1016/j.jallcom.2015.07.151
IF₂₀₁₉ 4.65 IF5-₂₀₁₉ 4.082 Cytowania 35 (29)
 2. Marcin Runowski, Jędrzej Marciniak, Tomasz Grzyb, Dominika Przybylska, Andrii Shyichuk, Bolesław Barszcz, Andrzej Katrusiak, Stefan Lis,
Lifetime Nanomanometry - High-Pressure Luminescence of Up - converting Lanthanide Nanocrystals - SrF₂ :Yb³⁺, Er³⁺,
Nanoscale, 9, **2017**, 16030–16037, DOI: 10.1039/c7nr04353h
IF₂₀₁₉ 6.895 IF5-₂₀₁₉ 7.315 Cytowania 39 (19)
 3. Marcin Runowski, Szymon Goderski, Dominika Przybylska, Tomasz Grzyb, Stefan Lis, Inocencio R. Martin
Sr₂LuF₇: Yb³⁺-Ho³⁺-Er³⁺ Upconverting Nanoparticles as Luminescent Thermometers in the First, Second and Third Biological Windows,
ACS Applied Nano Materials, **2020**, DOI: 10.1021/acsnm.0c00839
IF₂₀₁₉ - (w trakcie obliczania) Cytowania 0 (0)
 4. Agata Szczeszak, Małgorzata Skwierczyńska, Dominika Przybylska, Marcin Runowski, Emilia Śmiechowicz, Aleksandra Erdman, Olena Ivashchenko, Stefan Lis, Piotr Kulpiński, Konrad Olejnik
Upconversion luminescence in cellulose composites (fibers & paper) modified with lanthanide-doped SrF₂ nanoparticles
Journal of Materials Chemistry C, Major Revision
IF₂₀₁₉ 7.059 IF5-₂₀₁₉ 6.404
- Cytowania na podstawie bazy Web of science. W nawiasie podano wartości z wyłączeniem cytowania przez któregokolwiek z autorów.*

Udział w konferencjach naukowych

Najważniejsze komunikaty przedstawione na konferencjach naukowych

- D. Przybylska, T. Grzyb, *Core@shell nanoparticles based on SrF₂, doped with lanthanide ions under 808 nm and 975 nm excitation wavelength*, 8th Workshop on Photoluminescence in Rare Earths: Photonic Materials and Devices, 04-06.09.2019, Nicea, Francja, **(poster)**
- D. Przybylska, T. Grzyb, *Upconversion in nanocrystalline fluorides of alkaline earth metals and rare earth metals, doped with Yb³⁺ and Er³⁺ ions, obtained by the hydrothermal method*, 12th Frolic Goats Workshop on High Pressure Diffraction, 14-16.04.2019, Poznań, Polska, **(poster)**
- D. Przybylska, T. Grzyb, *Alkaline-rare earth fluorides as promising up - conversion nanomaterials*, NanoTech Poland 2018 International Conference & Exhibition, 06-09.06.2018, Poznań, Polska, **(wystąpienie ustne)**
- D. Przybylska, T. Grzyb, *SrF₂:Yb³⁺, Ln³⁺ as an efficient upconversion nanomaterials (Ln= Ho³⁺, Er³⁺, Tm³⁺)*, 2nd Conference and Spring School on Properties, Design and Applications of Upconverting Nanomaterials, 4-6.04.2018, Walencja, Hiszpania, **(poster)**
- D.Przybylska, T. Grzyb, S. Lis, *SrF₂ as a perfect host for upconversion phenomenon*, NanoTech Poland 2017 Conference and Exhibition, 23-27.05.2017, Poznań, Polska, **(wystąpienie ustne)**
- D.Przybylska, T. Grzyb, S. Lis, *Nanomateriały oparte na matrycy fluorkowej jako wydajne luminofory up – konwersyjne*, VI Ogólnokrajowa konferencja Młodzi Naukowcy w Polsce- Badania i Rozwój, 08.05.2017, Poznań, Polska, **(wystąpienie ustne)**
- D.Przybylska, T. Grzyb, S. Li, *Shortened excitation wavelength based on M^{II}F₂ fluorides (M^{II} = Ba, Ca, Sr), doped lanthanide ions (Yb³⁺, Tm³⁺, Er³⁺, Ho³⁺) showing up - conversion*, 19th JCF-Fruhjahrssymposium, 29.03-01.04.2017, Mainz, Niemcy, **(poster)**
- D.Przybylska, T. Grzyb, S. Lis, *Fluoride matrices doped by lanthanide ions showing up - conversion*, 1st Conference and Spring School on Properties, Design and Applications of Upconverting Nanomaterials, 23-27.05.2016, Wrocław, Polska, **(poster)**
- D. Przybylska, T. Grzyb, S.Lis, *Synthesis, characterization and physicochemical properties of nanocrystalline fluorides doped by lanthanide ions showing up - conversion*, 17th JCF-Fruhjahrssymposium, 25-28.03.2015, Munster, Niemcy, **(poster)**
- D. Przybylska, T. Grzyb, S. Lis, *Upconversion nanoparticles based on M^{II}REF₅ matrices doped by lanthanide ions Yb³⁺/Er³⁺, Yb³⁺/Ho³⁺, Yb³⁺/Tm³⁺*, 4th International Conference on RARE EARTH MATERIALS (REMAT), 26-28.10.2015, Wrocław, Polska, **(poster)**

- D. Przybylska, T. Grzyb, A. Gruszczyńska, R. J. Wiglus, S. Lis, *Up - conversion on REPO₄ nanocrystals doped with Yb³⁺/Er³⁺, Yb³⁺/Tm³⁺ and Yb³⁺/Tb³⁺*, 15th JCF Frühjahrssymposium, 06-09.03.2013, Berlin, Niemcy, **(poster)**
- D. Przybylska, T. Grzyb, S. Lis, *Synthesis and physicochemical studies of nanoparticles showing up - conversion based on BaYF₅ doped Yb³⁺ and Tm³⁺, Ho³⁺ or Er³⁺ ions*, 17th International Conference on Luminescence and Optical Spectroscopy of Condensed Matter (ICL'14), 13-18.0.2014, Wrocław, Polska, **(poster)**
- D. Przybylska, T. Grzyb, S. Lis, *Up - conversion on REPO₄ nanocrystals doped with Yb³⁺/Er³⁺, Yb³⁺/Tm³⁺ and Yb³⁺/Tb³⁺*, 3rd International Conference on RARE EARTH MATERIALS Advances in Synthesis, Studies and Applications, 26-28.04.2013 Wrocław, Polska, **(poster)**

Wstęp teoretyczny

Nanotechnologia

Nanotechnologia to interdyscyplinarny dział nauki zajmujący się projektowaniem, syntezą, charakterystyką oraz zastosowaniem struktur oraz materiałów, których co najmniej jeden wymiar mieści się w zakresie od 1 do 100 nm. I choć sama koncepcja nanotechnologii została zapoczątkowana przez fizyka Richarda Feynmana w 1959 roku to nanomateriały są znane od stuleci, np. czerwone witraże z nanocząstkami złota.

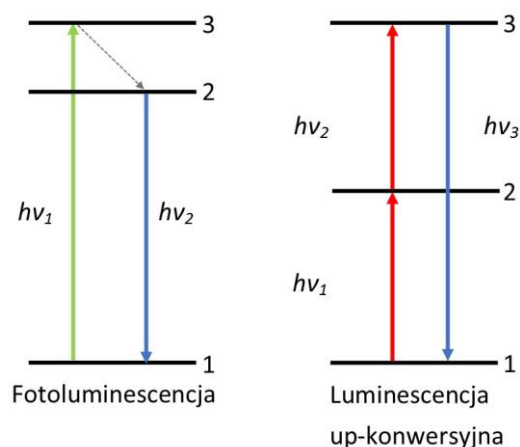
Nanomateriały znajdują zastosowanie w dziedzinach takich jak chemia, fizyka, biologia, medycyna, inżynieria materiałowa czy elektronika. Możliwości wykorzystania nanomateriałów są bardzo duże przede wszystkim ze względu na ich odmienne właściwości od analogów grubokrystalicznych. Istotne znaczenie ma również duży stosunek powierzchni do objętości cząstki, niewielki rozmiar umożliwiający przenikanie przez membrany czy zmianę kolorów zależną od wielkości, a także ich samoorganizacja.

Nanotechnologia może znacząco wpłynąć na rozwiązanie problemów współczesnych ludzi, przedstawionych przez znanego chemika, Richarda Smalley'a¹¹ laureata Nagrody Nobla (1996 odkrycie fulerenów) oraz głównego rzeczownika *National Nanotechnology Initiative* w 2003, m.in. poprzez produkcję wyspecjalizowanych materiałów, katalizatorów, ogniw słonecznych i paliwowych, akumulatorów, czujników, bioczujników, sprzętu analitycznego, w terapiach genowych, naprawianiu tkanek, dostarczaniu leków czy bioobrazowaniu.¹²

Up - konwersja

Znaczącą rolę w nanotechnologii ze względu na możliwości aplikacyjne, odgrywają materiały luminescencyjne, m.in. kropki kwantowe czy barwniki organiczne. Większość tych materiałów podlega prawu Stokes'a, tzn. długość fali wzbudzenia jest krótsza od długości fali emisji, z czym wiąże się emitowanie fotonu o energii niższej niż foton wzbudzający (ang. *downconversion*, konwersja energii „w dół” oraz *downshifting*, przeniesienie „w dół”). Ciekawym zjawiskiem, odwrotnym czy też przeciwnym do klasycznej emisji jest up - konwersja (UC, ang. *upconversion*, *konwersja energii w górę*), która umożliwia konwersję promieniowania z zakresu podczerwieni do światła widzialnego oraz ultrafioletu. Proces ten odpowiada za absorpcję dwóch lub większej liczby fotonów w skutek czego następuje emisja promieniowania o energii wyższej niż zaabsorbowana. Up - konwersja jest również nazywana

emisją anty-Stokesowską. Poniższy schemat przedstawia w uproszczony sposób różnice między fotoluminescencją a luminescencją up - konwersyjną.



Rys. 1. Schematyczne przedstawienie procesów klasycznej luminescencji oraz luminescencji up - konwersyjnej.¹³

Pierwsze informacje o up - konwersji, a właściwie o możliwości wykrycia oraz zliczania fotonów w podczerwieni (IRQC, ang. *Infrared quantum counter*) w ciele stałym za pomocą detektora, pojawiły się w 1959 roku.¹⁴ W 1966 roku Auzel zaproponował mechanizm transferu energii zachodzący pomiędzy stanami wzbudzonymi jonów w procesie up - konwersji.^{15,16} Od tego momentu zainteresowanie zjawiskiem UC wciąż rośnie, do czego znacznie przyczynił się rozwój nanotechnologii w XXI wieku.

Nanomateriały up - konwersyjne ze względu na możliwość wzbudzenia promieniowaniem podczerwonym, umożliwiają głębszą penetrację tkanek biologicznych, nie powodując przy tym ich uszkodzenia, charakteryzują się wysoką stabilnością fotochemiczną, a także dużym przesunięciem anty-Stokesowskim.^{13,17,18} Istotny jest również brak autofluorescencji tła, ze względu na stosowany zakres wzbudzenia.¹⁹ Dodatkową zaletą jest możliwość wykorzystania tanich laserów pracy ciągłej o niskiej mocy ($1-10^3 \text{ Wcm}^{-2}$).¹⁵

Materiały wykazujące up - konwersję

Zjawisko up - konwersji można zaobserwować dla związków które charakteryzują się tzw. budową drabinkową, czyli wykazują wiele długożyjących, metastabilnych poziomów energetycznych. Warunek ten spełniają związki zarówno organiczne, np. wielopierścieniowe węglowodory aromatyczne oraz nieorganiczne np. jony metali z bloku *d* oraz *f*.

Dla większości organicznych nanocząstek up - konwersyjnych emisja promieniowania zachodzi wg mechanizmu **anihilacji tryplet-tryplet** (TTA, ang. *triplet-triplet annihilation*),

polegający na wzbudzeniu sensybilizatora do jego stanu singletowego S_1 , następnie poprzez przejście międzysystemowe do stanu trypletowego T_1 , skąd energia poprzez tzw. transfer energii tryplet-tryplet przechodzi do anihilatora, zwanego również emiterem, a sam wraca do stanu podstawowego S_0 . Gdy pomiędzy dwoma wzbudzonymi anihilatorami w stanie trypletowym zajdzie interakcja, zostaje utworzony wyżej energetyczny stan singletowy z którego następuje emisja UC, a anihilator wraca do stanu podstawowego.^{13,20,21}

Grupę związków nieorganicznych wykazujących UC można podzielić na materiały domieszkowane jonami lantanowców, materiały oparte o metale przejściowe (TM, ang. *transition metals*), materiały zawierające jony Ln^{3+} oraz TM, a także materiały półprzewodnikowe.

Właściwości fizykochemiczne oraz spektroskopowe jonów lantanowców zostały opisane w dalszej części rozprawy (rozdział *Charakterystyka Lantanowców*). W tym podrozdziale zostaną przedstawione jedynie w połączeniu z metalami przejściowymi.

Właściwości **metali przejściowych** należących do bloku *d*, a także zaliczane do tej grupy aniony zawierające w swoim składzie metale *d*-elektronowe (MoO_6^{6-} , VO_4^{3-} , TiO_4^{4-}), ze względu na obecność elektronów na podpowłoce *d* jako elektronów walencyjnych, są silnie zależne od ich chemicznego otoczenia. Szerokie pasma absorpcji są charakterystyczne dla tych metali, a prawdopodobieństwo przejść bezpromienistych pomiędzy ich stanami energetycznymi jest wysokie, szczególnie w temperaturze pokojowej, co znacząco zmniejsza wydajność procesów UC.² Jednakże dużą zaletą tych związków jest możliwość obserwacji przestrajalnej luminescencji w bliskiej podczerwieni (Mn^{2+} , Cr^{3+}), ich właściwości magnetyczne czy katalityczne. Przykładami związków bazujących na metalach przejściowych, które wykazują UC są $MgCl_2:Ti^{2+}$, $CsCdCl_3:Ni^{2+}$, $Cs_2NaYCl_6:Mo^{3+}$.²² W związku z ograniczeniami TM często stosowane jest ich połączenie z Ln^{3+} czy kropkami kwantowymi. Umożliwia to zminimalizowanie relaksacji bezpromienistej oraz wykorzystanie powszechnie stosowanych laserów diodowych jako źródła wzbudzenia, pomimo braku poziomów energetycznych o odpowiedniej energii.

Dość nową grupą związków wykazujących zjawisko up - konwersji, a zarazem bardzo ciekawą są **półprzewodniki nanokrystaliczne (NCs)**, będące połączeniem popularnych kropek kwantowych i cząstek organicznych.^{23,24} Kropki kwantowe wykazują bardzo dobrą absorpcję promieniowania o szerokim spektrum,²⁵ w przeciwieństwie do cząstek organicznych, absorbujących jedynie w zakresie bliskiej podczerwieni, które natomiast są idealnymi emiterami. Mechanizm UC związany jest z anihilacją typu tryplet-tryplet, która opisana została powyżej dla związków organicznych wykazujących UC. W omawianych strukturach, dzięki użyciu półprzewodników (np. CdSe, PbS) jako fotosensybilizatora, a molekuł organicznych jako transmitera (np. kwas antraceno-9-karboksylowy, 9-ACA) oraz anihilatora/emitera (np. 9,10-difenyloantracen, DPA) możliwe jest

osiągnięcie znacznie większej wydajności procesu up - konwersji, nawet ok. 30-40%.²³ Dodatkową zaletą obu materiałów jest możliwość wytworzenia z nich elastycznych urządzeń optoelektronicznych.

Mechanizmy up - konwersji

Obecnie wyróżnia się pięć mechanizmów związanych ze zjawiskiem up - konwersji: **absorpcja w stanie wzbudzonym** (ESA, ang. *excited state absorption*), **up - konwersyjny transfer energii** (ETU, ang. *energy transfer upconversion*), **kooperatywna up - konwersja** (CUC, ang. *cooperative upconversion*), **fotonowy efekt lawinowy** (PA, ang. *photon avalanche*) oraz **up - konwersyjna pośrednia migracja energii** (EMU, ang. *energy mediated- migration upconversion*).¹ Z pośród wymienionych procesów najczęściej obserwowany jest up - konwersyjny transfer energii oraz up - konwersyjna pośrednia migracja energii zachodząca w strukturach typu rdzeń/powłoka.²⁶

Up - konwersyjny transfer energii zachodzi poprzez sekwencyjną absorpcję fotonów, w układzie gdzie występują dwa różne jony- sensybilizator i aktywator, o zbliżonych energiach wzbudzenia oraz będące w niewielkiej odległości od siebie. Mechanizm polega na bezpromienistym przeniesieniu energii od wzbudzonego sensybilizatora do aktywatora, również znajdującego się w stanie wzbudzonym. Dzięki zaabsorbowanej energii możliwe jest osiągnięcie wyższego stanu wzbudzonego.¹⁵ Procesem towarzyszącymi temu mechanizmowi może być przeniesienie energii z asystą fononu, umożliwiając zajście procesu pomimo różnicy energetycznej pomiędzy jonami.²⁷ ETU może również zachodzić innymi drogami, np. poprzez sukcesywny transfer energii, up - konwersyjną relaksację krzyżową czy kooperatywną luminescencję.^{13,17} Mechanizm ten uznawany jest za jeden z najbardziej efektywnych procesów UC, zwłaszcza dla par jonów $\text{Yb}^{3+}/\text{Er}^{3+}$ oraz $\text{Yb}^{3+}/\text{Tm}^{3+}$.^{13,15}

Up - konwersyjna pośrednia migracja energii to mechanizm opisujący transfer energii w strukturach typu rdzeń/powłoka, gdzie fotony zaabsorbowane przez sensybilizator przechodzą kolejno do tzw. akumulatora (typ II), następnie przez donory (typ III) trafiają do jonu aktywatora, emitującego promieniowanie.²⁸ Struktura typu rdzeń/powłoka umożliwia rozdział jonów biorących udział w procesie up - konwersji na różne obszary, dzięki czemu wzajemne wygaszanie się jonów jest minimalizowane. Dodatkową zaletą jest również transfer energii pomiędzy oddalonymi od siebie jonami na większe odległości (kilka nm) bez strat energetycznych. Takie podejście pozwala na domieszkowanie nanomateriałów takimi jonami jak Eu^{3+} , Tb^{3+} czy Dy^{3+} o zawartości zoptymalizowanej do danego zastosowania (od kilku do kilkudziesięciu procent).^{15,26,29}

Charakterystyka Lantanowców

Właściwości fizykochemiczne

Lantanowce to grupa metali z szóstego okresu układu okresowego, o liczbie atomowej od 58 do 71, tj. od ceru do lutetu, które zawierają w swojej budowie elektrony na podpowłóce $4f$. Choć od lantanu wzięła się nazwa grupy i jest on często do niej zaliczany, to formalnie poprzez brak elektronów na podpowłóce $4f$ nie należy on do lantanowców. Jednakże, ze względu na duże podobieństwo fizyczne oraz chemiczne lantanu, a także itru i skandu do opisywanych metali, wspólnie z nimi tworzą one grupę pierwiastków ziem rzadkich.

21 Sc																		
39 Y																		
57 La	58 Ce	59 Pr	60 Nd	61 Pm	62 Sm	63 Eu	64 Gd	65 Tb	66 Dy	67 Ho	68 Er	69 Tm	70 Yb	71 Lu				

Rys. 3. Pierwiastki układu okresowego tworzące grupę pierwiastków ziem rzadkich

Istotną cechą lantanowców jest wspomniane podobieństwo chemiczne, m.in. struktura elektronowa powłoki walencyjnej, długość promienia atomowego i jonowego, trwałe stopień utlenienia +3 czy właściwości paramagnetyczne (z wyjątkiem lutetu).

Konfiguracja elektronowa lantanowców $[Xe] 6s^2 4f^n$ (oraz $5d^1$ jeśli występuje) związana jest z charakterystycznym dla tych pierwiastków stopniowym obsadzaniem podpowłoki $4f$, która jest ekranowana przez wypełnione podpowłoki $5s$ oraz $5p$ o niższej energii. Wszystkie jony lantanowców występują na wspomnianym stopniu utlenienia +3, jako najtrwalszym. Jednakże niektóre jony występują również na stopniu +2 (np. Eu^{2+} , Yb^{2+}) oraz +4 (Ce^{4+} , Tb^{4+}). Najbardziej stabilne struktury elektronowe na trzecim stopniu utlenienia wykazują: La^{3+} , ze względu na brak elektronów f , Gd^{3+} , mający połowicznie wypełnioną podpowłokę $4f$ oraz Lu^{3+} , z 14-stoma elektronami na podpowłóce $4f$.^{30,31}

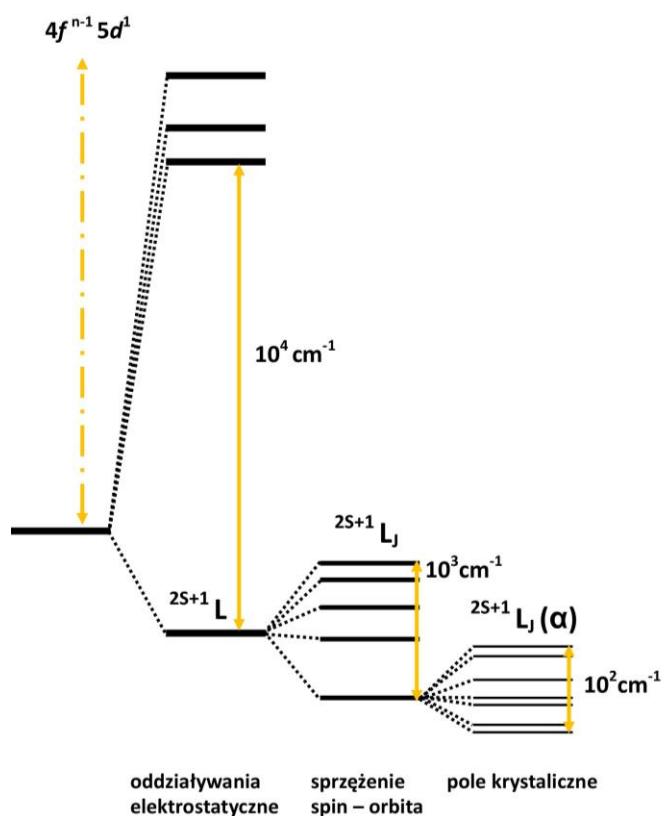
Cechą charakterystyczną dla lantanowców jest również zjawisko kontrakcji, tj. wraz ze wzrostem liczby atomowej, zmniejsza się promień jonowy oraz atomowy danego pierwiastka. Jest to rezultat silniejszego przyciągania elektronów do jądra atomowego, wynikający z rosnącej liczby elektronów przy stałej liczbie powłok elektronowych.³²

Właściwości spektroskopowe pierwiastków ziem rzadkich

Przejścia elektronowe jonów lantanowców można podzielić na trzy rodzaje:

- przejścia z przeniesieniem ładunku (ang. *chargé transfer*, ligand-orbital *f*), polegające na zaabsorbowaniu fotonów przez ligand, stanowiący donor i przekazaniu ich do podpowłoki *4f* jonu Ln^{3+} , który emituje promieniowanie. Przejścia te charakteryzują się dużą intensywnością i szerokością spektralną, występują na widmach absorpcji w zakresie ultrafioletu. Ponadto są przejściami dozwolonymi regułą Laporte'a (następuje zmiana parzystości przejść dipola elektrycznego między poziomami energetycznymi);
- przejścia międzykonfiguracyjne, $nf \rightarrow (n+1)d$, najczęściej $4f - 5d$ obserwowane dla jonów Ce^{3+} oraz Pr^{3+} , przejścia te są przejściami dozwolonymi, charakteryzują się dużą intensywnością w zakresie UV;
- przejścia wewnątrzkonfiguracyjne, $f - f$, najbardziej charakterystyczne dla jonów Ln^{3+} , są to przejścia wzbronione regułą Laporte'a, mimo to pasma tych przejść są obserwowane na widmach lantanowców.^{30,32}

Spośród wymienionych typów, przejścia $4f - 4f$ są najczęstszym przedmiotem badań. Ze względu na ich wzbroniony charakter, głównym czynnikiem wpływającym na elektrony lantanowców są oddziaływania elektrostatyczne oraz w mniejszym stopniu magnetyczne, czego następstwem jest sprzężenie spinowego i orbitalnego momentu pędu elektronów, tzw. sprzężenie spin-orbita bądź sprzężenie Russella-Saundersa. Przedstawia ono rozszczepienie poziomów energetycznych elektronów (termów) podpowłoki $4f$ na poszczególne multiplety, opisywane zależnością pomiędzy liczbami kwantowymi, $^{2S+1}L_J$, gdzie S to spinowy, L orbitalny a J całkowity moment pędu. Jak już wspomniano, w wyniku ekranowania elektronów $4f^n$ poprzez powłoki $5s$ i $5p$, otoczenie jonów Ln^{3+} ma niewielki wpływ na rozszczepienie poziomów energetycznych. Powoduje jednak podział poszczególnych multipletów na tzw. poziomy Starka. Degeneracja tych poziomów zależy od symetrii otoczenia, np. matrycy, im niższa symetria sieci krystalicznej, tym mniejsze rozszczepienie multipletów.^{30,33,34}



Rys. 4 Struktura elektronowa jonów lantanowców. Od lewej- oddziaływania elektrostatyczne, sprzężenie spin-orbita, pole krystaliczne jako czynniki wpływające na degenerację poziomów wraz z wartościami rozszczepień.³⁵

Ze względu opisany powyżej charakter przejść elektronowych $4f - 4f$ w jonach Ln^{3+} , ich widma luminescencji charakteryzują się wąskimi pasmami, o małej szerokości spektralnej. Każdy jon charakteryzuje się specyficznym rozmieszczeniem pasm na widmach emisji, o konkretnej długości fali, dzięki czemu rozróżnienie jonów za pomocą pomiarów spektrofluorymetrycznych jest bardzo łatwe. Dodatkowo przejścia ze stanów wzbudzonych do podstawowego są bardzo wolne, mogą trwać nawet kilka milisekund, co ma szczególne znaczenie przy praktycznym zastosowaniu związków z jonami lantanowców.

Lantanowce a up - konwersja

Lantanowce ze względu na budowę swoich poziomów energetycznych, które są dobrze rozdzielone oraz charakteryzują się długimi czasami życia, stanowią idealny materiał do konwersji energii w górę. Dodatkowo, stany wzbudzone jonów Ln^{3+} znajdują się w zakresie od ultrafioletu do podczerwieni, dzięki czemu możliwa jest obserwacja promieniowania w szerokim spektrum fal.

Budowa materiałów up - konwersyjnych

W temperaturze pokojowej nieorganiczne kryształy wykazują znikomą bądź brak emisji pod wpływem wzbudzenia z zakresu promieniowania podczerwonego.^{5,36} Dlatego nanomateriały up - konwersyjne zbudowane są jonów emitujących/ domieszkujących (guest), będących źródłem UC oraz z nieorganicznej matrycy (host), o strukturze krystalograficznej zapewniającej odpowiednie rozmieszczenie centrów luminescencyjnych.³⁷ Dzięki odpowiedniemu dobraniu obu komponentów możliwe jest sterowanie właściwościami spektroskopowymi nanomateriałów, a tym samym zaprojektowanie materiału o cechach istotnych w konkretnym zastosowaniu.

Dobór odpowiedniej **matrycy** wchodzącej w skład UCNPs ma kluczowe znaczenie przy projektowaniu układów o właściwościach optycznych takich jak wydajność kwantowa czy kolor emisji. Głównym czynnikiem wpływającym na dobór matrycy jest wartość energii drgań sieci krystalicznej, a dokładniej im niższa wartość tym mniejsze prawdopodobieństwo zachodzenia relaksacji bezpromienistej, będącej czynnikiem wygaszającym UC. Duże znaczenie ma również stabilność fizykochemiczna matrycy. Oba wymagania spełniają matryce fluorkowe, które charakteryzują się niską energią fononów ($\sim 350 \text{ cm}^{-1}$) oraz wspomnianą wysoką stabilnością fizykochemiczną, np. NaYF_4 czy LaF_3 ,^{4,6,38} w przeciwieństwie do chlorków czy bromków, które co prawda wykazują niską energię drgania sieci krystalicznej, jednakże ze względu na ich dużą higroskopijność mają ograniczone zastosowania.^{37,39} Z tych względów matryce fluorkowe zostały zastosowane w artykule P1, P2, P3 oraz P4. Powszechnie stosowane są również tlenki, np. Y_2O_3 , Gd_2O_3 .^{15,38,40}

Dodatkowym aspektem wartym rozważenia przy projektowaniu wydajnych UCNPs jest układ krystalograficzny matrycy oraz promień jonowy kationów wchodzących w jej skład. Idealnym przykładem potwierdzającym powyższe stwierdzenie jest matryca NaYF_4 , występująca w układzie regularnym oraz heksagonalnym, gdzie w układzie o niższej symetrii obserwowano nawet 10-krotnie bardziej intensywną UC niż w układzie regularnym.⁴¹ Jest to związane z większą asymetrią pola krystalicznego wokół jonów emitujących, co wpływa na zwiększenie prawdopodobieństwa przejść wzbronionych $4f-4f$ jonów Ln^{3+} .³⁹ Drugi wspomniany aspekt to promień jonowy kationów, który powinien być zbliżony rozmiarem do jonów emitujących, zapobiegając tym samym tworzenie się defektów sieci krystalicznej podczas wymiany jonów, np. jony Na^+ , Ca^{2+} czy Zr^{4+} , mają zbliżone promienie jonowe do jonów lantanowców i ich nieorganiczne związki są często wykorzystywane jako matryce.^{5,42}

Nieorganiczne matryce nie biorą udziału w procesie UC, w związku z czym wymagana jest obecność tzw. **aktywatorów**, tj. jonów domieszkujących matryce, których struktura energetyczna

składa się z wielu metastabilnych stanów wzbudzonych o długich czasach życia. Z tego względu bardzo często stosowanymi aktywatorami są jony lantanowców (Ln^{3+}), zawierające w swojej budowie elektrony na podpowłoce $4f$, pomiędzy którymi zachodzą przejścia $f-f$ elektronowe. W związku z tym dla wszystkich jonów Ln^{3+} mających więcej niż jeden elektron na podpowłoce powinno być obserwowane zjawisko konwersji energii w górę. Jednakże, tylko dla nielicznych jonów można zarejestrować UC (Pr^{3+} , Nd^{3+} , Er^{3+} , Tm^{3+} , Ho^{3+}), z czego tylko Ho^{3+} , Er^{3+} oraz Tm^{3+} wykazują intensywną up - konwersję, ze względu na dobrze rozseparowane stany wzbudzone.

Na wydajność aktywatora wpływ mają takie czynniki jak prawdopodobieństwo zachodzenia przejść bezpromienistych ze względu na niewielkie odległości pomiędzy stanami wzbudzonymi, jego stężenie w matrycy oraz przekrój czynny na absorpcję promieniowania. Niestety, lantanowce wykazujące luminescencję charakteryzują się niskim przekrojem czynnym absorpcji promieniowania NIR, a co za tym idzie niewielką wydajnością UC. Również zwiększenie zawartości aktywatora w matrycy nie jest możliwe, ze względu na proces relaksacji krzyżowej znajdujących się w niewielkiej odległości jonów. Maksymalne stężenie domieszek to np. dla jonu Er^{3+} 3% a dla Tm^{3+} 0.5%.^{13,37,39} Rozwiązaniem tych ograniczeń jest domieszkowanie matrycy dodatkowym jonem, o wysokim współczynniku absorpcji, który będzie pełnił rolę tzw. sensybilizatora, tj. jonu absorbującego promieniowanie NIR, gdzie poprzez mechanizm ETU, wydajnie przenosi energię do jonu aktywatora.¹⁵ Najczęściej wykorzystywane w tym celu są jony Yb^{3+} , ze względu na prostą budowę oraz względnie wysoki przekrój czynny na absorpcję promieniowania o długości 980 nm. Ponadto jony Yb^{3+} wykazują słabszą tendencję do wygaszenia stężeniowego, przez co możliwe jest zwiększenie ilości jonów w matrycy, nawet do 100%.⁴³ Wpływa to na wzrost molowego współczynnika absorpcji jonów Yb^{3+} oraz skrócenie odległości między sensybilizatorem a emiterem, zwiększając tym samym transfer energii.

Możliwości wzmocnienia UC

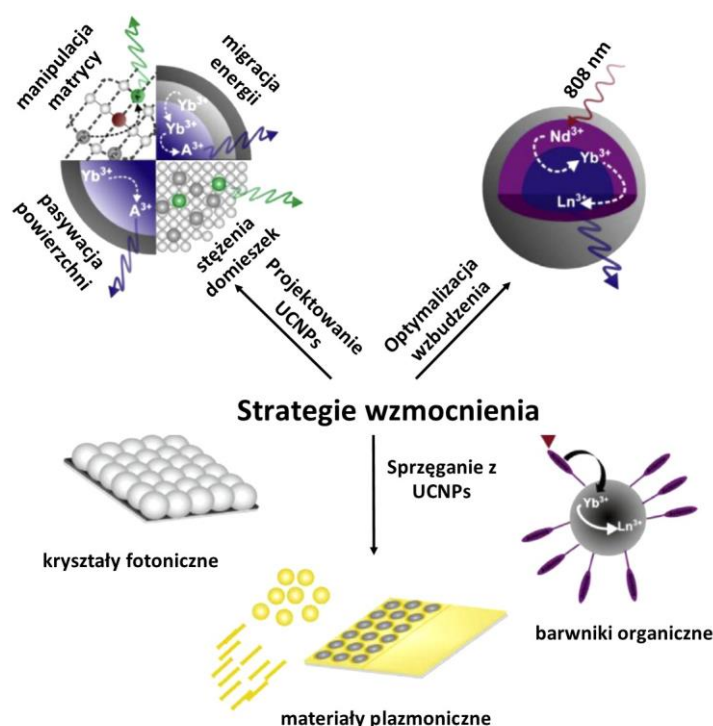
Pomimo wspomnianych powyżej możliwości wzmocnienia UC poprzez zastosowanie jonów Yb^{3+} jako sensybilizatora, czy optymalizację stężenia domieszek w matrycy, obserwowana luminescencja jest nadal znacznie mniej wydajna niż np. dla barwników organicznych. Ograniczenie bowiem stanowi nie tylko niewielki przekrój czynny na absorpcję jonów Ln^{3+} (np. Yb^{3+} jako sensybilizator wykazuje ok. 1000-10 000 razy mniejszy przekrój czynny na absorpcję niż powszechnie stosowane barwniki organiczne), niska wartość molowego współczynnika absorpcji promieniowania z zakresu NIR,^{10,44} procesy relaksacji krzyżowej między jonami znajdującymi się w niewielkich odległościach między sobą oraz idący za tym brak możliwości zwiększenia wspomnianego przekroju czynnego,⁴⁴ ale również niewielki rozmiar cząstek czy ligandy

powierzchniowe oraz medium w którym znajdują się cząstki. Nanometryczny rozmiar, gdzie obserwuje się duży stosunek powierzchni NPs do jej objętości, a tym samym obecność większości jonów na powierzchni, prowadzi do defektów sieci oraz wygaszenia emisji poprzez jej otoczenie.⁴⁴ Natomiast ligandy powierzchniowe oraz medium rozpraszające są często bogate w oscylatory -OH, -NH, czy -CH, których energie wibracyjne mają podobne wartości do poziomów energetycznych jonów Ln³⁺, przez co znacznie wygaszają procesy relaksacji promienistej.⁴⁵

Jednakże ze względu na interesujące właściwości UCNP's zawierające jony Ln³⁺, takie jak brak autofluorescencji tła, wysoki stosunek sygnału do szumów, wąskie pasma absorpcji i emisji oraz długie czasy życia, naukowcy testują nowe metody syntezy oraz strategie mające na celu wzmocnienie luminescencji wspomnianych nanomateriałów up - konwersyjnych.

Najpowszechniej stosowane strategie w celu wzmocnienia obserwowanej UC to racjonalne projektowanie materiałów wykazujących ten proces oraz połączenie UCNP's z innymi materiałami.

Do pierwszej strategii zalicza się odpowiedni dobór matrycy oraz jonów emitujących, w tym ich stężenie, optymalizacja transferu energii między jonami, pasywacja powierzchni cząstek, projektowanie struktur typu core/shell, a także modyfikacja wzbudzenia UC. Drugi rodzaj wzmocnienia UC bazuje na połączeniu nanocząstek wykazujących emisję z plazmonami powierzchniowymi, kryształami fonicznymi oraz barwnikami organicznymi.



Rys. 5 Strategie wzmocnienia up - konwersji.⁴⁶

W podrozdziale **Budowa materiałów up - konwersyjnych** została już opisana strategia wzmocnienia UC poprzez odpowiedni dobór matrycy oraz domieszek. Warto jednak wspomnieć

również, iż na wzmocnienie obserwowanej luminescencji może wpłynąć **dodatek takich jonów** jak Li^+ , Na^+ , czy metali przejściowych np. Sc^{3+} , Bi^{3+} , Zn^{2+} , Fe^{3+} , poprzez zwiększanie asymetrii struktury krystalograficznej,⁴⁷⁻⁴⁹ co przedstawiono w artykule **P1** oraz **P2**. Może to powodować częściowo dozwolony charakter przejść elektronowych ze względu na mieszanie się poziomów $4f$ z poziomami energetycznymi dodatkowych jonów (np. $d-f$). Inny efekt wpływający na zwiększanie luminescencji poprzez dodatkowe domieszkowanie wspomnianymi jonami to m.in. zmniejszenie wielkości komórki elementarnej czy zwiększenie sprzężenia elektron-foton.⁴⁴

Racjonalne projektowanie nanomateriałów zakłada niskie stężenia jonów emitujących ze względu na procesy relaksacji krzyżowej. Co ciekawe, zastosowanie **dużej mocy lasera**, (powyżej energii powodującej efekt wysycenia, nawet do $5 \times 10^6 \text{ W cm}^{-2}$)^{50,51} może częściowo zniwelować wygaszanie UC przy zastosowaniu wysokich zawartości jonów Ln^{3+} , wpływać na zmianę barwy emisji czy fotonowość procesu.^{50,52} Również zastosowanie kilku długości fal wzbudzenia np. 980 oraz 1532 nm w tym samym momencie, wpływa pozytywnie na efektywność up - konwersji.⁵³

Inna możliwość poprawienia wydajności UC wiąże się z użyciem długości fali wzbudzenia różnej od powszechnie stosowanego 980 nm. Główną zaletą takiego podejścia jest zminimalizowanie efektu nagrzewania się komórek, wynikającego z wysokiej absorpcji promieniowania o długości fali 980 nm przez wodę, która stanowi ich główny składnik. Rozwiązaniem tego problemu jest **skrócenie długości fali wzbudzenia** poprzez zastosowanie jonów Nd^{3+} , absorbujących promieniowanie o długości ok. 808 nm, gdzie absorpcja wody jest znacznie niższa. Co istotne, Nd^{3+} może pełnić rolę sensybilizatora jak i aktywatora.⁵⁴ Stosuje się również domieszkowanie matrycy jonami Nd^{3+} wraz z Yb^{3+} oraz jonem emitera, jednakże ze względu na proces relaksacji krzyżowej pomiędzy jonami, stężenie Nd^{3+} nie może przekraczać ok. 2-3%. W celu ominięcia tego ograniczenia, powstała koncepcja kaskadowego transferu energii, gdzie jony Nd^{3+} byłyby oddzielone od jonów emitera w strukturze typu aktywny rdzeń/aktywna powłoka ($\text{NaYF}_4:\text{Nd}^{3+}/\text{Yb}^{3+}/\text{Er}^{3+}@\text{NaYF}_4:\text{Nd}^{3+}/\text{Yb}^{3+}$) zaproponowanej przez Huang i Lin.⁵¹

Projektowanie struktur typu **core/shell** umożliwia wzmocnienie obserwowanej luminescencji poprzez uzyskanie efektywnego transferu energii między jonami, pasywację powierzchni oraz zmianę długości fali wzbudzenia.

Pierwsze badania odnośnie struktur core/shell pojawiły się w 2007 gdzie Yi oraz Chow⁵¹ zastosowali pokrycie matrycy zawierającej jony Ln^{3+} , $\text{NaYF}_4:\text{Yb}^{3+}$, Er^{3+} (Tm^{3+}) pasywną warstwą ochronną, NaYF_4 , oddzielającą jony od otaczającego je medium,⁵⁵ np. cząsteczek wody, osiągając 29 - krotne wzmocnienie emisji w porównaniu do emisji samego rdzenia. Struktury typu rdzeń/powłoka zabezpieczają również przed zmniejszeniem emisji spowodowanej przypadkową migracją energii od wzbudzonych jonów do wygaszaczy na powierzchni cząstek. Powłoka ta może

zostać otrzymana poprzez wzrost anizotropowy, mieszanie się rdzenia oraz powłoki, a także poprzez nukleację cząstek powłoki na rdzeniu.^{56–58} Często powłoki bazują na takich samych matrycach jak rdzenie. Jednakże gdy są to struktury heterogeniczne najczęściej stosowane związki jako powłoki to NaYF₄, CaF₂, SrF₂ oraz krzemionka, ze względu na możliwość dalszej modyfikacji oraz biokonjugacji. Istotna jest również grubość warstwy ochronnej, najczęściej wynosząca kilka nm, która jest często ściśle powiązana z intensywnością luminescencji, umożliwiając jej wzrost nawet kilkudziesięciokrotnie.⁵⁸ Jest to szczególnie ważna strategia dla małych cząstek (poniżej 20 nm), gdzie większość jonów występuje na powierzchni NPs ze względu na duży stosunek powierzchni do jej objętości. Powoduje to wygaszanie emisji poprzez zachodzące procesy relaksacji krzyżowej pomiędzy położonymi w niewielkiej odległości od siebie jonami jak i oddziaływania NPs z otaczającymi je ligandami oraz środowiskiem.^{10,46}

Interesującym rozwiązaniem jest również pokrycie rdzenia **aktywną powłoką**, tzn. domieszkowaną jonami, np. Yb³⁺, dzięki czemu możliwe jest zastosowanie większej ilości sensybilizatora, a tym samym zwiększenie absorpcji promieniowania. Poprzez zastosowanie struktury rdzeń/powłoka energia może być przeniesiona z jonów Yb³⁺ znajdujących się w powłoce do jonów Yb³⁺ w rdzeniu, a następnie do jonów emitera.^{28,59,60} Takie rozwiązanie umożliwia lepsze rozłożenie jonów w matrycy minimalizując zachodzenie relaksacji krzyżowej czy przejść bezpromienistych.⁴⁶ Otrzymane zostały również bardziej zaawansowane struktury, tzw. multipowłokowe (ang. *multilayer shell*), umożliwiające domieszkowanie każdej powłoki innym jonem. Dzięki temu możliwe jest uzyskanie przestrajalnej luminescencji czy wzbudzenie pod wpływem różnych długości fal, np. 980 oraz 808 nm, waz ze znacznym wzmocnieniem luminescencji.^{61–63} Dodatkowo, wspomniane struktury umożliwiają zastosowanie większego stężenia jonów Nd³⁺ niż było to w przypadku potrójnie domieszkowanej matrycy (np. jonami Yb³⁺, Er³⁺ oraz Nd³⁺), uzyskując dzięki temu emisję UC pod wpływem 808 nm o podobnej bądź nawet większej efektywności.^{63–65} Taka strategia wzmocnienia UC oraz skrócenie długości fali wzbudzenia zastosowano w artykule **P3**, gdzie właściwości luminescencyjne struktury rdzeń/powłoka zostały porównane z właściwościami trójdomieszkowanej matrycy, dla której zaobserwowano znaczne wygaszenie luminescencji. Ponadto, stosując odpowiednie metody syntezy można sterować bardzo precyzyjnie grubością powłok, a tym samym końcowym rozmiarem cząstek.^{66–68}

Druga strategia wzmocnienia up - konwersji opiera się na połączeniu nieorganicznych nanocząstek zawierających jony lantanowców z barwnikami organicznymi, plazmonami powierzchniowymi oraz kryształami fonicznymi.

Plazmony powierzchniowe mogą być wytworzone przez metale lub półprzewodniki, poprzez ich naświetlenie, w wyniku którego uwolnione elektrony gromadzą się na powierzchni danego

materiału, gdzie poprzez oscylację tworzą powierzchniowy rezonans plazmonowy.^{44,69,70} Najczęściej wykorzystywane metale do wzmocnienia absorpcji jak i emisji w procesie UC to złoto oraz srebro w postaci metalicznych nanocząstek, powłok lub cienkich warstw.^{15,71}

Kryształy fotoniczne to dielektryczne materiały optycznie, o periodycznie zmieniającym się współczynniku załamania światła, wpływając tym samym na ruch fotonów. Ze względu na naprzemiennie występujące warstwy o dużym i małym współczynniku załamania światła, część fal jest przepuszczana, a część jest odbita. Podobnie jak w kryształach występuje pasmo wzbronione, tzw. fotoniczna przerwa energetyczna. Kryształy fotoniczne mogą wpływać na długość fali emisji, jej kierunek i intensywność. W celu wzmocnienia absorpcji jak i emisji UC wykorzystuje się kryształy na bazie odwróconego opalu, krzemionki, azotku krzemu czy siarczku kadmu.⁷²⁻⁷⁵

Znaczne wzmocnienie UC jest również obserwowane poprzez połączenie UCNPs z molekułami organicznymi, a dokładniej **barwnikami organicznymi**, zawierające w swojej budowie układy sprzężonych wiązań π (tzw. chromofory). Umożliwiają one znacznie większą absorpcję promieniowania w szerokim zakresie, charakteryzując się nawet 10 000 - krotnie większym przekrojem czynnym na absorpcję od jonów Ln^{3+} .⁷⁶ Dodatkowo możliwa jest zmiana długości fali wzbudzenia, np. 808 nm co pozwoli na zminimalizowanie efektu nagrzewania się układu.⁷¹

Modyfikacja powierzchni

Dzięki połączeniu specyficznych właściwości fizykochemicznych oraz optoelektronicznych NPs z biologiczną aktywnością (np. selektywne wiązanie) możliwe jest otrzymanie wyspecjalizowanych narzędzi diagnostycznych oraz terapeutycznych. Jednakże, aby stworzenie takich układów było możliwe, powierzchnia nanocząstek powinna być hydrofilowa, biokompatybilna, o niskiej toksyczności. Z tego względu oraz poprzez stosowane metody syntezy nanocząstek (głównie w rozpuszczalnikach organicznych powodując obecność hydrofobowych ligandów na powierzchni NPs) wymagana jest modyfikacja powierzchni UCNPs. Główne strategie modyfikacji to usunięcie ligandu, wymiana ligandu, utlenianie ligandu, absorpcja ligandu, silanizacja powierzchni oraz osadzanie warstw na powierzchni cząstki. Najpowszechniej stosowane metody zostaną opisane poniżej.

Usunięcie liganda, (ang. *ligand removal*), najczęściej organicznego z powierzchni nanocząstek poprzez protonację, jest metodą bardzo prostą i często stosowaną. Potraktowanie NPs z kwasem oleinowym na powierzchni kwasem solnym w środowisku kwaśnym (pH 4) powoduje jego uwolnienie. Drugim etapem tej modyfikacji jest przyłączenie grup elektroujemnych, takich jak -SH,

- COOH, - NH₂ oraz - OH do powierzchni nanocząstek, w celu umożliwienia biokoniugacji do molekuł.⁷⁷ Inny używany odczynnik do usunięcia liganda to roztwór tetrafluoroboranu nitrosonu (NOBF₄) w dimetylosulfotlenku (DMSO) lub dimetyloformamid (DMF).⁷⁸

Równie efektywną metodą jest **absorpcja ligandu** (ang. *ligand attraction*), gdzie zachodzą oddziaływania van der Waals'a pomiędzy hydrofobowymi częściami oryginalnego liganda oraz nowego (najczęściej polimery amfifilowe), przy czym drugi koniec polimeru, hydrofilowy, poprawia powinowactwo cząstek do wody, a tym samym umożliwia stworzenie stabilnych wodnych koloidów.⁷⁹ Najczęściej stosowane układy polimerowe to poli(L-lizyna) (PLL), kwas 6 - aminoheksanowy (6AA), kwas poliakrylowy (PAA), zastosowany w artykule P2, kopolimer glikolu polietylenowego oraz polikaprolaktonu (PEG-block-PCL), bezwodnik polimaleinowy-alt-1-oktadecen (PMAO), oktyloamina-kwas poliakrylowy- glikol polietylenowy (OA-PAA-PEG) oraz inne.^{5,77,79-81}

Równie często wykorzystywana metoda, to pokrywanie NPs **powłoką krzemionkową** oraz **silaniczacja powierzchni** (ang. *silica shell and surface silanisation*). Modyfikacja ta polega na pokryciu nanocząstek cienką warstwą krzemionki, którą następnie można modyfikować pochodnymi silanowymi, bogatymi w grupy aminowe, karboksylowe czy tiolowe. Obie modyfikacje można przeprowadzić w tym samym etapie, bądź jeden po drugim. Modyfikacja powierzchni krzemionką ma wiele zalet, powłoka krzemionkowa jest całkowicie transparentna, nietoksyczna, biokompatybilna, nie wpływa (bądź w bardzo niewielkim stopniu) na właściwości optyczne materiału, może być stosowana zarówno dla materiałów hydrofilowych jak i hydrofobowych, przy czym te ostatnie dzięki modyfikacji mogą zostać zdyspergowane w wodzie.^{5,78,80} W celu pokrywania cząstek warstwą krzemionki oraz przeprowadzeniu procesu silaniczacji, stosowana jest metoda Stöbera oraz odwróconych mikroemulsji.⁷⁷

Zastosowania UCNPs

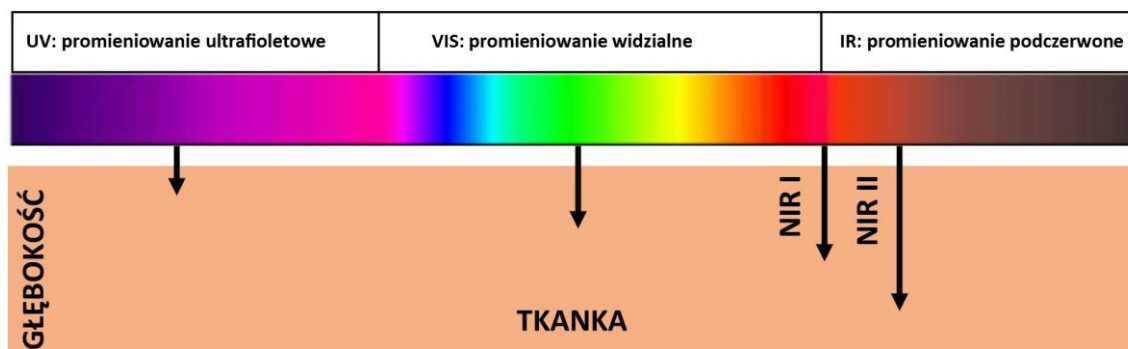
Ze względu na unikalne właściwości UCNPs domieszkowanych jonami lantanowców (wąskie pasma na widmach wzbudzenia i absorpcji, stabilność fotochemiczna, duże przesunięcie anty - Stokesowskie, wzbudzenie w zakresie podczerwieni, brak autofluorescencji tła oraz niezubywanie się materiału) są one powszechnie wykorzystywane w wielu dziedzinach nauki jak i codziennego życia.

Duża grupa UCNPs wykorzystywana jest w zaawansowanych technologiach czy optoelektronice (np. ogniwa słoneczne, lasery półprzewodnikowe, wzmacniacze światłowodowe, wyświetlacze 3D, falowody optyczne).⁸²⁻⁸⁷ Coraz więcej badań prowadzonych jest również w obszarze zabezpieczeń dokumentów, papierów wartościowych, leków oraz kryminalistyce (odciski

palców).^{88,89} Ciekawe zastosowanie przedstawił You i inni, wykorzystując fluorescencyjne kody QR oparte o UCNPs wykorzystujące trzy kolory (czerwony, zielony oraz niebieski, RGB) do znakowania kapsułek leków z możliwością znalezienia informacji o nim w dedykowanej aplikacji po zeskanowaniu kodu.⁹⁰ Nieorganiczne nanomateriały up - konwersyjne wykorzystywane są również w reakcjach fotokatalizy czy fotoizomeryzacji.^{13,91-93}

Materiały UC mają również szerokie zastosowanie analityczne, do wykrywania określonego pH, temperatury, jonów metali, anionów, wolnych rodników czy biomolekuł.^{79,94-99} Najczęściej detekcja odbywa się w wyniku rezonansowego transferu energii (LRET, lub FRET), gdzie nanocząstki stanowią donor energii, a badana substancja akceptor. W wyniku obecności w analizie danej substancji, obserwuje się zmiany w widmach absorpcji czy różnice w odległościach między donorem i akceptorem.⁷⁹

Jednakże najwięcej badań i ciekawych rozwiązań wiąże się z zastosowaniem UCNPs w biologii, medycynie oraz naukach pokrewnych. Coraz częstsze zastosowanie we wspomnianych dziedzinach jest związane z istnieniem tzw. okna optycznego zwanego też biologicznym. Wyróżnia się trzy okna optyczne, pierwsze, (NIR I, 750-900 nm), drugie, (NIR II, 1100-1350 nm) oraz trzecie (NIR III, 1500-1700 nm).¹⁰⁰⁻¹⁰² Stosując wzbudzenie w przedstawionych zakresach, możliwa jest głęboka penetracja tkanek (im większa długość fali tym głębsza penetracja, Rys.6), przy zmniejszonym rozpraszaniu fotonów i minimalnej autofluorescencji. Dodatkowo ze względu na zastosowanie promieniowania podczerwonego, szkodliwy wpływ na zdrowe komórki jest zmniejszony w porównaniu do wzbudzenia UV.



Rys. 6 Schematyczna penetracja tkanki przez promieniowanie o różnej długości fali.¹⁰³

Przykładami zastosowań UCNPs w biologii czy medycynie jest przede wszystkim bioobrazowanie (np. luminescencja UC, połączenie luminescencji UC z techniką rezonansu magnetycznego czy z tomografią komputerową, środki kontrastowe),⁷⁹ terapię komórkową (terapia fotodynamiczna, fototermiczna),¹⁰⁴ wspomniane już sensory temperatury i pH^{96,105,106}

oraz biomolekuł,¹⁰⁷ monitorowanie uwalniania leków oraz ich dostarczanie,^{108,109} testy diagnostyczne¹¹⁰ i inne.

Bardzo ciekawą oraz rozwijającą się techniką jest optogenetyka, gdzie za pomocą światła prowadzona jest kontrola oraz stymulacja neuronów. Wprowadzone do organizmu UCNPs mogą np. poprzez zieloną lub niebieską luminescencje wywołaną promieniowaniem NIR stymulować/hamować dane neurony np. brzuszego obszaru nakrywkowego (VTA) mózgu.¹¹¹

Szeroko rozwijają się również techniki obrazowania, jak obrazowanie 3D czy Mikroskopia Wymuszonego Wygaszania Emisji. Obrazowanie 3D komórek oparte o UCNPs jest możliwe poprzez mikroskopię konfokalną, pozwalającą na uzyskanie obrazów o wysokim kontraście i rozdzielczości. Co ciekawe, możliwe jest śledzenie pojedynczej komórki. Następcą mikroskopii konfokalnej jest natomiast Mikroskopia Wymuszonego Wygaszania Emisji (*STED*, ang. *STimulated Emission Depletion*), w której dzięki pokonaniu limitu dyfrakcyjnego uzyskuje się obrazy o wysokiej rozdzielczości.⁶ Ze względu na brak obserwowanego fotowysbielenia UCNPs, w przeciwieństwie do stosowanych w tej technice barwników organicznych, nanocząstki zawierające jony Ln^{3+} są z powodzeniem wprowadzane do mikroskopii STED.^{112,113}

Toksyczność UCNPs

Coraz szersze wykorzystanie nanocząstek zawierających jony Ln^{3+} w wielu dziedzinach nauki wymaga rozważenia ich wpływu na organizmy żywe oraz środowisko naturalne, m.in. toksyczność, usuwanie z organizmu, degradacja czy rozkład. Ze względu na krótki okres badań nad nanomateriałami up - konwersyjnymi, a także ich wciąż niewielkie wykorzystanie w życiu codziennym, trudno obecnie przewidzieć wpływ UCNPs na nas samych i środowisko w dłuższej perspektywie czasu. W związku z tym bardzo istotne są badania określające oddziaływania nanocząstek na oraz z organizmami żywymi i materią nieożywioną.¹⁰

Wpływ na toksyczność nanocząstek może mieć ich rozmiar, kształt, ładunek i modyfikacja powierzchni, skład i zawartość danych pierwiastków oraz czystość produktu, a także stabilność w wodzie.^{114,115} Pomimo prowadzonych testów *in vitro*, trudno przewidzieć jak nanocząstki mogą się zachowywać w organizmach o dużo bardziej złożonej budowie.¹¹⁶ Jednakże dotychczasowe badania wskazują na znikomą cytotoxycywność UCNPs na bazie lantanowców. Wg Li i pozostałych, nanocząstki $\text{NaYF}_4:\text{Yb}^{3+},\text{Tm}^{3+},\text{Gd}^{3+}@\text{PEG}$ po wstrzyknięciu myszom, po 1 h akumulują się głównie w wątrobie i śledzionie, po 24 h ich największa ilość znajduje się w nerkach, malejąc tym samym w wątrobie i śledzionie, a po 30 dniach niewielka ilość znajduje się w płucach. Dodatkowo zbadano wpływ nanocząstek na komórki śledziony i nerek, nie odnotowując ich negatywnego wpływu.¹¹⁷ Również inne badania

przedstawiają znikomą bądź brak toksyczności UCNPs dla komórek i organizmów, przy czym bardzo duże znaczenie ma rodzaj ligandów znajdujących się na powierzchni cząstek.^{79,118–124}

Zwraca się jednak uwagę na możliwość generowania przez nanocząstki reaktywnych form tlenu (ROS), który może negatywnie wpływać na procesy odbywające się w komórkach, a także powodować ich uszkodzenia.¹¹⁶ Z drugiej jednak strony ROS lub tlen singletowy ($^1\text{O}_2$) może niszczyć komórki chorobowe w organizmie, np. komórki nowotworowe. Odpowiednie połączenie nanocząstek z określonym fotouczulaczem (np. ftalocyjaniną cynku, ZnPc, tetrafenyloporfiryną, błękitem metylenowym czy różem bengalskim), absorbującym promieniowanie emitowane przez NPs, a następnie wytwarzającym ROS, powoduje skierowanie reaktywnych form tlenu na komórki które mają ulec zniszczeniu.^{124–127}

Istotny aspekt to również trwałość i stabilność nanocząstek. Możliwość rozpuszczania się materiału w wodzie, może spowodować uwalnianie jonów takich jak fluor,¹²⁸ który gromadzony w nadmiarze w organizmie powoduje zaburzenia wielu procesów enzymatycznych. Dodatkowo, brak odpowiedniej trwałości może spowodować uwalnianie się jonów lantanowców. Kolejny niepokojący aspekt to często występujące agregacje nanocząstek, gromadzące się w narządach, gdzie makrofagi mogą spowodować ich rozkład, a powstające związki negatywnie wpływać na procesy zachodzące w komórkach i je same.¹²⁹ Tworzące się agregaty mogą również tamować naturalny przepływ krwi.¹¹⁵

Nanomateriały up - konwersyjne, zawierające jony Ln^{3+} mają bardzo szerokie możliwości aplikacyjne w biologii i medycynie, jednakże istotne jest również bardzo dokładne zbadanie efektów niepożądanych jakie mogą wystąpić w organizmach przy ich stosowaniu. Pomimo badań *in vitro* oraz *in vivo* wskazujących na niską toksyczność NPs, badania fizykochemiczne UCNPs jak ich interakcje z komórkami, tkankami i skomplikowanymi żywymi organizmami są bardzo istotne. Bez dokładnych testów i analiz wpływu nanocząstek, zwłaszcza w trakcie długotrwałego oddziaływania z organizmami, ich bezpieczne stosowanie będzie niemożliwe.

Metody syntezy nanomateriałów użyte w pracy doktorskiej

W pracy doktorskiej została wykorzystana metoda hydrotermalna jedno- bądź dwuetapowa. Jest to metoda syntezy, prowadzona w warunkach wysokiego ciśnienia (do 250 MPa) i temperatury (max 300°C), w specjalnym autoklawie, gdzie woda pełni rolę rozpuszczalnika. Umożliwia ona otrzymanie produktu o wysokim stopniu krystalizacji, charakterze hydrofilowym, małym rozmiarze oraz zapewnia kontrolę warunków syntezy. Dodatkowo, przeprowadzana w środowisku wodnym nie wytwarza toksycznych produktów ubocznych.^{42,130}

Najważniejsze metody charakterystyki nanomateriałów użyte w pracy doktorskiej

Główne metody charakterystyki nanomateriałów można podzielić na dwie grupy, pierwsza opisuje właściwości fizykochemiczne oraz morfologiczne, a druga spektroskopowe.

Metody opisujące właściwości morfologiczne:

Dyfrakcja promieniowania rentgenowskiego (XRD, ang. *X-ray diffraction*), pozwala na określenie struktury krystalograficznej badanych nanokryształów na podstawie dopasowania do wzorca z krystalograficznej bazy danych. Dodatkowo, możliwe jest wyznaczenie parametrów komórki oraz obliczenie wielkości kryształitów poprzez wykorzystanie równania Scherrer'a. Poznanie struktury umożliwia zjawisko interferencji, zachodzące na płaszczyznach kryształu. Dyfraktogram powstaje poprzez rejestrację obrazów dyfrakcyjnych, tworzących się poprzez oddziaływanie promieniowania rentgenowskiego z chmurą elektronów wokół atomu. Promieniowanie odbijane jest od kryształu pod różnymi kątami θ , tworząc przestrzenny obraz komórek, z których zbudowany jest kryształ.

Transmisyjna mikroskopia elektronowa (TEM, ang. *transmission electron microscopy*), to wysokorozdzielcza metoda służąca do obrazowania struktury wewnętrznej nanomateriału, pozwala określić wielkości poszczególnych nanokryształów oraz analizę ich morfologii. Jest to możliwe poprzez oddziaływanie wiązki wysokoenergetycznych elektronów z badanym materiałem, gdzie część elektronów przechodzi przez próbkę i trafia do detektora, a część z nich ulega rozproszeniu na atomach badanej próbki. Rozproszenie jest tym większe, im wyższa jest liczba atomowa pierwiastków wchodzących w skład próbki.

Spektroskopia dyspersji energii promieniowania rentgenowskiego (EDX/EDS ang. *Energy-dispersive X-ray spectroscopy*), umożliwia poznanie składu pierwiastkowego oraz ilościowego danej próbki na podstawie oddziaływań wiązki elektronów z atomami w próbce, które następnie wytwarzają promieniowanie X i przesyłają go do detektora, przetwarzającego sygnał, formując w ten sposób widmo.

Analiza elementarna, metoda służąca do określenia zawartości jonów takich jak azot, węgiel, wodór i siarka w próbce. Analiza przeprowadzana poprzez pomiar powstających tlenków, będących wynikiem przeprowadzonego katalitycznego spalania próbki w temperaturze 1200°C.

Optyczna spektrometria emisyjna ze wzbudzeniem w plazmie indukcyjnej sprzężonej (ICP - OES ang. *inductively coupled plasma optical emission spectrometry*) oraz **Spektrometria mas ze**

wzbudzeniem w plazmie indukcyjnie sprzężonej (ICP-MS, ang. *Inductively Coupled Plasma Mass Spectrometry*), metody służące do określania składu oraz wykrywania śladowych ilości metali w badanej próbce, poprzez jonizację w plazmie, a następnie określenie ilości za pomocą spektroskopii emisyjnej/spektrometru masowego.

Spektroskopia w podczerwieni, (FT-IR, ang. *Fourier transform infrared spectroscopy*), określenie obecności związków organicznych oraz nieorganicznych w badanym materiale, poprzez absorpcję przez cząstki promieniowania z zakresu podczerwonego, o porównywalnej energii do energii drgań oscylacyjnych/rotacyjnych wiązań chemicznych, charakterystycznych dla obecnych w próbce grup funkcyjnych.

Dynamiczne rozpraszanie światła, (DLS, ang. *Dynamic light scattering*) oraz **potencjał zeta** (ang. *Zeta potential*), metody umożliwiające pomiar średnicy hydrodynamicznej nanocząstek, stopnia tworzenia przez nie agregatów oraz ich ładunek powierzchniowy. Analiza rozmiaru cząstek wykonywana jest na podstawie zbierania przez detektor światła rozproszonego przez cząstki znajdujące się w próbce w stanie ciekłym, będące w ciągłym ruchu, na skutek ruchów Browna. Natomiast potencjał zeta zostaje obliczony na podstawie ruchliwości elektroforetycznej, wywołanej poprzez przyłożone do próbki pole elektryczne.

Spektroskopia luminescencyjna

Spektroskopia luminescencyjna to metoda badająca emisję promieniowania elektromagnetycznego przez badaną substancję. W przypadku nanomateriałów up - konwersyjnych, źródłem wzbudzenia są lasery pracy ciągłej (CW), emitujące promieniowanie o stałym natężeniu lub lasery impulsowe, emitujące impulsy. W celu określenia właściwości spektroskopowych wykonuje się pomiary widm wzbudzenia i emisji, krzywe zaniku luminescencji, zależność intensywności emisji od mocy lasera oraz pomiary wydajności kwantowej. Na podstawie widm emisji i wzbudzenia w zakresie NIR - światło widzialne – UV, wiele istotnych informacji, takich jak zależność pomiędzy strukturą, morfologią, oraz zawartością jonów Ln^{3+} w związku a efektywnością obserwowanej emisji czy poznanie mechanizmów biorących udział w UC, mających wpływ na obserwowane wzbudzenie i emisję, może być określona. Na podstawie widm emisji można również wyznaczyć koordynaty chromatyczności, określające rzeczywistą barwę próbki.

Wiele cennych informacji odnośnie kinetyki procesów promienistych w badanych układach dostarczają pomiary narostów oraz zaników luminescencyjnych, na podstawie których oblicza się czasy życia dla przejść energetycznych danego jonu. Również wykonanie pomiarów

przedstawiających zależność intensywności emisji próbki od mocy lasera, umożliwia poznanie ilości fotonów biorących udział we wzbudzeniu danego poziomu energetycznego.

Istotne są również pomiary wydajności kwantowej (QY, ang. *quantum yield*), danego materiału, którą określa się na podstawie stosunku jonów wyemitowanych do zaabsorbowanych. Znaczenie tych pomiarów jest tym bardziej istotne, gdyż jest to jedyna wartość dzięki której można porównać próbki pochodzące z różnych laboratoriów między sobą, ze względu na duże podobieństwo w technice wykonywania pomiarów, czego niestety nie można powiedzieć o pozostałych badaniach spektroskopowych.

Część eksperymentalna

P1. Tailoring structure, morphology and up - conversion properties of $\text{CaF}_2:\text{Yb}^{3+},\text{Er}^{3+}$ nanoparticles by the route of synthesis

Fluorki metali ziem alkalicznych mają szerokie zastosowanie w zaawansowanych technologiach, a także biologii oraz medycynie. Budowa ich sieci krystalicznej charakteryzuje się niską energią fononów, (drgań sieci), a związki, które tworzą, są stabilne, stanowią dobry akceptor elektronów, a także luminofory na ich bazie charakteryzują się wysoką wartością wydajności kwantowej luminescencji. Dodatkowo jony metali ziem alkalicznych mają podobny promień jonowy do jonów lantanowców, dzięki czemu możliwe jest wbudowywanie się jonów Ln^{3+} w ich miejsce, bez powodowania zniekształceń w sieci krystalicznej. Pomimo iż ich wydajność kwantowa jest niższa od luminoforów opartych o NaYF_4 , to stanowią przedmiot wielu badań. Jednakże ze względu na rosnące zainteresowanie nanomateriałami up - konwersyjnymi oraz coraz większymi wymaganiami odnośnie powtarzalności syntez, monodispersyjności związków oraz efektywnej luminescencji, istotna jest optymalizacja strategii syntezy i jej przeprowadzanie. W związku z tym wykonano szereg syntez fluorku wapnia, CaF_2 , domieszkowanego jonami Yb^{3+} oraz Er^{3+} różniących się między sobą zastosowanym surfaktantem podczas syntezy, zmienną ilością fluorku amonu, (stosowanego jako źródło jonów fluoru oraz czynnik strącający), różną objętością roztworu zawierającego prekursor nanocząstek, a także brak lub obecność mieszania w trakcie syntezy. Wyniki badań zostały zawarte w publikacji **P1**. Przedstawiony został znaczący wpływ surfaktantu, cytrynianu sodu, na otrzymany produkt oraz jego właściwości spektroskopowe. Zaobserwowane zostało również jednoczesne tworzenie się struktury heksagonalnej jak i klasterów dla jonu Yb^{3+} , jako rezultat wprowadzenia jonów Na^+ do sieci krystalicznej, w celu uzyskania kompensacji ładunku po domieszkowaniu matrycy jonami Ln^{3+} . Na podstawie analizy otrzymanych wyników ustalono optymalne warunki syntezy hydrotermalnej fluorku wapnia domieszkowanego jonami iterbu oraz erbu, (czas trwania reakcji 12 h, niewielki nadmiar jonów fluoru (1, 5), cytrynian sodu jako surfaktant, mała objętość (50 mL) oraz brak mieszania roztworu podczas syntezy), które umożliwiły otrzymać NPs charakteryzujące się niewielkim rozmiarem oraz intensywną luminescencją pod wpływem wzbudzenia z zakresu bliskiej podczerwieni.

P2. Upconverting SrF_2 nanoparticles doped with $\text{Yb}^{3+}/\text{Ho}^{3+}$, $\text{Yb}^{3+}/\text{Er}^{3+}$ and $\text{Yb}^{3+}/\text{Tm}^{3+}$ ions – optimisation of synthesis method, structural, spectroscopic and cytotoxicity studies

Optymalizacja procedury przygotowania próbki oraz jej syntezy zostały również przeprowadzone dla układu $\text{SrF}_2:\text{Yb}^{3+}, \text{Ln}^{3+}$ ($\text{Ln} = \text{Ho}^{3+}, \text{Er}^{3+}, \text{Tm}^{3+}$). Dla wspomnianych struktur wykonano analizę wpływu surfaktantu (cytrynian sodu, cytrynian amonu), nadmiar źródła jonów

fluoru (1,5 lub 3-krotny nadmiar fluorku amonu) oraz długość syntezy (6 lub 12 h) na właściwości morfologiczne oraz spektroskopowe. Uzyskane rezultaty przedstawiono w artykule **P2**. Istotny wpływ na wielkość nanocząstek, ich stopień agregacji oraz kształt miał użyty w trakcie przygotowania próbki nadmiar jonów fluoru. Mniejsze, sferyczne nanocząstki, bez widocznych agregatów uzyskano dla 1,5-krotnego nadmiaru fluorku amonu, natomiast przy użyciu większego nadmiaru, otrzymano większe cząstki, o nieregularnej strukturze oraz tendencji do agregacji. Z pośród wszystkich próbek nanocząstki otrzymane z trzykrotnym nadmiarem fluorku amonu oraz cytrynianem sodu, jako surfaktantem, charakteryzowały się najbardziej intensywną emisją oraz najdłuższymi czasami życia. Zaobserwowany został również istotny wpływ cytrynianu amonu na wygaszenie uzyskanej emisji, w produktach gdzie wykorzystano go w trakcie syntezy. Na bazie uzyskanych próbek przygotowane zostały również wodne koloidy oraz koloidy w roztworze soli fizjologicznej. Z pośród nich wybrano cząstki o sferycznym kształcie oraz intensywnej luminescencji w celu przeprowadzenia modyfikacji ich powierzchni, w której zastosowany został kwas poliakrylowy (PAA) oraz glikol polietylenowy eteru bis karboksymetylenowego (PEG - (COOH)₂). Tak zmodyfikowane nanocząstki wykorzystano w badaniach wpływu NPs SrF₂:Yb³⁺, Ln³⁺ na żywe komórki- ludzkie fibroblasty. Według przeprowadzonych testów, nanocząstki wpływają na proliferację komórek w zależności od zastosowanego stężenia oraz jonów lantanowców, co obrazują wyniki dla jonu Tm³⁺, który wykazał znacznie większy wpływ na zmniejszone namnażanie się komórek. Co ciekawe zaobserwowano podobny wpływ nanocząstek modyfikowanych oraz niemodyfikowanych na komórki. Dodatkowo wykonano zdjęcia pod mikroskopem konfokalnym obrazujące rozmieszczenie się NPs w komórkach.

P3. Synthesis and up - conversion of core/shell SrF₂:Yb³⁺,Er³⁺@SrF₂:Yb³⁺,Nd³⁺ nanoparticles under 808, 975, and 1532 nm excitation wavelengths

Badania nad nanomateriałami fluorku strontu domieszkowanego jonami lantanowców wykorzystano w dalszych etapach prac badawczych nad tym układem, a dokładniej przy otrzymaniu struktur typu rdzeń/powłoka w środowisku wodnym. Związki te uzyskano w dwuetapowej syntezie hydrotermalnej, modyfikując odpowiednio procedurę z wcześniejszych badań. Otrzymane wyniki przedstawiono w publikacji **P3**. Dzięki strukturze rdzeń/powłoka możliwe jest rozdzielanie domieszek pomiędzy rdzeń i powłokę, a tym samym zwiększenie stężeń stosowanych jonów Ln³⁺ oraz minimalizacja relaksacji krzyżowej między jonami. Dodatkową zaletą takich układów jest możliwość wprowadzenia kilku sensybilizatorów, w tym przypadku Yb³⁺ oraz Nd³⁺ uzyskując tym samym wzbudzenie o długości 975 oraz 808 nm. Ma to istotne znaczenie w przypadku zastosowania otrzymanych związków w biologii czy medycynie, ze względu na

skrócenie długości fali wzbudzenia, minimalizując przez to efekt nagrzewania się komórek poprzez absorpcję promieniowania (980 nm) przez wodę. Przedstawiono szereg badań odnośnie morfologii otrzymanych NPs, a także ich dogłębną analizę spektroskopową. Ze względu na homogeniczną strukturę związku ($\text{SrF}_2@\text{SrF}_2$) zdjęcia TEM nie stanowią dowodu na otrzymanie core/shell, dlatego w celu potwierdzenia uzyskania założonego związku, wykorzystana została spektroskopia laserowa, a dokładniej widma emisji pod wpływem wzbudzenia 975 nm w zakresie 900-1700 nm, obserwując tym samym zjawisko down-konwersji oraz wzbudzenie 1532 nm w zakresie 450-1200 nm (zjawisko up - konwersji). Widma uzyskanych próbek typu rdzeń/powłoka porównano z emisją $\text{SrF}_2:\text{Yb}^{3+}$, Er^{3+} , Nd^{3+} , dla której zarejestrowano przejście $\text{Nd}^{3+}: ^4\text{F}_{3/2} \rightarrow ^4\text{I}_{11/2}$, nie pojawiające się na pozostałych widmach. Potwierdza to transfer energii pomiędzy jonami $\text{Er}^{3+} \rightarrow \text{Nd}^{3+}$ pod wpływem wzbudzenia o długości 1532 nm, która to w omawianych NPs jest jedynie absorbowana przez jony erbu. Proces ten nie jest obserwowany dla struktur rdzeń/powłoka, co potwierdza rozdzielanie par jonów $\text{Yb}^{3+}/\text{Er}^{3+}$ znajdujących się w rdzeniu oraz $\text{Yb}^{3+}/\text{Nd}^{3+}$ obecnych w powłoce. Otrzymane struktury mogą być wykorzystane w aplikacjach biomedycznych ze względu na możliwość wzbudzenia promieniowaniem znajdującym się w zakresie okien biologicznych, a także w ogniwach słonecznych.

P4. Formation Mechanism, Structural and Upconversion Properties of Alkaline Rare-Earth Fluoride Nanocrystals Doped With $\text{Yb}^{3+}/\text{Er}^{3+}$ Ions

Istotne znaczenie w badaniach dotyczących zjawiska up - konwersji i jego praktycznych zastosowań ma poszukiwanie nowych nanomateriałów, wykazujących efektywną konwersję promieniowania energii w górę, a także poszerzanie wiedzy o mało poznanych układach. W przeciwieństwie do NaYF_4 , fluorki oparte o stechiometrię $\text{M}_x\text{RE}_y\text{F}_z$ (gdzie $\text{M} = \text{Ca}, \text{Sr}, \text{Ba}$ oraz $\text{RE} = \text{Y}, \text{La}, \text{Gd}, \text{Lu}$) są słabo poznane (np. Sr_2LuF_7 , Ba_2YF_7 , and Ba_2GdF_7), bądź nie są dostępne żadne badania naukowe na ich temat, (np. Ca_2YF_7 , Ca_2GdF_7 czy Ba_2LuF_7). Bazując na wynikach opublikowanych dla związków BaGdF_5 oraz BaYF_5 , które wykazują intensywną emisję UC, otrzymano szereg matryc $\text{M}_x\text{RE}_y\text{F}_z$ oraz matryc domieszkowanych jonami Yb^{3+} , Er^{3+} przedstawiając ich charakterystykę morfologiczną i właściwości spektroskopowe w artykule **P4**. Po dokładnej analizie składu pierwiastkowego zsyntezowanych związków, wykorzystując do tego optyczną spektrometrię emisyjną ze wzbudzeniem w plazmie indukcyjnej sprzężonej (ICP – OES), ustalono otrzymanie trzech różnych stechiometrii: MREF_5 (SrLaF_5), M_2REF_7 (Ca_2YF_7 , Sr_2YF_7 , Ba_2YF_7 , Ba_2LaF_7 , Ca_2GdF_7 , Sr_2GdF_7 , Ba_2GdF_7 , Sr_2LuF_7 , Ba_2LuF_7) i $\text{M}_{1-x}\text{RE}_x\text{F}_{2+x}$ dla struktur zawierających jony Ca^{2+} oraz Lu^{3+} . Kolejnym etapem badań była analiza mechanizmu powstawania przedstawionych NPs w celu wyjaśnienia uzyskania różnych stechiometrii, pomimo użycia takiej samej procedury syntezy dla

wszystkich związków (stosunek molowy chlorów MCl_2 oraz $RECl_3$ wynosił 1:1) oraz niższej zawartości domieszek jonów Ln^{3+} niż założona. Bazując na analizie stabilności kompleksów przejściowych jonów metali z EDTA (kwas (etylenodiamino)tetraoctowy), różnicach w promieniach jonowych metali wchodzących w skład związków oraz rozpuszczalności fluorków zastosowanych w syntezie metali, zaproponowano mechanizm formowania się przedstawionych fluorków metali ziem alkalicznych i pierwiastków ziem rzadkich. Scharakteryzowano również właściwości spektroskopowe otrzymanych nanomateriałów. Z pośród nich matryce Ba_2LuF_7 oraz Sr_2LuF_7 , dla których określono najwyższą zawartość Yb^{3+} oraz Er^{3+} , wykazywały najbardziej intensywną emisję oraz największą wydajnością kwantową (odpowiednio $0.0176 \pm 0.001\%$ oraz $0.0192 \pm 0.001\%$). Związki te są bardzo obiecujące ze względu na swoje właściwości i zostaną wykorzystane w dalszych badaniach.

Podsumowanie

W niniejszej pracy doktorskiej przedstawiona została synteza oraz charakterystyka fizykochemiczna nanomateriałów wykazujących zjawisko konwersji energii w górę pod wpływem promieniowania z zakresu bliskiej podczerwieni. Otrzymane metodą hydrotermalną związki zostały oparte o matryce fluorkowe metali ziem alkalicznych i rzadkich, domieszkowane jonami lantanowców Ln^{3+} ($Ln = Yb, Nd, Ho, Er, Tm$).

Wszystkie otrzymane materiały mają nanometryczny rozmiar poniżej 60 nm, a także hydrofilowy charakter, ze względu na wykorzystane wody jako rozpuszczalnika w syntezie.

Przygotowane nanocząstki bazujące na matrycy $M^{II}F_2$ ($M = Ca, Sr$) zostały zoptymalizowane pod kątem morfologii oraz właściwości spektroskopowych wykorzystując zmienne czynniki, takie jak rodzaj dodanego surfaktantu, nadmiar źródła jonów fluoru, czas reakcji oraz jej objętość czy obecność bądź brak mieszania. Dzięki temu ustalono optymalne parametry syntezy oraz sposób przygotowania próbki w celu uzyskania pożądanego rozmiaru, kształtu oraz stopnia agregacji, a także intensywnej luminescencji pod wpływem wzbudzenia z zakresu bliskiej podczerwieni o długości fali 975 nm. Dodatkowo dla nanocząstek fluorku wapnia, domieszkowanych jonami Ln^{3+} ($Ln = Yb, Er$) przeprowadzono dokładną analizę symetrii otoczenia jonów Yb^{3+} obecnego w otrzymanych NPs, zależnej od zastosowanego rodzaju jonów pełniących funkcję kompensacji ładunku (tutaj Na^+). Natomiast dla fluorku strontu, domieszkowanego parami jonów Yb^{3+}/Er^{3+} , Yb^{3+}/Tm^{3+} , Yb^{3+}/Ho^{3+} została wykonana modyfikacja powierzchni nanocząstek, w celu otrzymania stabilnych koloidów, a także badania cytotoxycności UCNPs względem żywych komórek. W wyniku przeprowadzonych testów stwierdzono podobny stosunek komórek żywych do martwych

dla próbek kontrolnych oraz inkubowanych z NPs, jednakże obecność nanocząstek powoduje spadek namnażania się komórek zależny od zastosowanego stężenia cząstek w analizie.

Wykorzystując procedurę syntezy nanocząstek SrF_2 opisaną w artykule P2, przeprowadzono dwuetapową syntezę NPs fluorku strontu w celu otrzymania struktury typu rdzeń/powłoka. Zastosowanie związku tego typu, umożliwiło rozdzielenie jonów aktywatora (Er^{3+}) znajdujących się w rdzeniu, od jonów sensybilizatora (Nd^{3+} , Yb^{3+}) obecnych w powłoce. Dzięki temu zminimalizowany został proces relaksacji krzyżowej pomiędzy jonami, a także zwiększone zostało stężenie jonów Nd^{3+} , w porównaniu do matrycy SrF_2 domieszkowanej trzema jonami (Nd^{3+} , Er^{3+} , Yb^{3+}), nie posiadającej powłoki. Co istotne, zastosowanie jonów Nd^{3+} umożliwiło otrzymanie up - konwersji pod wpływem wzbudzenia o długości fali 808 nm. Ma to znaczący wpływ na minimalizację efektu nagrzewania się wodnych koloidów, ze względu na niski współczynnik absorpcji wspomnianego promieniowania przez wodę. Otrzymanie struktur typu rdzeń/powłoka zostało potwierdzone dzięki wykorzystaniu spektroskopii laserowej, stosując wzbudzenie o długości 808, 975 oraz 1532 nm.

W wyniku przeprowadzonych badań otrzymano też szereg nowych bądź słabo poznanych struktur o stechiometrii $\text{M}_x\text{RE}_y\text{F}_z$ (gdzie $\text{M} = \text{Ca}, \text{Sr}, \text{Ba}$ oraz $\text{RE} = \text{Y}, \text{La}, \text{Gd}, \text{Lu}$). Dzięki dokładnej analizie składu otrzymanych związków, ustalono dokładny skład pierwiastkowy zsyntezowanych nanocząstek. Ponadto, zaproponowany został mechanizm powstawania opisywanych złożonych fluorków w oparciu o analizę stabilności kompleksów przejściowych jonów metali z EDTA, różnicach w promieniach jonowych metali wchodzących w skład związków oraz rozpuszczalności fluorków metali utworzonych z zastosowanych w syntezie prekursorów jonów M^{2+} oraz RE^{3+} . Dla związków o najintensywniejszej emisji wyznaczono również wartości wydajności kwantowej, która jest istotnym parametrem w jakościowej ocenie nanocząstek oraz umożliwia porównanie związków otrzymanych przez różne grupy badawcze.

Wyniki przeprowadzonych badań przedstawiono w formie czterech artykułów, opublikowanych w międzynarodowych czasopismach naukowych, z tzw. listy filadelfijskiej. Zsyntezowane nanomateriały mają szerokie potencjalne zastosowanie, m.in. w bioobrazowaniu, dostarczaniu leków, jako sensory temperatury i ciśnienia, w kryminalistyce, a także przy produkcji ogniw fotowoltaicznych czy urządzeniach optycznych.

Literatura

- 1 F. Auzel, *Chem. Rev.*, 2004, **104**, 139–173.
- 2 S. Ye, E. H. Song and Q. Y. Zhang, *Adv. Sci.*, 2016, **3**, 1600302.
- 3 A. Ronchi, P. Brazzo, M. Sassi, L. Beverina, J. Pedrini, F. Meinardi and A. Monguzzi, *Phys. Chem. Chem. Phys.*, 2019, **21**, 12353–12359.
- 4 R. Naccache, Q. Yu and J. A. Capobianco, *Adv. Opt. Mater.*, 2015, **3**, 482–509.
- 5 F. Wang and X. Liu, *Chem. Soc. Rev.*, 2009, **38**, 976.
- 6 K. Zheng, K. Y. Loh, Y. Wang, Q. Chen, J. Fan, T. Jung, S. H. Nam, Y. D. Suh and X. Liu, *Nano Today*, 2019, **29**, 100797.
- 7 M. Pedroni, F. Piccinelli, T. Passuello, S. Polizzi, J. Ueda, P. Haro-González, L. Martinez Maestro, D. Jaque, J. García-Solé, M. Bettinelli and A. Speghini, *Cryst. Growth Des.*, 2013, **13**, 4906–4913.
- 8 J. Yao, F. Zhao, C. Pan and J. Zhuang, *Nanoscale Res. Lett.*, 2017, **12**, 0–5.
- 9 H. Wang, M. Li, Z. Yin, T. Zhang, X. Chen, D. Zhou, J. Zhu, W. Xu, H. Cui and H. Song, *ACS Appl. Mater. Interfaces*, 2017, **9**, 37128–37135.
- 10 S. Wilhelm, *ACS Nano*, 2017, **11**, 10644–10653.
- 11 R. E. Smalley, *MRS Bull.*, 2005, **30**, 412–417.
- 12 M. Bardosova and T. Wagner, *Nanomaterials and Nanoarchitectures*, 2015.
- 13 J. Zhou, Q. Liu, W. Feng, Y. Sun and F. Li, *Chem. Rev.*, 2015, **115**, 395–465.
- 14 N. Bloembergen, *Phys. Rev. Lett.*, 1959, **2**, 84–85.
- 15 M. V. DaCosta, S. Doughan, Y. Han and U. J. Krull, *Anal. Chim. Acta*, 2014, **832**, 1–33.
- 16 F. Auzel, *C. R. Acad. Sci. Paris B*, 1966, **263**, 819–821.
- 17 M. Wang, G. Abbineni, A. Clevenger, C. Mao and S. Xu, *Nanomedicine Nanotechnology, Biol. Med.*, 2011, **7**, 710–729.
- 18 B. Del Rosal and D. Jaque, *Methods Appl. Fluoresc.*, 2019, **7**, 022001.
- 19 M. Shamsipur, A. Barati and Z. Nematifar, *J. Photochem. Photobiol. C Photochem. Rev.*, 2019, **39**, 76–141.
- 20 T. N. Nguyen, F. M. Ebrahim and K. C. Stylianou, *Coord. Chem. Rev.*, 2018, **377**, 259–306.
- 21 E. Y. Chen, C. Milleville, J. M. O. Zide, M. F. Doty and J. Zhang, *MRS Energy Sustain.*, 2018, **5**, 1–17.
- 22 D. R. Gamelin and H. U. Güdel, *Acc. Chem. Res.*, 2000, **33**, 235–242.
- 23 Z. Huang and M. Lee Tang, *J. Phys. Chem. Lett.*, 2018, **9**, 6198–6206.
- 24 N. Nishimura, J. R. Allardice, J. Xiao, Q. Gu, V. Gray and A. Rao, *Chem. Sci.*, 2019, **10**, 4750–4760.
- 25 S. F. Himmelstoß and T. Hirsch, *Methods Appl. Fluoresc.*, 2019, **7**, 022002.
- 26 L. Tu, X. Liu, F. Wu and H. Zhang, *Chem. Soc. Rev.*, 2015, **44**, 1331–1345.
- 27 J. Chen and J. X. Zhao, *Sensors*, 2012, **12**, 2414–2435.
- 28 F. Wang, R. Deng, J. Wang, Q. Wang, Y. Han, H. Zhu, X. Chen and X. Liu, *Nat. Mater.*, 2011, **10**, 968–973.
- 29 S. Guo, M. K. Tsang, W. S. Lo, J. Hao and W. T. Wong, *Nanoscale*, 2018, **10**, 2790–2803.
- 30 R. Pązik, *Synteza i zbadanie własności optycznych i elektrycznych nanokrystalicznych materiałów BaTiO₃ domieszkowanych jonami ziem rzadkich*, Wrocław, 2008.
- 31 S. Cotton, *Lanthanide and Actinide Chemistry*, John Wiley & Sons, Chichester, 2006.

- 32 S. F. A. Kettle, *Fizyczna chemia nieorganiczna*, Wydawnictwo Naukowe PWN, Warszawa, 1999.
- 33 A. Strzęp, Państwowa Akademia Nauk, 2014.
- 34 J.-C. G. Bünzli and S. V. Eliseeva, *Springer Ser. Fluoresc.*, 2010, **13**, 1–45.
- 35 S.-D. Jiang, B.-W. Wang and S. Gao, in *Molecular Nanomagnets and Related Phenomena*, ed. S. Gao, Springer Berlin Heidelberg, Berlin, Heidelberg, 2015, pp. 111–141.
- 36 H. S. Mader, P. Kele, S. M. Saleh and O. S. Wolfbeis, *Curr. Opin. Chem. Biol.*, 2010, **14**, 582–596.
- 37 M. Haase and H. Schäfer, *Angew. Chemie - Int. Ed.*, 2011, **50**, 5808–5829.
- 38 S. Wang and L. Wang, *TrAC - Trends Anal. Chem.*, 2014, **62**, 123–134.
- 39 A. Gulzar, J. Xu, P. Yang, F. He and L. Xu, *Nanoscale*, 2017, **9**, 12248–12282.
- 40 J. Liu, H. Deng, Z. Huang, Y. Zhang, D. Chen and Y. Shao, *Phys. Chem. Chem. Phys.*, 2015, **17**, 15412–15418.
- 41 S. Heer, K. Kömpe, H. U. Güdel, M. Haase, K. Kmpe, H. U. Gdel and M. Haase, *Adv. Mater.*, 2004, **16**, 2102–2105.
- 42 A. Escudero, A. I. Becerro, C. Carrillo-Carrión, N. O. Núñez, M. V. Zyuzin, M. Laguna, D. González-Mancebo, M. Ocanã and W. J. Parak, *Nanophotonics*, 2017, **6**, 881–921.
- 43 J. Wang, R. Deng, M. A. MacDonald, B. Chen, J. Yuan, F. Wang, D. Chi, T. S. Andy Hor, P. Zhang, G. Liu, Y. Han and X. Liu, *Nat. Mater.*, 2014, **13**, 157–162.
- 44 L. Lyu, H. Cheong, X. Ai, W. Zhang, J. Li, H. H. Yang, J. Lin and B. Xing, *NPG Asia Mater.*, 2018, 685–702.
- 45 A. Beeby, I. M. Clarkson, R. S. Dickins, S. Faulkner, D. Parker, L. Royle, A. S. De Sousa, J. A. G. Williams and M. Woods, *J. Chem. Soc. Perkin Trans. 2*, 1999, 493–503.
- 46 L. M. Wiesholler and T. Hirsch, *Opt. Mater. (Amst.)*, 2018, **80**, 253–264.
- 47 W.-B. Pei, B. Chen, L. Wang, J. Wu, X. Teng, R. Lau, L. Huang and W. Huang, *Nanoscale*, 2015, **7**, 4048–4054.
- 48 X. Chuai, X. Guo, X. Liu, G. He, K. Zheng, C. He and W. Qin, *Opt. Mater. (Amst.)*, 2015, **44**, 13–17.
- 49 D. Li, W. Qin, T. Aidilibike, P. Zhang, S. Liu, L. Wang and S. Li, *J. Alloys Compd.*, 2016, **675**, 31–36.
- 50 Y. Liu, Y. Lu, X. Yang, X. Zheng, S. Wen, F. Wang, X. Vidal, J. Zhao, D. Liu, Z. Zhou, C. Ma, J. Zhou, J. A. Piper, P. Xi and D. Jin, *Nature*, 2017, **543**, 229–233.
- 51 Y. Wang, R. Deng, X. Xie, L. Huang and X. Liu, *Nanoscale*, 2016, **8**, 6666–6673.
- 52 C. F. Gainer, G. S. Joshua, C. R. De Silva and M. Romanowski, *J. Mater. Chem.*, 2011, **21**, 18530–18533.
- 53 M. Saboktakin, X. Ye, S. J. Oh, S.-H. Hong, A. T. Fafarman, U. K. Chettiar, N. Engheta, C. B. Murray and C. R. Kagan, *ACS Nano*, 2012, **6**, 8758–8766.
- 54 Y. Fan and F. Zhang, *Adv. Opt. Mater.*, 2019, **7**, 1–14.
- 55 G. Yi and G. Chow, *Chem. Mater.*, 2007, **19**, 341–343.
- 56 T. Rinkel, A. N. Raj, S. Dühnen and M. Haase, *Angew. Chemie - Int. Ed.*, 2016, **55**, 1164–1167.
- 57 S. Dühnen and M. Haase, *Chem. Mater.*, 2015, **27**, 8375–8386.
- 58 S. Fischer, N. D. Bronstein, J. K. Swabeck, E. M. Chan and A. P. Alivisatos, *Nano Lett.*, 2016, **16**, 7241–7247.

- 59 H. S. Qian and Y. Zhang, *Langmuir*, 2008, **24**, 12123–12125.
- 60 D. Yang, C. Li, G. Li, M. Shang, X. Kang and J. Lin, *J. Mater. Chem.*, 2011, **21**, 5923.
- 61 S. Hao, G. Chen, C. Yang, W. Shao, W. Wei, Y. Liu and P. N. Prasad, *Nanoscale*, 2017, **9**, 10633–10638.
- 62 J. E. Choi, D. Kim and H. S. Jang, *Chem. Commun.*, 2019, **55**, 2261–2264.
- 63 Z. Ba, M. Hu, Y. Zhao, Y. Wang, J. Wang and Z. Zhang, *Nanotechnology*, 2018, **29**, 66–77.
- 64 N. Song, B. Zhou, L. Yan, J. Huang and Q. Zhang, *Front. Chem.*, 2019, **6**, 1–8.
- 65 P. Singh, P. K. Shahi, Z. Yi, T. Zeng and P. P. Sukul, *Nanotechnology*, 2018, **29**, 345704.
- 66 A. R. Hong, Y. Kim, T. S. Lee, S. Kim, K. Lee, G. Kim and H. S. Jang, *ACS Appl. Mater. Interfaces*, 2018, **10**, 12331–12340.
- 67 F. Zhang, R. Che, X. Li, C. Yao, J. Yang, D. Shen, P. Hu, W. Li and D. Zhao, *Nano Lett.*, 2012, **12**, 2852–2858.
- 68 J. Meng, Z. Zhang, B. Zhang, Y. Gao, G. Li, Z. Fu and H. Zheng, *New J. Chem.*, 2019, **43**, 1770–1774.
- 69 N. C. Bigall, W. J. Parak and D. Dorfs, *Nano Today*, 2012, **7**, 282–296.
- 70 H. Zong, X. Mu and M. Sun, *Appl. Mater. Today*, 2019, **15**, 43–57.
- 71 U. Resch-Genger and H. H. Gorris, *Anal. Bioanal. Chem.*, 2017, **409**, 5855–5874.
- 72 B. Liu, Z. Meng, S. Wu, Y. Wu and S. Zhang, *Nanoscale Horizons*, 2018, **3**, 616–623.
- 73 H. Zhang, L. Xu, F. Liu, C. Huang and J. Wei, *Nanotechnology*, , DOI:10.1088/1361-6528/ab4244.
- 74 C. Mao, K. Min, K. Bae, S. Cho, T. Xu, H. Jeon and W. Park, *ACS Photonics*, 2019, **6**, 1882–1888.
- 75 Y. Shi, F. Zhang, J. Xu, K. Zhou, C. Chen, J. Cheng and P. Li, *J. Mater. Sci.*, 2019, **54**, 8461–8471.
- 76 X. Huang, *J. Alloys Compd.*, 2017, **690**, 356–359.
- 77 L. Sun, R. Wei, J. Feng and H. Zhang, *Coord. Chem. Rev.*, 2018, **364**, 10–32.
- 78 V. Muhr, S. Wilhelm, T. Hirsch and O. S. Wolfbeis, *Acc. Chem. Res.*, 2014, **47**, 3481–3493.
- 79 C. Chen, C. Li and Z. Shi, *Adv. Sci.*, 2016, **3**, 1600029.
- 80 A. Sedlmeier and H. H. Gorris, *Chem. Soc. Rev.*, 2015, **44**, 1526–1560.
- 81 G. Jiang, J. Pichaandi, N. J. J. Johnson, R. D. Burke and F. C. J. M. Van Veggel, *Langmuir*, 2012, **28**, 3239–3247.
- 82 X. Chen, T. Sun and F. Wang, *Chem. - An Asian J.*, 2020, **15**, 21–33.
- 83 X. Ge, J. Liu and L. Sun, *Dalt. Trans.*, 2017, **46**, 16729–16737.
- 84 B. M. van der Ende, L. Aarts and A. Meijerink, *Phys. Chem. Chem. Phys.*, 2009, **11**, 11081.
- 85 T. R. Hinklin, S. C. Rand and R. M. Laine, *Adv. Mater.*, 2008, **20**, 1270–1273.
- 86 A. Rapaport, J. Milliez, M. Bass, A. Cassanho and H. Jenssen, *IEEE/OSA J. Disp. Technol.*, 2006, **2**, 68–78.
- 87 R. Y. S. Zampiva, C. G. Kaufmann, L. H. Acauan, R. L. Seeger, F. Bonatto, C. D. Boeira, W. Q. Santos, C. Jacinto, C. A. Figueroa, L. S. Dorneles, A. K. Alves, C. P. Bergmann and C. S. ten Caten, *Sol. Energy*, 2018, **170**, 752–761.
- 88 M. Wang, M. Li, M. Yang, X. Zhang, A. Yu, Y. Zhu, P. Qiu and C. Mao, *Nano Res.*, 2015, **8**, 1800–1810.
- 89 C. M. Liu, L. Y. Zhang, L. Li, B. Y. Li, C. G. Wang and T. T. Wang, *Dye. Pigment.*, 2018, **149**, 822–829.

- 90 M. You, M. Lin, S. Wang, X. Wang, G. Zhang, Y. Hong, Y. Dong, G. Jin and F. Xu, *Nanoscale*, 2016, **8**, 10096–10104.
- 91 C. Zhang, H. P. Ou, L. Y. Liao, W. Feng, W. Sun, Z. X. Li, C. H. Xu, C. J. Fang, L. D. Sun, Y. W. Zhang and C. H. Yan, *Adv. Mater.*, 2010, **22**, 633–637.
- 92 J. C. Boyer, C. J. Carling, B. D. Gates and N. R. Branda, *J. Am. Chem. Soc.*, 2010, **132**, 15766–15772.
- 93 W. Wang, W. Huang, Y. Ni, C. Lu and Z. Xu, *ACS Appl. Mater. Interfaces*, 2014, **6**, 340–348.
- 94 D. Parker, *Coord. Chem. Rev.*, 2000, **205**, 109–130.
- 95 A. Serrano-Medina, I. Oroz-Parra, V. E. Gomez-Resendiz, A. Licea-Navarro, A. Licea-Claverie and J. M. Cornejo-Bravo, *Int. J. Polym. Mater. Polym. Biomater.*, 2018, **67**, 20–26.
- 96 S. Du and Y. Wang, *CrystEngComm*, 2019, **21**, 1452–1457.
- 97 M. N. Getz, O. Nilsen and P.-A. Hansen, *Sci. Rep.*, 2019, **9**, 10247.
- 98 Q. Liu, J. Peng, L. Sun and F. Li, *ACS Nano*, 2011, **5**, 8040–8048.
- 99 S. Christ and M. Schäferling, *Methods Appl. Fluoresc.*, 2015, **3**, 34004.
- 100 P. Cortelletti, A. Skripka, C. Facciotti, M. Pedroni, G. Caputo, N. Pinna, M. Quintanilla, A. Benayas, F. Vetrone and A. Speghini, *Nanoscale*, 2018, **10**, 2568–2576.
- 101 M. Quintanilla, Y. Zhang and L. M. Liz-Marzán, *Chem. Mater.*, 2018, **30**, 2819–2828.
- 102 I. Villa, A. Vedda, I. X. Cantarelli, M. Pedroni, F. Piccinelli, M. Bettinelli, A. Speghini, M. Quintanilla, F. Vetrone, U. Rocha, C. Jacinto, E. Carrasco, F. S. Rodríguez, Á. Juarranz, B. del Rosal, D. H. Ortgies, P. H. Gonzalez, J. G. Solé and D. J. García, *Nano Res.*, 2015, **8**, 649–665.
- 103 S. He, J. Song, J. Qu and Z. Cheng, *Chem. Soc. Rev.*, 2018, **47**, 4258–4278.
- 104 F. Lu, L. Yang, Y. Ding and J. J. Zhu, *Adv. Funct. Mater.*, 2016, **26**, 4778–4785.
- 105 H. S. Mader and O. S. Wolfbeis, *Anal. Chem.*, 2010, **82**, 5002–5004.
- 106 L. Xie, Y. Qin and H.-Y. Chen, *Anal. Chem.*, 2012, **84**, 1969–1974.
- 107 H. Zhu, Y. Ding, A. Wang, X. Sun, X.-C. Wu and J.-J. Zhu, *J. Mater. Chem. B*, 2015, **3**, 458–464.
- 108 C. Wang, L. Cheng and Z. Liu, *Biomaterials*, 2011, **32**, 1110–1120.
- 109 Y. Liu, C. Zhang, H. Liu, Y. Li, Z. Xu, L. Li and A. Whittaker, *J. Alloys Compd.*, 2018, **749**, 939–947.
- 110 Z. Farka, M. J. Mickert, A. Hlaváček, P. Skládal and H. H. Gorris, *Anal. Chem.*, 2017, **89**, 11825–11830.
- 111 S. Chen, A. Z. Weitemier, X. Zeng, L. He, X. Wang, Y. Tao, A. J. Y. Huang, Y. Hashimoto-dani, M. Kano, H. Iwasaki, L. K. Parajuli, S. Okabe, D. B. Loong Teh, A. H. All, I. Tsutsui-Kimura, K. F. Tanaka, X. Liu and T. J. McHugh, *Science (80-.)*, 2018, **359**, 679–684.
- 112 H. H. Gorris and U. Resch-Genger, *Anal. Bioanal. Chem.*, 2017, **409**, 5875–5890.
- 113 Q. Zhan, H. Liu, B. Wang, Q. Wu, R. Pu, C. Zhou, B. Huang, X. Peng, H. Ågren and S. He, *Nat. Commun.*, 2017, **8**, 1–11.
- 114 Y. Li, X. Li, Z. Xue, M. Jiang, S. Zeng and J. Hao, *Biomaterials*, 2018, **169**, 35–44.
- 115 A. Gnach, T. Lipinski, A. Bednarkiewicz, J. Rybka and J. A. Capobianco, *Chem. Soc. Rev.*, 2015, **44**, 1561–1584.
- 116 H. Huang and J. F. Lovell, *Adv. Funct. Mater.*, 2017, **27**, 1603524.
- 117 Q. Li, Z. Wang, Y. Chen and G. Zhang, *Metallomics*, 2017, **9**, 1150–1156.
- 118 P. Du, P. Zhang, S. H. Kang and J. S. Yu, *Sensors Actuators, B Chem.*, 2017, **252**, 584–591.

- 119 C. Yao, P. Wang, R. Wang, L. Zhou, A. M. El-Toni, Y. Lu, X. Li and F. Zhang, *Anal. Chem.*, 2016, **88**, 1930–1936.
- 120 Z.-L. Wang, J. Hao, H. L. W. Chan, G.-L. Law, W.-T. Wong, K.-L. Wong, M. B. Murphy, T. Su, Z. H. Zhang and S. Q. Zeng, *Nanoscale*, 2011, **3**, 2175.
- 121 S. H. Tang, J. Wang, C. X. Yang, L. X. Dong, D. Kong and X. P. Yan, *Nanoscale*, 2014, **6**, 8037–8044.
- 122 H. Y. Peng, B. Bin Ding, Y. C. Ma, S. Q. Sun, W. Tao, Y. C. Guo, H. C. Guo, X. Z. Yang and H. S. Qian, *Appl. Surf. Sci.*, 2015, **357**, 2408–2414.
- 123 L. Mancic, A. Djukic-Vukovic, I. Dinic, M. G. Nikolic, M. D. Rabasovic, A. J. Krmpot, A. M. L. M. Costa, D. Trisic, M. Lazarevic, L. Mojovic and O. Milosevic, *Mater. Sci. Eng. C*, 2018, **91**, 597–605.
- 124 X. long Tang, J. Wu, B. lan Lin, S. Cui, H. mei Liu, R. tong Yu, X. dong Shen, T. wei Wang and W. Xia, *Acta Biomater.*, 2018, **74**, 360–373.
- 125 M. H. Chan, Y. T. Pan, I. J. Lee, C. W. Chen, Y. C. Chan, M. Hsiao, F. Wang, L. Sun, X. Chen and R. S. Liu, *Small*, 2017, **13**, 1–12.
- 126 Z. Hou, K. Deng, C. Li, X. Deng, H. Lian, Z. Cheng, D. Jin and J. Lin, *Biomaterials*, 2016, **101**, 32–46.
- 127 Y. Wang, S. Song, S. Zhang and H. Zhang, *Nano Today*, 2019, **25**, 38–67.
- 128 D. Lisjak, O. Plohl, J. Vidmar, B. Majaron and M. Ponikvar-Svet, *Langmuir*, 2016, **32**, 8222–8229.
- 129 L. Cheng, K. Yang, M. Shao, X. Lu and Z. Liu, *Nanomedicine*, 2011, **6**, 1327–1340.
- 130 C. Yan, H. Zhao, D. F. Perepichka and F. Rosei, *Small*, 2016, 3888–3907.

Kopie oświadczeń współautorów



mgr Dominika Przybylska
Zakład Ziem Rzadkich
Uniwersytet im. Adama Mickiewicza
Wydział Chemii

Poznań, 7 lipca 2020 roku

Oświadczenie o współautorstwie

Potwierdzam swój udział w następujących publikacjach:

P1. Dominika Przybylska, Tomasz Grzyb,

Tailoring structure, morphology and up-conversion properties of $\text{CaF}_2:\text{Yb}^{3+}, \text{Er}^{3+}$ nanoparticles by the route of synthesis, Journal of Materials Science, **2020**, DOI:10.1007/s10853-020-05049-9

Mój wkład w powstanie pracy polegał na określeniu koncepcji pracy, syntezie badanych materiałów oraz scharakteryzowaniu ich morfologii, wykonaniu analiz oraz pomiarów potrzebnych do opisanie właściwości strukturalnych oraz spektroskopowych, opracowanie oraz analiza części wyników, a także zredagowanie manuskryptu i odpowiedzi na recenzje.

P2. Dominika Przybylska, Anna Ekner-Grzyb, Bartosz F. Grześkowiak, Tomasz Grzyb,

Upconverting SrF_2 nanoparticles doped with $\text{Yb}^{3+}/\text{Ho}^{3+}$, $\text{Yb}^{3+}/\text{Er}^{3+}$ and $\text{Yb}^{3+}/\text{Tm}^{3+}$ ions – optimisation of synthesis method, structural, spectroscopic and cytotoxicity studies, Scientific Reports, 9 **2019**, 8669, DOI:10.1038/s41598-019-45025-1

Mój wkład w powstanie pracy polegał na określeniu koncepcji pracy, syntezie badanych materiałów oraz scharakteryzowaniu ich morfologii, wykonaniu analiz oraz pomiarów potrzebnych do opisanie właściwości strukturalnych oraz spektroskopowych, opracowanie oraz analiza części wyników, a także zredagowanie manuskryptu i odpowiedzi na recenzje.

P3. Dominika Przybylska, Tomasz Grzyb,

Synthesis and up - conversion of core/shell $\text{SrF}_2:\text{Yb}^{3+}, \text{Er}^{3+}@\text{SrF}_2:\text{Yb}^{3+}, \text{Nd}^{3+}$ nanoparticles under 808, 975, and 1532 nm excitation wavelengths, Journal of Alloys and Compounds, 831, **2020**, 154797, DOI:10.1016/j.jallcom.2020.154797

Mój wkład w powstanie pracy polegał na określeniu koncepcji pracy, syntezie badanych materiałów oraz scharakteryzowaniu ich morfologii, wykonaniu analiz oraz pomiarów potrzebnych do opisanie właściwości strukturalnych oraz spektroskopowych, opracowanie oraz analiza części wyników, a także zredagowanie manuskryptu i odpowiedzi na recenzje.

P4. Tomasz Grzyb, Dominika Przybylska,

Formation Mechanism, Structural, and Upconversion Properties of Alkaline Rare-Earth Fluoride Nanocrystals Doped with $\text{Yb}^{3+}/\text{Er}^{3+}$ Ions, Inorganic Chemistry, 57, **2018**, 6410–6420, DOI:10.1021/acs.inorgchem.8b00484

Mój wkład w powstanie pracy polegał na syntezie badanych materiałów oraz scharakteryzowaniu ich morfologii, wykonaniu analiz oraz pomiarów potrzebnych do opisanie właściwości strukturalnych oraz spektroskopowych (emisja oraz wzbudzenie, czasy życia oraz fotonowość procesu), opracowanie oraz analiza części wyników, a także współudział w redagowaniu manuskryptu odnośnie opracowanych wyników.

Dominika Przybylska

Collegium Chemicum,
ul. Uniwersytetu Poznańskiego 8, 61-614 Poznań
dominika.przybylska@amu.edu.pl

www.chemia.amu.edu.pl



Poznań, 07.07.2020 r.

Oświadczenie o współautorstwie

Potwierdzam swój udział w następujących publikacjach:

P1. Dominika Przybylska, Tomasz Grzyb,

Tailoring structure, morphology and up-conversion properties of $\text{CaF}_2:\text{Yb}^{3+}, \text{Er}^{3+}$ nanoparticles by the route of synthesis, Journal of Materials Science, **2020**, DOI:10.1007/s10853-020-05049-9

Mój wkład w powstanie pracy polegał na określeniu koncepcji pracy, współudziale w wykonywaniu pomiarów spektroskopowych, analizie oraz dyskusji wyników, a także współredagowaniu manuskryptu i korespondencji z edytorem czasopisma.

P2. Dominika Przybylska, Anna Ekner-Grzyb, Bartosz F. Grześkowiak, Tomasz Grzyb,

Upconverting SrF_2 nanoparticles doped with $\text{Yb}^{3+}/\text{Ho}^{3+}$, $\text{Yb}^{3+}/\text{Er}^{3+}$ and $\text{Yb}^{3+}/\text{Tm}^{3+}$ ions – optimisation of synthesis method, structural, spectroscopic and cytotoxicity studies,

Scientific Reports, **9** **2019**, 8669, DOI: 10.1038/s41598-019-45025-1

Mój wkład w powstanie pracy polegał na określeniu koncepcji pracy, współudziale w wykonywaniu pomiarów spektroskopowych, analizie oraz dyskusji wyników, a także współredagowaniu manuskryptu i korespondencji z edytorem czasopisma.

P3. Dominika Przybylska, Tomasz Grzyb,

Synthesis and up - conversion of core/shell $\text{SrF}_2:\text{Yb}^{3+}, \text{Er}^{3+}@ \text{SrF}_2:\text{Yb}^{3+}, \text{Nd}^{3+}$ nanoparticles under 808, 975, and 1532 nm excitation wavelengths, Journal of Alloys and Compounds, **831**, **2020**, 154797, DOI:10.1016/j.jallcom.2020.154797

Mój wkład w powstanie pracy polegał na określeniu koncepcji pracy, współudziale w wykonywaniu pomiarów spektroskopowych, analizie oraz dyskusji wyników, a także współredagowaniu manuskryptu i korespondencji z edytorem czasopisma.

P4. Tomasz Grzyb, Dominika Przybylska,

Formation Mechanism, Structural, and Upconversion Properties of Alkaline Rare-Earth Fluoride Nanocrystals Doped with $\text{Yb}^{3+}/\text{Er}^{3+}$ Ions, Inorganic Chemistry, **57**, **2018**, 6410–6420, DOI:10.1021/acs.inorgchem.8b00484

Mój wkład w powstanie pracy polegał na określeniu koncepcji pracy, współudziale w wykonywaniu pomiarów spektroskopowych, analizie oraz dyskusji wyników, a także współredagowaniu manuskryptu i korespondencji z edytorem czasopisma.

Tomasz Grzyb

ul. Uniwersytetu Poznańskiego 8, Collegium Chemicum, 61-614 Poznań
tel.: +48 61 829 1672, e-mail: tgrzyb@amu.edu.pl

www.chemia.amu.edu.pl

strona 1 z 1

Oświadczenie o współautorstwie

P2. Dominika Przybylska, Anna Ekner-Grzyb, Bartosz F. Grześkowiak, Tomasz Grzyb,

Upconverting SrF₂ nanoparticles doped with Yb³⁺/Ho³⁺, Yb³⁺/Er³⁺ and Yb³⁺/Tm³⁺ ions – optimisation of synthesis method, structural, spectroscopic and cytotoxicity studies,

Scientific Reports, 9 **2019**, 8669, DOI: 10.1038/s41598-019-45025-1

Mój wkład w powstanie pracy polegał na przeprowadzeniu testów cytotoksyczności nanocząstek, obrazowaniu komórek potraktowanych nanocząstkami, analizie otrzymanych wyników, a także współdziałaniu w redagowaniu manuskryptu oraz odpowiedzi na pytania recenzentów

Anna Ekner-Grzyb

Anna Ekner-Grzyb

Oświadczenie o współautorstwie

P2. Dominika Przybylska, Anna Ekner-Grzyb, Bartosz F. Grześkowiak, Tomasz Grzyb,

Upconverting SrF₂ nanoparticles doped with Yb³⁺/Ho³⁺, Yb³⁺/Er³⁺ and Yb³⁺/Tm³⁺ ions – optimisation of synthesis method, structural, spectroscopic and cytotoxicity studies,

Scientific Reports, 9 2019, 8669, DOI: 10.1038/s41598-019-45025-1

Mój wkład w powstanie pracy polegał na przeprowadzeniu testów cytotoksyczności nanocząstek, obrazowaniu komórek potraktowanych nanocząstkami, analizie otrzymanych wyników, a także współudział w redagowaniu manuskryptu oraz odpowiedzi na pytania recenzentów

Bartosz F. Grześkowiak



Kopie publikacji stanowiących rozprawę doktorską

-wraz z materiałami uzupełniającymi

Tailoring structure, morphology and up-conversion properties of $\text{CaF}_2:\text{Yb}^{3+},\text{Er}^{3+}$ nanoparticles by the route of synthesis

*Dominika Przybylska, Tomasz Grzyb**

Department of Rare Earths, Faculty of Chemistry, Adam Mickiewicz University in
Poznań, Uniwersytetu Poznańskiego 8, 61-614 Poznań, Poland

***Corresponding Author**

e-mail: tgrzyb@amu.edu.pl

Abstract

Control of morphology and spectroscopic properties during the synthesis of up-converting nanoparticles (NPs) is a great challenge. One of the most popular ways of NPs synthesis is the hydrothermal method, which is relatively simple, effective, environmentally friendly and permits easy control of synthesis parameters. For these reasons the hydrothermal method was applied for the synthesis of $\text{CaF}_2:\text{Yb}^{3+},\text{Er}^{3+}$ NPs and optimized. The effects of synthesis conditions on the properties of the product were carefully analysed. The tests were performed to check the impact of two surfactants: sodium citrate (NaCit) and ammonium citrate (NH_4Cit), different excess of ammonium fluoride used as a precipitation agent and different volume of solution with reactants. The type of co-reagent was found to influence the size of the obtained NPs and charge compensation, required after Yb^{3+} and Er^{3+} doping into Ca^{2+} sites. Depending on the synthesis conditions, the formation of Yb^{3+} clusters and alterations in the Yb^{3+} site symmetry were detected. The excitation and emission spectra revealed the importance of the presence of the Na^+ ions on the energy transfer mechanism and the resulting emission intensity. The presented results show that applying stirring during the synthesis or changing the type of anti-agglomeration agent, have a great influence on the luminescence intensity and colour as well as maximum of excitation when Yb^{3+} ions are used. Analysis of the excitation spectra and Yb^{3+} emission decays showed the complex structure of $\text{CaF}_2:\text{Yb}^{3+},\text{Er}^{3+}$ NPs, with Yb^{3+} ions in two different environments within the volume of NPs with different site-symmetries. The samples prepared in the presence of Na^+ ions were characterized by long Yb^{3+}

emission rise times, revealing energy migration between Yb^{3+} at different symmetries and, at the same time, improved the overall luminescence intensity of NPs.

Keywords: calcium fluoride, up-conversion, hydrothermal method optimization, Yb^{3+} clusters

Introduction

Up-converting nanoparticles (UCNPs) have been intensively investigated in last years because of their unusual properties allowing, in general, for conversion of near-infrared light (NIR) to higher energetic, visible and even ultraviolet [1–5]. This phenomenon can be observed for materials containing lanthanide ions (Ln^{3+}) because of the possibility of electronic transitions within their 4f subshell. Because of the properties of the 4f shell, sharp emission spectra, long luminescence lifetimes and massive Stoke's shifts can be observed [6–8]. Nanomaterials containing Ln^{3+} ions are very attractive in many fields of science and industry. Their small size and the possibility of conversion of NIR light make them excellent for many applications, e.g. optical materials, displays, sensors, biological markers, drug delivery systems and many others [9–12].

Considering UCNPs for different applications, particularly in the biomedical field, the ability to control their morphology and spectroscopic properties are essential. These issues are still a challenge [13]. The simplest solution is to adjust the type and conditions of the synthesis route. So far a few main synthesis methods have been proposed, e.g. thermal decomposition, solvo(hydro)thermal synthesis or co-precipitation with polyols [14–16]. The most common and useful method is the thermal decomposition of precursors, which leads to highly uniform nanoparticles of specific shapes and sizes [15, 17–19]. However, in the hydrothermal synthesis, it is also possible to control the conditions so that to obtain particles of desired properties. The hydrothermal synthesis is usually conducted in water, under high pressure and temperature, in a special type of autoclave [15, 20, 21]. Moreover, the process, as well as equipment needed, are quite simple [22–24].

During hydrothermal synthesis, there are many variables like pressure, temperature, synthesis time, the volume of solution or stirring that can significantly influence the morphology and spectroscopic properties of UCNPs. Great importance in synthesis route have also the addition of hydrophilic compounds like sodium citrate, ethylenediaminetetraacetic acid (EDTA), cetyl trimethylammonium bromide (CTAB), as well as polymers, e.g. polyethylene glycol (PEG), polyethylenimine (PEI) and other [14, 16, 25]. These additives not only promote the formation of particles of certain size and shape but also improve the dispersion of UCNPs in water and stabilize the colloids. Additionally, surfactants may affect the spectroscopic properties of NPs.

Calcium fluoride, CaF₂ is one of the best hosts for Ln³⁺ ions, thanks to its stability, low phonon energy, fluorite structure and very good compatibility with Ln³⁺ ions [26–28]. Moreover, CaF₂ is a material with high rigidity, low refractive index and is optically transparent in a range from mid-infrared to UV [29]. As a host compound, CaF₂ can be used in lasers [30], for bioimaging (high biocompatibility with living cell, non-toxic material) [31], biomedical sensors [32], and other applications. Also, this material can be easily obtained by a variety of methods such as sol-gel, solvo(hydro)thermal methods, polyol-mediated, thermal decomposition of precursors, or colloidal techniques [33–37]. CaF₂ is also easier to obtain by hydrothermal method as nanocrystals than NaREF₄ materials [38–40]. Furthermore, our previous research indicated that using similar to presented here, hydrothermal method, sub-microspheres can be synthesised instead of nanoparticles and by incorporation of Mn²⁺ ions into CaF₂ sub-microspheres the colour of up-conversion can be tuned [41].

In this work, CaF₂ was used as a model, allowing to track the way in which dopant ions are incorporated, which allows for a better understanding of the UC process in similar materials. Moreover, the presented results of synthesis in different volumes or with, and without stirring give insight into problems of production of Ln³⁺-doped nanomaterials at larger scale.

Experimental section

Characterization

Powder diffractograms were recorded on a Bruker AXS D8 Advance diffractometer, with Cu K_{α1} radiation $\lambda = 1.5406 \text{ \AA}$. The reference data were taken from the International Centre for Diffraction Data (ICDD). The composition of prepared materials was analysed by Energy-dispersive X-ray spectroscopy (EDS), using Quanta 250 FEG, FEI, with voltage 30kV. Transmission-electron-microscopy (TEM) images were recorded on a JEOL 1400 Transmission Electron Microscope, which used an accelerating voltage of 120 kV. Fourier transform infrared spectra (FT-IR) were recorded using a JASCO 4200 FT-IR spectrophotometer. Dynamic light scattering (DLS) and zeta potential measurements were performed by using a Malvern Zetasizer Nano ZS instrument, where the sample concentration was 0.25 mg/mL.

UV-Vis-NIR absorption spectra of powders were recorded with spectrophotometer JASCO V-770. The excitation and emission spectra of the prepared samples in the form of solid powders were measured on a Photon Technology International QuantaMasterTM 40 spectrofluorometer equipped with an Opolette 355LD UVDM tuneable laser, with a repetition rate of 20 Hz and a Hamamatsu R928 photomultiplier used as a detector. A continuous CNI multiwavelength (808, 975, 1208 and 1532 nm) 2W CW diode laser was used as the excitation

source, coupled to a 200 μm optical fibre and collimator for emission measurements and examination of relations between emission intensity and laser power. Laser beam size and power were measured by Ophir 10A-PPS sensor (CW laser) or by Coherent EnergyMax-USB J-10MB-HE Energy Sensor (pulsed laser). As a detector, a Digital CCD Camera made by Princeton Instruments PIXIS:256E, equipped with an SP-2156 Imaging Spectrograph was applied, corrected for the instrumental response. Luminescence decay curves were recorded using a 200 MHz Tektronix MDO3022 oscilloscope, coupled to the R928 PMT and the QuantaMaster™ 40 spectrofluorometer. All spectra, i.e. excitation and emission were corrected for the instrumental response and OPO laser energy.

Synthesis of $\text{CaF}_2:20\%\text{Yb}^{3+},1\%\text{Er}^{3+}$ nanoparticles

In order to obtain 3.5 mmol of CaF_2 doped with 20% of Yb^{3+} and 1% of Er^{3+} , the aqueous solution of chlorides with concentration 1 M or 0.25 M was used. CaCl_2 (2.77 mmol) and YbCl_3 mixed with ErCl_3 (0.7 mmol Yb^{3+} and 0.035 mmol Er^{3+}) was added to 20 mL of 1 M aqueous solution of sodium citrate (NaCit) or 20 mL of 1 M aqueous solution of ammonium citrate (NH_4Cit). Then, 5 mL of 2.10 M (1.5 excess to the stoichiometric amount, $1.5\times \text{NH}_4\text{F}$) or 5 mL of 4.2 M aqueous solution of NH_4F (3 times excess to the stoichiometric amount, $3\times \text{NH}_4\text{F}$) as a source of fluoride ions, were added to the solution containing CaCl_2 and LnCl_3 salts. The pH of the final solution was 7.5. The as-prepared transparent solution was transferred into 50 mL (35 mL of solution) or 100 mL (75 mL of solution) the Teflon-lined vessel and hydrothermally treated for 12 h (200 $^\circ\text{C}$, 15 bar), in an externally heated autoclave. Two different Berghof autoclaves were used: DAB-2 reactor for the smaller volume sample, without a stirrer and BR - 100 for the larger volume sample, with a stirrer. When the reaction was complete, the obtained white precipitate was purified by centrifugation and rinsed several times with water and ethanol. The final product was dried under ambient conditions. Additionally, $\text{CaF}_2:20\%\text{Yb}^{3+}$, NaCit, $1.5\times \text{NH}_4\text{F}$ in 35 mL of solution was prepared to investigate the influence of complexing agent on spectroscopic properties. Dopant concentrations were established based on literature data and earlier research, as well as synthesis conditions [25, 42].

Results and discussion

Structure and morphology

Cubic nanocrystals of CaF_2 doped with lanthanide ions (Ln^{3+}) were obtained by the hydrothermal synthesis in the presence of sodium citrate (NaCit) or ammonium citrate (NH_4Cit) as a complexing agent. The prepared samples showed a single-phase structure with $Fm\bar{3}m$ space group, for both reactor volumes used (Fig. 1).

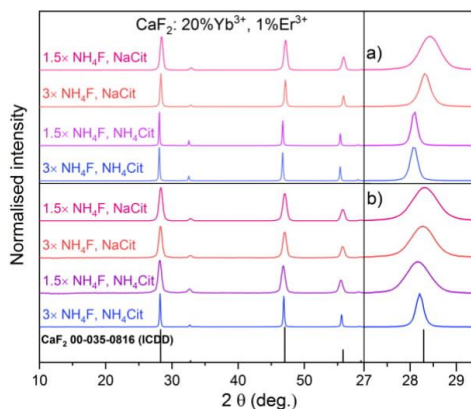


Fig. 1. XRD patterns of the $\text{CaF}_2:\text{Yb}^{3+}$, Er^{3+} samples synthesized by the hydrothermal method: a) without stirring, in 35 mL volume, b) with stirring, 75 mL volume. The patterns are labelled according to the scheme: an excess of NH_4F precipitating compound, a source of citric ions.

Additional information about the physical properties of prepared NPs was obtained from the cell parameter analysis (Table S1). An increase in the cell volume of all samples (163.26 to 166.57 \AA^3) in comparison to that of undoped CaF_2 (163.04 \AA^3), was observed. The larger cell volumes were interpreted as a result of electronic repulsion between F^- ions distributed in a cell in different positions due to local or nonlocal charge compensation as well as clusters formation [43, 44]. Additionally, differences in the cell size between the samples prepared with NaCit and NH_4Cit are presented, which confirms the occurrence of two types of charge compensation processes (1st: $2 \text{Ca}^{2+} \rightarrow \text{Ln}^{3+} + \text{Na}^+$, 2nd: $\text{Ca}^{2+} \rightarrow \text{Ln}^{3+} + \text{F}^-$). During the synthesis with NaCit, Na^+ ions are incorporated into the structure replacing interstitial fluorine ions because their ionic radii are similar to those of calcium ions ($r_{\text{Na}^+} = 1.18$, $r_{\text{Ca}^{2+}} = 1.12$, for coordination number CN = 8). In the process of synthesis using NH_4Cit , F^- ions act as a charge compensator, as the size of NH_4^+ cations is bigger ($r_{\text{NH}_4^+} = 1.54 \text{\AA}$) [45–48]. Moreover, the change of cell size is also noticeable in the XRD patterns (Fig. 1) as a slight shift of the peaks towards lower angles for the samples prepared with

NH₄Cit and a shift towards higher angles for the sample with NaCit, obtained in the small volume, with 1.5× NH₄F excess.

TEM images were used to determine the accurate size of CaF₂ nanoparticles and the results are listed in Table 1.

Table 1. Size of obtained NPs, calculated from TEM analysis

Volume	Stirring	Co- reagent	TEM analysis	
			NH ₄ F excess	CaF ₂ :20%Yb ³⁺ ,1%Er ³⁺
				Size (nm)
35 mL	No	NaCit	1.5 ×	17.4 ± 3.9
			3 ×	27.2 ± 5.8
		NH ₄ Cit	1.5 ×	35.9 ± 24.7
			3 ×	46.5 ± 11.5
75 mL	Yes	NaCit	1.5 ×	19.5 ± 7.4
			3 ×	14.4 ± 3.4
		NH ₄ Cit	1.5 ×	13.8 ± 2.4
			3 ×	40.4 ± 11.8

NPs sizes were in the range of 17.4 nm to 46.5 nm when the small volume was used and 13.8 nm to 40.4 nm for the larger volume (Table 1 and Fig. 2). Additionally, some particle agglomerations can be observed in TEM pictures, which was also confirmed by DLS histograms (Fig. S1 in Electronic Supplementary Information, ESI). The tendency to agglomeration is visible mainly for the samples prepared without stirring (Figs. 2a-2d). Moreover, the NPs, obtained with the use of NH₄Cit for the synthesis, had irregular shapes and were of larger sizes. To investigate the incorporation of Ln³⁺ ions and the real structure of the obtained compound, EDS mapping was made and the results are presented in Table S2. The amount of Ln³⁺ dopants is lower than assumed, but similar in all samples, i.e.: Yb³⁺ 11.03 - 14.50% and Er³⁺ 0.47 - 1.14%, with one exception, for the sample prepared in the presence of NH₄Cit with 3× NH₄F and in 75 mL of solution. The EDS analysis confirmed the incorporation of Na⁺ ions into the structure at the sites occupied by Ca²⁺ and F⁻ ions when the samples were prepared in the presence of NaCit. The amount of Na⁺ ions was estimated to be between 16.50 and 28.11%. Additionally, the presence of citrate groups on NPs surface was confirmed by FT-IR measurements (Fig. S2). Prepared samples exhibited negative charge on

the surface, except for the samples prepared in the presence of NH_4Cit with $3 \times \text{NH}_4\text{F}$ in 35 mL, and NH_4Cit , $1.5 \times \text{NH}_4\text{F}$ in 75 mL (Table S3) which had a positive charge. What is more, the NPs showed different stability in water (zeta potentials varied between $[-20.3]$ and $[7.75]$ mV) at physiological pH for 24 h.

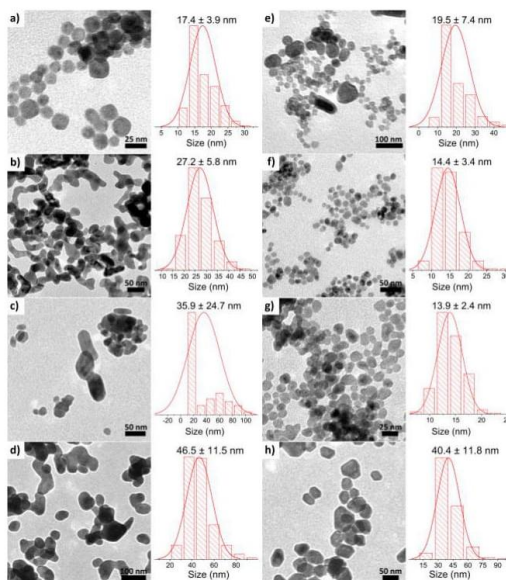


Fig. 2. Nanocrystals size distribution of hydrothermally synthesized samples: (a) $\text{CaF}_2:\text{Yb}^{3+},\text{Er}^{3+}$, NaCit , $1.5 \times \text{NH}_4\text{F}$ (b) $\text{CaF}_2:\text{Yb}^{3+},\text{Er}^{3+}$, NaCit , $3 \times \text{NH}_4\text{F}$ (c) $\text{CaF}_2:\text{Yb}^{3+},\text{Er}^{3+}$, NH_4Cit , $1.5 \times \text{NH}_4\text{F}$ (d) $\text{CaF}_2:\text{Yb}^{3+},\text{Er}^{3+}$, NH_4Cit , $3 \times \text{NH}_4\text{F}$, (e) $\text{CaF}_2:\text{Yb}^{3+},\text{Er}^{3+}$, NaCit , $1.5 \times \text{NH}_4\text{F}$ (f) $\text{CaF}_2:\text{Yb}^{3+},\text{Er}^{3+}$, NaCit , $3 \times \text{NH}_4\text{F}$ (g) $\text{CaF}_2:\text{Yb}^{3+},\text{Er}^{3+}$, NH_4Cit , $1.5 \times \text{NH}_4\text{F}$ (h) $\text{CaF}_2:\text{Yb}^{3+},\text{Er}^{3+}$, NH_4Cit , $3 \times \text{NH}_4\text{F}$, where a)-d) 35 mL, without stirring, and e)-h) 75 mL, with stirring.

Summarizing, it is possible to control the $\text{CaF}_2:\text{Yb}^{3+},\text{Er}^{3+}$ NPs morphology by selecting the appropriate concentration of NH_4F and the type of co-reagent. From the above-presented results, it is also seen that the synthesis in a reactor with stirring should be more favourable, resulting in lower agglomeration of NPs. It is possible to obtain small NPs of the size below to 20 nm even with a high content of NH_4F , which is quite essential when the synthesis is conducted in water.

Spectroscopic properties

It is well known from the literature, that only for low concentrations (<0.1%), the Ln^{3+} dopants form isolated centres. Yb^{3+} ions are sensitive to the site symmetry and their absorption spectra reflect this feature [49]. The mentioned centres have trigonal, tetragonal or cubic symmetry, depending on the location of charge compensating F^- ions. In the heavily-doped materials, Yb^{3+} ions form clusters, mainly cubooctahedral hexamers with the six Yb^{3+} ions site in square antiprisms [44, 50]. Cluster formation is well confirmed on the basis of the broad Yb^{3+} excitation bands that do not allow drawing conclusions on the Yb^{3+} ions site symmetries as it overlaps any other possible signals. However, for the samples prepared with NaCit, in 35 mL of solution, the formation of centres with the cubic symmetry (O_h) is responsible for the presence of peaks at 966 nm (10352 cm^{-1}) and 920 nm (10870 cm^{-1}), which are intense and well separated (Fig. 3a). After Na^+ ions introduction into the structure as a charge compensator, Yb^{3+} - Na^+ ion pairs are formed. At the same time, a decrease in the number of Yb^{3+} - Yb^{3+} pairs and formation of Yb^{2+} , which are responsible for quenching luminescence through cooperative energy transfer from Er^{3+} ions, are observed [47].

As a result, the emission of particles with incorporated Na^+ ions is more intense, which is observed in Figs. 4 and S3. What is interesting, the domination of O_h symmetry is only visible for the sample prepared with NaCit, $3\times\text{NH}_4\text{F}$ in 35 mL solution, where more effective incorporation of Na^+ ions replacing interstitial F^- ions occurred. Furthermore, in the analogous sample but prepared in larger volume (75 mL) with stirring, a lower amount of Yb^{3+} sites with the O_h symmetry are present, despite the fact that the determined concentration of Na^+ ions was higher (28%) than for the sample described above. It is worth noting that Na^+ ions can be also present on the surface of NPs due to the bonding to citrate groups, which are incorporated into CaF_2 NPs (Fig. S2). Interestingly, the excitation peak near 966 nm can be detected in the excitation spectra of all of the synthesized samples (Fig. 3), hence confirming the presence of the O_h symmetry of Yb^{3+} ions in the prepared NPs, regardless of the used surfactant, which has been also observed by another research group [44]. Absorption spectra of samples prepared are presented in Fig. S11 showing different characteristics of the Yb^{3+} absorption peaks, hence revealing also different efficiency of energy transfer between various types of Yb^{3+} ions and Er^{3+} ions.

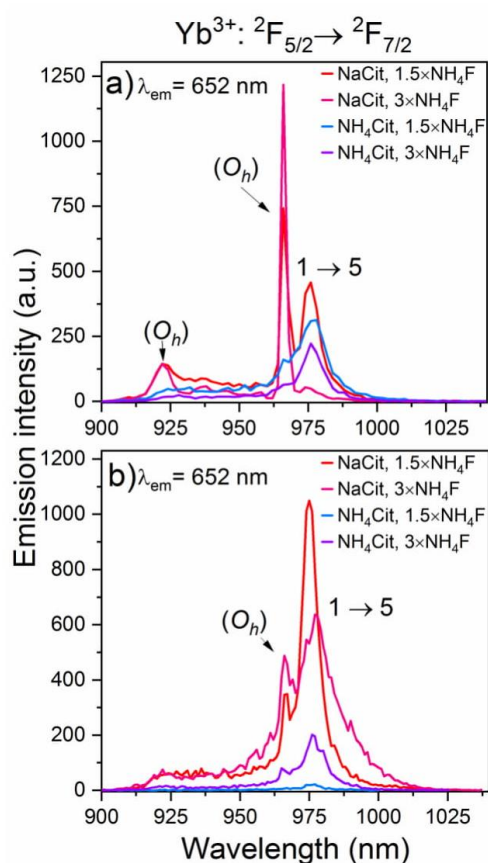


Fig. 3. Excitation spectra of $\text{CaF}_2:20\% \text{Yb}^{3+}, 1\% \text{Er}^{3+}$ samples (900 – 1050 nm): a) small volume, without stirring, b) large volume, with stirring; excited by pulsed laser as excitation source (at $25 \text{ mJ} \cdot \text{cm}^{-2}$).

For prepared samples the emission spectra were measured under continuous diode laser with $\lambda_{\text{ex}} = 975 \text{ nm}$ wavelength and are presented in Fig. 4. The brightest luminescence was recorded for the samples synthesized in the presence of NaCit and with $1.5 \times \text{NH}_4\text{F}$ in both volumes used, 35 mL, without stirring and 75 mL with stirring. The observed luminescence intensities confirm the influence of sodium ions on the effectiveness of emission. Additionally, samples prepared without stirring, with NaCit in 35 mL, exhibited twice time stronger emission than the best samples obtained in 75 mL solution with stirring. High luminescence can be connected with a decreased number of formed $\text{Yb}^{3+}\text{-Yb}^{3+}$ clusters which reduced the non-radiative energy losses. Changes in the cooperative energy transfer between Yb^{3+} ions and shorter distances between Yb^{3+} and Er^{3+} ions (see Table S1) can improve energy transfer.

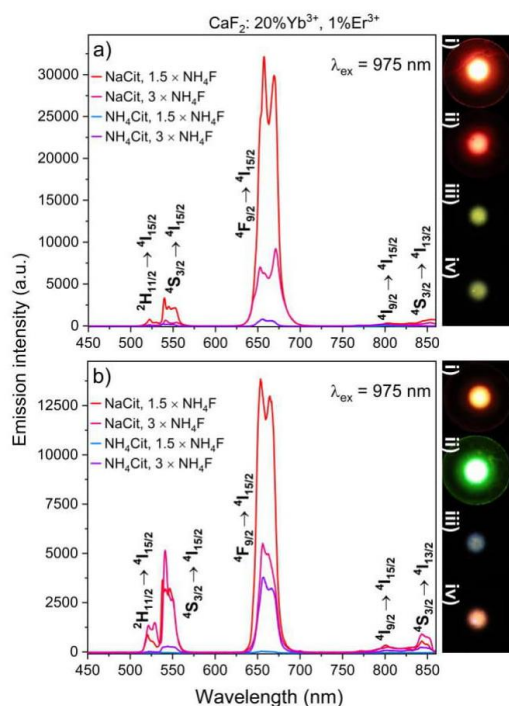


Fig. 4. Luminescence (450 – 860 nm) spectra and emission color of $\text{CaF}_2:20\% \text{Yb}^{3+}, 1\% \text{Er}^{3+}$ samples: a) small volume, without stirring, b) large volume, with stirring, where: (i) NaCit, $1.5 \times \text{NH}_4\text{F}$, (ii) NaCit, $3 \times \text{NH}_4\text{F}$, (iii) NH_4Cit , $1.5 \times \text{NH}_4\text{F}$, (iv) NH_4Cit , $3 \times \text{NH}_4\text{F}$, excited by laser under continuous excitation source (at $25 \text{ W} \cdot \text{cm}^{-2}$).

The synthesis procedure also influences the samples emission colour, which is illustrated in the photographs, the calculated ratios between two of the strongest bands and the chromaticity diagrams (Figs. 4, S4, S5). Interestingly, for the samples prepared without stirring and in the small volume the domination of red band over green is strongly visible, in comparison to the luminescence of the samples obtained with stirring and in larger volume, for which the $4\text{S}_{3/2} \rightarrow 4\text{I}_{15/2}$ and $4\text{F}_{9/2} \rightarrow 4\text{I}_{15/2}$ intensities are similar. As a result, the samples obtained in larger volume, with stirring, showed the yellow-green colour of emission. The most significant shift to the green region was recorded for the sample prepared in 75 mL with stirring, NaCit as co-reagent and $3 \times \text{NH}_4\text{F}$, which is also noticeable in Figs. 4b)ii) and S5. Comparing the luminescence of the obtained samples prepared in the same way, it is possible to receive different emission intensity and colour, just by changing the volume and application of stirring.

More information about spectroscopic properties of synthesized CaF_2 NPs was obtained from the luminescence decays of Er^{3+} ions, measured under $\lambda_{\text{ex}} = 976$ and 966 nm wavelength

with pulsed laser as the excitation source (for experimental data see ESI, Figs. S6 and S7). Moreover, luminescence rise times as well as decays of Yb^{3+} under $\lambda_{\text{ex}} = 966/977$ nm pulsed laser excitation were also recorded to investigate the energy transfer between Yb^{3+} ions in different sites and the influence of complexing agent on their lifetimes (Fig. S8). On the basis of these measurements, luminescence lifetimes were calculated for transitions of Er^{3+} and Yb^{3+} ions (collected in Tables 2, S4 and S5).

Table 2. Emission lifetimes calculated from the measured luminescence decay of $\text{CaF}_2: \text{Yb}^{3+}, \text{Er}^{3+}$ NPs under 976 nm laser excitation (for decays see Fig. S6, err < 1.6 μs). The number of photons involved in the up-conversion mechanism, determined from the dependencies of luminescence intensity on laser energy for $\text{CaF}_2: \text{Yb}^{3+}, \text{Er}^{3+}$ NPs (for experimental results see Fig. S9, err < 0.06).

		CaF ₂ :20%Yb ³⁺ ,1%Er ³⁺										
Volume	Stirring	Co- reagent	NH ₄ F excess	Lifetime (μs)					Number of photons			
				² H _{9/2} → ⁴ I _{15/2}	² H _{11/2} → ⁴ I _{15/2}	⁴ S _{3/2} → ⁴ I _{15/2}	⁴ F _{9/2} → ⁴ I _{15/2}	⁴ F _{9/2} → ⁴ I _{15/2}	² H _{11/2} → ⁴ I _{15/2}	⁴ S _{3/2} → ⁴ I _{15/2}	⁴ F _{9/2} → ⁴ I _{15/2}	⁴ F _{9/2} → ⁴ I _{15/2}
35 mL	No	NaCit	1.5 ×	22.4	24.2	24.0	99.4	23.9	2.2	2.0	2.0	1.3
			3 ×	39.0	58.4	50.1	200.5	54.2	1.4	1.6	1.6	1.4
		NH ₄ Cit	1.5 ×	9.5	14.3	14.3	31.3	16.2	1.3	1.4	1.6	1.2
			3 ×	12.1	12.3	12.6	26.7	16.6	1.0	1.1	1.2	1.0
75 mL	Yes	NaCit	1.5 ×	44.1	47.1	49.3	206.9	21.0	1.4	1.3	1.2	1.1
			3 ×	25.3	26.5	24.9	179.8	32.8	1.9	1.7	2.0	1.2
		NH ₄ Cit	1.5 ×	-	8.4	8.6	16.4	8.2	0.4	0.6	1.2	0.5
			3 ×	-	33.3	33.2	137.5	45.3	1.3	1.4	1.6	1.3

The longest luminescence decay of Er^{3+} ions was recorded for the sample prepared in the presence of NaCit and with 3× NH₄F, without stirring in 35 mL solution as well as NPs with NaCit, 1.5× NH₄F, in 75 mL solution. From all Er^{3+} transitions, the decay of ${}^4\text{F}_{9/2} \rightarrow {}^4\text{I}_{15/2}$ was recorded as the longest one for all samples (16.4 μs to 206.9 μs), which may be a result of strong emission of this band and the mechanism responsible for ${}^4\text{F}_{9/2}$ energy level excitation. Importantly, for the samples with a large number of Yb^{3+} ions at O_h symmetry sites (NaCit, 1.5× NH₄F and 3× NH₄F in 35 mL of solution), longer lifetimes for Er^{3+} were calculated under 966 nm excitation than under 976 nm.

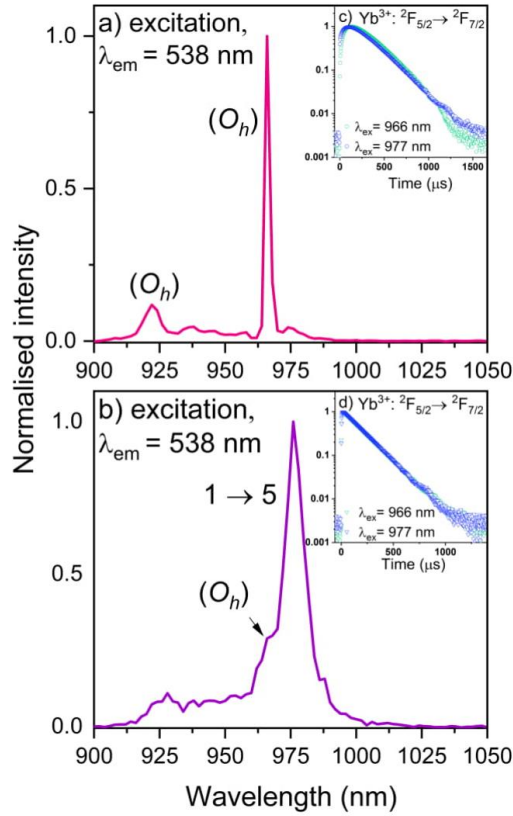


Fig. 5. Excitation spectra of $\text{CaF}_2: \text{Yb}^{3+}, \text{Er}^{3+}$ a,b) and decay time of $\text{Yb}^{3+} {}^2\text{F}_{5/2} \rightarrow {}^2\text{F}_{7/2}$ transition c, d) under 966/977 nm pulsed excitation source (at $15 \text{ mJ}\cdot\text{cm}^{-2}$), observed at 1050 nm, where a, c) sample with NaCit, $3\times \text{NH}_4\text{F}$, 35 mL solution, b, d) sample with NH_4Cit , $3\times \text{NH}_4\text{F}$, 35 mL solution.

The Yb^{3+} decay time measurements did not reveal significant changes in the lifetimes of Yb^{3+} ions upon excitation with 966 or 976 nm wavelengths, even for the samples with a large number of Yb^{3+} ions at the sites of O_h symmetry. Taking into account a significant impact of site symmetry on Ln^{3+} emission lifetimes, it is expected to find longer lifetimes for the structure with sites of higher symmetry [51]. The explanation of the difference between the literature-based expectation and observations can be the domination of Yb^{3+} - Yb^{3+} clusters in the sample's structure or at least the presence of a mixture of sites of different symmetries, which makes it impossible to excite Yb^{3+} ions at the sites of a single symmetry. However, for the samples prepared in the presence of NaCit, relatively long rise times were observed, especially in comparison to those of the samples obtained with NH_4Cit . What is more, the difference was

also detectable for the same samples obtained by the two synthesis routes (NaCit, $3\times$ NH₄F, 35 mL and NaCit, $3\times$ NH₄F, 35 mL, Table S5, Fig. 5). The reason for this observation is related to the energy transfer from O_h centres of Yb³⁺ of higher energy (10 352 cm⁻¹) to Yb³⁺ cluster centres with lower energy (10 246 cm⁻¹, 5→5 transitions, Fig. 6a). On the basis of these measurements and calculations, it can be concluded that the values of Yb³⁺ lifetimes are independent of the dominant symmetry (the presence or absence of Na⁺ ions) as well as of the excitation wavelength. At the same time, the luminescence rise times seem to be sensitive to the site symmetry of Yb³⁺ ions. This result is an additional confirmation of Yb³⁺ ions multisite positions in NPs, there is a fraction at sites of O_h symmetry and a fraction of those in clusters. According to the Hraiech et al., when a high number of Na⁺ ions are present in the sample, the band characteristic of Yb³⁺ ions with O_h symmetry appears in the NIR emission spectra with a maximum near 1028 nm. However, when a small number of Na⁺ ions were added, or for the samples without sodium ions, only the broad electronic transitions 5 → 3 and 5 → 4 of Stark's level with a band maximum near 1030 and 1050 nm appeared in the spectra [51]. For the all obtained samples, the lifetime, as well as rise time, were measured for the emission at 1050 nm, which proves the presence of Yb³⁺ ions at the sites of O_h symmetry and clusters in all of obtained NPs.

To establish the up-conversion mechanism of the prepared NPs and investigate the effects of the synthesis methodology on it, the dependencies of the luminescence intensity on the laser power were measured. The results of the slope calculations are collected in Table 2 (measurement results Fig. S9). The slope coefficients calculated for the samples studied took values from the range 1 to 2, which is lower than the theoretical value for energy transitions in Er³⁺ ions [25]. The highest slope coefficient was calculated for the CaF₂: Yb³⁺, Er³⁺ samples prepared with NaCit and $1.5\times$ NH₄F in the small volume (35 mL), without stirring and with NaCit and $3\times$ NH₄F with magnetic stirring and in the large volume (75 mL). Such a result can be connected with effective emission, long luminescent lifetimes and high crystallinity of these two samples (appropriate distance between Yb³⁺ and Er³⁺ ions, can minimize quenching effects). The highest slope was determined for the ⁴F_{9/2}→⁴I_{15/2} transition. This result can be explained by the relaxation from ²H_{11/2} or ⁴S_{3/2} level and the highest emission of a band corresponding to the described transition for all samples. For the few prepared nanomaterials, the slope coefficient is close to one, however, the up-conversion emission can be treated as a two-photon process [52]. There are many factors, which can influence the experimental slope like saturation effect, heating of samples or cross-relaxation process between dopants [53, 54].

Furthermore, quite often the saturation effect which is attributed to the competition between linear decay and up-conversion depletion of the intermediate state when excitation density is high takes place [19, 55, 56].

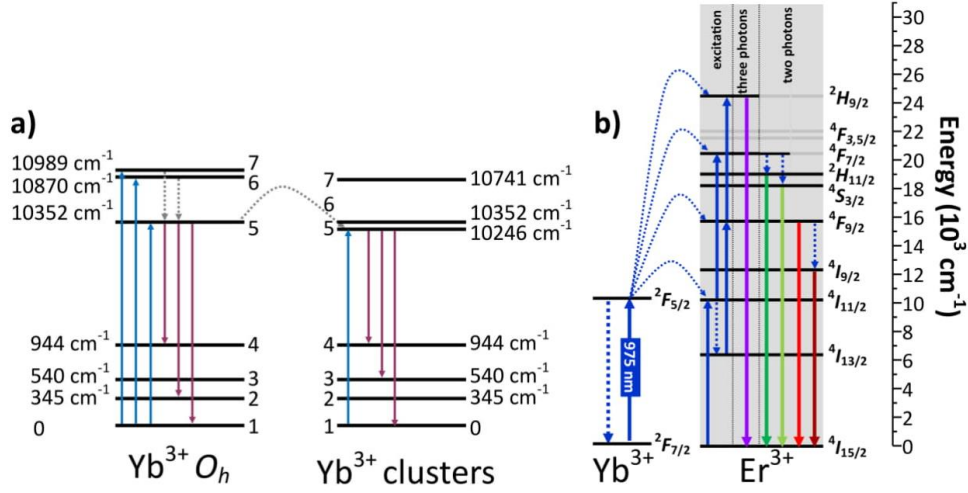


Fig. 6. Scheme of the up-conversion mechanism for $\text{CaF}_2:\text{Yb}^{3+},\text{Er}^{3+}$ systems, where a) proposed mechanism of energy transfer between Yb^{3+} ions with different symmetry, b) up-conversion energy transfer in $\text{Yb}^{3+}-\text{Er}^{3+}$ system, under NIR excitation ($\lambda_{\text{ex}} = 975 \text{ nm}$).

On the basis of the number of photons established for a population of each excited level, a UC mechanism- energy transfer up-conversion (ETU) can be proposed (Fig. 6 and S10). In the first step, Yb^{3+} ion absorbs a photon and excitation of $^2F_{5/2}$ from $^2F_{7/2}$ is observed. For the Yb^{3+} ions at O_h symmetry sites present in the structure, absorption from the ground state to 5 and 6 Stark's sublevel is observed, from which the energy can be transferred to $\text{Yb}^{3+}-\text{Yb}^{3+}$ clusters or directly to Er^{3+} ions ($^4I_{15/2} \rightarrow ^4I_{11/2}$ transition). For the hexameric clusters, the energy is absorbed from ground state mostly to 5 Stark's sublevel and transferred to activator ions. These two possible ways of excitation of Yb^{3+} ions can occur simultaneously in one sample with mixed symmetry. The next step of the mechanism is the energy transfer from the excited $\text{Yb}^{3+}:^2F_{5/2}$ to $\text{Er}^{3+}:^4I_{11/2}$ and the absorption of the second photon, to populate $^4F_{7/2}$, from which relaxation to $^2H_{11/2}$, $^4S_{3/2}$ occurs. Two photons emission is also observed from $^4F_{9/2}$ and $^4I_{9/2}$ to $^4I_{15/2}$.

Conclusions

Up-converting nanoparticles based on CaF_2 matrix doped with lanthanide ions (Yb^{3+} and Er^{3+}) were synthesized by the hydrothermal method. The influence of such factors as the

type of co-reagent, excess of fluoride ions, volume and stirring on the morphology and spectroscopic properties of the nanoparticles were investigated. The results provided the evidence illustrating the importance of the synthesis procedure because of its effect on emission intensity, colour and excitation mechanism.

The main factor influencing NPs morphology was the excess of NH_4F ; with the higher concentration of F^- ions in the solution, the obtained NPs were bigger. It can be related to a more effective precipitation process. The effect of size of NPs as a result of NH_4F excess used in the synthesis on the spectroscopic properties was also investigated. Moreover, in both synthesis route, the samples prepared with NaCit and $1.5\times \text{NH}_4\text{F}$ were characterized by the most intense emission. Additionally, the presence of Na^+ ions changes the symmetry of Yb^{3+} ions, which was visible for the products prepared in 35 mL of the solution without stirring whose luminescence was almost twice higher than that of the other NPs. Moreover, luminescence lifetimes of Er^{3+} and the rise times of Yb^{3+} ions depended on the surfactant used for the synthesis and shows that NaCit is more favourable.

Summarizing, we have established the ideal hydrothermal conditions to obtain small NPs with bright up-conversion luminescence under 975 nm (see comparison with $\text{NaYF}_4:\text{Yb}^{3+},\text{Er}^{3+}$ in Fig. S12), which are: synthesis in the presence of NaCit as an anti-agglomeration agent, suppression of NPs growth and $1.5\times \text{NH}_4\text{F}$ precipitating agent and 12 h time of synthesis. Avoiding stirring during the reaction and small reaction volume, 35 mL, resulted in the highest intensity of luminescence from all prepared samples. However, increasing reaction volume to 75 mL and the introduction of stirring during synthesis also brought products with satisfactory luminescence intensity and NPs sizes.

Conflicts of interest

There are no conflicts to declare.

CRedit authorship contribution statement

Dominika Przybylska: Conceptualization, Investigation, Writing - original draft, Visualization. **Tomasz Grzyb:** Conceptualization, Resources, Writing - review & editing, Visualization, Supervision.

Acknowledgements Funding

Funding for this research was provided by the Polish Ministry of Science and Higher Education, Poland, grant No. ID IP2014 014573 and by the National Science Centre, Poland, under grant No. 2016/22/E/ST5/00016.

Appendix A. Electronic Supplementary Material

Supplementary data to this article can be found online at

References

1. Li D, Chen G (2019) Upconversion-Enhanced Dye-Sensitized Solar Cells. In: Dye-Sensitized Solar Cells. Elsevier, pp 325–340
2. Qin X, Xu J, Wu Y, Liu X (2019) Energy-Transfer Editing in Lanthanide-Activated Upconversion Nanocrystals: A Toolbox for Emerging Applications. *ACS Cent Sci* 5:29–42. <https://doi.org/10.1021/acscentsci.8b00827>
3. Resch-Genger U, Gorris HH (2017) Perspectives and challenges of photon-upconversion nanoparticles - Part I: routes to brighter particles and quantitative spectroscopic studies. *Anal Bioanal Chem* 409:5855–5874. <https://doi.org/10.1007/s00216-017-0499-z>
4. Hudry D, Howard IA, Popescu R, et al (2019) Structure–Property Relationships in Lanthanide-Doped Upconverting Nanocrystals: Recent Advances in Understanding Core–Shell Structures. *Adv Mater* 1900623:1900623. <https://doi.org/10.1002/adma.201900623>
5. Auzel F (2004) Upconversion and Anti-Stokes Processes with f and d Ions in Solids. *Chem Rev* 104:139–173. <https://doi.org/10.1021/cr020357g>
6. Mahalingam V, Thirumalai J, Krishnan R, Mantha S (2016) Up/down conversion luminescence and charge compensation investigation of $\text{Ca}_{0.5}\text{Y}_{1-x}(\text{WO}_4)_2:\text{xLn}^{3+}$ (Ln = Pr, Sm, Eu, Tb, Dy, Yb/Er) phosphors. *Spectrochim Acta - Part A Mol Biomol Spectrosc* 152:172–180. <https://doi.org/10.1016/j.saa.2015.06.129>
7. Bünzli J-CG, Piguet C (2005) Taking advantage of luminescent lanthanide ions. *Chem Soc Rev* 34:1048. <https://doi.org/10.1039/b406082m>
8. Bünzli JCG (2016) Lanthanide Luminescence: From a Mystery to Rationalization, Understanding, and Applications. *Handb Phys Chem Rare Earths* 50:141–176. <https://doi.org/10.1016/bs.hpre.2016.08.003>
9. Niu N, Yang P, Liu Y, et al (2011) Controllable synthesis and up-conversion properties of tetragonal $\text{BaYF}_5:\text{Yb/Ln}$ (Ln=Er, Tm, and Ho) nanocrystals. *J Colloid Interface Sci* 362:389–96. <https://doi.org/10.1016/j.jcis.2011.07.001>
10. Sun J, Xian J, Du H (2011) Facile synthesis of well-dispersed $\text{SrF}_2:\text{Yb}^{3+}/\text{Er}^{3+}$ upconversion nanocrystals in oleate complex systems. *Appl Surf Sci* 257:3592–3595. <https://doi.org/10.1016/j.apsusc.2010.11.082>
11. Wang Z-L, Hao J, Chan HLW, et al (2011) Simultaneous synthesis and functionalization of water-soluble up-conversion nanoparticles for in-vitro cell and nude mouse imaging. *Nanoscale* 3:2175. <https://doi.org/10.1039/c1nr10090d>
12. Runowski M, Marciniak JJ, Grzyb T, et al (2017) Lifetime Nanomanometry - High-Pressure Luminescence of Up-converting Lanthanide Nanocrystals - $\text{SrF}_2:\text{Yb}^{3+},\text{Er}^{3+}$. *Nanoscale* 9:16030–16037. <https://doi.org/10.1039/C7NR04353H>
13. Wolfbeis OS (2015) An overview of nanoparticles commonly used in fluorescent bioimaging.

Chem Soc Rev 44:4743–4768. <https://doi.org/10.1039/C4CS00392F>

14. Escudero A, Becerro AI, Carrillo-Carrión C, et al (2017) Rare earth based nanostructured materials: Synthesis, functionalization, properties and bioimaging and biosensing applications. *Nanophotonics* 6:881–921. <https://doi.org/10.1515/nanoph-2017-0007>
15. Sun L, Wei R, Feng J, Zhang H (2018) Tailored lanthanide-doped upconversion nanoparticles and their promising bioapplication prospects. *Coord Chem Rev* 364:10–32. <https://doi.org/10.1016/j.ccr.2018.03.007>
16. Yan C, Zhao H, Perepichka DF, Rosei F (2016) Lanthanide Ion Doped Upconverting Nanoparticles: Synthesis, Structure and Properties. *Small* 3888–3907. <https://doi.org/10.1002/sml.201601565>
17. DaCosta M V., Doughan S, Han Y, Krull UJ (2014) Lanthanide upconversion nanoparticles and applications in bioassays and bioimaging: A review. *Anal Chim Acta* 832:1–33. <https://doi.org/10.1016/j.aca.2014.04.030>
18. Wang F, Deng R, Liu X (2014) Preparation of core-shell NaGdF₄ nanoparticles doped with luminescent lanthanide ions to be used as upconversion-based probes. *Nat Protoc* 9:1634–1644. <https://doi.org/10.1038/nprot.2014.111>
19. Zhou J, Chen G, Zhu Y, et al (2015) Intense multiphoton upconversion of Yb³⁺-Tm³⁺ doped β-NaYF₄ individual nanocrystals by saturation excitation. *J Mater Chem C* 3:364–369. <https://doi.org/10.1039/c4tc02363c>
20. Liu Y, Zhang C, Liu H, et al (2018) Controllable synthesis of up-conversion nanoparticles UCNPs@MIL-PEG for pH-responsive drug delivery and potential up-conversion luminescence/magnetic resonance dual-mode imaging. *J Alloys Compd* 749:939–947. <https://doi.org/10.1016/j.jallcom.2018.03.355>
21. Shao W, Hua R, Zhang W, et al (2013) Hydrothermal synthesis of poly(acrylic acid)-functionalized α-(β-)NaYF₄:Yb, Er up-conversion nano-/micro-phosphors. *Powder Technol* 237:326–332. <https://doi.org/10.1016/j.powtec.2012.12.010>
22. Wang M, Abbineni G, Clevenger A, et al (2011) Upconversion nanoparticles: synthesis, surface modification and biological applications. *Nanomedicine Nanotechnology, Biol Med* 7:710–729. <https://doi.org/10.1016/j.nano.2011.02.013>
23. Chen J, Zhao JX (2012) Upconversion nanomaterials: Synthesis, mechanism, and applications in sensing. *Sensors* 12:2414–2435. <https://doi.org/10.3390/s120302414>
24. Qiu P, Zhou N, Chen H, et al (2013) Recent advances in lanthanide-doped upconversion nanomaterials: synthesis, nanostructures and surface modification. *Nanoscale* 5:11512. <https://doi.org/10.1039/c3nr03642a>
25. Przybylska D, Ekner-Grzyb A, Grześkowiak BF, Grzyb T (2019) Upconverting SrF₂ nanoparticles doped with Yb³⁺/Ho³⁺, Yb³⁺/Er³⁺ and Yb³⁺/Tm³⁺ ions – optimisation of synthesis method, structural, spectroscopic and cytotoxicity studies. *Sci Rep* 9:8669.

- <https://doi.org/10.1038/s41598-019-45025-1>
26. Lin M, Zhao Y, Wang S, et al (2012) Recent advances in synthesis and surface modification of lanthanide-doped upconversion nanoparticles for biomedical applications. *Biotechnol Adv* 30:1551–1561. <https://doi.org/10.1016/j.biotechadv.2012.04.009>
 27. Li Y, Liu T, Du Y (2012) Accelerated fabrication and upconversion luminescence of Yb³⁺/Er³⁺-Codoped CaF₂ nanocrystal by microwave heating. *Appl Phys Express* 5:7–10. <https://doi.org/10.1143/APEX.5.086501>
 28. Cortelletti P, Pedroni M, Boschi F, et al (2018) Luminescence of Eu³⁺ Activated CaF₂ and SrF₂ Nanoparticles: Effect of the Particle Size and Codoping with Alkaline Ions. *Cryst Growth Des* 18:686–694. <https://doi.org/10.1021/acs.cgd.7b01050>
 29. Ansari AA, Yadav R, Rai SB (2017) Physicochemical properties of greatly enhanced photoluminescence of aqueous dispersible upconversion CaF₂:Yb/Er nanoparticles. *Photochem Photobiol Sci* 16:890–896. <https://doi.org/10.1039/c6pp00448b>
 30. Kaczmarek SM, Tsuboi T, Ito M, et al (2005) Optical study of Yb³⁺/Yb²⁺ conversion in CaF₂ crystals. *J Phys-Condens Mat* 17:3771–3786. <https://doi.org/10.1088/0953-8984/17/25/005>
 31. Misiak M, Skowicki M, Lipiński T, et al (2017) Biofunctionalized upconverting CaF₂:Yb,Tm nanoparticles for *Candida albicans* detection and imaging. *Nano Res* 10:3333–3345. <https://doi.org/10.1007/s12274-017-1546-y>
 32. Marino V, Astegno A, Pedroni M, et al (2014) Nanodevice-induced conformational and functional changes in a prototypical calcium sensor protein. *Nanoscale* 6:412–423. <https://doi.org/10.1039/C3NR04978G>
 33. Dolcet P, Mambri A, Pedroni M, et al (2015) Room temperature crystallization of highly luminescent lanthanide-doped CaF₂ in nanosized droplets: first example of the synthesis of metal halogenide in miniemulsion with effective doping and size control. *RSC Adv* 5:16302–16310. <https://doi.org/10.1039/C4RA12006J>
 34. Hong BC, Kawano K (2008) Syntheses of CaF₂:Eu nanoparticles and the modified reducing TCRA treatment to divalent Eu ion. *Opt Mater (Amst)* 30:952–956. <https://doi.org/10.1016/j.optmat.2007.05.023>
 35. Pandurangappa C, Lakshminarasappa BN, Nagabhushana BM (2010) Synthesis and characterization of CaF₂ nanocrystals. *J Alloys Compd* 489:592–595. <https://doi.org/10.1016/j.jallcom.2009.09.118>
 36. Claus F, Marcus R, Trampert K (2006) Polyol-Mediated Synthesis of Nanoscale CaF₂ and CaF₂:Ce,Tb. *Small* 2:1248–1250. <https://doi.org/10.1002/sml.200600140>
 37. Aubry P, Bensalah A, Gredin P, et al (2009) Synthesis and optical characterizations of Yb-doped CaF₂ ceramics. *Opt Mater (Amst)* 31:750–753. <https://doi.org/10.1016/j.optmat.2008.03.022>
 38. Jiang T, Qin W, Di W, et al (2012) Citric acid-assisted hydrothermal synthesis of α -

- NaYF₄:Yb³⁺,Tm³⁺ nanocrystals and their enhanced ultraviolet upconversion emissions. *CrystEngComm* 14:2302. <https://doi.org/10.1039/c2ce06311e>
39. Tang H, Xu Y, Cheng X (2020) Growth and enhanced upconversion luminescence intensity of Mg²⁺ and Cr³⁺ co-doped β-NaYF₄:Yb³⁺/Er³⁺ microcrystals. *J Solid State Chem* 285:. <https://doi.org/10.1016/j.jssc.2020.121229>
 40. Sagaidachnaya EA, Konyukhova JG, Kazadaeva NI, et al (2020) Effect of hydrothermal synthesis conditions on up-conversion luminescence intensity of β-NaYF₄:Er³⁺,Yb³⁺ particles. *Quantum Electron* 50:109–113. <https://doi.org/10.1070/qel17205>
 41. Szczeszak A, Grzyb T, Nowaczyk G, Ekner-Grzyb A (2020) Emission colour changes in the CaF₂ sub-microspheres doped with Yb³⁺, Er³⁺ and Mn²⁺ ions. *J Alloys Compd* 817:152718. <https://doi.org/10.1016/j.jallcom.2019.152718>
 42. Zhao X, Yang Z, Yang X, et al (2019) Controlling the multicolor upconversion luminescence in CaF₂ nanocrystals doped with Yb³⁺, Er³⁺ and Nd³⁺ ions under the excitation of a 808 nm laser. *Opt Mater Express* 9:4578. <https://doi.org/10.1364/ome.9.004578>
 43. Zhao J, Zhu YJ, Wu J, Chen F (2015) Microwave-assisted solvothermal synthesis and upconversion luminescence of CaF₂:Yb³⁺/Er³⁺ nanocrystals. *J Colloid Interface Sci* 440:39–45. <https://doi.org/10.1016/j.jcis.2014.10.031>
 44. Petit V, Camy P, Doualan JL, et al (2008) Spectroscopy of Yb³⁺:CaF₂: From isolated centers to clusters. *Phys Rev B - Condens Matter Mater Phys* 78:1–12. <https://doi.org/10.1103/PhysRevB.78.085131>
 45. Zhang C, Hou Z, Chai R, et al (2010) Mesoporous SrF₂ and SrF₂:Ln³⁺ (Ln = Ce, Tb, Yb, Er) hierarchical microspheres: Hydrothermal synthesis, growing mechanism, and luminescent properties. *J Phys Chem C* 114:6928–6936. <https://doi.org/10.1021/jp911775z>
 46. Pedroni M, Piccinelli F, Passuello T, et al (2013) Water (H₂O and D₂O) Dispersible NIR-to-NIR Upconverting Yb³⁺/Tm³⁺ Doped MF₂ (M = Ca, Sr) Colloids: Influence of the Host Crystal. *Cryst Growth Des* 13:4906–4913. <https://doi.org/10.1021/cg401077v>
 47. Su L, Xu J, Li H, et al (2005) Codoping Na⁺ to modulate the spectroscopy and photoluminescence properties of Yb³⁺ in CaF₂ laser crystal. *Opt Lett* 30:1003. <https://doi.org/10.1364/OL.30.001003>
 48. Sidey V (2016) On the effective ionic radii for ammonium. *Acta Crystallogr Sect B Struct Sci Cryst Eng Mater* 72:626–633. <https://doi.org/10.1107/S2052520616008064>
 49. Kallel T, Hassairi MA, Dammak M, et al (2014) Spectra and energy levels of Yb³⁺ ions in CaF₂ transparent ceramics. *J Alloys Compd* 584:261–268. <https://doi.org/10.1016/j.jallcom.2013.09.057>
 50. Nicoara I, Stef M (2012) Study of Na⁺ ions influence on the charge compensating defects in CaF₂:YbF₃ crystals using dielectric relaxation. *Eur Phys J B* 85:1–7. <https://doi.org/10.1140/epjb/e2012-20914-8>

51. Hraiech S, Jouini A, Jin Kim K, et al (2010) Role of monovalent alkali ions in the Yb³⁺ centers of CaF₂ laser crystals. *Radiat Meas* 45:323–327. <https://doi.org/10.1016/j.radmeas.2009.11.017>
52. Tymiński A, Grzyb T (2017) Are rare earth phosphates suitable as hosts for upconversion luminescence? Studies on nanocrystalline REPO₄(RE=Y, La, Gd, Lu) doped with Yb³⁺ and Eu³⁺, Tb³⁺, Ho³⁺, Er³⁺ or Tm³⁺ ions. *J Lumin* 181:411–420. <https://doi.org/10.1016/j.jlumin.2016.09.028>
53. Grzyb T, Gruszczyńska A, Wiglusz RJ, et al (2012) Multifunctionality of GdPO₄:Yb³⁺, Tb³⁺ nanocrystals – luminescence and magnetic behaviour. *J Mater Chem* 22:22989. <https://doi.org/10.1039/c2jm34863b>
54. Wang F, Deng R, Wang J, et al (2011) Tuning upconversion through energy migration in core-shell nanoparticles. *Nat Mater* 10:968–973. <https://doi.org/10.1038/nmat3149>
55. Lei Y, Song H, Yang L, et al (2005) Upconversion luminescence, intensity saturation effect, and thermal effect in Gd₂O₃:Er³⁺, Yb³⁺ nanowires. *J Chem Phys* 123:174710. <https://doi.org/10.1063/1.2087487>
56. Vetrone F, Mahalingam V, Capobianco JA (2009) Near-Infrared-to-Blue Upconversion in Colloidal BaYF₅:Tm³⁺, Yb³⁺ Nanocrystals. *Chem Mater* 21:1847–1851. <https://doi.org/10.1021/cm900313s>

Electronic Supplementary Information for:

Tailoring structure, morphology and up-conversion properties of CaF₂:Yb³⁺,Er³⁺ nanoparticles by the route of synthesis

*Dominika Przybylska, Tomasz Grzyb**

Department of Rare Earths, Faculty of Chemistry, Adam Mickiewicz University in
Poznań, Uniwersytetu Poznańskiego 8, 61-614 Poznań, Poland

*Corresponding Author

e-mail: tgrzyb@amu.edu.pl

1. Structure and morphology

Table S1. Cell parameter for cubic structure CaF₂:Yb³⁺,Er³⁺ calculated in Maud software.¹

Volume	Stirring	Co- reagent	NH ₄ F excess	CaF ₂ :20% Yb ³⁺ ,1% Er ³⁺	
				a [Å]	V [Å ³]
35 mL	No	NaCit	1.5 ×	5.47(8)	164.39(4)
			3 ×	5.46(6)	163.26(7)
		NH ₄ Cit	1.5 ×	5.49(9)	166.57(1)
			3 ×	5.50(2)	166.65(0)
75 mL	Yes	NaCit	1.5 ×	5.48(1)	164.67(8)
			3 ×	5.46(8)	163.47(0)
		NH ₄ Cit	1.5 ×	5.48(8)	165.26(6)
			3 ×	5.48(8)	165.29(6)
Reference CaF₂				5.462	163.04 (0)

During the synthesis with NaCit Na⁺ ions are incorporated into the structure replacing interstitial fluorine ions because their ionic radii are similar to those of calcium ions ($r_{\text{Na}^+} = 1.18$, $r_{\text{Ca}^{2+}} = 1.12$, for coordination number CN = 8). In the process of synthesis using NH₄Cit, F⁻ ions act as a charge compensator, as the size of NH₄⁺ cations is bigger ($r_{\text{NH}_4^+} = 1.54 \text{ \AA}$) [1–4]. Moreover, the

change of cell size is also visible in the XRD patterns (Fig. 1) as a slight shift of the peaks towards lower angles for the sample prepared with NH_4Cit and a shift towards higher angles for the sample with NaCit .

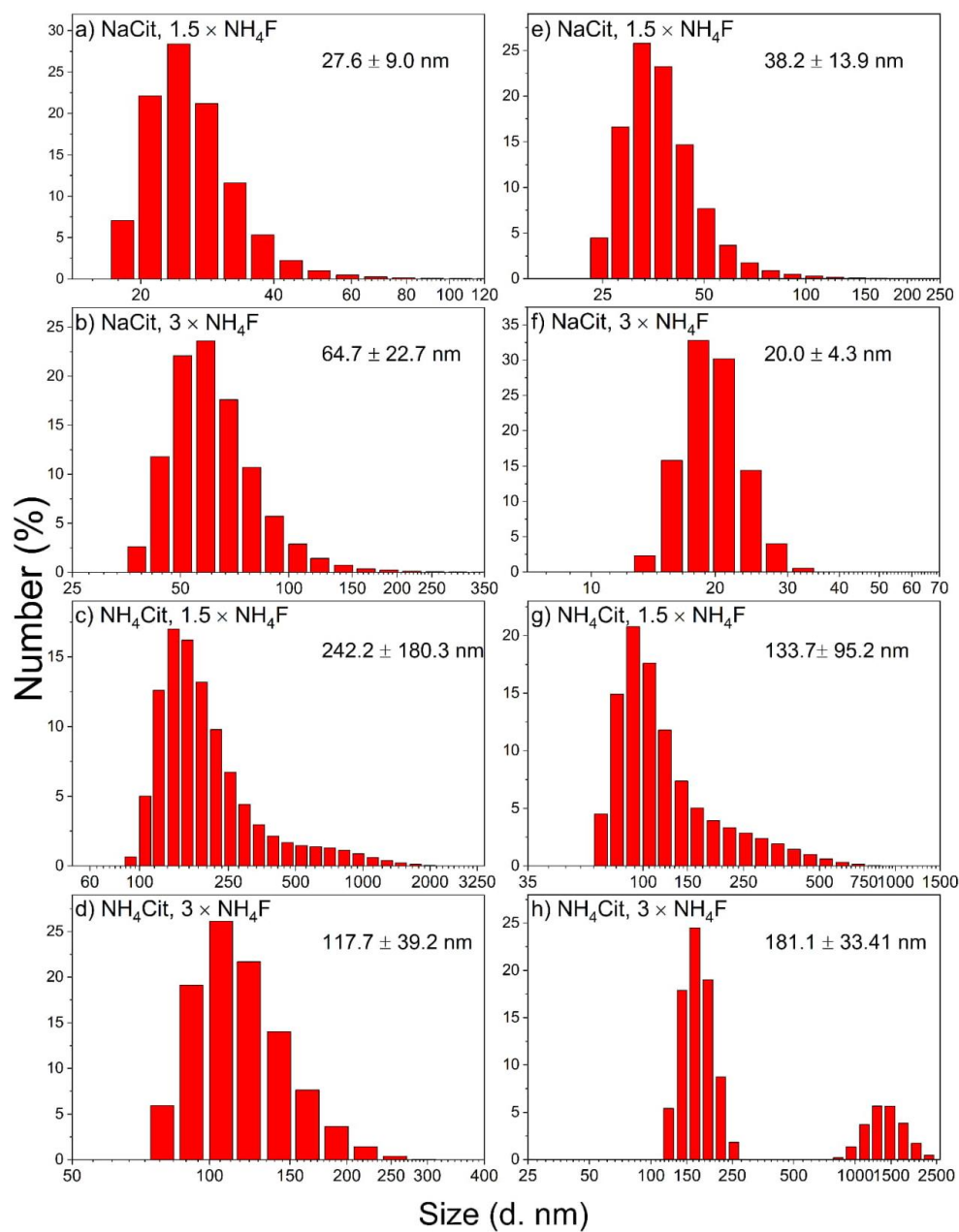


Fig. S1. Hydrodynamic diameters obtained by DLS analysis of the synthesized $\text{CaF}_2:\text{Yb}^{3+},\text{Er}^{3+}$ NPs, where a)-d) synthesis conducted in small volume, without stirring, e)-h) large volume, with stirring

Table S2. Composition of the synthesized NPs obtained by EDS analysis.

Volume	Stirring	Co- reagent	NH ₄ F excess	Atomic percentage (%) CaF ₂ :20% Yb ³⁺ , 1% Er ³⁺					Formula
				Ca ²⁺	Yb ³⁺	Er ³⁺	F ⁻	Na ⁺	
35 mL	No	NaCit	1.5 ×	67.91	11.77	0.55	69.23	19.77	Ca _{0.68} Yb _{0.12} Er _{0.006} F _{2.25}
			3 ×	71.43	11.56	0.47	59.50	16.50	Ca _{0.71} Yb _{0.12} Er _{0.005} F _{1.47}
		NH ₄ Cit	1.5 ×	84.80	14.50	0.70	69.50	0	Ca _{0.85} Yb _{0.15} Er _{0.007} F _{2.28}
			3 ×	85.60	13.90	0.50	66.58	0	Ca _{0.86} Yb _{0.14} Er _{0.005} F _{2.00}
75 mL	Yes	NaCit	1.5 ×	68.86	13.62	0.49	65.37	17.03	Ca _{0.69} Yb _{0.14} Er _{0.005} F _{1.89}
			3 ×	59.71	11.03	1.14	63.04	28.11	Ca _{0.83} Yb _{0.15} Er _{0.016} F _{1.71}
		NH ₄ Cit	1.5 ×	86.60	12.70	0.60	71.60	0	Ca _{0.87} Yb _{0.13} Er _{0.006} F _{2.52}
			3 ×	93.01	5.53	1.46	64.64	0	Ca _{0.93} Yb _{0.055} Er _{0.015} F _{1.87}
CaF₂:20% Yb³⁺, NaCit, 3×NH₄F, 35 mL				69.06	13.05	0	62.72	17.90	Ca _{0.69} Yb _{0.13} F _{1.68}

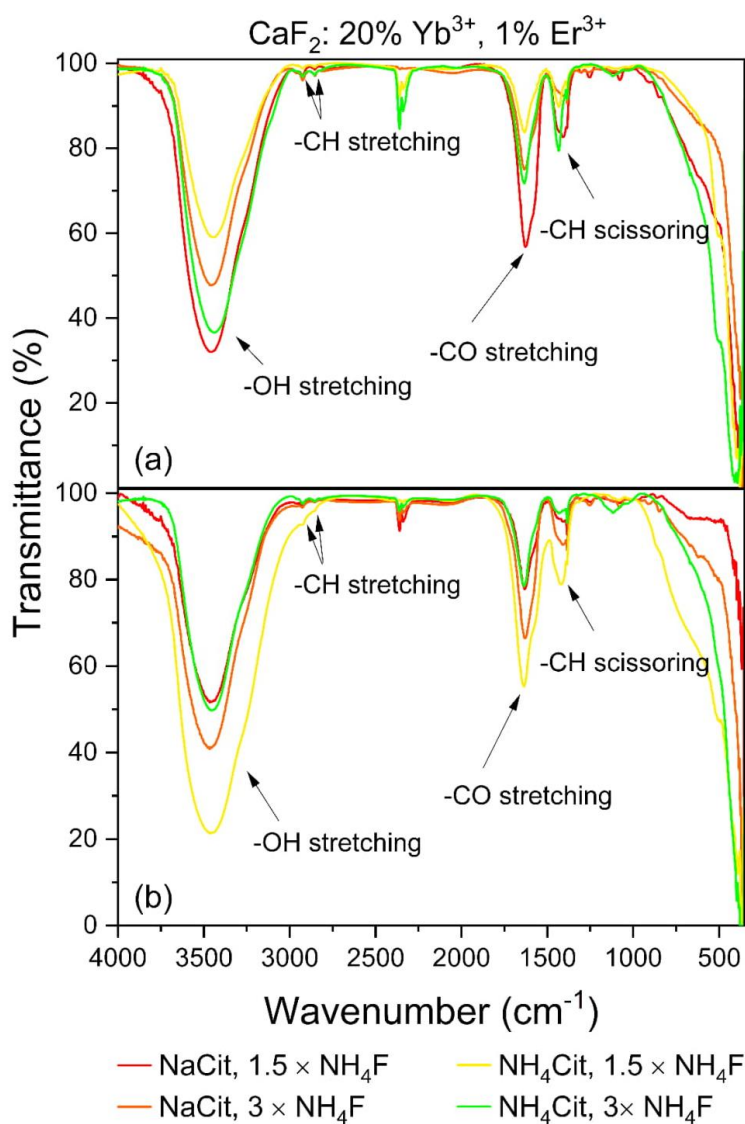


Fig. S2. Fourier transform infrared spectroscopy (FT-IR) spectra of obtained samples, where a) synthesis conducted in the small volume (35 mL), without stirring, b) large volume (75 mL), with stirring.

The presence of citrate groups on NPs surface was inferred from the appearance of the signals assigned to: OH stretching vibration (3457 cm⁻¹), -CH asymmetric and symmetric stretching vibrations (2962 and 2840 cm⁻¹), -C=O stretching vibrations (1622 cm⁻¹) and -CH scissoring (1400 cm⁻¹).

Table S3. Summary of zeta potential measurements for obtained $\text{CaF}_2:\text{Yb}^{3+},\text{Er}^{3+}$ particles at physiological pH value.

Volume	Stirring	Co-reagent	NH_4F excess	$\text{CaF}_2:20\% \text{Yb}^{3+},1\% \text{Er}^{3+}$	
				pH	Zeta potential (mV)
35 mL	No	NaCit	1.5×	7.46	-20.3 ± 5.8
			3×	7.44	-17.8 ± 4.6
		NH_4Cit	1.5×	7.39	-10.6 ± 5.9
			3×	7.37	11.3 ± 4.7
75 mL	Yes	NaCit	1.5×	7.43	-14.3 ± 5.8
			3×	7.39	-10.0 ± 5.4
		NH_4Cit	1.5×	7.40	7.8 ± 5.09
			3×	7.32	-17.0 ± 6.1

2. Spectroscopic properties

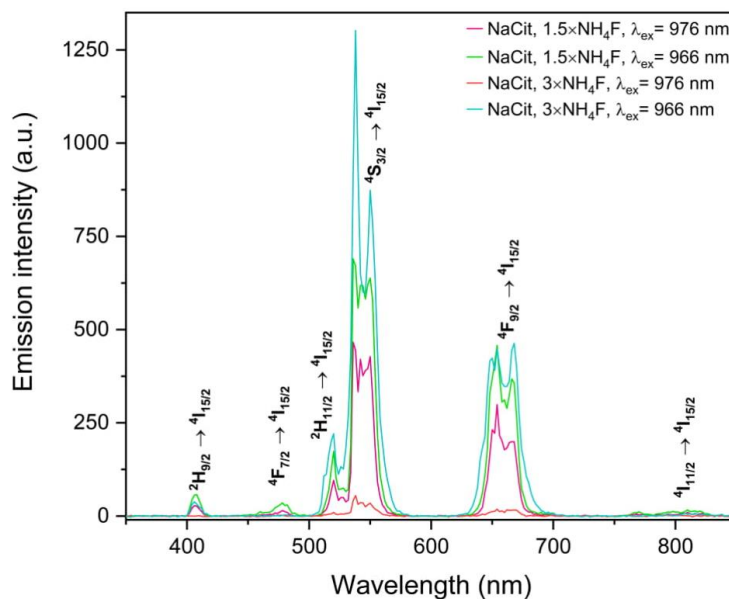


Fig. S3 Emission spectra of $\text{CaF}_2:20\%\text{Yb}^{3+},1\%\text{Er}^{3+}$ samples obtained in the small volume, without stirring, measured under $\lambda_{\text{ex}} = 966$ and 976 nm with pulsed excitation source ($25 \text{ mJ}\cdot\text{cm}^{-2}$).

Similarly to the excitation spectra presented in Fig. 3, the excitation by 966 nm wavelength results in a brighter up-conversion intensity than that by 976 nm, for the samples prepared with NaCit in the small volume (35 mL). The excitation via Yb^{3+} ions at the sites of O_h symmetry is more favourable than via the clustered ones.

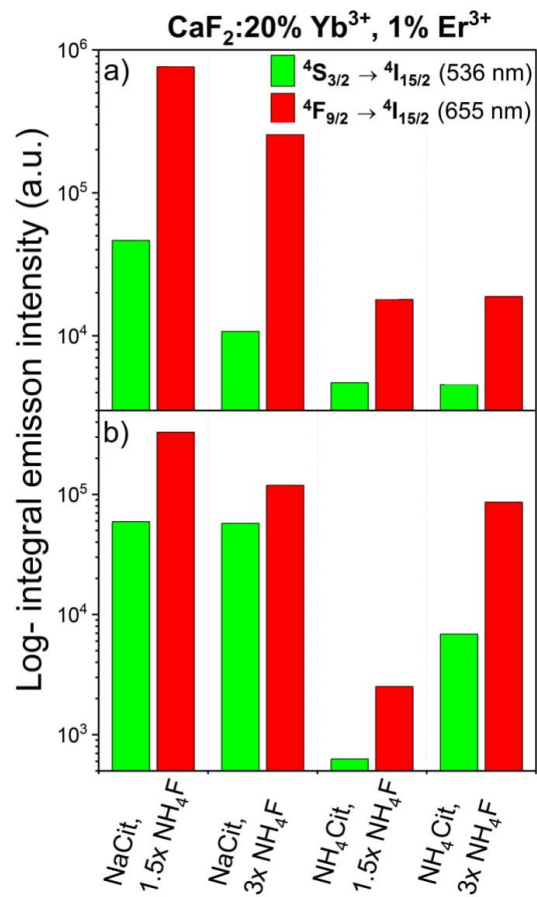


Fig. S4. Integrated luminescence intensities of CaF₂:20%Yb³⁺,1%Er³⁺ samples: a) small volume, without stirring, b) large volume, with stirring, calculated from the spectra measured under $\lambda_{\text{ex}} = 975 \text{ nm}$ continuous excitation source (at $25 \text{ W} \cdot \text{cm}^{-2}$).

CIE 1931

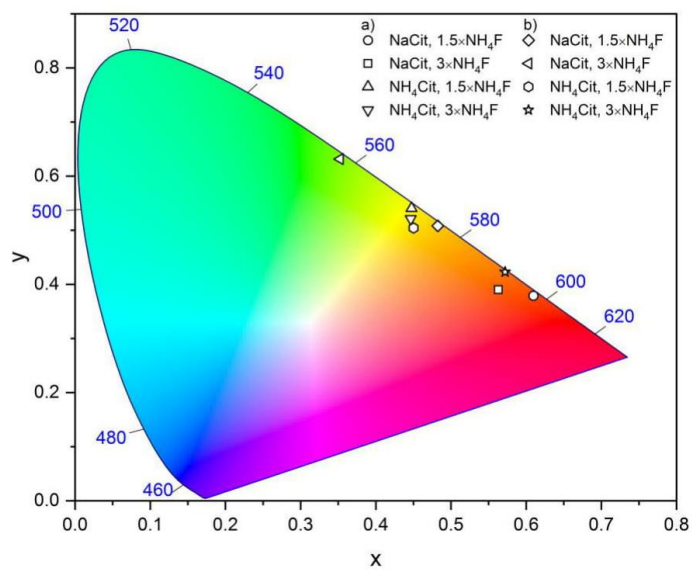


Fig. S5. CIE chromaticity diagrams of CaF₂:Yb³⁺,Er³⁺ NPs, where a) small volume, without stirring, b) large volume, with stirring, taken from the emission spectra measured under $\lambda_{\text{ex}} = 975 \text{ nm}$ continuous excitation source (at $25 \text{ W}\cdot\text{cm}^{-2}$).

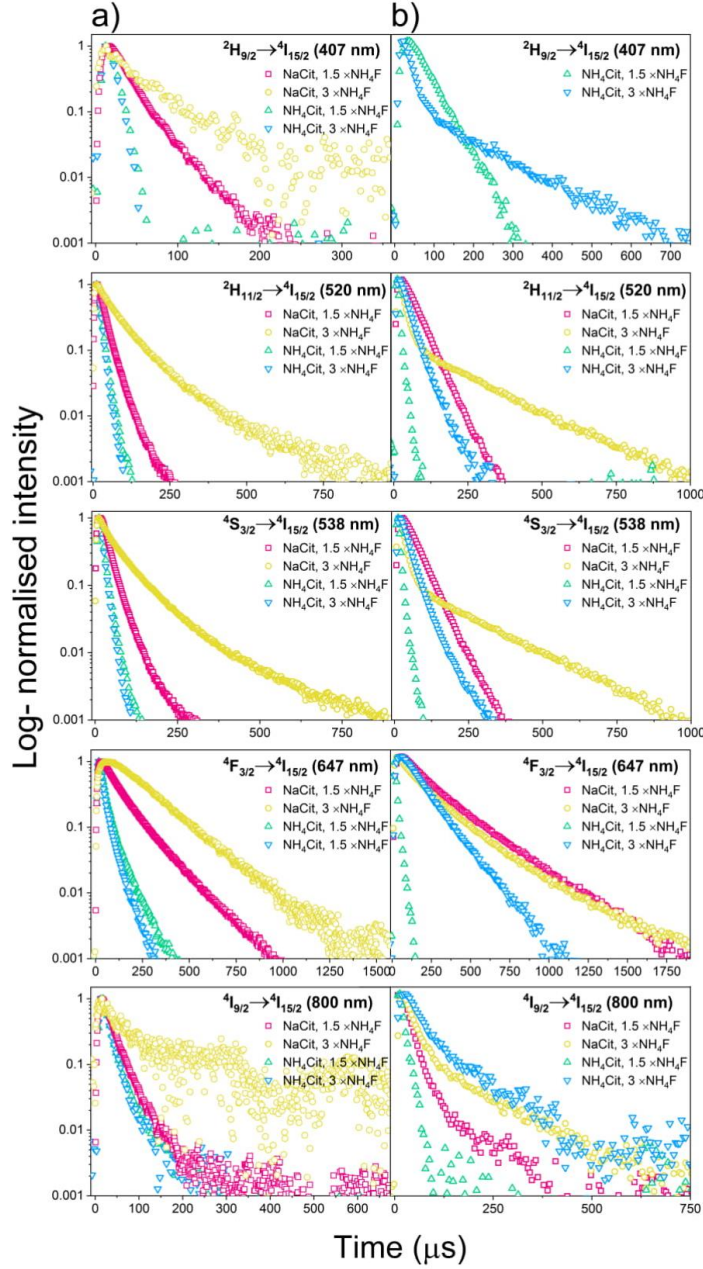


Fig. S6. Emission decays of $\text{CaF}_2:\text{Yb}^{3+},\text{Er}^{3+}$ NPs, where a) small volume, without stirring, b) large volume, with stirring, measured under $\lambda_{\text{ex}} = 976 \text{ nm}$ pulsed excitation source (at $15 \text{ mJ}\cdot\text{cm}^{-2}$).

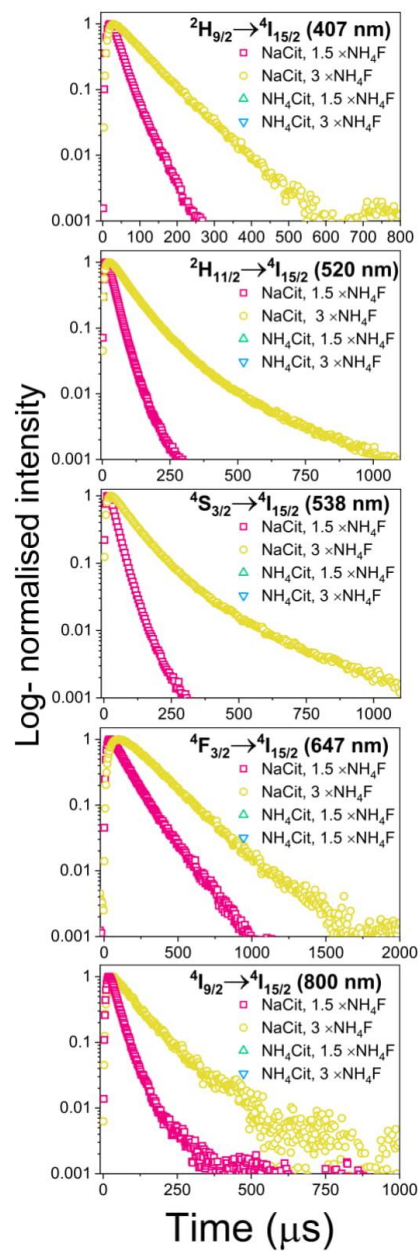


Fig. S7. Emission decays of CaF₂:Yb³⁺,Er³⁺ NPs, for small volume, without stirring, measured under $\lambda_{\text{ex}} = 966 \text{ nm}$ pulsed excitation source (at $15 \text{ mJ}\cdot\text{cm}^{-2}$).

Table S4. Emission lifetimes calculated from the measured luminescence decays of $\text{CaF}_2:\text{Yb}^{3+},\text{Er}^{3+}$ NPs under 966 nm laser excitation (for decays see Fig. 7, err < 1.6 μs).

		$\text{CaF}_2:20\% \text{Yb}^{3+}, 1\% \text{Er}^{3+}$						
Volume	Stirring	Co- reagent	NH_4F excess	Lifetime (μs)				
				$^2\text{H}_{9/2} \rightarrow ^4\text{I}_{15/2}$	$^2\text{H}_{11/2} \rightarrow ^4\text{I}_{15/2}$	$^4\text{S}_{3/2} \rightarrow ^4\text{I}_{15/2}$	$^4\text{F}_{9/2} \rightarrow ^4\text{I}_{15/2}$	$^4\text{I}_{9/2} \rightarrow ^4\text{I}_{15/2}$
35 mL	No	NaCit	1.5 ×	28.0	29.0	30.1	112.4	31.4
			3 ×	77.2	80.3	79.5	213.4	81.0

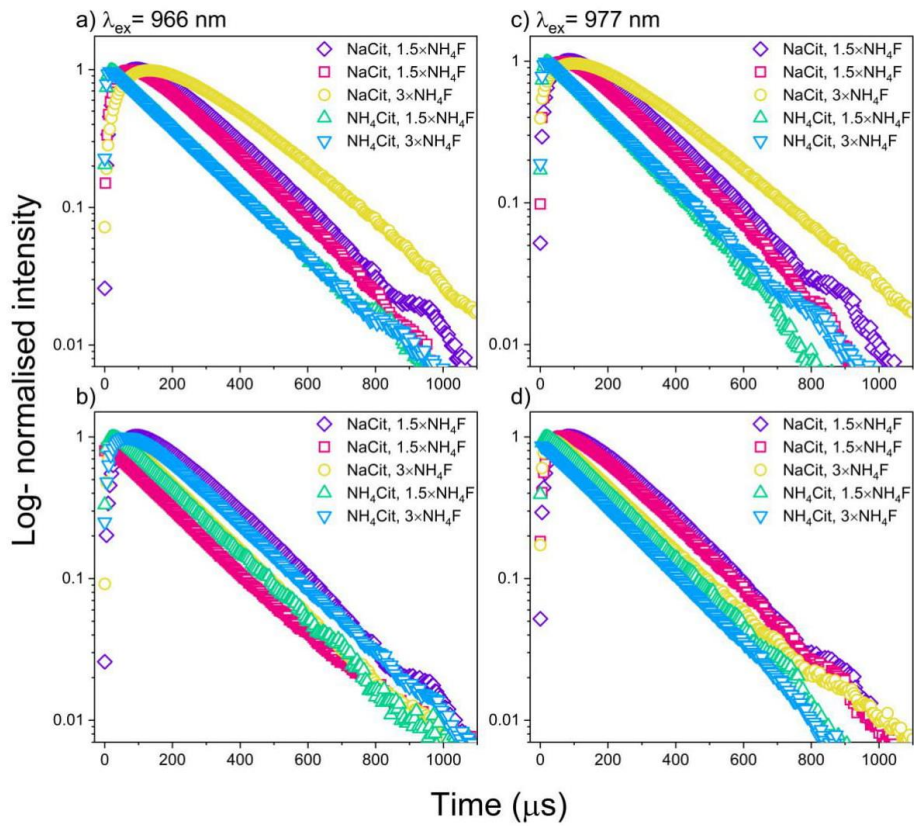


Fig. S8. Emission decays of Yb^{3+} of $\text{CaF}_2:\text{Yb}^{3+},\text{Er}^{3+}$ NPs, where a,c) small volume, without stirring, b, d) large volume, with stirring, measured under $\lambda_{\text{ex}} = 966/977$ nm pulsed excitation source (at $15 \text{ mJ}\cdot\text{cm}^{-2}$), observed at 1050 nm.

Table S5. Emission rise and decay times of Yb³⁺ calculated from the measured luminescence decay of CaF₂: Yb³⁺, Er³⁺ NPs under 966/977 nm laser excitation (for decays see Fig. 8, err < 1.6 μs).

Volume	Stirring	Co- reagent	NH ₄ F excess	Lifetime (μs)			
				CaF ₂ :20% Yb ³⁺ ,1% Er ³⁺ ² F _{5/2} → ² F _{7/2} (1050 nm)			
				λ _{ex} = 966 nm		λ _{ex} = 977 nm	
τ _r	τ _d	τ _r	τ _d				
35 mL	No	NaCit	1.5 ×	49.30	205.20	45.80	193.90
			3 ×	156.70	228.00	136.00	228.00
		NH ₄ Cit	1.5 ×	5.71	185.93	5.61	187.31
			3 ×	4.60	185.20	4.88	185.10
75 mL	Yes	NaCit	1.5 ×	14.53	185.19	8.05	188.24
			3 ×	46.97	201.78	45.80	201.85
		NH ₄ Cit	1.5 ×	9.01	195.86	5.47	193.58
			3 ×	15.60	191.80	12.00	197.10
CaF₂:20% Yb³⁺, NaCit, 1.5×NH₄F, 35 mL				65.85	221.94	54.39	232.06

According to the Hraiech et al., when a high number of Na⁺ ions are present in the sample, the band characteristic of Yb³⁺ ions with *O_h* symmetry appears in the NIR emission spectra with a maximum near 1028 nm. However, when a small number of Na⁺ ions were added, or for the samples without sodium ions, only the broad electronic transitions 5 → 3 and 5 → 4 of Stark's level with a band maximum near 1030 and 1050 nm appeared in the spectra [5]. For the all obtained samples, the lifetime as well as rise time were measured for the emission at 1050 nm, which proves the presence of Yb³⁺ ions at the sites of *O_h* symmetry and clusters in all of obtained NPs.

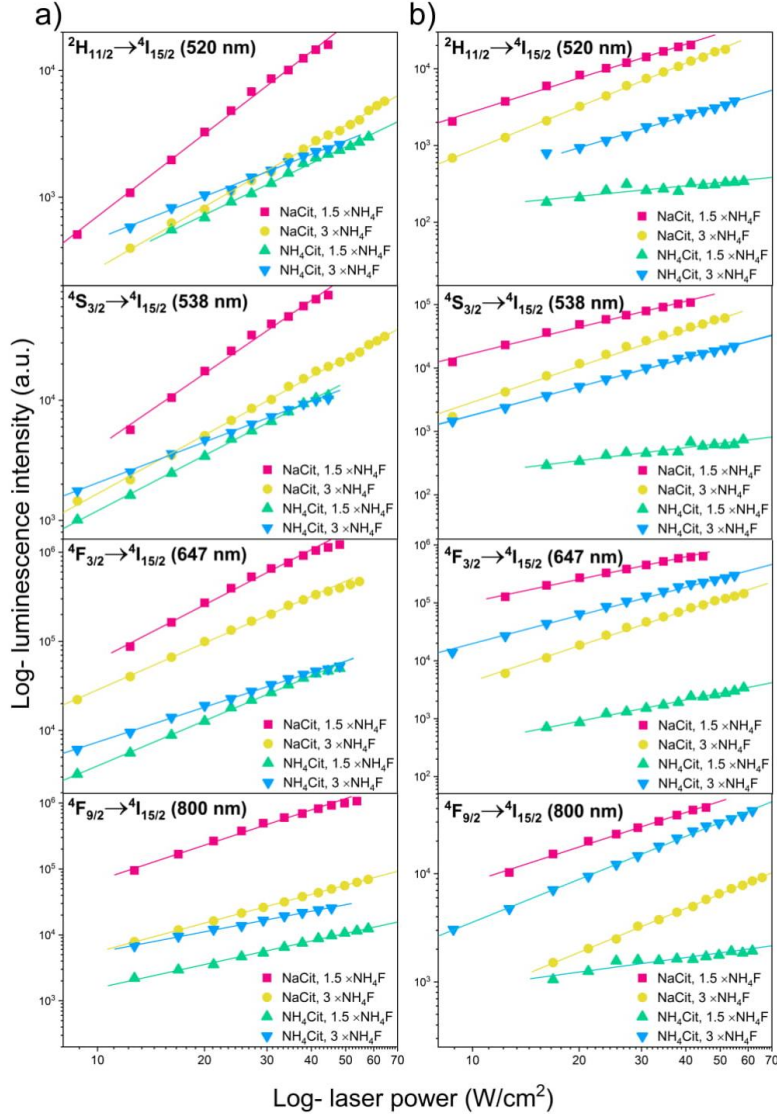


Fig. S9. Double-logarithmic plots of the upconversion emission intensity versus laser power density ($\lambda_{\text{ex}} = 975 \text{ nm}$), for $\text{CaF}_2:\text{Yb}^{3+},\text{Er}^{3+}$ NPs, where a) small volume, without stirring, b) large volume, with stirring.

The number of photons taking part in the UC process can be estimated from the equation [6]:

$$I \propto P^n$$

where I is UC intensity, P is the pumping excitation power density and n is the number of photons required to populate the excited state, indicated by the slope coefficient, determined from dependence of the luminescence intensity versus pump power in double-logarithmic plot [7].

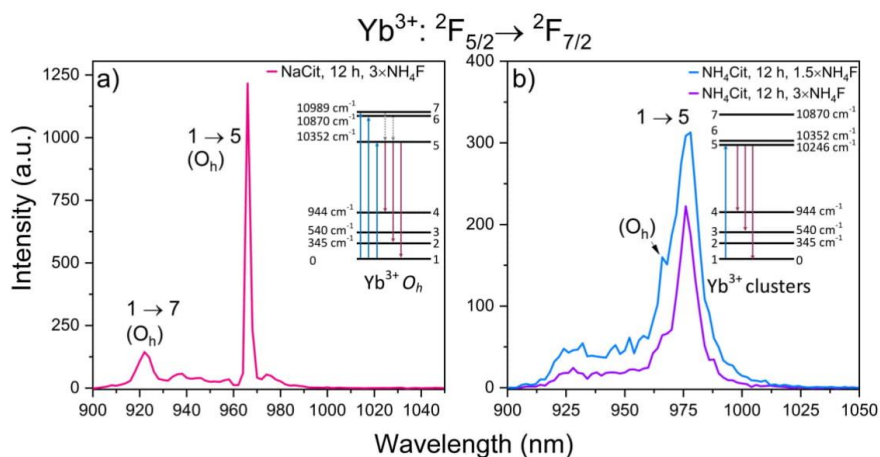


Fig. S10. Proposed mechanism dependent from Yb^{3+} symmetry, where all samples are obtained in small volume (35 mL) without stirring.

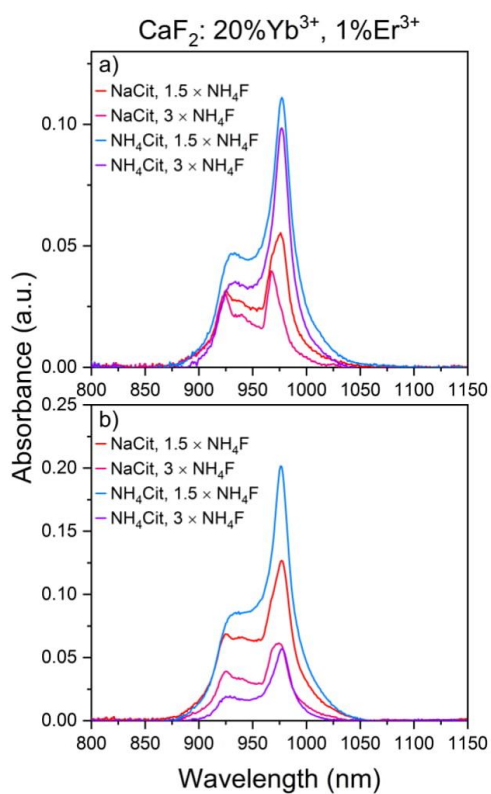


Fig. S11. Absorption spectra of $\text{CaF}_2:20\% \text{Yb}^{3+}, 1\% \text{Er}^{3+}$ samples obtained in a) small volume, without stirring, b) large volume, with stirring.

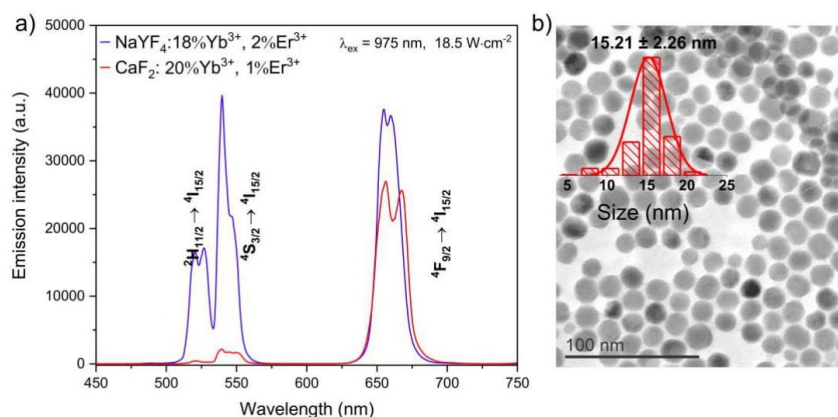


Fig. S12. a) Comparison of up-conversion between the best emitting $\text{CaF}_2:\text{Yb}^{3+},\text{Er}^{3+}$ sample (NaCit, with $1.5\times \text{NH}_4\text{F}$ and without stirring) and $\text{NaYF}_4:\text{Yb}^{3+},\text{Er}^{3+}$ reference NPs prepared with procedure published by Homann et al. [8], b) TEM image with NPs sizes distribution obtained for prepared $\text{NaYF}_4:\text{Yb}^{3+},\text{Er}^{3+}$ sample.

References

- Zhang C, Hou Z, Chai R, et al (2010) Mesoporous SrF_2 and $\text{SrF}_2:\text{Ln}^{3+}$ ($\text{Ln} = \text{Ce}, \text{Tb}, \text{Yb}, \text{Er}$) hierarchical microspheres: Hydrothermal synthesis, growing mechanism, and luminescent properties. *J Phys Chem C* 114:6928–6936. <https://doi.org/10.1021/jp911775z>
- Pedroni M, Piccinelli F, Passuello T, et al (2013) Water (H_2O and D_2O) Dispersible NIR-to-NIR Upconverting $\text{Yb}^{3+}/\text{Tm}^{3+}$ Doped MF_2 ($\text{M} = \text{Ca}, \text{Sr}$) Colloids: Influence of the Host Crystal. *Cryst Growth Des* 13:4906–4913. <https://doi.org/10.1021/cg401077v>
- Su L, Xu J, Li H, et al (2005) Codoping Na^+ to modulate the spectroscopy and photoluminescence properties of Yb^{3+} in CaF_2 laser crystal. *Opt Lett* 30:1003. <https://doi.org/10.1364/OL.30.001003>
- Sidey V (2016) On the effective ionic radii for ammonium. *Acta Crystallogr Sect B Struct Sci Cryst Eng Mater* 72:626–633. <https://doi.org/10.1107/S2052520616008064>
- Hraiech S, Jouini A, Jin Kim K, et al (2010) Role of monovalent alkali ions in the Yb^{3+} centers of CaF_2 laser crystals. *Radiat Meas* 45:323–327. <https://doi.org/10.1016/j.radmeas.2009.11.017>
- Pollnau M, Gamelin D, Lüthi S, et al (2000) Power dependence of upconversion luminescence in lanthanide and transition-metal-ion systems. *Phys Rev B* 61:3337–3346. <https://doi.org/10.1103/PhysRevB.61.3337>
- Chuai X, Yin F, Liu Z, et al (2013) Tunable upconversion emission in $\text{Ba}_2\text{YF}_7:\text{Yb}^{3+}/\text{Er}^{3+}$ nanocrystals with different Yb^{3+} concentration. *Mater Res Bull* 48:8–11. <https://doi.org/10.1016/j.materresbull.2013.02.075>
- Homann, C., Krukewitt, L., Frenzel, F., Grauel, B., Würth, C., Resch-Genger, U., and Haase, M. (2018) $\text{NaYF}_4:\text{Yb},\text{Er}/\text{NaYF}_4$ Core/Shell Nanocrystals with High Upconversion Luminescence Quantum Yield. *Angew. Chemie Int. Ed.*, 57 (28), 8765–8769. <http://doi.wiley.com/10.1002/anie.201803083>

SCIENTIFIC REPORTS

OPEN Upconverting SrF₂ nanoparticles doped with Yb³⁺/Ho³⁺, Yb³⁺/Er³⁺ and Yb³⁺/Tm³⁺ ions – optimisation of synthesis method, structural, spectroscopic and cytotoxicity studies

Received: 19 February 2019
Accepted: 29 May 2019
Published online: 17 June 2019

Dominika Przybylska¹, Anna Ekner-Grzyb², Bartosz F. Grześkowiak³ & Tomasz Grzyb¹

For a number of years nanomaterials have been continuously devised and comprehensively investigated because of the growing demand for them and their multifarious applications, especially in medicine. This paper reports on the properties of SrF₂ nanoparticles (NPs) for applications in biomedicine, showing effective ways of their synthesis and luminescence under near infrared radiation - upconversion. NPs doped with lanthanide, Ln³⁺ ions (where Ln = Yb, Ho, Er, Tm) were prepared by the hydrothermal method and subjected to comprehensive studies, from determination of their structure and morphology, revealing small, 15 nm structures, through spectroscopic properties, to cytotoxicity *in vitro*. The effects of such factors as the reaction time, type and amount of precipitating compounds and complexing agents on the properties of products were characterized. The cytotoxicity of the synthesized and functionalized NPs was investigated, using human fibroblast cell line (MSU-1.1). The synthesized structures may decrease cells' proliferation in a dose-dependent manner in the measured concentration range (up to 100 µg/mL). However, the cells remain alive according to the fluorescent assay. Moreover, the treated cells were imaged using confocal laser scanning microscopy. Cellular uptake was confirmed by the presence of upconversion luminescence in the cells.

Lanthanides are known as excellent for application in luminescent materials, have unique physicochemical and optical properties, being a result of 4f electronic configuration. Nowadays the growing interest in research is focused on upconverting nanoparticles (UCNPs) based on host materials doped with lanthanide ions (Ln³⁺). These materials can convert low energy photons from the near-infrared range (NIR) to higher energy ones, through the multiphoton absorption process¹. Upconverting materials can be used in various applications such as displays, solar cells, sensors, lasers, biosensors, drug delivery and many others^{2–6}. Especially interesting is the application of UCNPs as biomarkers what is possible due to their excitation within biological transparency window (in the range 700–1000 nm)⁴. Thanks to this property and by using of NIR radiation, harmful effects to healthy cells are reduced in comparison to those taking place under UV excitation.

As potential biomarkers, UCNPs should exhibit high emission intensity, small size (below 50 nm) and low cytotoxicity. Their surface should also allow conjugation with biomolecules. The most prominent phosphors, which exhibit efficient emission of light under NIR radiation are based on fluoride matrices, such as, MF₂ host materials doped with Ln³⁺ ions (where M = Ca, Sr, Ba; for more details see Table S1)^{3,7–22}. These materials are

¹Department of Rare Earths, Faculty of Chemistry, Adam Mickiewicz University in Poznań, Uniwersytetu Poznańskiego 8, Poznań, 61-614, Poland. ²Faculty of Biology, Adam Mickiewicz University in Poznań, Uniwersytetu Poznańskiego 6, Poznań, 61-614, Poland. ³NanoBioMedical Centre, Adam Mickiewicz University in Poznań, Wszechnicy Piastowskiej 3, Poznań, 61-614, Poland. Correspondence and requests for materials should be addressed to T.G. (email: tgrzyb@amu.edu.pl)

characterized by low phonons energy and high chemical stability, which have direct influence on their potential applications^{23,24}.

The most important step, determining NPs utilization is their effective synthesis. For this purpose, the most promising for preparing MF₂ materials is the solvo(hydro)thermal method allowing carrying out the process under high pressure and temperature²⁴. The advantages of the method are: obtaining single-phased products with small sizes of NPs, possibility of carrying out the synthesis in water, easy control of the synthesis conditions and, what is the most important, good crystallinity of products which improves their luminescence efficiency²⁴.

Hydrothermal method is very common for synthesis of upconverting SrF₂ what is reflected by many of published articles^{12,14,15,23,25,26}. One of the first papers was published by J. Sun *et al.*²⁶, where particles were obtained in one-step hydrothermal method with different surfactants (citric acid, EDTA, PVP, OA) to change their size and morphology. The same group of researchers obtained SrF₂:Yb³⁺, Er³⁺ in oleate complex system in a mixture of water, ethanol and oleic acid, what allowed to obtain much smaller particles, around 5–25 nm¹¹. The most known and cited method for synthesis of SrF₂ NPs, was published by M. Pedroni *et al.*¹². This procedure allows obtaining very small particles with a size around 8 nm and intense emission in water colloids. Based on this synthesis route, a lot of research has been done, e.g. I. Villa *et al.* obtained SrF₂:Nd³⁺ particles for deep tissue, autofluorescence free, high resolution *in vivo* imaging using emission band at 1.340 μm¹³; M. Quintanilla *et al.* synthesized 9 nm SrF₂:Yb³⁺, Tm³⁺ NPs in water/D₂O colloids, with intense emission in ultraviolet range; S. Balabhada *et al.*¹⁷ based on SrF₂:Yb³⁺, Er³⁺ reported a straightforward method to predict the temperature calibration curve of any upconverting thermometer based on two thermally coupled electronic levels independently of the medium. Besides, many research groups modified Pedroni's method of SrF₂ NPs synthesis, especially to obtain core@shell structures, e.g. S. Zanzoni *et al.*¹⁶ synthesized SrF₂:Yb³⁺, Tm³⁺@SrF₂:Yb³⁺, Er³⁺ in two-step hydrothermal synthesis for investigation of interactions between Ln-doped fluoride NPs and biomolecules whereas P. Cortelletti *et al.* published synthesis of multishell NPs¹⁹ used for optical thermometry. A lot of research was focused on different applications and properties of upconverting SrF₂, (Table S1). The aqueous environment of NPs synthesis may be responsible for quenching of luminescence by –OH modes, due to non-radiative relaxation process. Therefore, design of accurate nanosized bioimaging probe requires optimization of the standard synthesis methods. Apart from the appropriate composition of the starting mixture, time and temperature of reaction, also adequate co-regents present in the synthesis medium, e.g. sodium citrate, ethylenediaminetetraacetic acid (EDTA) or cetyl trimethyl ammonium bromide (CTAB) may influence luminescence intensity of the final product and have effect on the size, shape, and degree of agglomeration of particles^{3,8,12,27}. In MF₂ doped with Ln³⁺ ions, the composition of the starting mixture may also be crucial for charge compensation within the crystal structure^{12,28}.

In this paper, we present structural and spectroscopic properties of SrF₂:Yb³⁺, Ln³⁺ NPs. Most of the published articles present spectroscopic properties of SrF₂:Yb³⁺, Er³⁺ or just single Ln³⁺-doped NPs^{9,11,13,15,26,29}. Herein we report comparison of three upconverting systems with Ho³⁺, Er³⁺ or Tm³⁺ ions as luminescence activators. NPs were prepared by hydrothermal synthesis, with two surfactants - trisodium citrate (NaCit) or ammonium citrate tribasic (NH₄Cit) as chelating agents. Alternative synthesis procedure, for the most common, NaCit-based was developed. Also, the effects of such factors as time and amount of precipitation agent on size, the shape and agglomeration of particles, and especially spectroscopic properties were investigated. Because of potential biological applications of the synthesized NPs also their cytotoxicity was assessed. The prepared NPs were also examined as potential biomarkers. NPs may interfere with the functioning of cells, e.g. by plasma membrane integrity disruption, disturbance with organelle function or damage of the cytoskeleton³⁰. The cytotoxicity depends on a lot of traits, such as size, shape, functionalization, coating, cell line used during the experiment, etc.³¹. Therefore, it is essential to assess the toxicity of newly produced NPs, which was one of the aims of the presented study. Toxicity analysis distinguishes our article from many other. Moreover, the cellular uptake of the nanostructures was imaged using confocal microscopy. Our article presents complex and wide report covering optimization of synthesis procedure, comparison of luminescence properties between products prepared in various conditions as well as with three different emitting lanthanide ions. Additionally cytotoxicity of prepared products was analysed for bare and functionalised NPs.

Results

Structure and morphology. Strontium fluoride doped with Ln³⁺ crystallized as cubic crystals with *Fm* $\bar{3}m$ space group (Fig. 1). Samples showed single-phased structure, however, they had different crystal sizes, which was reflected in the width of XRD peaks. NPs' sizes determined from Scherrer equation and DLS measurements are collected in Tables S2 and S6 (for experimental results see Figs S1 and S2). Synthesis of the samples with 1.5× excess of NH₄F within 6 and 12 h resulted in similar NPs with 11–14 nm diameter, no matter which co-regent was used. By increasing the excess of F[−] ions to 3×, more than twice larger NPs with sizes between 28 and 39 nm were obtained. These differences in the size and morphology were caused by changes in the kinetics of the reaction and rapid growth of crystallites in the presence of higher concentration of F[−] ions. Determined hydrodynamic diameters of the obtained NPs also confirmed the growth of their sizes from around 20–40 nm to above 100 nm when a higher amount of NH₄F was used. The results indicate also, the tendency to agglomeration of NPs prepared with threefold excess of NH₄F.

TEM images show small spherical NPs with narrow size distribution when 1.5× excess of NH₄F was used (Fig. 2a,b). The determined sizes were: 14.7 ± 2.5 nm for products obtained in the presence of NaCit as a co-reagent and 13.3 ± 2.5 nm when NH₄Cit was used. With a 3× excess of NH₄F much larger NPs precipitated: 42.4 ± 9.7 nm for NaCit used as a co-reagent and 38.4 ± 10.6 nm when NH₄Cit was used. NPs prepared with higher excess of NH₄F were of irregular shape with a wider distribution of their sizes and with visible agglomeration.

The composition of obtained products analysed by the ICP-OES technique (results in Table S3) revealed higher than expected amount of Yb³⁺ in all samples: between 21–24% when a 1.5× excess of NH₄F was used

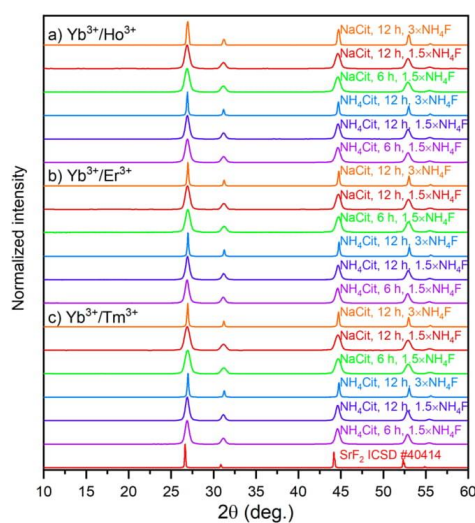


Figure 1. XRD patterns of the SrF_2 samples synthesized by hydrothermal method. The patterns are described according to the scheme: source of citric ions, time of reaction, excess of NH_4F precipitating compound (the used concentrations were: 20% Yb^{3+} , 1% Ho^{3+} , 1% Er^{3+} and 0.25% Tm^{3+}).

and between 23–28% when the excess was $3\times$. The explanation of the extra amount of Yb^{3+} ions is complex. The smallest ionic radius of Yb^{3+} ions from all the elements used in the synthesis allowed efficient incorporation of these ions into the SrF_2 crystal lattice ($r_{\text{Sr}^{2+}} = 1.26 \text{ \AA}$, $r_{\text{Tm}^{3+}} = 0.9994 \text{ \AA}$, $r_{\text{Er}^{3+}} = 1.004 \text{ \AA}$, $r_{\text{Ho}^{3+}} = 1.0015 \text{ \AA}$, $r_{\text{Yb}^{3+}} = 0.985 \text{ \AA}$ for coordination number $\text{CN} = 8$)³². High amount of charge compensating F^- ions presented when $3\times$ excess of NH_4F was added, additionally allowed embedding Yb^{3+} into the SrF_2 structure to a higher extent. Another factor increasing the concentration of dopant ions, is the difference in solubility between SrF_2 and LnF_3 . The latter one is less soluble in water, which favours incorporation of Ln^{3+} into the forming fluoride structure. The presence of higher amount of F^- ions also leads to this process (according to the solubility constant).

Elemental analysis revealed higher amount of nitrogen atoms in the samples synthesised in the presence of NH_4Cit as co-reagent (see Table S4) in comparison with those obtained in presence of NaCit . The increased amount of nitrogen is related to NH_4^+ ions presented on the surface of NPs as well as ions embedded into structure of particles.

Higher concentration of Yb^{3+} in the materials resulted in reduced crystal cell volumes in comparison to those doped to a lower degree (for more see Table S5). The smallest cell volumes were calculated for the samples with $3\times$ excess of NH_4F and prepared with NH_4Cit as co-reagent (for $\text{Yb}^{3+}/\text{Ho}^{3+}$, $V = 188.09(4) \text{ \AA}^3$; $\text{Yb}^{3+}/\text{Er}^{3+}$, $V = 188.10(5) \text{ \AA}^3$; $\text{Yb}^{3+}/\text{Tm}^{3+}$, $V = 188.16(5) \text{ \AA}^3$). The reference, taken from the ICSD database, shows the cell volume for the pure SrF_2 , $V = 194.50(7) \text{ \AA}^3$.

In the fluorite-type structure of MF_2 , the cations are located at the centre of a cubic unit cell, surrounded by eight F^- anions. The doping by Ln^{3+} replaces M^{2+} ions introducing a local charge. Charge balance may be achieved by the addition of interstitial F^- ions, occurring simultaneously or by introduction of M^+ ions^{12,23,28}. Along with charge compensation process, structural and spectroscopic properties of NPs may be affected. Monovalent cations (e.g. Na^+), lead to a reduction in interatomic distance which can significantly improve upconversion properties of these materials^{23,33}. In the prepared SrF_2 NPs, there are two possibilities of charge compensation. The first, with creation of interstitial fluorine ions: $\text{Sr}^{2+} \rightarrow \text{Ln}^{3+} + \text{F}^-$, and the second with incorporation of monovalent cations, which were Na^+ or NH_4^+ depending on the type of reagent: $2\text{Sr}^{2+} \rightarrow \text{Na}^+/\text{NH}_4^+ + \text{Ln}^{3+}$ ²⁸. However, NH_4^+ ions are larger than Na^+ and Sr^{2+} , thus their ability to compensate charge imbalance is rather low ($r_{\text{NH}_4^+} = 1.54 \text{ \AA}$, $r_{\text{Na}^+} = 1.18 \text{ \AA}$)³².

Zeta potentials were measured to determine the surface charge of the prepared NPs. All samples exhibited negative surface charge from $-14.9 \pm 5.4 \text{ mV}$ to $-33.3 \pm 4.4 \text{ mV}$ (Table S7) at physiological pH, which indicates their good stability in water as colloids and confirm the presence of negative COO^- groups on the surface. Furthermore, the FT-IR spectra also revealed citrate anions on the surface of the obtained particles via the presence of stretching vibrations assigned to the $-\text{CO}$, $-\text{CH}$, $-\text{COO}^-$ and $-\text{OH}$ bonds (Supplementary Materials, Fig. S3). As the result of higher amount of NH_4^+ ions in the materials prepared in presence of NH_4Cit , absorption band located at around 1610 cm^{-1} revealed shift towards $-\text{NH}$ bending range in comparison to samples prepared in the presence of NaCit .

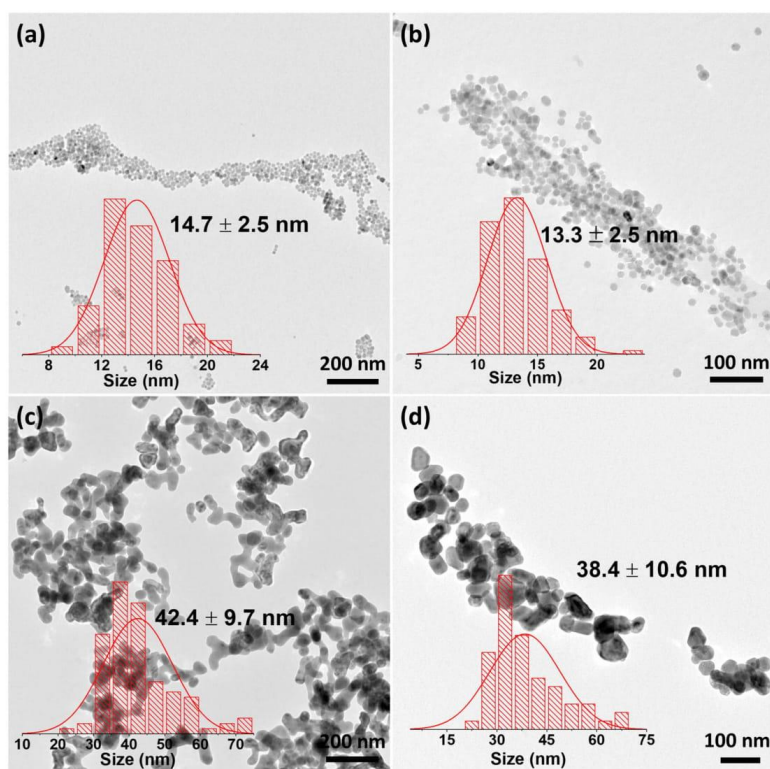


Figure 2. TEM images and nanocrystal size distribution of hydrothermally synthesized samples: (a) $\text{SrF}_2:\text{Yb}^{3+},\text{Er}^{3+}$, NaCit, 12 h, $1.5 \times \text{NH}_4\text{F}$ (b) $\text{SrF}_2:\text{Yb}^{3+},\text{Er}^{3+}$, NH_4Cit , 12 h, $1.5 \times \text{NH}_4\text{F}$ (c) $\text{SrF}_2:\text{Yb}^{3+},\text{Er}^{3+}$, NaCit, 12 h, $3 \times \text{NH}_4\text{F}$ (d) $\text{SrF}_2:\text{Yb}^{3+},\text{Er}^{3+}$, NH_4Cit , 12 h, $3 \times \text{NH}_4\text{F}$.

Spectroscopic properties. Under excitation with the NIR radiation (at 976 nm) all samples exhibited emission that resulted from the used Ho^{3+} , Er^{3+} or Tm^{3+} dopant ions (Fig. 3). The brightest emissions were observed for the samples, obtained in 12 h synthesis with $3 \times$ excess of NH_4F . The weakest emissions were recorded for the samples obtained in shorter reaction time (6 h) and with $1.5 \times$ excess of F^- ions.

For all samples, spectroscopic measurements revealed the emission typical of Ln^{3+} ions and energetic processes taking place in the products, such as energy transfer from Yb^{3+} to Ln^{3+} ions, excitation into higher energetic levels or emission quenching. The excitation spectra (Fig. 3a 900–1050 nm range) measured for the samples show broad and intense bands with the maximum at 976 nm, which are characteristic of the ${}^2\text{F}_{7/2} \rightarrow {}^2\text{F}_{5/2}$ transition of Yb^{3+} ions. These ions play a role of sensitizers in the studied systems, absorbing laser light. Yb^{3+} ion is perfect for this function because of its simple energy structure: one excitation energy level (${}^2\text{F}_{7/2}$), produced by the absorption of radiation with a wavelength at around 980 nm. The intensity of this band was the highest for the samples obtained in 12 h synthesis, with $3 \times$ excess of NH_4F , where NaCit was used as a co-reagent. The excitation band is broad in each sample, which is the effect of crystal field on the local environment of the ion resulting in Stark-splitting of the ground ${}^2\text{F}_{7/2}$ multiplet.

The strongest emissions, similarly to the excitation spectra, were recorded for the products obtained in the 12 h synthesis with NaCit and $3 \times$ excess of NH_4F (see also Fig. S4). High luminescence intensity was also observed for the samples doped with $\text{Yb}^{3+}/\text{Ho}^{3+}$ and $\text{Yb}^{3+}/\text{Er}^{3+}$ obtained in 12 h synthesis with NaCit and $1.5 \times \text{NH}_4\text{F}$ or NH_4Cit and $3 \times \text{NH}_4\text{F}$. The above results can be explained by a relatively large size of NPs, obtained during longer reaction time and with excess of fluorine ions. Small NPs are known to be prone for surface- and defects-related quenching to a greater extent than large ones³⁴. Also, an increased amount of sensitizer ions (Yb^{3+}), found in the samples prepared during longer synthesis (Table S5) is a factor which improved luminescence of the described structures.

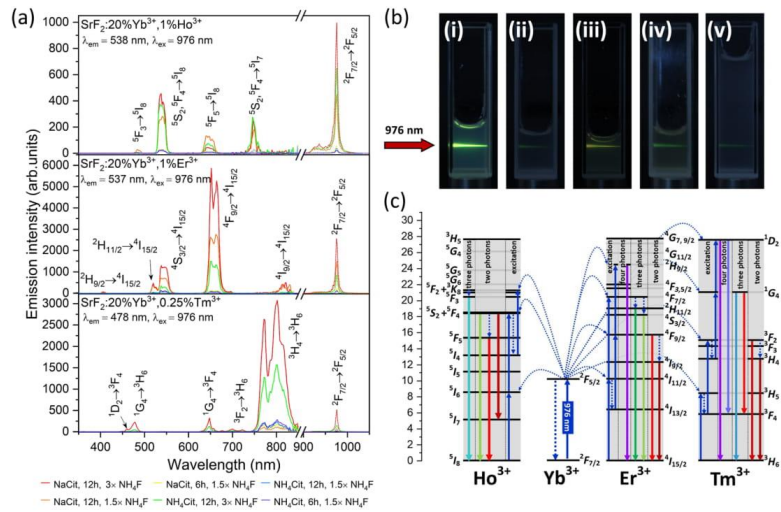


Figure 3. (a) Luminescence (300–900 nm) and excitation (>900 nm) spectra of the NPs obtained under pulsed excitation source (at 15 mJ·cm⁻²). (b) Emission of SrF₂:20%Yb³⁺, 1%Er³⁺ samples, where: (i) NaCit, 12 h, 3 × NH₄F, (ii) NaCit, 12 h, 1.5 × NH₄F, (iii) NH₄Cit, 12 h, 3 × NH₄F, (iv) NH₄Cit, 12 h, 1.5 × NH₄F, (v) NaCit, 12 h, 1.5 × NH₄F, excited by laser (λ_{exc} = 976 nm) in water (i–iv) or phosphate-buffered saline (v) with concentration 0.1 mg/mL. (c) Simplified scheme of upconversion mechanism for SrF₂: Yb³⁺, Ln³⁺ systems.

The used co-reagent had a significant effect on the emission of NPs prepared. When NH₄Cit was used, luminescence quenching was observed. This effect was caused by a larger number of NH₄⁺ ions present on the surface of NPs in comparison to that on the products prepared in the presence of NaCit. The N–H vibrations are more efficient quenchers than O–H and our results confirm this fact.

Analysis of the ratio of intensities of the two most intense bands present in the emission spectra brings additional information about the studied systems (see Fig. 3a for the spectra or Fig. S5 for comparison of integrated emission intensities). The samples doped with a Yb³⁺/Ho³⁺ pair of ions showed the ⁵S₂³F₄ → ⁵I₈ band as the most intense, which resulted in green colour of emission (for CIE chromaticity diagram see Fig. S5). In the products whose emission was of lower intensity, the green (⁵S₂³F₄ → ⁵I₈) and red (⁵F₅ → ⁵I₈) emission bands had similar intensities, which was the result of decreased efficiency of excitation to the ⁵S₂³F₄ higher excited state. Excitation into higher levels of Ln³⁺ ions usually require good crystallinity of the material and lack of quenching factors, such as NH₄⁺ ions.

NPs doped with Yb³⁺/Er³⁺ pair ions, showed yellowish-green emission colour, as an effect of mixing of the transitions ³F_{9/2} → ⁴I_{15/2} (in the red range) and ⁴S_{3/2} → ⁴I_{15/2} (green range). The first one was the most intense from all observed transitions. NPs doped with Yb³⁺/Er³⁺ pair ions were characterized by the highest emission intensity from the whole studied group of compounds. The high upconversion intensity of Yb³⁺ and Er³⁺ doped samples is connected with the best match of the energies of the excited levels of the used activator ions (Yb³⁺ ⁴F_{3/2} → Er³⁺ ⁴I_{11/2}), thanks to which the energy transfer between these ions is more efficient. Depending on the synthesis conditions, the ratio between red and green transition bands was slightly different, revealing the influence of NPs' sizes and charge compensation issues on the UC mechanism and quenching processes efficiency (see Figs S5 and S6). Increased red emission band is usually connected with non-radiative relaxation from the ⁴S_{3/2} excited state what in the presented results is an effect of NH₄⁺ ions presence and lower crystallinity of the products obtained at shorter time and with smaller NPs' sizes.

The samples doped with Yb³⁺/Tm³⁺ pairs of ions showed blue or pink-blue UC with the domination of ³H₄ → ³H₆ transition (NIR band) in the spectra (Figs 3a, S5 and S6). The ratio between ¹G₄ → ³H₆ and ³H₄ → ³H₆ transitions was similar for each type of co-reagent used. However, for the systems in which quenching through to the presence of –NH oscillators was noticeable in the emission intensity, the colour of emission was slightly shifted to the red (Fig. S6). The ¹D₂ and ¹G₄ excited states of Tm³⁺ are more sensitive to the quenching factors as evidenced by a change in the emission colour. The observed spectroscopic properties of SrF₂:Yb³⁺, Tm³⁺ NPs shows that colour of luminescence may be controlled during the synthesis, by co-reagents affecting the quenching processes.

Figure 3b shows the luminescence of SrF₂:20%Yb³⁺, 1%Er³⁺ NPs in the form of water colloids under excitation with 976 nm laser light. The intense emission of water colloids allow a description of prepared NPs as potentially

Co-reagent	NH ₄ F excess	Reaction time (h)	Lifetime (μs)											
			SrF ₂ :20%Yb ³⁺ ,1%Ho ³⁺				SrF ₂ :20%Yb ³⁺ ,1%Er ³⁺				SrF ₂ :20%Yb ³⁺ ,0.25%Tm ³⁺			
			⁵ F ₅ → ³ I ₈	⁵ S ₂ → ³ F ₄	⁵ F ₅ → ³ I ₈	⁵ S ₂ → ³ I ₇	² H _{9/2} → ⁴ I _{13/2}	² H _{11/2} → ⁴ I _{13/2}	⁴ S _{3/2} → ⁴ I _{13/2}	⁴ F _{9/2} → ⁴ I _{13/2}	¹ D ₂ → ³ F ₄	¹ G ₄ → ³ H ₆	¹ G ₄ → ³ F ₄	³ H ₄ → ³ H ₆
NaCit	1.5×	6	13.5	21.0	29.2	16.8	16.9	25.4	49.3	48.7	118.3	374.0	364.8	214.0
		12	15.7	27.3	35.0	24.0	30.3	33.4	33.5	108.6	204.2	425.8	420.6	284.2
	3×	12	51.5	117.8	146.5	103.9	74.4	82.1	90.6	235.7	309.3	596.6	592.3	492.2
NH ₄ Cit	1.5×	6	17.6	22.1	39.5	24.4	29.8	41.2	37.9	89.4	145.8	341.9	352.8	263.5
		12	11.4	31.6	37.1	24.1	26.0	29.7	30.4	97.0	147.0	357.0	366.3	252.7
	3×	12	44.4	96.7	110.8	81.3	46.2	55.2	63.7	174.4	248.6	511.7	500.5	368.6

Table 1. Emission lifetimes calculated on the basis of the measured luminescence decays of SrF₂:Yb³⁺,Ln³⁺ NPs under 976 nm laser excitation (for decays see Fig. S8, err < 0.1 μs).

useful for biomedical applications especially for bioimaging as we show below. A scheme of the upconversion mechanism responsible for the observed emissions is presented in Fig. 3c.

On the basis of luminescence decays measured for the obtained product (Supplementary Materials, Fig. S7), the luminescence lifetimes were calculated and are collected in Table 1. The values of lifetimes for the Yb³⁺/Ho³⁺ doped samples are strongly related to the luminescence intensity. The longest lifetimes (147 μs for the ³F₅ → ³I₈ and 118 μs for ⁵S₂, ⁵F₄ → ³I₈ transition) were determined for the best emitting sample prepared in 12 h synthesis, with NaCit as co-reagent and 3× excess of NH₄F. An analogous sample, but prepared in the presence of NH₄Cit, had a similar value of lifetime. Luminescence lifetimes determined for the ⁵F₅ → ³I₈ transition, which occurred in the red spectral range, were usually the longest ones, which is related to the necessity of non-radiative transition between the ⁵S₂, ⁵F₄ and ⁵F₅ excited states. The shortest decay time was measured for the sample obtained in 6 h synthesis and with NaCit as co-reagent. The reason is very weak luminescence of this highly quenched sample.

Analysis of luminescence decays measured for the samples doped with Yb³⁺/Er³⁺ ions, revealed that the longest lifetimes were typical of products obtained in 12 h synthesis in the presence of NaCit and 3× excess of NH₄F, similarly to the Yb³⁺/Ho³⁺ doped samples. The lifetime assigned to the ⁴F_{9/2} → ⁴I_{13/2} transition was 236 μs for the sample prepared in the presence of NaCit and 174 μs when NH₄Cit was used as co-reagent. Lifetimes were slightly shorter for the compounds prepared with NH₄Cit as a chelating agent, because of the earlier mentioned quenching effect of -NH modes. The longest lifetimes calculated for the red band can be related to the Er³⁺ excitation mechanism to the ⁴F_{9/2} level. There are two possibilities of the excitation: one connected with non-radiative transition from ²H_{11/2} level and the other with non-radiative transition from ⁴I_{11/2} to ⁴I_{13/2} excited state followed by absorption of a photon to ⁴F_{9/2} level (⁴I_{13/2} (Er³⁺) + ²F_{5/2} (Yb³⁺) → ⁴F_{9/2} (Er³⁺) + ²F_{7/2} (Yb³⁺)). The first excitation pathway occurs when the emission lifetime of ⁴F_{9/2} → ⁴I_{13/2} transition is similar to that of ⁴S_{3/2} → ⁴I_{13/2}, which is observed for the compound synthesized in a 6 h process with 1.5× excess of NH₄F and in the presence of NaCit. The second mechanism can explain the observed spectroscopic properties if the decay time of the transition ⁴F_{9/2} → ⁴I_{13/2} is twice as long (or even more) as the ⁴S_{3/2} → ⁴I_{13/2} transition lifetime. That is true for all samples except the one mentioned above. If the first pathway of the ⁴F_{9/2} population dominates, the decay time of ⁴F_{9/2} level should be similar to that of ⁴S_{3/2}. But if the energy transfer prevails, the decay time of the ⁴F_{9/2} level depends on the decay times of ⁴I_{13/2} (Er³⁺) and ²F_{5/2} (Yb³⁺).

The SrF₂:Yb³⁺,Tm³⁺ NPs showed the longest decays from all obtained samples. Furthermore, similarly as for the samples doped with Yb³⁺/Ho³⁺ or Yb³⁺/Er³⁺ ions described above, the sample prepared in 12 h synthesis, with 3× NH₄F and with the use of NaCit, was characterized by the highest value of emission lifetime (596.6 μs for ¹G₄ → ³H₆ and 592.3 μs ¹G₄ → ³F₄). Similarly to the samples with Yb³⁺/Ho³⁺ and Yb³⁺/Er³⁺, those prepared with NH₄Cit as a complexing agent showed shorter lifetimes in comparison to that of the analogous product prepared with NaCit. Decay times strongly depended on the population mechanism of the excited states. Also, quenching factors present in the system affected the determined emission lifetimes.

For better understanding of the upconversion mechanism, dependencies of the luminescence intensity on laser powers were measured. The relation between the UC intensity *I* and the pumping excitation power density, *P* is given by the equation³⁵:

$$I \propto P^n$$

where *n* is the number of photons required to populate the excited state. The results of the calculations are collected in Table 2 (see Fig. S8 for the experimental data).

To achieve ⁵S₂/⁵F₄ or ⁵F₅ excited state of Ho³⁺ ions two photons are required. The result of experiments, shown in Table 2, are in some cases different from the theoretical ones. For the samples prepared in 6 h synthesis and with NaCit as well as with NH₄Cit as co-reagents, the number of photons was lower than expected, which was caused by non-radiative relaxation to the ³F₅ lower excited state. The highest slope value was obtained for the sample prepared with 3× excess of NH₄F, which is also connected with intense emission and long lifetimes determined for this sample. The slope coefficients determined for NPs doped with a Yb³⁺/Er³⁺ pair of ions are higher than those for almost all samples (except the samples prepared in the presence of NH₄Cit), which confirms the two-photon excitation process. For the samples doped with Yb³⁺/Tm³⁺ ions, the dependencies of the emission intensity on laser energies were measured for four transitions. According to the scheme in Fig. 3c, the ¹D₂ energy level requires four photons in the excitation process, ¹G₄ three photons, and ³H₄ two photons. From the experimental data only for the ³H₄ → ³H₆ transition (two-photon process), the number of photons was close to the theoretical value.

Co-reagent	NH ₄ F excess	Reaction time (h)	Number of photons									
			SrF ₂ :20%Yb ³⁺ ,1%Ho ³⁺					SrF ₂ :20%Yb ³⁺ ,1%Er ³⁺			SrF ₂ :20%Yb ³⁺ ,0.25Tm ³⁺	
			⁵ S ₂ / ² F ₄ → ⁵ I ₈	⁵ F ₅ → ⁵ I ₈	⁵ S ₂ / ⁵ F ₄ → ⁵ I ₇	² H _{11/2} → ⁴ I _{15/2}	⁴ S _{3/2} → ⁴ I _{15/2}	⁴ F _{9/2} → ⁴ I _{15/2}	¹ D ₂ → ³ F ₄	¹ G ₄ → ³ H ₆	¹ G ₄ → ³ F ₄	³ H ₄ → ³ H ₅
NaCit	1.5×	6	1.9	2.0	1.0	1.7	1.8	1.7	2.4	2.5	1.3	1.9
		12	2.0	2.2	1.5	1.7	1.8	1.8	1.8	2.1	2.0	1.7
	3×	12	1.8	1.8	1.5	1.8	1.6	1.7	1.2	1.1	2.1	1.2
NH ₄ Cit	1.5×	6	0.7	1.6	0.7	0.9	1.1	1.2	0.8	1.6	1.9	1.7
		12	1.0	1.2	0.8	1.0	1.1	1.3	1.3	1.0	1.5	1.3
	3×	12	1.8	1.9	1.6	0.8	0.8	1.0	1.3	1.3	1.3	1.2

Table 2. Number of photons involved in the upconversion mechanism, determined from the dependencies of luminescence intensity on laser power for SrF₂:Yb³⁺,Ln³⁺ NPs (for experimental results see Fig. S9, err < 0.15).

Summarising, for almost all samples the slope coefficient values are lower than expected, especially for Yb³⁺/Tm³⁺ dopants. There are many factors which can affect the UC process and lower slope values, e.g. saturation effect, heating of samples or cross-relaxation process between dopants. Nanomaterials are particularly prone to quenching processes, and their crystal structure is often defected which yields luminescence deactivation centres.

On the basis of the collected and literature data, the UC mechanism proposed for SrF₂:Yb³⁺,Ln³⁺ NPs is presented in Fig. 3c. In these systems, Yb³⁺ ions absorb photons, which results in excitation of the Yb³⁺ ion from ²F_{7/2} to ²F_{5/2} excited state. In the next step, the energy may be dissipated, leading to Yb³⁺ ion in its ground state or, as a result of energy transfer upconversion (ETU), to the Ln³⁺ ion (³I₆ energy level for Ho³⁺, ⁴I_{11/2} for Er³⁺ and ³H₅ for Tm³⁺). To achieve an appropriate energy level for Ho³⁺ and Er³⁺ in the samples, the two-photon process is required. For Tm³⁺ from two to four photons must be transferred.

Biological properties. Cell health and growth can be determined by quantifying different parameters. In the presented study, the viability of cells treated with the studied NPs was investigated using the WST-1 and Live/Dead cell viability assays (see Supplementary Materials for more details). The WST-1 assay determines the cell metabolic activity and proliferation, whereas the Live/Dead assay determines the ratio of alive to dead cells in the population. Fluorescent Live/Dead cell viability assay showed that the proportions of alive and dead cells incubated with NPs were similar to the control cells (Fig. 4a). Representative images of the cells exposed to the analysed NPs are displayed in Fig. 5 and Figs S9–11. However, the WST-1 test showed contrary results. Namely, NPs caused a significant decrease in the proliferation rate in a dose-dependent manner in the measured concentration range (up to 100 µg/mL) (Fig. 4b). Moreover, the cytotoxic effect differs between the NPs doped with various ions. From among bare NPs (not coated with PEG-(COOH)₂ or PAA) the structures doped with Tm³⁺ were more cytotoxic than those doped with Ho³⁺ and Er³⁺. Namely, the cells treated with SrF₂:20%Yb³⁺,0.25%Tm³⁺ at concentration 25 µg/mL showed significantly lower proliferation rate than the control cells, whereas the other two bare nanostructures showed a negative influence on the cells at 50 µg/mL. The obtained results are in contrast to some of the earlier reports claiming that the synthesized fluorides doped with Ln³⁺ ions had no or low impact on mammalian cells^{36,37}. However, other authors reported that some of the NPs may decrease cell viability even at relatively low concentrations³⁸.

To improve the bio-application and decrease the cytotoxicity NPs are usually coated and functionalized as described previously^{31,39}. These procedures were also generally used to improve other properties of nanostructures, such as dispersion ability and stability of NPs in aqueous solutions, luminescence properties, shape or protection from the surrounding environment. The studied NPs were coated with two different organic compounds, namely PEG-(COOH)₂ and PAA. In the case of NPs doped with Ho³⁺ their modification with the PEG-(COOH)₂ and PAA caused a slight increase of the cytotoxicity (Fig. 4b). This effect was not observed when the cells were incubated with SrF₂:20%Yb³⁺,1%Er³⁺ and SrF₂:20%Yb³⁺,0.25%Tm³⁺. The obtained results are in accordance with those Das and co-authors, who claim that PEG-oleate capped NaYF₄:Yb³⁺,Er³⁺ significantly decrease the viability of Human Aortic Endothelial Cells in comparison to bare NPs⁴⁰, although in most of the previous research, NPs coated with PEG-(COOH)₂ and PAA were considered as a less toxic than bare NPs^{38,39}.

The confocal microscopy study demonstrated that all of the synthesized NPs were easily internalized by the fibroblast cells (Fig. 6 and Figs S12, S13), despite their negative charge, as confirmed by the presence of upconversion luminescence. High cellular uptake of negatively charged NPs results from strong and nonspecific interactions with the plasma membrane⁴¹. The results are in accordance with previous research, showing that upconverting fluorides doped with Ln³⁺ ions are suitable for imaging^{42,43}.

Discussion

SrF₂:Yb³⁺,Ln³⁺ nanoparticles (where Ln = Ho, Er, Tm) can be synthesised by hydrothermal method using metal salts and NH₄F as reagents, NaCit or NH₄Cit used as co-reagents allowing for control reaction kinetics. The influence of complexation agents, as well as reaction time and amount of ammonium fluoride on morphology and spectroscopic properties, was studied in details. The size of obtained NPs was slightly depended on the reaction time, which was 6 or 12 h. Much more important was the concentration of NH₄F precipitating reagent. Two concentrations were used: 1.5× and 3× excess to the stoichiometric amount. Lower concentration of NH₄F resulted in NPs with sizes around 11–15 nm, however, higher excess caused precipitation of slightly agglomerated NPs with sizes between 28–39 nm. The used synthesis conditions also affected dopants concentrations what was especially

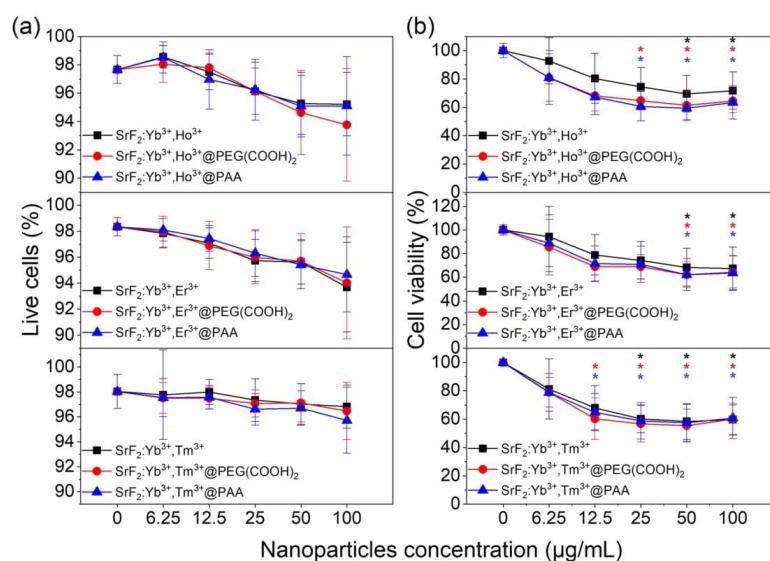


Figure 4. (a) Influence of $\text{SrF}_2:\text{Yb}^{3+}, \text{Ln}^{3+}$, $\text{SrF}_2:\text{Yb}^{3+}, \text{Ln}^{3+}@ \text{PEG}(\text{COOH})_2$, $\text{SrF}_2:\text{Yb}^{3+}, \text{Ln}^{3+}@ \text{PAA}$ on human fibroblasts' viability, determined by the Live/Dead cell viability assay. The data are shown as mean values with the standard deviation (means \pm SD). (b) Influence of $\text{SrF}_2:\text{Yb}^{3+}, \text{Ln}^{3+}$, $\text{SrF}_2:\text{Yb}^{3+}, \text{Ln}^{3+}@ \text{PEG}(\text{COOH})_2$, $\text{SrF}_2:\text{Yb}^{3+}, \text{Ln}^{3+}@ \text{PAA}$ on human fibroblasts' proliferation, determined by WST assay. Asterisks indicate results significantly different from those obtained for the control (Kruskal-Wallis test, significance at $p < 0.05$). The data are shown as mean values with the standard deviation (means \pm SD).

visible in case of Yb^{3+} ions. Smaller particles, prepared in the presence of $1.5 \times$ excess of NH_4F , usually had between 20–23% mol. of Yb^{3+} ions, where those prepared with $3 \times$ excess of NH_4F 23–28% mol. The applied conditions also had the influence of hydrodynamic diameter of NPs in water colloids. $1.5 \times$ excess of NH_4F resulted in NPs with diameter around 18–47 nm, whereas $3 \times$ excess in the formation of larger clusters with diameter 100–250 nm, most probably consisted of several NPs. The prepared NPs were negatively charged at physiological pH, what was a result of the presence of citrate groups on their surface. Determined zeta potentials were in the range of -15 to -33 mV.

The applied synthesis conditions had a great influence on the spectroscopic properties of obtained NPs. The most intense emission under NIR wavelengths was obtained for products prepared in 12 h synthesis, with $3 \times \text{NH}_4\text{F}$ excess and NaCit as a complexing agent. Furthermore, reaction time and added co-reagent had also effect on the upconversion colour, what was a result of changes in the intensity of emission bands. Measured luminescence decays as well as dependences of luminescence intensity on laser powers confirmed energy transfer between Yb^{3+} and Ho^{3+} , Er^{3+} or Tm^{3+} as process responsible for observed upconversion.

Summarising, high upconversion intensity can be achieved only if a large excess of NH_4F reagent is used, the reaction time is long (12 h) and as co-reagent, NaCit is used. On the other hand, small NPs with narrow size distribution can be obtained when reaction time is short (6 h) and NH_4F precipitating agent is at low concentration.

The cytotoxicity of the synthesized and functionalized NPs was investigated, using WST-1 cell proliferation assay and Live/Dead cell viability assay. We demonstrated that the synthesized structures exhibited proliferative inhibition in fibroblast cells in a dose-dependent manner, whereas they appeared to be alive according to fluorescent assay. Further *in vitro* toxicity evaluation with the aim to discover the mechanisms of impact of NPs on the cells has to be performed. Cellular uptake of the NPs was confirmed by the presence of upconversion luminescence in the cells. The luminescent properties of the nanoparticles allow them to be used as fluorescent agents in bio-imaging applications.

Methods

Materials. Rare earth (RE) oxides: Er_2O_3 and Yb_2O_3 (99.99%, Stanford Materials, United States) were dissolved separately in hydrochloric acid, HCl (ultra-pure, Sigma-Aldrich, 37%, Poland) in order to obtain respective rare earth chloride solutions in a concentration with 1 or 0.25 M. Ammonium fluoride, NH_4F (98+%, Sigma-Aldrich, Poland) was used as the source of fluoride ions. Strontium chloride hexahydrate $\text{SrCl}_2 \cdot 6\text{H}_2\text{O}$ (Sigma-Aldrich, 99+%, Poland), citric acid trisodium salt dihydrate, (Sigma-Aldrich, 97%, Poland) and ammonium citrate tribasic, (Sigma-Aldrich, $\geq 97\%$, Poland), phosphate buffered saline (BioShop), poly(ethylene glycol)

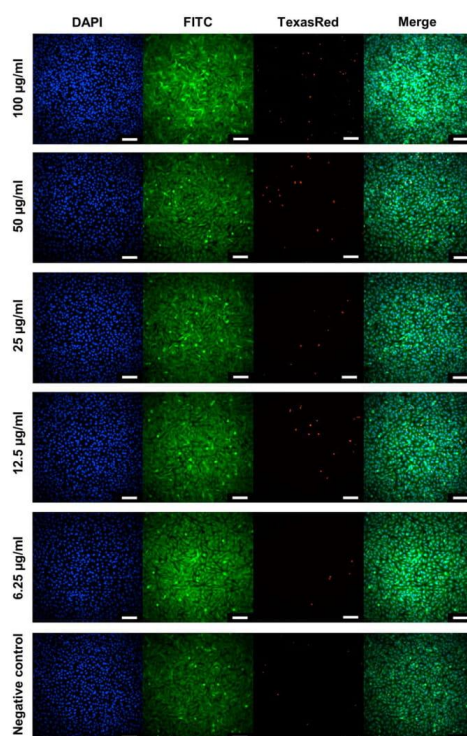


Figure 5. Representative high-content images of MSU1.1 cells exposed to $\text{SrF}_2:20\% \text{Yb}^{3+}, 0.25\% \text{Tm}^{3+}$ nanoparticles (6.25–100 $\mu\text{g}/\text{mL}$). Images were obtained using different filters to detect nuclei (DAPI), live cells (FITC), and dead cells (TexasRed). The scale bars denote 100 μm .

bis(carboxymethyl) ether (average M_n 250, Sigma-Aldrich, Poland), polyacrylic acid (average M_w 1800, Sigma-Aldrich, Poland) were used as received, without further purification. Deionized water was used for the synthesis.

Synthesis of $\text{SrF}_2:\text{Ln}^{3+}$ nanoparticles. To obtain 3.5 mmol of SrF_2 doped with 20% of Yb^{3+} and 1% of Ho^{3+} , 2.77 mL of 1 M SrCl_2 solution and YbCl_3 mixed with HoCl_3 (0.70 mL of 1 M YbCl_3 and 0.14 mL of 0.25 M HoCl_3) were added to 20 mL of 1 M sodium citrate, NaCit solution (anti-agglomeration and complexing agent) or 1 M solution of ammonium citrate, NH_4Cit . Then, 5 mL of 2.10 M or 4.20 M solution of NH_4F (depending on the NH_4F excess) were added to the solution containing SrCl_2 and LnCl_3 salts. The pH of the final mixture was equal to 7.5. The as-prepared transparent solution was transferred into the 50 mL Teflon-lined vessel and hydrothermally treated for 6 h or 12 h (180 $^\circ\text{C}$, 15 bars), in an externally heated autoclave (Berghof DAB-2). When the reaction was completed, the obtained white precipitate was purified by centrifugation and rinsed several times with water and ethanol. The final product was dried under ambient conditions. NPs doped with Er^{3+} or Tm^{3+} were prepared analogously.

Surface functionalization of $\text{SrF}_2:\text{Yb}^{3+}, \text{Ln}^{3+}$ nanoparticles. Three samples: $\text{SrF}_2:20\% \text{Yb}^{3+}, 1\% \text{Ho}^{3+}$, $\text{SrF}_2:20\% \text{Yb}^{3+}, 1\% \text{Er}^{3+}$ and $\text{SrF}_2:20\% \text{Yb}^{3+}, 0.25\% \text{Tm}^{3+}$ prepared by 12 h synthesis in the presence of NaCit and with $1.5\times$ excess of NH_4F were selected for cytotoxicity studies. The samples showed necessary parameters for bioimaging such as good spectroscopic properties and small NPs' sizes, around 15 nm.

To modify surface of NPs, 100 mg of each sample was dissolved in 30 mL of phosphate-buffered saline (PBS). After that, the solution was ultrasonicated for 1 h. Next, 4 mL of each NPs solution was mixed with 4 mL of 1% solution of poly(ethylene glycol) bis(carboxymethyl) ether (PEG-(COOH)₂) in PBS or 4 mL of 1% solution of polyacrylic acid (PAA) in PBS. After another 0.5 h of sonification, samples were centrifuged, washed with PBS solution three times, and dissolved in PBS. As prepared colloids were diluted by PBS solution to receive 100 $\mu\text{g}/\text{mL}$ concentration of NPs.

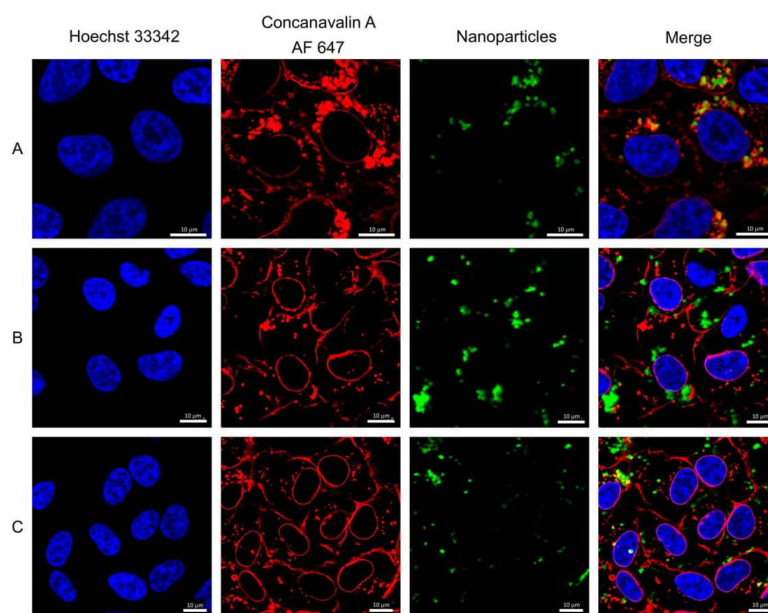


Figure 6. Human fibroblasts after 24 h incubation with the: (A) $\text{SrF}_2:20\% \text{Yb}^{3+}, 0.25\% \text{Tm}^{3+}$, (B) $\text{SrF}_2:20\% \text{Yb}^{3+}, 0.25\% \text{Tm}^{3+} @ \text{PEG}(\text{COOH})_2$, (C) $\text{SrF}_2:20\% \text{Yb}^{3+}, 0.25\% \text{Tm}^{3+} @ \text{PAA}$, imaged using confocal laser scanning microscopy equipped with a tuneable infrared laser. Red colour - cell membrane (concanavalin 647, exc. 633 nm), blue colour - cell nuclei (DAPI, exc. 405 nm), green colour - NPs (NPs' luminescence, infrared excitation).

Characterization. Powder diffractograms were recorded on a Bruker AXS D8 Advance diffractometer in the Bragg-Brentano geometry, with $\text{Cu K}_{\alpha 1}$ radiation $\lambda = 1.5406 \text{ \AA}$, in the 2θ range from 6 to 60° . The reference data was taken from the Inorganic Crystal Structure Database (ICSD). The composition of prepared materials was analysed by Inductively Coupled Plasma-Optical Emission Spectrometer Varian ICP-OES VISTA-MPX and EA Vario EL III. Transmission-electron-microscopy (TEM) images were recorded on an FEI Tecnai G2 20 X-TWIN transmission electron microscope, which used an accelerating voltage of 200 kV. Fourier transform infrared spectra (FT-IR) were recorded using a JASCO 4200 FT-IR spectrophotometer. DLS and zeta potential measurements were performed by using a Malvern Zetasizer Nano ZS instrument.

The luminescence characteristics (excitation, emission spectra, luminescence decays) of the prepared samples were measured on a QuantaMasterTM 40 spectrophotometer equipped with an Opolette 355LD UVDM tunable laser, with a repetition rate of 20 Hz and a Hamamatsu R928 photomultiplier used as a detector for emission/excitation spectra and decay time measurements. A continuous Dragon Lasers DPSS 980 nm laser was used as the excitation source, coupled to a 200 μm optical fibre and collimator to determine dependencies between emission intensity and laser power.

Cytotoxicity. *Cell culture.* Human fibroblast (MSU-1.1) cell line from Prof. C. Kieda (CBM, CNRS, Orleans, France), was cultured in Dulbecco's modified Eagle's medium (DMEM, Gibco), supplemented with 10% fetal bovine serum (FBS, Sigma-Aldrich) and 1% penicillin-streptomycin antibiotics (Sigma-Aldrich). The cells were maintained at 37°C in a humidified atmosphere supplemented with 5% CO_2 . The cell morphology was checked using an inverted microscope (Leica DMIL LED).

Cytotoxicity assays. For the cytotoxicity test, $5 \cdot 10^3$ cells/well were seeded at 96-well plate and incubated for 24 h. Afterwards, 50 μl of several different concentrations of the NPs diluted in PBS were added to 150 μl of culture medium in each well resulting in a final concentration of 100, 50, 25, 12.5 and 6.25 $\mu\text{g}/\text{mL}$, and the cells were further incubated for 48 h. Phosphate buffered saline (PBS, Sigma-Aldrich) was used as a control. For more details see Supporting Information.

References

- Auzel, F. Upconversion and anti-Stokes processes with f and d ions in solids. *Chem. Rev.* **104**, 139–73 (2004).
- Wang, Z.-L. *et al.* Simultaneous synthesis and functionalization of water-soluble up-conversion nanoparticles for *in-vitro* cell and nude mouse imaging. *Nanoscale* **3**, 2175 (2011).
- Runowski, M. *et al.* Lifetime Nanomanometry-High-Pressure Luminescence of Up-converting Lanthanide Nanocrystals - $\text{SrF}_2:\text{Yb}^{3+}, \text{Er}^{3+}$. *Nanoscale* **9**, 16030–16037 (2017).
- Xu, S. *et al.* Mesoporous silica coating $\text{NaYF}_4:\text{Yb}, \text{Er} @ \text{NaYF}_4$ upconversion nanoparticles loaded with ruthenium(II) complex nanoparticles: Fluorometric sensing and cellular imaging of temperature by upconversion and of oxygen by downconversion. *Microchim. Acta* **185** (2018).
- Lan, J. *et al.* Upconversion luminescence assay for the detection of the vascular endothelial growth factor, a biomarker for breast cancer. *Microchim. Acta* **183**, 3201–3208 (2016).
- van der Ende, B. M., Aarts, L. & Meijerink, A. Lanthanide ions as spectral converters for solar cells. *Phys. Chem. Chem. Phys.* **11**, 11081 (2009).
- Zhao, J., Zhu, Y. J., Wu, J. & Chen, F. Microwave-assisted solvothermal synthesis and upconversion luminescence of $\text{CaF}_2:\text{Yb}^{3+}/\text{Er}^{3+}$ nanocrystals. *J. Colloid Interface Sci.* **440**, 39–45 (2015).
- Pedroni, M. *et al.* Lanthanide doped upconverting colloidal CaF_2 nanoparticles prepared by a single-step hydrothermal method: toward efficient materials with near infrared-to-near infrared upconversion emission. *Nanoscale* **3** (2011).
- Balabhadr, S., Debasu, M. L., Brites, C. D. S., Ferreira, R. A. S. & Carlos, L. D. Radiation-to-heat conversion efficiency in $\text{SrF}_2:\text{Yb}^{3+}/\text{Er}^{3+}$ upconverting nanoparticles. *Opt. Mater.* **83**, 1–6 (2018).
- Pak, A. M. *et al.* Efficient visible range $\text{SrF}_2:\text{Yb}, \text{Er}$ and $\text{SrF}_2:\text{Yb}, \text{Tm}$ -based up-conversion luminophores. *J. Fluor. Chem.* **194**, 16–22 (2017).
- Sun, J., Xian, J. & Du, H. Facile synthesis of well-dispersed $\text{SrF}_2:\text{Yb}^{3+}/\text{Er}^{3+}$ upconversion nanocrystals in oleate complex systems. *Appl. Surf. Sci.* **257**, 3592–3595 (2011).
- Pedroni, M. *et al.* Water (H_2O and D_2O) Dispersible NIR-to-NIR Upconverting $\text{Yb}^{3+}/\text{Tm}^{3+}$ Doped MF_2 ($\text{M} = \text{Ca}, \text{Sr}$) Colloids: Influence of the Host Crystal. *Cryst. Growth Des.* **13**, 4906–4913 (2013).
- Villa, I. *et al.* 1.3 μm emitting $\text{SrF}_2:\text{Nd}^{3+}$ nanoparticles for high contrast *in vivo* imaging in the second biological window. *Nano Res.* **8**, (649–665 (2015)).
- Quintanilla, M., Cantarelli, I. X., Pedroni, M., Speghini, A. & Vetroni, F. Intense ultraviolet upconversion in water dispersible $\text{SrF}_2:\text{Tm}^{3+}, \text{Yb}^{3+}$ nanoparticles: the effect of the environment on light emissions. *J. Mater. Chem. C* **3**, 3108–3113 (2015).
- Li, A. H. *et al.* Upconversion-luminescent/magnetic dual-functional sub-20 nm core-shell $\text{SrF}_2:\text{Yb}, \text{Tm} @ \text{CaF}_2:\text{Gd}$ heteronanoparticles. *Dalt. Trans.* **45**, 5800–5807 (2016).
- Zanzoni, S., Pedroni, M., D'Onofrio, M., Speghini, A. & Assfalg, M. Paramagnetic Nanoparticles Leave Their Mark on Nuclear Spins of Transiently Adsorbed Proteins. *J. Am. Chem. Soc.* **138**, 72–75 (2016).
- Balabhadr, S., Debasu, M. L., Brites, C. D. S., Ferreira, R. A. S. & Carlos, L. D. Upconverting Nanoparticles Working As Primary Thermometers In Different Media. *J. Phys. Chem. C* **121**, 13962–13968 (2017).
- Pedroni, M. *et al.* Colloidal nanothermometers based on neodymium doped alkaline-earth fluorides in the first and second biological windows. *Sensors Actuators, B Chem.* **250**, 147–155 (2017).
- Cortelletti, P. *et al.* Tuning the sensitivity of lanthanide-activated NIR nanothermometers in the biological windows. *Nanoscale* **10**, 2568–2576 (2018).
- Lyapin, A. A. *et al.* Upconversion Luminescence of Fluoride Phosphors $\text{SrF}_2:\text{Er}, \text{Yb}$ under Laser Excitation at 1.5 μm . *Opt. Spectrosc.* **125**, 537–542 (2018).
- Du, S. & Wang, Y. A broad-range temperature sensor dependent on the magnetic and optical properties of $\text{SrF}_2:\text{Yb}^{3+}, \text{Ho}^{3+}$. *CrystEngComm* **21**, 1452–1457 (2019).
- Kuznetsov, S. *et al.* Up-conversion quantum yields of $\text{SrF}_2:\text{Yb}^{3+}, \text{Er}^{3+}$ sub-micron particles prepared by precipitation from aqueous solution. *J. Mater. Chem. C* **6**, 598–604 (2018).
- Zhang, C. *et al.* Mesoporous SrF_2 and $\text{SrF}_2:\text{Ln}^{3+}$ ($\text{Ln} = \text{Ce}, \text{Tb}, \text{Yb}, \text{Er}$) hierarchical microspheres: Hydrothermal synthesis, growing mechanism, and luminescent properties. *J. Phys. Chem. C* **114**, 6928–6936 (2010).
- Jiang, T. *et al.* Citric acid-assisted hydrothermal synthesis of $\alpha\text{-NaYF}_4:\text{Yb}^{3+}, \text{Tm}^{3+}$ nanocrystals and their enhanced ultraviolet upconversion emissions. *Cryst. Eng. Comm.* **14**, 2302 (2012).
- Cortelletti, P. *et al.* Luminescence of Eu^{3+} Activated CaF_2 and SrF_2 Nanoparticles: Effect of the Particle Size and Codoping with Alkaline Ions. *Cryst. Growth Des.* **18**, 686–694 (2018).
- Sun, J., Xian, J., Zhang, X. & Du, H. Hydrothermal synthesis of $\text{SrF}_2:\text{Yb}^{3+}/\text{Er}^{3+}$ micro-/nanocrystals with multiform morphologies and upconversion properties. *J. Rare Earths* **29**, 32–38 (2011).
- Chen, G., Qiu, H., Prasad, P. N. & Chen, X. Upconversion nanoparticles: design, nanochemistry, and applications in theranostics. *Chem. Rev.* **114**, 5161–214 (2014).
- Jin, Y. Hydrothermal Synthesis and Luminescent Properties of $(\text{Sr}, \text{Ba})\text{F}_2:\text{Eu}^{3+}$ Nanostructures. *J. Nanosci. Nanotechnol.* **16**, (9856–9861 (2016)).
- Ritter, B. *et al.* Novel and easy access to highly luminescent Eu and Tb doped ultra-small CaF_2 , SrF_2 and BaF_2 nanoparticles-structure and luminescence. *Dalt. Trans.* **46**, 2925–2936 (2017).
- Unfried, K. *et al.* Cellular responses to nanoparticles: Target structures and mechanisms. *Nanotoxicology* **1**, 52–71 (2007).
- Richards, D. & Ivanisevic, A. Inorganic material coatings and their effect on cytotoxicity. *Chem. Soc. Rev.* **41**, 2052–2060 (2012).
- Shannon, R. D. Revised effective ionic radii and systematic studies of interatomic distances in halides and chalcogenides. *Acta Crystallogr. A* **32**, 751–767 (1976).
- Dong, N.-N. *et al.* NIR-to-NIR Two-Photon Excited $\text{CaF}_2:\text{Tm}^{3+}, \text{Yb}^{3+}$ Nanoparticles: Multifunctional Nanoprobes for Highly Penetrating Fluorescence Bio-Imaging. *ACS Nano* **5**, 8665–8671 (2011).
- Kaiser, M. *et al.* Power-dependent upconversion quantum yield of $\text{NaYF}_4:\text{Yb}^{3+}, \text{Er}^{3+}$ nano- and micrometer-sized particles – measurements and simulations. *Nanoscale* **9**, 10051–10058 (2017).
- Xia, Z., Du, P. & Liao, L. Facile hydrothermal synthesis and upconversion luminescence of tetragonal $\text{Sr}_2\text{LnF}_7:\text{Yb}^{3+}/\text{Er}^{3+}$ ($\text{Ln} = \text{Y}, \text{Gd}$) nanocrystals. *Phys. status solidi* **4**, 1–4 (2013).
- Gulzar, A., Xu, J., Yang, P., He, F. & Xu, L. Upconversion processes: versatile biological applications and biosafety. *Nanoscale* **9**, 12248–12282 (2017).
- Chen, G., Yang, C. & Prasad, P. N. Nanophotonics and Nanochemistry: Controlling the Excitation Dynamics for Frequency Up- and Down-Conversion in Lanthanide-Doped Nanoparticles. *Acc. Chem. Res.* **46** (2013).
- Wysokińska, E. *et al.* Cytotoxic interactions of bare and coated $\text{NaGdF}_4:\text{Yb}^{3+}, \text{Er}^{3+}$ nanoparticles with macrophage and fibroblast cells. *Toxicol. Vitro* **32**, 16–25 (2016).
- Fröhlich, E. The role of surface charge in cellular uptake and cytotoxicity of medical nanoparticles. *Int. J. Nanomedicine* **7**, 5577 (2012).
- Das, G. K., Stark, D. T. & Kennedy, I. M. Potential toxicity of Up-converting nanoparticles encapsulated with a bilayer formed by ligand attraction. *Langmuir* **30**, 8167–8176 (2014).

41. Wilhelm, C. *et al.* Intracellular uptake of anionic superparamagnetic nanoparticles as a function of their surface coating. *Biomaterials* **24**, 1001–1011 (2003).
42. Bogdan, N. *et al.* Bio-functionalization of ligand-free upconverting lanthanide doped nanoparticles for bio-imaging and cell targeting. *Nanoscale* **4**, 3647–50 (2012).
43. Woźniak, A. *et al.* Cytotoxicity and imaging studies of β -NaGdF₄:Yb³⁺,Er³⁺@PEG-Mo nanorods. *RSC Adv.* **6**, 95633–95643 (2016).

Acknowledgements

Funding for this research was provided by National Science Centre, Poland, under grant numbers UMO-2016/22/E/ST5/00016 and UMO-2016/21/B/ST8/00477.

Author Contributions

D.P. conducted nanoparticles synthesis and performed spectroscopic measurements. A.E.-G. and B.G. performed cytotoxicity tests, imaging of cells treated with nanoparticles and analysed received results. D.P. together with T.G. analysed the results related to structure, morphology and spectroscopic properties. All authors contributed to discussion about the results and wrote the manuscript. All authors reviewed the manuscript.

Additional Information

Supplementary information accompanies this paper at <https://doi.org/10.1038/s41598-019-45025-1>.

Competing Interests: The authors declare no competing interests.

Publisher's note: Springer Nature remains neutral with regard to jurisdictional claims in published maps and institutional affiliations.



Open Access This article is licensed under a Creative Commons Attribution 4.0 International License, which permits use, sharing, adaptation, distribution and reproduction in any medium or format, as long as you give appropriate credit to the original author(s) and the source, provide a link to the Creative Commons license, and indicate if changes were made. The images or other third party material in this article are included in the article's Creative Commons license, unless indicated otherwise in a credit line to the material. If material is not included in the article's Creative Commons license and your intended use is not permitted by statutory regulation or exceeds the permitted use, you will need to obtain permission directly from the copyright holder. To view a copy of this license, visit <http://creativecommons.org/licenses/by/4.0/>.

© The Author(s) 2019

Upconverting SrF₂ nanoparticles doped with Yb³⁺/Ho³⁺, Yb³⁺/Er³⁺ and Yb³⁺/Tm³⁺ ions – optimisation of synthesis method, structural, spectroscopic and cytotoxicity studies

Dominika Przybylska¹, Anna Ekner-Grzyb², Bartosz F. Grześkowiak³, and Tomasz Grzyb^{1,*}

¹Department of Rare Earths, Faculty of Chemistry, Adam Mickiewicz University in Poznań, Uniwersytetu Poznańskiego 8, Poznań, 61-614, Poland

²Department of Plant Ecophysiology, Faculty of Biology, Adam Mickiewicz University in Poznań, Uniwersytetu Poznańskiego 6, Poznań, 61-614, Poland

³NanoBioMedical Centre, Adam Mickiewicz University in Poznań, Wszechnicy Piastowskiej 3, Poznań, 61-614, Poland

*E-mail: tgrzyb@amu.edu.pl

Supplementary Materials

Introduction

Table S1 shows review of literature about SrF₂ upconverting nanoparticles with basic information about synthesis conditions and conclusion from the presented research.

Table S1. Examples of synthesis method and properties of upconverting SrF₂ from literature.

Material	Size (nm)	Novelty	Synthesis method	Ref.
SrF ₂ :Yb ³⁺ , Er ³⁺	5 - 25	nanocrystals with different size due to reaction time	solvothermal in a mixture of water/ethanol/oleic acid/sodium oleate, T=180°C, t=4/16/72 h	1
SrF ₂ :Yb ³⁺ , Tm ³⁺	8	influence of Na ⁺ and K ⁺ on spectroscopic properties of SrF ₂ :Yb ³⁺ , Tm ³⁺ in water and D ₂ O	hydrothermal synthesis, sodium citrate, T=190 °C, t= 6 h, 2.5x NH ₄ F	2
SrF ₂ :Nd ³⁺	10	NPs for deep tissue, autofluorescence free and high resolution in vivo imaging using emission band at 1.340 μ, toxicological research	hydrothermal synthesis with potassium citrate, T=190 °C, t= 6 h, 2.5x NH ₄ F	3
SrF ₂ :Yb ³⁺ , Tm ³⁺	9	intense emission in UV of water colloid, correlation between the temperature and upconversion emission intensities in a D2O colloidal dispersion at different temperatures (10°C and 60°C)	hydrothermal synthesis, sodium citrate, T=190 °C, t= 6 h, 1.5x NH ₄ F	4
SrF ₂ :Yb ³⁺ , Tm ³⁺ @CaF ₂ :Gd ³⁺	20	first synthesis of core-shell NPs via a two-step hydrothermal method, magnetic characterization of core-shell SrF ₂ :Yb ³⁺ , Tm ³⁺ @CaF ₂ :Gd ³⁺	two-step hydrothermal method, with sodium citrate, 1 st step T=190 °C, t= 6 h, 2 nd step T=200°C, t= 6 h	5
SrF ₂ :Yb ³⁺ , Tm ³⁺ @SrF ₂ :Yb ³⁺ , Er ³⁺	10-12	investigation of interactions between Ln-doped fluoride NPs and biomolecules (ubiquitin)	two step hydrothermal synthesis, sodium citrate, T=190 °C, t= 3 h, 2.5x NH ₄ F (1 st and 2 nd step)	6
SrF ₂ :Yb ³⁺ , Er ³⁺	8-41	developed the method to predict the temperature calibration curve of any upconverting thermometer, independently of the	hydrothermal synthesis, sodium citrate, T=190 °C, t= 6 h	7
SrF ₂ :Nd ³⁺ SrF ₂ :Nd ³⁺ , Gd ³⁺	6.5-9	high thermal relative sensitivity in range 20 C - 65 C,	hydrothermal synthesis, potassium citrate, T=190 °C, t= 3 h or 10 min	8
SrF ₂ :Yb ³⁺ , Er ³⁺	100-300	quantum yield of upconversion SrF ₂ , with different amount of Yb ³⁺ ions	precipitation with further calcination in 600°C	9
SrF ₂ :Eu ³⁺	10-40	investigation of symmetry site of Eu ³⁺ in cubic SrF ₂ , achieving long Eu ³⁺ lifetime	hydrothermal method with sodium/potassium citrate, T=190 °C, t= 10, 35, 360, and 480 min, 2.5x	10
SrF ₂ :Yb ³⁺ , Tm ³⁺ @ Y ³⁺ @Yb ³⁺ , Er ³⁺ , Nd ³⁺ @Nd ³⁺	8.5-26.6	optimization of thermal relative sensitivity by changing Er ³⁺ content in 20–50 °C temperature range, measured in water colloid, possibility of a multicolour UC emission	four sequential hydrothermal reaction steps with potassium citrate, 2.5x NH ₄ F, T=190 °C, t= 3 h for each step	11
SrF ₂ :Yb ³⁺ , Er ³⁺	10/ 41	calculation of photothermal conversion efficiencies, investigation of photon-to-heat conversion efficiency	hydrothermal reaction with sodium citrate, T=190 °C, t= 6 h	12
SrF ₂ :Yb ³⁺ , Er ³⁺	-	investigation of upconversion luminescence of Er ³⁺ ions for a concentration series of phosphors upon excitation by laser radiation in the region of 1.5 μm	co-precipitation from aqueous solutions	13
SrF ₂ :Yb ³⁺ , Ho ³⁺	39	investigation of magnetization values and abnormal thermal of band at 656 nm	hydrothermal method, with EDTA and NH ₄ BF ₄ T=200 °C, t= 5 h, pH 5	14

Structure and morphology

Table S2. Size of obtained NPs, calculated from the Scherrer equation on the basis of XRD analysis¹⁵.

Co-reagent	Reaction time (h)	Size (nm)					
		SrF ₂ :20%Yb ³⁺ ,1%Ho ³⁺		SrF ₂ :20%Yb ³⁺ ,1%Er ³⁺		SrF ₂ :20%Yb ³⁺ ,0.25%Tm ³⁺	
		1.5× NH ₄ F	3× NH ₄ F	1.5× NH ₄ F	3× NH ₄ F	1.5× NH ₄ F	3× NH ₄ F
NaCit	6	11.7 ± 0.1		11.8 ± 0.2		11.6 ± 0.2	
	12	12.8 ± 0.1	28.1 ± 0.3	13.5 ± 0.4	38.5 ± 0.4	11.5 ± 0.1	38.9 ± 0.4
NH ₄ Cit	6	12.6 ± 0.1		14.7 ± 0.5		14.1 ± 0.3	
	12	14.2 ± 0.3	36.2 ± 0.9	15.1 ± 0.5	38.8 ± 0.7	15.3 ± 0.2	36.6 ± 0.7

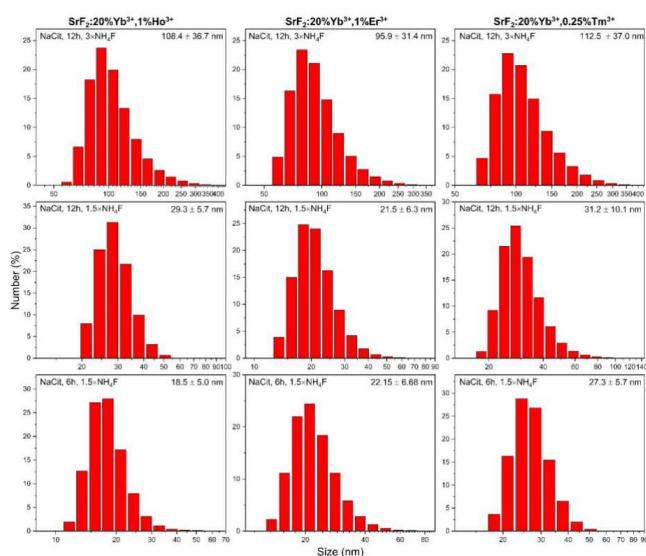


Fig. S1. Hydrodynamic diameters obtained by DLS analysis of the synthesised SrF₂:Yb³⁺,Ln³⁺ NPs in the presence of NaCit as a co-reagent.

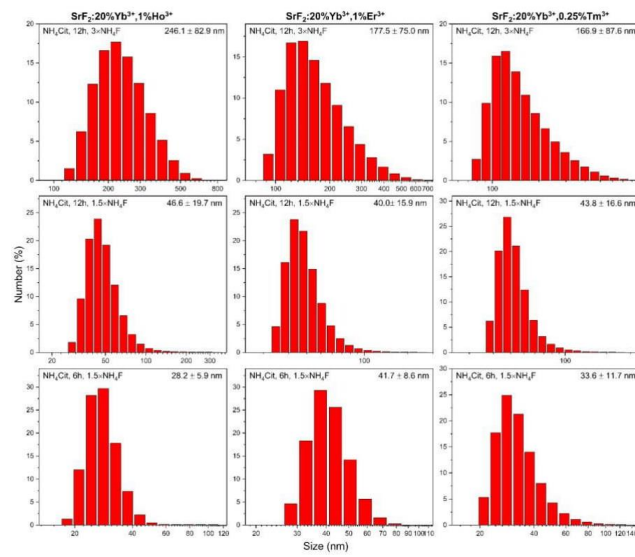


Fig. S2. Hydrodynamic diameters obtained by DLS analysis of the synthesised SrF₂:Yb³⁺,Ln³⁺ NPs in the presence of NH₄Cit as a co-reagent.

Table S3. Metal ions composition of synthesised NPs analysed by ICP-OES (uncertainty of ICP-OES analysis was below ± 5% of the value).

Co-reagent	Reaction time (h)	Dopants	Molar percentage (%)					
			1.5× NH ₄ F			3× NH ₄ F		
			Sr ²⁺	Yb ³⁺	Ln ³⁺	Sr ²⁺	Yb ³⁺	Ln ³⁺
NaCit	6	20%Yb ³⁺ ,1%Ho ³⁺	75.42	23.46	1.12			
		20%Yb ³⁺ ,1%Er ³⁺	77.79	21.39	0.82			
		20%Yb ³⁺ ,0.25%Tm ³⁺	76.97	22.71	0.32			
	12	20%Yb ³⁺ ,1%Ho ³⁺	74.51	24.17	1.32	74.61	24.02	1.37
		20%Yb ³⁺ ,1%Er ³⁺	77.40	20.97	1.63	75.22	23.63	1.15
		20%Yb ³⁺ ,0.25%Tm ³⁺	75.43	24.34	0.23	75.54	24.24	0.22
NH ₄ Cit	6	20%Yb ³⁺ ,1%Ho ³⁺	75.63	23.07	1.30			
		20%Yb ³⁺ ,1%Er ³⁺	75.95	22.76	1.29			
		20%Yb ³⁺ ,0.25%Tm ³⁺	76.90	22.76	0.34			
	12	20%Yb ³⁺ ,1%Ho ³⁺	75.16	22.99	1.85	70.43	28.26	1.31
		20%Yb ³⁺ ,1%Er ³⁺	74.52	23.42	2.07	70.70	28.29	1.00
		20%Yb ³⁺ ,0.25%Tm ³⁺	76.66	22.98	0.36	71.28	28.51	0.22

Table S4. Results of elemental analysis of chosen samples (doped with 20%Yb³⁺,1%Er³⁺).

Synthesis conditions	N (wt%)	C (wt%)	H (wt%)
NH ₄ Cit, 12h, 1.5x NH ₄ F	0.246	1.935	0.296
	0.270	1.950	0.299
NH ₄ Cit, 12h, 3x NH ₄ F	0.106	0.529	0.387
	0.112	0.535	0.090
NaCit, 12h, 3x NH ₄ F	0.020	0.645	0.116
	0.030	0.526	0.098

Table S5. Cell parameter for cubic structure SrF₂:Yb³⁺,Ln³⁺ calculated in Maud software¹⁶.

Co-reagent	NH ₄ F excess	Reaction time (h)	SrF ₂ :20%Yb ³⁺ ,1%Ho ³⁺		SrF ₂ :20%Yb ³⁺ ,1%Er ³⁺		SrF ₂ :20%Yb ³⁺ ,0.25 %Tm ³⁺	
			a (Å)	V (Å ³)	a [Å]	V (Å ³)	a [Å]	V (Å ³)
NaCit	1.5x	6	5.73(8)	188.92(2)	5.73(8)	188.94(8)	5.73(7)	188.86(1)
		12	5.73(7)	188.86(9)	5.73(7)	188.86(9)	5.73(8)	188.89(7)
	3x	12	5.73(2)	188.31(1)	5.73(3)	188.39(1)	5.73(4)	188.48(9)
NH ₄ Cit	1.5x	6	5.73(4)	188.56(9)	5.73(6)	188.71(7)	5.73(7)	188.78(1)
		12	5.73(7)	188.82(4)	5.73(7)	188.85(7)	5.73(8)	188.90(6)
	3x	12	5.73(0)	188.09(4)	5.73(0)	188.10(5)	5.73(0)	188.16(5)
Reference pattern SrF ₂ ICSD #40414, a = 5.794 Å, V = 194.50(7) Å ³								

Table S6. Hydrodynamic diameters of obtained NPs determined by DLS measurements.

Co-reagent	Reaction time (h)	Hydrodynamic diameter (nm)					
		SrF ₂ :20%Yb ³⁺ ,1 %Ho ³⁺		SrF ₂ :20%Yb ³⁺ ,1%Er ³⁺		SrF ₂ :20%Yb ³⁺ ,0.25%Tm ³⁺	
		1.5x NH ₄ F	3x NH ₄ F	1.5x NH ₄ F	3x NH ₄ F	1.5x NH ₄ F	3x NH ₄ F
NaCit	6	18.5± 5.0		22.15 ± 6.68		27.3±5.7	
	12	29.3± 5.7	108.4± 36.7	21.5± 6.3	95.9± 31.4	31.2± 10.1	112.5± 37.0
NH ₄ Cit	6	28.2± 5.9		41.7± 8.6		33.6± 11.7	
	12	46.6± 19.7	246.1± 82.9	40.0± 15.9	177.5± 75.0	43.8± 16.6	166.9± 87.6

Table S7. Summary of zeta potential measurements for obtained $\text{SrF}_2:\text{Yb}^{3+}, \text{Ln}^{3+}$ particles for physiological pH value.

Co-reagent	Reaction time (h)	$\text{SrF}_2:20\%\text{Yb}^{3+}, 1\%\text{Ho}^{3+}$				$\text{SrF}_2:20\%\text{Yb}^{3+}, 1\%\text{Er}^{3+}$				$\text{SrF}_2:20\%\text{Yb}^{3+}, 0.25\%\text{Tm}^{3+}$			
		1.5× NH_4F		3× NH_4F		1.5× NH_4F		3× NH_4F		1.5× NH_4F		3× NH_4F	
		pH	Zeta potential (mV)	pH	Zeta potential (mV)	pH	Zeta potential (mV)	pH	Zeta potential (mV)	pH	Zeta potential (mV)	pH	Zeta potential (mV)
NaCit	6	7.36	-22.7 ± 8.5			7.44	-23.3 ± 8.38			7.34	-20.1 ± 3.7		
	12	7.37	-14.9 ± 5.4	7.40	-33.3 ± 4.4	7.40	-21.0 ± 4.2	7.46	-19.5 ± 8.1	7.52	-27.9 ± 5.8	7.32	-29.8 ± 4.2
NH_4Cit	6	7.33	-28.3 ± 4.2			7.41	-24.7 ± 4.5			7.34	-23.3 ± 4.9		
	12	7.32	-27.8 ± 3.8	7.43	-27.9 ± 4.9	7.45	-20.1 ± 3.8	7.37	-29.6 ± 3.8	7.44	-27.7 ± 4.5	7.34	-26.0 ± 3.4

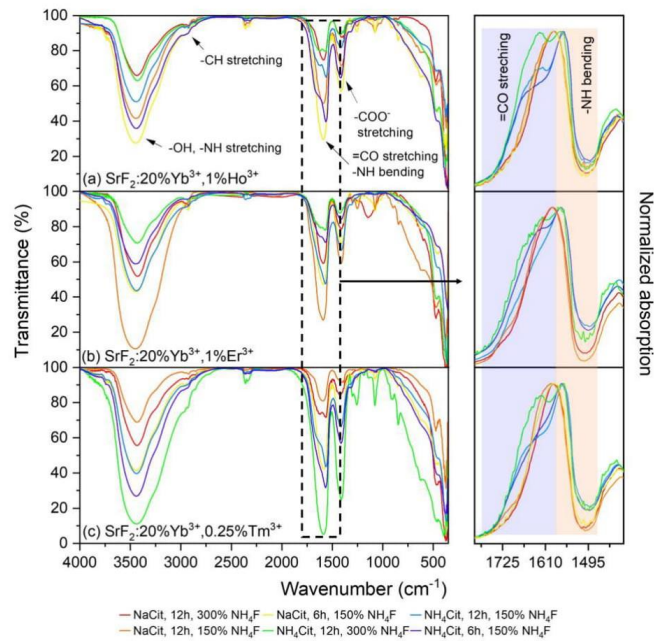


Fig. S3. Fourier transformed infrared spectroscopy (FT-IR) spectra of the obtained samples (left) and normalized absorption of samples in the 1400-1800 cm^{-1} range (right). Absorption of samples obtained in the presence of NH_4Cit presented small shift to shorter wavenumber as the result of higher amount of NH_4^+ ions.

Luminescence properties

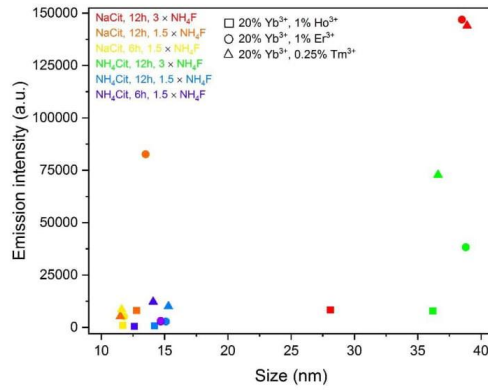


Fig. S4. Relationships between the integral emission intensity and NPs size of SrF₂:Yb³⁺,Ln³⁺. Calculations based on the emission spectra, measured under $\lambda_{\text{ex}} = 976$ nm pulsed excitation source (at 15 mJ·cm⁻²).

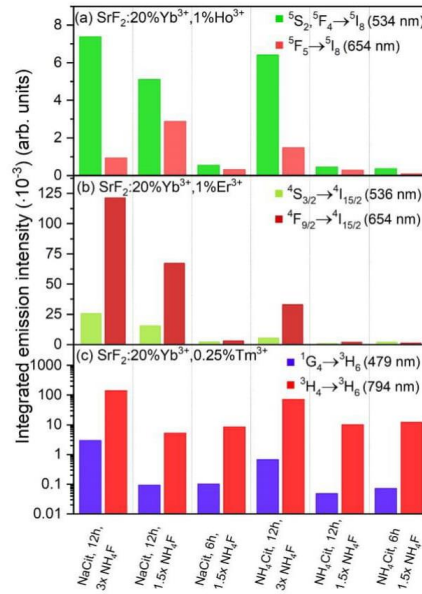


Fig. S5. Integrated luminescence intensities of SrF₂:20%Yb³⁺,x%Ln³⁺ samples: a) 20%Yb³⁺,1%Ho³⁺, b) 20%Yb³⁺,1%Er³⁺, c) 20%Yb³⁺,0.25%Tm³⁺, calculated from the spectra measured under $\lambda_{\text{ex}} = 976$ nm pulsed excitation source (at 15 mJ·cm⁻²).

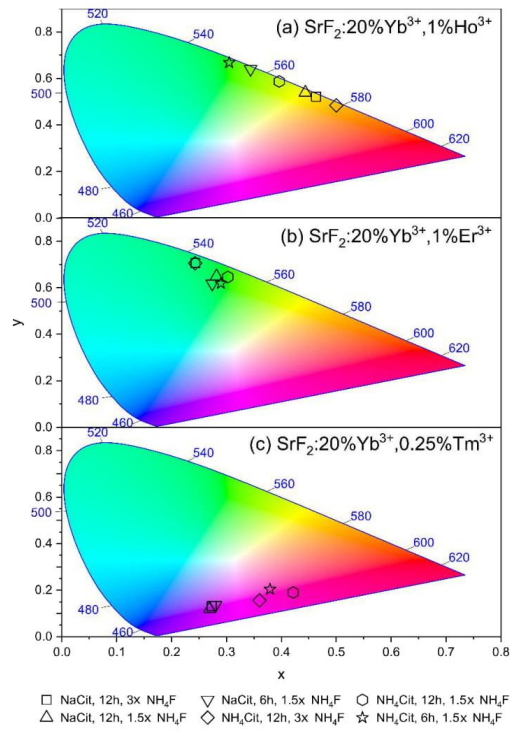


Fig. S6. CIE chromaticity diagrams of $\text{SrF}_2:\text{Yb}^{3+}, \text{Ln}^{3+}$ NPs, taken from the emission spectra measured under $\lambda_{\text{ex}} = 976$ nm pulsed excitation source (at $15 \text{ mJ}\cdot\text{cm}^{-2}$).

Because of the non-exponential character of luminescence decays, the following equation was used for lifetimes calculation:

$$\tau = \frac{\int_0^{\infty} tI(t)dt}{\int_0^{\infty} I(t)dt}$$

where τ is the decay time, and $I(t)$ is the intensity at time t .¹⁷

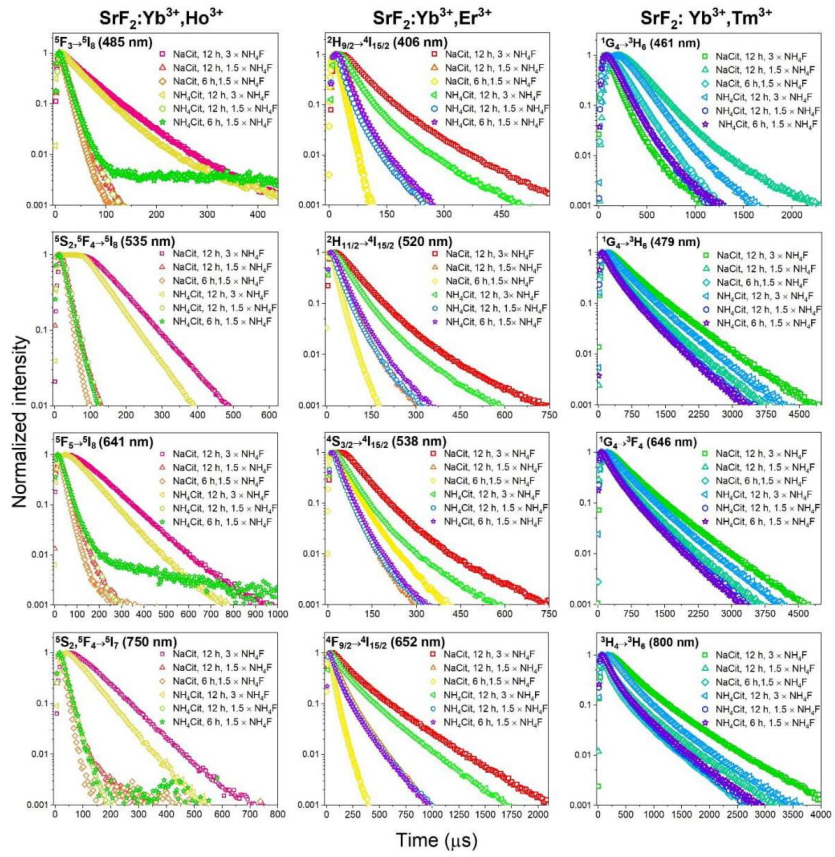


Fig. S7. Emission decays of $\text{SrF}_2:\text{Yb}^{3+},\text{Ln}^{3+}$ NPs measured under $\lambda_{\text{ex}} = 976$ nm pulsed excitation source (at $15 \text{ mJ}\cdot\text{cm}^{-2}$).

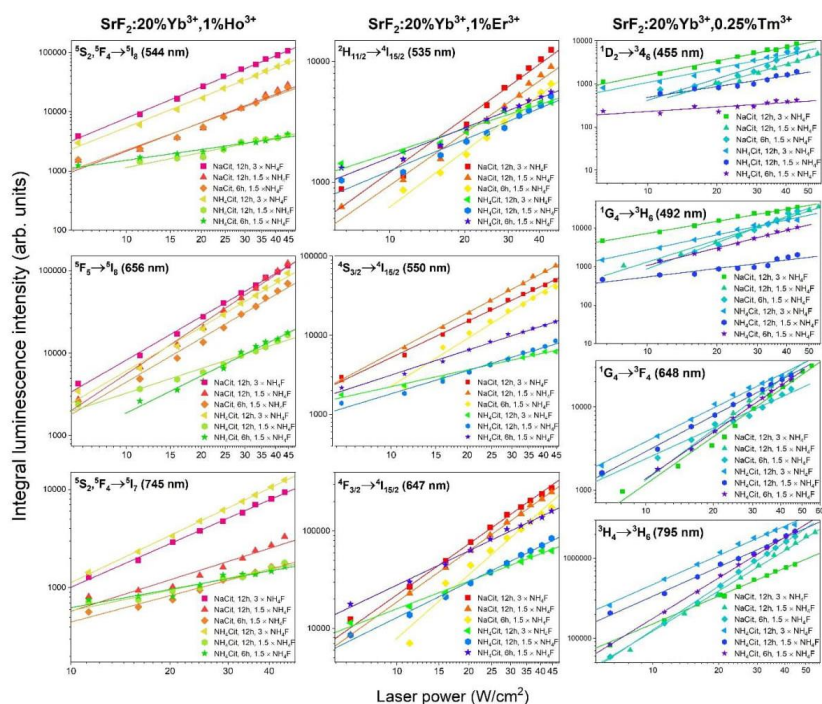


Fig. S8. Double-logarithmic plots of the upconversion emission intensity versus laser power density ($\lambda_{\text{ex}} = 976 \text{ nm}$), for $\text{SrF}_2:\text{Yb}^{3+},\text{Ln}^{3+}$ NPs.

Biological properties

Cytotoxicity assays

For the cytotoxicity test, $5 \cdot 10^3$ cells/well were seeded at 96-well plate and incubated for 24 h. Afterwards, 50 μl of several different concentrations of the NPs diluted in PBS were added to 150 μl of culture medium in the particular wells resulting in a final concentration of 100, 50, 25, 12.5 and 6.25 $\mu\text{g}/\text{mL}$, and the cells were further incubated for 48 h. Phosphate buffered saline (PBS, Sigma-Aldrich) was used as a control.

The influence of the studied NPs on the cells was investigated by cell proliferation WST-1 assay (Takara) according to literature.¹⁸ This colorimetric assay is based on the cleavage of tetrazolium salts by mitochondrial dehydrogenase in viable cells. After 48 h of incubation with the NPs, WST-1 Cell Proliferation Reagent was added (10 μL per each well) and the cells were incubated again for 4 h. Then, 100 μL of supernatant was transferred to fresh wells to avoid absorption of light by the NPs

and absorbance at 450 nm was measured using multiwell plate reader (Zenyth, Biochrom). The reference wavelength was 620 nm. The cell viability was expressed as the respiration activity normalised to untreated cells.

The fluorescent Live/Dead cell viability assay allows distinction of live cells with intact plasma membranes from dead cells with compromised membranes. In this test, the cells were seeded in black polystyrene 96-wells flat bottom plate with the transparent bottom (Greiner Bio-One GmbH). Following 48 h exposure to the NPs, the cells were incubated with 2 μ M calcein AM, 2 μ M ethidium homodimer-1 and 8 μ M Hoechst 33342 (ThermoFisher Scientific) containing DPBS (100 μ L/well) for 30 minutes at 37 °C. Finally, the cells were analysed with the IN Cell Analyzer 2000 (GE Healthcare Life Sciences). Viable cells were imaged using the FITC/FITC excitation/emission filters while for the dead cells the TexasRed/TexasRed ex/em filter combination was applied. DAPI/DAPI was applied to detect the Hoechst 33342 blue signal. A minimum of 20 fields was imaged per well with a 20 \times magnification. Analysis of the collected images was performed with the IN Cell Developer Toolbox software (GE Healthcare Life Sciences) using an in-house developed protocol. At first, the total cell number was retrieved from the DAPI images by means of defining and counting the nuclei. Subsequently, the number of viable cells from the FITC images and the number of dead cells from the TexasRed images were determined.

Each experiment was repeated three times and all of the samples in one experiment were tested in triplets. The results were analysed using the non-parametric Kruskal-Wallis test with the Statistica 13 software package. Differences were considered statistically significant at $p < 0.05$. The data are shown as mean values with the standard deviation (means \pm SD).

Cellular uptake of nanoparticles

To image the cells treated with the NPs, $1.25 \cdot 10^4$ cells/well were seeded at Lab-Tek™ chamber slides which consist of removable polystyrene media chambers attached to standard glass slides and grown for 24 h at 37 °C in a humidified atmosphere supplemented with 5% CO₂. Afterwards, 50 μ l of NPs (100 μ g/mL in PBS) was added to the cells which were further incubated for 24 h. Next, the cells were fixed with 4% formaldehyde solution (Sigma-Aldrich) and stained with concanavalin A (Alexa Fluor 647 Conjugate, ThermoFisher Scientific) and Hoechst 33342. Afterwards, the samples were imaged using confocal laser scanning microscopy (CLSM, Zeiss, LSM 780) equipped with a tuneable infrared laser. The fluorescence emission was detected using two channels: the spectrum of luminescence under infrared excitation (an up-conversion process made by NPs) and the spectrum

of fluorescence under VIS and UV excitation (Hoechst 33342 and concanavalin A). The above procedure was applied to make sure that the detection of some compounds inside the cells came from the up-converting NPs.

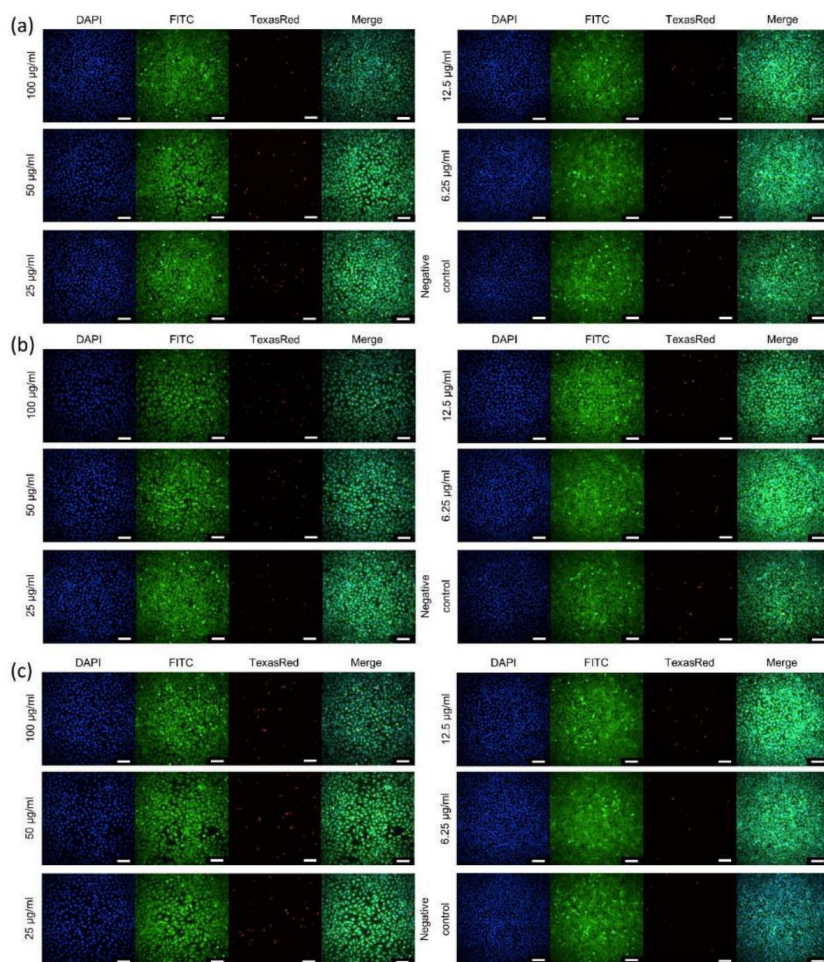


Fig. S9. Representative high-content images of MSU1.1 cells exposed to (a) $\text{SrF}_2:20\% \text{Yb}^{3+}, 1\% \text{Ho}^{3+}$, (b) $\text{SrF}_2:20\% \text{Yb}^{3+}, 1\% \text{Ho}^{3+} @ \text{PEG}(\text{COOH})_2$, (c) $\text{SrF}_2:20\% \text{Yb}^{3+}, 1\% \text{Ho}^{3+} @ \text{PAA}$ NPs (6.25 – 100 $\mu\text{g}/\text{mL}$). The images were obtained using different filters to detect the nuclei (DAPI), live cells (FITC), and dead cells (TexasRed). The scale bars denote 100 μm .

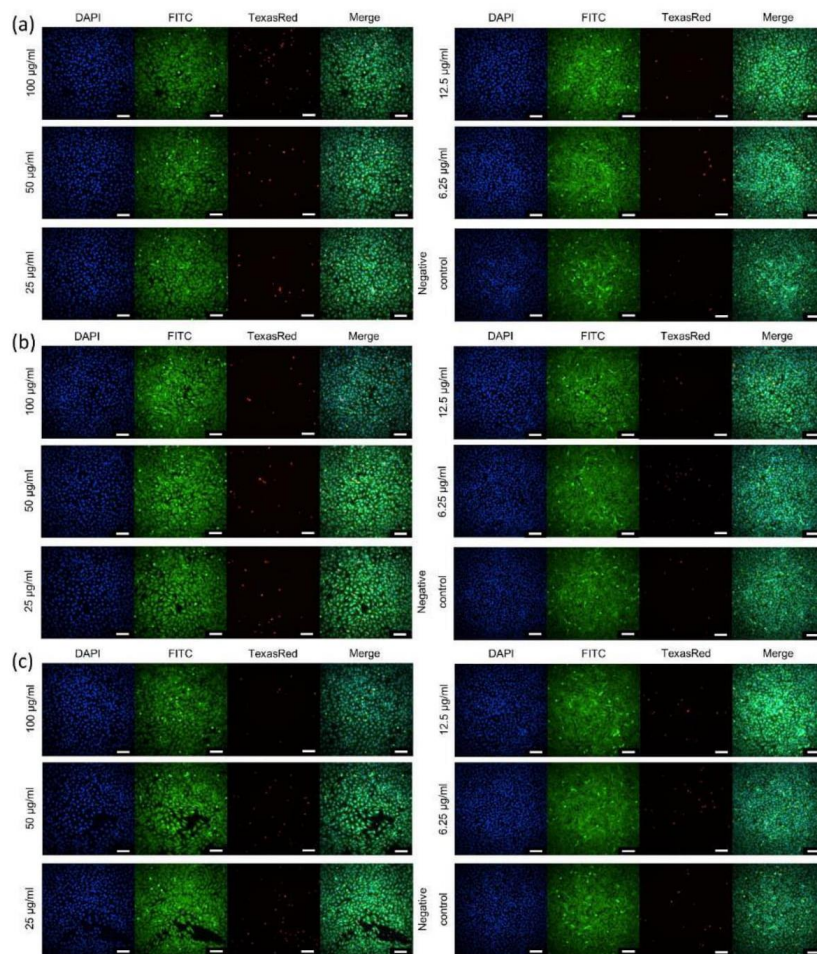


Fig. S10. Representative high-content images of MSU1.1 cells exposed to (a) $\text{SrF}_2:20\% \text{Yb}^{3+}, 1\% \text{Er}^{3+}$, (b) $\text{SrF}_2:20\% \text{Yb}^{3+}, 1\% \text{Er}^{3+} @ (\text{COOH})_2$, (c) $\text{SrF}_2:20\% \text{Yb}^{3+}, 1\% \text{Er}^{3+} @ \text{PAA}$ NPs (6.25 – 100 $\mu\text{g}/\text{mL}$). The images were obtained using different filters to detect the nuclei (DAPI), live cells (FITC), and dead cells (TexasRed). The scale bars denote 100 μm .

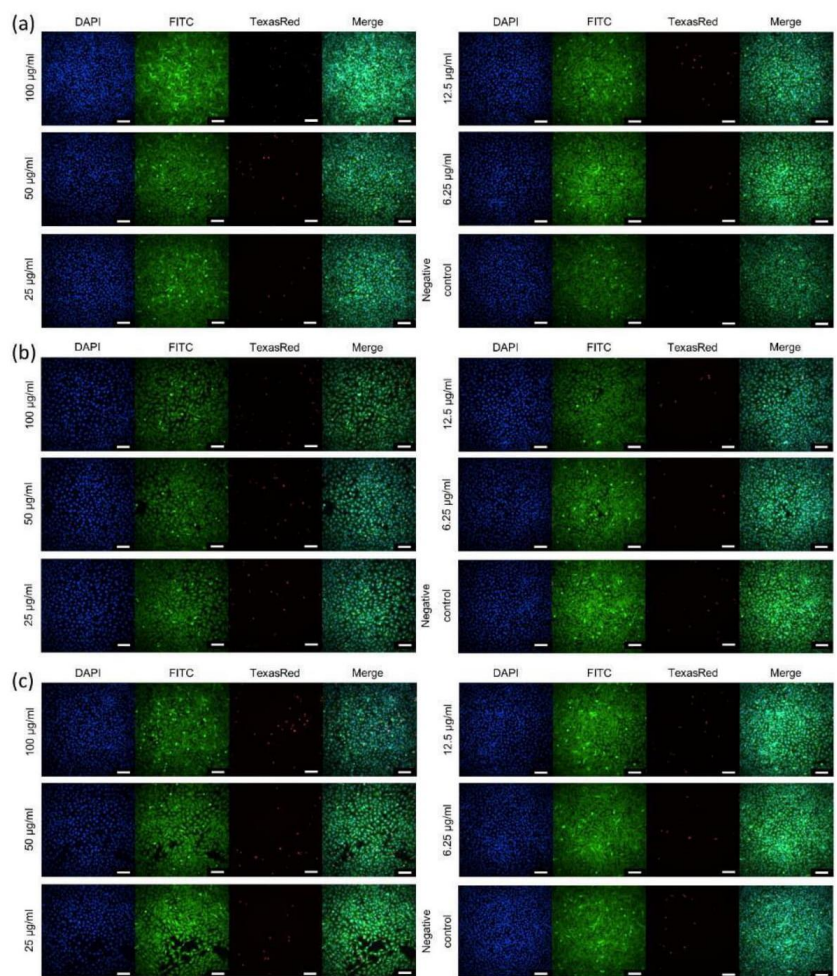


Fig. S11. Representative high-content images of MSU1.1 cells exposed to (a) $\text{SrF}_2:20\% \text{Yb}^{3+}, 0.25\% \text{Tm}^{3+}$, (b) $\text{SrF}_2:20\% \text{Yb}^{3+}, 0.25\% \text{Tm}^{3+} @ (\text{COOH})_2$, (c) $\text{SrF}_2:20\% \text{Yb}^{3+}, 0.25\% \text{Tm}^{3+} @ \text{PAA NPs}$ (6.25 – 100 $\mu\text{g}/\text{mL}$). The images were obtained using different filters to detect the nuclei (DAPI), live cells (FITC), and dead cells (TexasRed). The scale bars denote 100 μm .

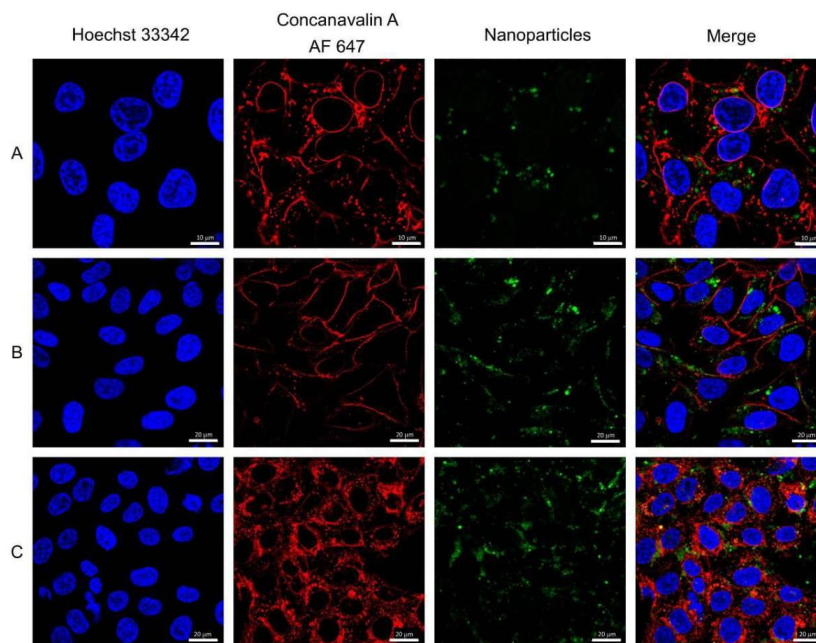


Fig. S12. Human fibroblasts after 24h incubation with (A) $\text{SrF}_2:20\%\text{Yb}^{3+},1\%\text{Ho}^{3+}$, (B) $\text{SrF}_2:20\%\text{Yb}^{3+},1\%\text{Ho}^{3+}@(\text{COOH})_2$, (C) $\text{SrF}_2:20\%\text{Yb}^{3+},1\%\text{Ho}^{3+}@PAA$ imaged using confocal laser scanning microscopy equipped with a tuneable infrared laser. Red colour - cell membrane (concanavalin 647, exc. 633 nm), blue colour – cell nuclei (DAPI, exc. 405 nm), green colour – NPs (NPs' luminescence, infrared excitation).

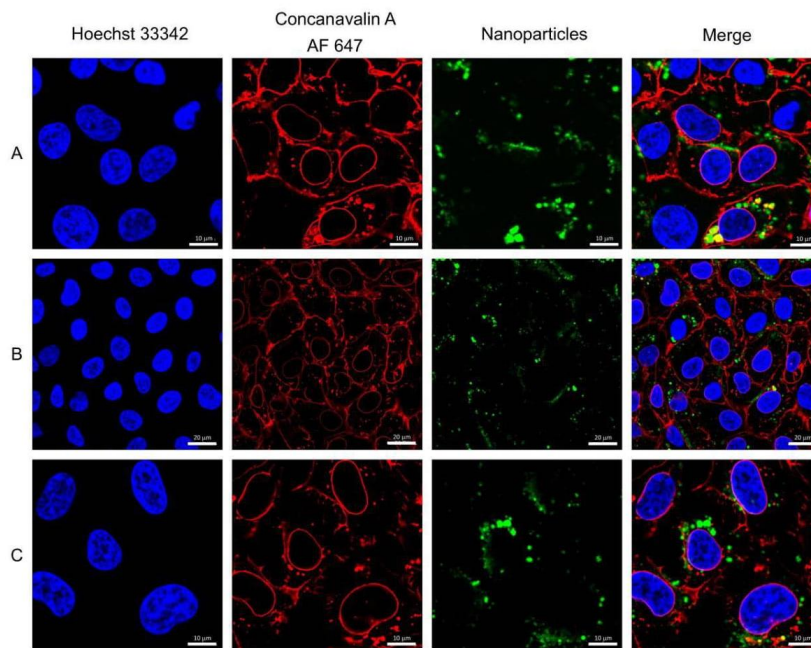


Fig. S13. Human fibroblasts after 24h incubation with (A) $\text{SrF}_2:20\%\text{Yb}^{3+},1\%\text{Er}^{3+}$, (B) $\text{SrF}_2:20\%\text{Yb}^{3+},1\%\text{Er}^{3+}@\text{(COOH)}_2$, (C) $\text{SrF}_2:20\%\text{Yb}^{3+},1\%\text{Er}^{3+}@\text{PAA}$, imaged using confocal laser scanning microscopy equipped with a tuneable infrared laser. Red colour - cell membrane (concanavalin 647, exc. 633 nm), blue colour – cell nuclei (DAPI, exc. 405 nm), green colour – NPs (NPs' luminescence, infrared excitation).

References

1. Sun, J., Xian, J. & Du, H. Facile synthesis of well-dispersed $\text{SrF}_2:\text{Yb}^{3+}/\text{Er}^{3+}$ upconversion nanocrystals in oleate complex systems. *Appl. Surf. Sci.* **257**, 3592–3595 (2011).
2. Pedroni, M. *et al.* Water (H_2O and D_2O) Dispersible NIR-to-NIR Upconverting $\text{Yb}^{3+}/\text{Tm}^{3+}$ Doped MF_2 (M = Ca, Sr) Colloids: Influence of the Host Crystal. *Cryst. Growth Des.* **13**, 4906–4913 (2013).
3. Villa, I. *et al.* 1.3 μm emitting $\text{SrF}_2:\text{Nd}^{3+}$ nanoparticles for high contrast in vivo imaging in the second biological window. *Nano Res.* **8**, 649–665 (2015).
4. Quintanilla, M., Cantarelli, I. X., Pedroni, M., Speghini, A. & Vetrone, F. Intense ultraviolet upconversion in water dispersible $\text{SrF}_2:\text{Tm}^{3+},\text{Yb}^{3+}$ nanoparticles: the effect of the environment on light emissions. *J. Mater. Chem. C* **3**, 3108–3113 (2015).
5. Li, A.-H. *et al.* Upconversion-luminescent/magnetic dual-functional sub-20 nm core-shell

- SrF₂:Yb,Tm@CaF₂:Gd heteronanoparticles. *Dalt. Trans.* **45**, 5800–5807 (2016).
6. Zanzoni, S., Pedroni, M., D'Onofrio, M., Speghini, A. & Assfalg, M. Paramagnetic Nanoparticles Leave Their Mark on Nuclear Spins of Transiently Adsorbed Proteins. *J. Am. Chem. Soc.* **138**, 72–75 (2016).
 7. Balabhadra, S., Debasu, M. L., Brites, C. D. S., Ferreira, R. A. S. & Carlos, L. D. Upconverting Nanoparticles Working As Primary Thermometers In Different Media. *J. Phys. Chem. C* **121**, 13962–13968 (2017).
 8. Pedroni, M. *et al.* Colloidal nanothermometers based on neodymium doped alkaline-earth fluorides in the first and second biological windows. *Sensors Actuators, B Chem.* **250**, 147–155 (2017).
 9. Kuznetsov, S. *et al.* Up-conversion quantum yields of SrF₂:Yb³⁺,Er³⁺ sub-micron particles prepared by precipitation from aqueous solution. *J. Mater. Chem. C* **6**, 598–604 (2018).
 10. Cortelletti, P. *et al.* Luminescence of Eu³⁺ Activated CaF₂ and SrF₂ Nanoparticles: Effect of the Particle Size and Codoping with Alkaline Ions. *Cryst. Growth Des.* **18**, 686–694 (2018).
 11. Cortelletti, P. *et al.* Tuning the sensitivity of lanthanide-activated NIR nanothermometers in the biological windows. *Nanoscale* **10**, 2568–2576 (2018).
 12. Balabhadra, S., Debasu, M. L., Brites, C. D. S., Ferreira, R. A. S. & Carlos, L. D. Radiation-to-heat conversion efficiency in SrF₂:Yb³⁺/Er³⁺ upconverting nanoparticles. *Opt. Mater.* **83**, 1–6 (2018).
 13. Lyapin, A. A. *et al.* Upconversion Luminescence of Fluoride Phosphors SrF₂:Er,Yb under Laser Excitation at 1.5 μm. *Opt. Spectrosc.* **125**, 537–542 (2018).
 14. Du, S. & Wang, Y. A broad-range temperature sensor dependent on the magnetic and optical properties of SrF₂:Yb³⁺,Ho³⁺. *CrystEngComm* **21**, 1452–1457 (2019).
 15. Scherrer, P. Bestimmung der Größe und der inneren Struktur von Kolloidteilchen mittels Röntgenstrahlen. *Nachr. Ges. Wiss. Göttingen* **26**, 98–100 (1918).
 16. Lutterotti, L. & Bortolotti, M. Object oriented programming and fast computation techniques in Maud, a program for powder diffraction analysis written in java. *Compcomm. Newsl.* **1**, 43–50 (2003).
 17. Lakowicz, J. R. *Principles of Fluorescence Spectroscopy*. (Springer, 2006).
 18. Woźniak, A. *et al.* Size and shape-dependent cytotoxicity profile of gold nanoparticles for biomedical applications. *J. Mater. Sci. Mater. Med.* **28**, 92 (2017).



Contents lists available at ScienceDirect

Journal of Alloys and Compounds

journal homepage: <http://www.elsevier.com/locate/jalcom>

Synthesis and up-conversion of core/shell SrF₂:Yb³⁺,Er³⁺@SrF₂:Yb³⁺,Nd³⁺ nanoparticles under 808, 975, and 1532 nm excitation wavelengths

Dominika Przybylska, Tomasz Grzyb*

Adam Mickiewicz University in Poznań, Faculty of Chemistry, Department of Rare Earths, Uniwersytetu Poznańskiego 8, 61-614, Poznań, Poland



ARTICLE INFO

Article history:

Received 15 January 2020
 Received in revised form
 18 February 2020
 Accepted 14 March 2020
 Available online 16 March 2020

Keywords:

SrF₂ fluoride
 Luminescence
 Down-conversion
 Biological windows
 Dual-range emission
 Hydrothermal method

ABSTRACT

Sensitization of nanoparticles (NPs) by appropriate lanthanide ions is crucial for the obtained spectroscopic properties. Nd³⁺ ions can absorb light at around 808 nm, allowing for deep tissue imaging. Yb³⁺ ions can be effectively excited by 975 nm radiation which is utilized in many areas, e.g. in anti-counterfeit applications, while Er³⁺ ions are capable of absorption around 1532 nm, which in turn, is important for solar energy conversion. Here, we describe a method for Nd³⁺ and Er³⁺ ions isolation in NPs by the synthesis of core/shell structures. As an alternative to the most commonly used core/shell thermal decomposition synthesis procedures, our products were obtained in water by a hydrothermal method. SrF₂:Yb³⁺,Er³⁺@SrF₂:Yb³⁺,Nd³⁺ NPs with sizes between 30 and 60 nm showed intense green to yellowish-red luminescence in the visible range, due to Er³⁺-doping. Yb³⁺ played the role of bridging ions, transferring energy absorbed by Nd³⁺ ions between the shell and core phases, limiting, in the same way, cross-relaxation between Nd³⁺ sensitizer ions and Er³⁺ luminescence centers. Structure, morphology and spectroscopic properties were investigated, revealing interesting processes taking place in the prepared NPs.

© 2020 Elsevier B.V. All rights reserved.

1. Introduction

Studies of the up-conversion phenomenon (UC), initiated by the theoretical proposal of Bloembergen in 1951 [1] and proved experimentally by Auzel in 1966 [2], have significantly influenced materials science. Especially in nanotechnology, the UC has raised the important property of nanoparticles (NPs) allowing their applications in nanomedicine for cancer treatment and diagnosis [3–8]. The unique nature of UC has also been utilized in 3D displays, solar cells, lasers and fiber amplifiers, security markers, forensic science and pressure or temperature sensors [9–15].

UC is characterized by the conversion of low energy photons, from the near-infrared range, (NIR) to higher energy ones through the multiphoton absorption process [16], while down-conversion (DC) is the conversion of higher-energy photons to photons with lower energy (also known as down-shifting) [17]. Excellent materials which exhibit UC, as well as DC, are host compounds doped with lanthanide ions (Ln³⁺). These ions, together with Sc³⁺ and Y³⁺

form a group of rare earth ions (RE³⁺). Ln³⁺ ions have unique physicochemical and optical properties, due to their 4f electronic configuration. The energy levels of Ln³⁺ ions are well-defined, due to the effective shielding of the 4f orbitals caused by the filled 5s and 5p orbitals, and lie in the range of UV to NIR. Therefore, transitions within 4f subshell are relatively insensitive to the outer environment. As a result, materials doped with Ln³⁺ ions are efficient luminophores and usually show sharp emission spectra, long luminescence lifetimes, and large Stoke's shifts [18–20].

The most popular dopants used for UC are Yb³⁺, Er³⁺, Tm³⁺, and Ho³⁺ ions. To enhance luminescence, Yb³⁺ ions usually play the role of sensitizers, due to their simple configuration of energy levels and large absorption cross-section between 900 and 1000 nm [21]. Energy absorbed by Yb³⁺ ions can be transferred to other Ln³⁺ ions resulting in their luminescence. This fact, and the existence of the so-called “first optical transparency window” in the range of 700–1000 nm [22], has been utilized in nanomedicine for optical imaging, drug delivery, and photothermal therapy [23]. However, NIR radiation with a wavelength of 980 nm is absorbed by water, which at higher power densities, may lead to the cell overheating effect [24]. The solution for this problem is the addition of Nd³⁺

* Corresponding author.

E-mail address: tgrzyb@amu.edu.pl (T. Grzyb).

ions to the structure of NPs, as sensitizers for NIR radiation at 808 nm [25]. The water absorption coefficient is much lower at 808 nm, which also improves tissue penetrability [26]. Furthermore, the absorption cross-section of Nd^{3+} around 800 nm is significantly higher than Yb^{3+} around 980 nm.

Recently, UC of NPs under 808 nm has been intensively studied, mainly in triple-doped systems with Nd^{3+} ions used as sensitizers, and Yb^{3+} transferring absorbed energy to luminescence centers, usually Ho^{3+} , Er^{3+} , Tm^{3+} , or Tb^{3+} ions [27–33]. Because of the electronic structure of Nd^{3+} and the above-mentioned luminescent Ln^{3+} ions, a cross-relaxation (CR) process may occur, effectively quenching the luminescence of NPs. Hence, the concentration of Nd^{3+} is usually very low (below 2–3%) when all types of ions are in the same phase, which, in turn, results in low absorption at 808 nm [34–36]. To overcome this problem a few possibilities are available. The most developed solution for avoiding the CR process is the synthesis of core/shell or multi-shell NPs, combining NPs with organic dyes and surface plasmon coupling [29,37,38]. The first method, especially, is very promising. Shell layer not only increases the distance between the sensitizing and luminescent ions, which reduces the quenching process but also introduces isolation from the surrounding environment. Synthesis of core/shell NPs allows for the manipulation of the dopant's composition which can be used to obtain the desired emission and excitation properties. There are numerous examples of the utilization of core/shell structure of NPs: enhancement of UC quantum yield [39], tunable emission color, dual-mode emission from NIR to UV–Vis or to NIR with a longer wavelength than excitation light [40,41], multifunctionality of NPs through the addition of Gd^{3+} or Mn^{2+} ions [42], conjugation to biomolecules, drug delivery systems [43–46], and many others.

The main synthesis method of the core/shell NPs is the thermal decomposition, or precipitation, in high boiling-point solvents such as octadecene, oleic acid, or oleylamine, which forces the synthesis to be conducted at high temperature and under neutral gas protection [47]. The synthesis is complicated, has many steps, and the obtained products are hydrophobic which require additional procedures to remove oleic acid and octadecene from the NPs surface [27,34,48,49]. An alternative method which can be adopted for the preparation of core/shell NPs is solvothermal synthesis. The overall process is usually conducted in ethanol, oleic acid, ethylene glycol, or water, under high pressure and temperature, in special types of autoclaves [50–52].

The most environmentally friendly is the solvothermal synthesis with the use of water as a solvent: the hydrothermal method, very common for obtaining simple UC fluorides [53–56].

In the case of core/shell hydrothermal synthesis, just a few reports have been published (see Table S1 for more details). The first article, by Zazoni et al. where $\text{SrF}_2:\text{Yb}^{3+}@\text{SrF}_2:\text{Yb}^{3+},\text{Tm}^{3+}$ UCNPs were obtained, was published in 2016 [57]. Shortly after, Li et al. reported on the hydrothermal synthesis of $\text{SrF}_2:\text{Yb}^{3+},\text{Tm}^{3+}@\text{CaF}_2:\text{Gd}^{3+}$ NPs with magnetic properties [58]. In 2017 Alkahtani et al. presented a way of preparing $\text{YVO}_4:\text{Er}^{3+},\text{Yb}^{3+}@\text{YVO}_4:\text{Yb}^{3+},\text{Nd}^{3+}$ NPs by precipitation in hydrothermal conditions [24]. Doping NPs with Nd^{3+} allowed authors to study UC under 808 nm excitation. Another study was reported by Cortelletti et al., in 2018 [59], where, during a fourth-step hydrothermal synthesis, SrF_2 NPs with a multi-shelled architecture were obtained. This complicated structure was tested as an NIR-activated nanothermometer.

Most papers referring to the hydrothermal synthesis of core/shell are based on the SrF_2 compound. This matrix is thermally stable also in high temperature and phase transition is not observed, which is important for light source applications [60]. Furthermore, strontium fluoride has low phonon energy (similar to NaYF_4) and high thermal conductivity [61]. What is more, SrF_2

doped with Yb^{3+} and Tm^{3+} shows better emission than prepared in the same way $\alpha\text{-NaYF}_4$ about a similar size, which is known as one from the best UC materials [62]. Not without significance is the high value of quantum yield for $\text{SrF}_2:\text{Yb}^{3+},\text{Er}^{3+}$ (2.8%), important for further applications [63]. In comparison to NaREF_4 (RE = rare earth element) NPs, the most often studied as hosts for 808/980 nm excited UC, SrF_2 NPs can be easily synthesized by the hydrothermal method. Synthesis of NaREF_4 -type core/shell NPs was reported only twice and they were obtained only by solvothermal method (see Table S1) [64,65]. Usually, NaREF_4 materials, prepared via hydrothermal method are comprised of micro-sized crystals rather than nanocrystals [66–68].

Despite existing research on hydrothermal core/shell synthesis, obtaining high-quality NPs during the process conducted in water is still challenging. The possibilities of an optimized synthesis route, as well as morphology and spectroscopic properties improvement, have to be considered. Especially, the mechanism of UC in core/shell systems excited by Nd^{3+} ions should be carefully examined. In this article, $\text{SrF}_2:\text{Yb}^{3+},\text{Er}^{3+}@\text{SrF}_2:\text{Yb}^{3+},\text{Nd}^{3+}$ core/shell NPs were prepared by a two-step hydrothermal synthesis in the presence of sodium citrate. In the described approach, the core/shell structure was proved spectroscopically by analysis of Nd^{3+} and Er^{3+} interactions. Furthermore, in our NPs, the chosen doping ions allowed for the excitation by three laser wavelengths: 808, 975, and 1532 nm, as well as luminescence in the Vis or NIR range. The obtained properties are promising for theranostics due to the emission from, and within, biological windows, as well as for energy conversion purposes highly demanded in solar cell development.

2. Methods

2.1. Materials

Lanthanide oxides: Er_2O_3 and Yb_2O_3 , Nd_2O_3 , (99.99%, Stanford Materials, United States) were dissolved separately in hydrochloric acid, HCl (ultra-pure, Sigma-Aldrich, 37%, Poland), in order to obtain the respective rare earth chloride solutions in a concentration of 1 or 0.25 M. Ammonium fluoride, NH_4F (98+%, Sigma-Aldrich, Poland), was used as the source of fluoride ions. Strontium chloride hexahydrate $\text{SrCl}_2 \cdot 6\text{H}_2\text{O}$ (Sigma-Aldrich, 99+%, Poland), citric acid trisodium salt dihydrate, NaCit (Sigma-Aldrich, 97%, Poland) were used as received, without further purification. Deionized water was used for the synthesis.

2.2. Synthesis of core $\text{SrF}_2:\text{Yb}^{3+},\text{Er}^{3+}$ nanoparticles

To obtain 2 mmol of SrF_2 NPs, doped with 20% Yb^{3+} and 1% Er^{3+} ions, 1.58 mL of 1 M SrCl_2 solution and YbCl_3 mixed with ErCl_3 (0.40 mL of 1 M YbCl_3 and 0.08 mL of 0.25 M ErCl_3) were added to 20 mL of 1 M NaCit solution (anti-agglomeration and complexing agent). Then, 5 mL of 2.40 M solution of NH_4F (3 × excess in comparison to the stoichiometric amount) was added to the solution containing SrCl_2 and LnCl_3 salts. The pH of the final mixture was equal to 7.5. The as-prepared transparent solution was transferred into a 100 mL Teflon-lined vessel and hydrothermally treated for 24 h (200 °C, 15 bars and mixed), in an externally heated autoclave (Berghof BR-100). When the reaction was completed, the obtained white precipitate was purified by centrifugation and rinsed several times with water and ethanol. For the synthesis of core/shell structures, the wet product was re-dispersed in water and 5 mL of the formed colloid was transferred to a clean Teflon-lined vessel for the next step.

The presented description was the basic synthesis method. SrF_2 NPs were also prepared via modification of the above-mentioned

procedure, i.e. for a higher amount of product (5 mmol), shorter time of reaction (12 h), or with smaller excess of NH_4F reagent ($2 \times$). The modifications are included in the names of the samples used in this article, in brackets, and presented in Table 1.

2.3. Synthesis of core/shell $\text{SrF}_2:\text{Yb}^{3+}, \text{Er}^{3+} @ \text{SrF}_2:\text{Yb}^{3+}, \text{Nd}^{3+}$ nanoparticles

$\text{SrF}_2:\text{Yb}^{3+}, \text{Er}^{3+}$ core NPs were coated by $\text{SrF}_2:\text{Yb}^{3+}, \text{Nd}^{3+}$ shell via a second step in hydrothermal conditions. In a typical procedure, to obtain 2 mmol of shell containing 20% Yb^{3+} and 10% of Nd^{3+} ions, 1.40 mL of 1 M SrCl_2 solution and YbCl_3 , mixed with NdCl_3 (0.40 mL of 1 M YbCl_3 and 0.80 mL of 0.25 M NdCl_3), were added to 20 mL of 1 M NaCit solution. Then, 5 mL of 2.4 M solution of NH_4F ($3 \times$ excess in comparison to the stoichiometric amount) was added to the solution containing SrCl_2 and LnCl_3 salts. The pH of the final mixture was equal to 7.5. The as-prepared transparent solution was transferred into the 100 mL Teflon-lined vessel, where the earlier core suspension was placed, and hydrothermally treated for 24 h (200°C , 15 bars with mixing). When the reaction was completed, the obtained white precipitate was purified by centrifugation and rinsed several times with water and ethanol. The final product was dried under ambient conditions. A scheme of the synthesis procedure is presented in Fig. 1.

From the prepared samples, the two best emitting NPs were chosen to present their properties ($\text{SrF}_2:20\%\text{Yb}^{3+}, 1\%\text{Er}^{3+} @ \text{SrF}_2:20\%\text{Yb}^{3+}, 10\%\text{Nd}^{3+}$, 5 mmol/5 mmol of LnCl_3 , 24 h/24 h; $\text{SrF}_2:20\%\text{Yb}^{3+}, 1\%\text{Er}^{3+} @ \text{SrF}_2:20\%\text{Yb}^{3+}, 10\%\text{Nd}^{3+}$, 2 mmol/2 mmol of LnCl_3 , 24 h/12 h). Additionally, a core sample ($\text{SrF}_2:20\%\text{Yb}^{3+}, 1\%\text{Er}^{3+}, 10\%\text{Nd}^{3+}$, 2 mmol/2 mmol of LnCl_3 , 24 h) was prepared as a reference using the same composition of reactants and synthesis conditions as in the base procedure. This core sample was used to compare the morphology and spectroscopic properties of the triple-doped core ($\text{Yb}^{3+}, \text{Er}^{3+}, \text{Nd}^{3+}$) and core/shell where Nd^{3+} is separated from the activator ions and placed in the shell. To simplified naming of samples, all are presented in the above Table 1. Furthermore, different synthesis conditions are included in brackets in the sample name. The other core/shell samples, X-ray diffraction (XRD) patterns, dynamic light scattering (DLS), and zeta potential measurements, as well as spectroscopic properties, are attached in the Supplementary Materials.

2.4. Characterization

Powder diffractograms (XRD) were recorded on a Bruker AXS D8 Advance diffractometer in the Bragg-Brentano geometry, with $\text{Cu K}\alpha_1$ radiation, $\lambda = 1.5406 \text{ \AA}$, in the 2θ range from 10° to 60° . The reference data was taken from the International Centre for

Diffraction Data (ICDD). The composition of the prepared materials was analyzed by Inductively Coupled Plasma Mass Spectrometer (ICP-MS) NexION 300D, PerkinElmer. Transmission-electron-microscopy (TEM) images were recorded on a Hitachi HT7700 with the voltage of 120 kV. Fourier transform infrared spectra (FT-IR) were recorded using a JASCO 4200 FT-IR spectrophotometer. DLS and zeta potential measurements were performed by using a Malvern Zetasizer Nano ZS instrument.

The luminescence characteristics (excitation, emission spectra, luminescence decay) of the prepared samples were measured on a QuantaMaster™ 40 spectrophotometer equipped with an Opolette 355LD UVDM tunable laser, with a repetition rate of 20 Hz, and a Hamamatsu R928 photomultiplier used as a detector for emission, excitation spectra, and decay times measurements. A CNi multi-wavelength 2W CW laser was used as the excitation source, coupled to a 200 μm optical fiber and collimator to determine dependencies between the emission intensity and laser power. As a detector, a Digital CCD Camera made by Princeton Instruments PIXIS:256E, equipped with an SP-2156 Imaging Spectrograph, was applied and corrected for the instrumental response.

3. Results and discussion

3.1. Structure and morphology

The prepared samples showed a single-phase structure with the $Fm\bar{3}m$ space group, for both the core (Fig. S1) and core/shell (Fig. 2 and S2). Depending on the conditions of the sample's preparation (higher amount of product or reaction time), particles of different sizes were obtained, as indicated by the widths of the XRD peaks. Furthermore, the shift of diffraction peaks towards a higher angle, in comparison to the reference pattern (ICDD, 01-086-2418, SrF_2), confirmed that Ln^{3+} ion doping into the host structure decreased the cell volume. This was caused by the smaller ionic radii of Yb^{3+} , Er^{3+} , and Nd^{3+} , compared to the Sr^{2+} ions ($r_{\text{Sr}^{2+}} = 1.26 \text{ \AA}$, $r_{\text{Nd}^{3+}} = 1.1090 \text{ \AA}$, $r_{\text{Er}^{3+}} = 1.004 \text{ \AA}$, $r_{\text{Yb}^{3+}} = 0.985 \text{ \AA}$ for coordination number $\text{CN} = 8$) [69]. Replacement of Sr^{2+} by Ln^{3+} ions, made structure of our products similar to $\text{Sr}_{0.84}\text{Lu}_{0.16}\text{F}_{2.16}$ reported in ICDD reference No. 01-082-0640, where $V = 186.27 \text{ \AA}^3$, whereas pure SrF_2 have cell volume, $V = 195.11 \text{ \AA}^3$.

To determine the size of the obtained compounds, three techniques were used: TEM, calculations via Scherrer's equation from XRD and DLS measurements (Table 2, S2 and Figs. 2 and 3, S1-S5).

Comparing the size of the core and core/shell NPs, calculated from Scherer's equation, the growth of particles is observed for both samples. The smaller size of the core, as well as the core/shell, had NPs synthesized in a shorter time and with a lower amount of precursors. The increase in size is similar for both samples (10 nm).

Table 1
List of samples described in this article.

Sample name	Core 1st step				Core/shell 2nd step			
	Amount of precursor (mmol)	Excess of NH_4F	Reaction time (h)	Other	Amount of precursor (mmol)	Excess of NH_4F	Reaction time (h)	Other
Base procedure: $20\%\text{Yb}^{3+}, 1\%\text{Er}^{3+} @ 20\%\text{Yb}^{3+}, 10\%\text{Nd}^{3+}$	2	3	24	—	2	3	24	—
$20\%\text{Yb}^{3+}, 1\%\text{Er}^{3+} @ 20\%\text{Yb}^{3+}, 10\%\text{Nd}^{3+}$ (5 mmol/5 mmol)	5	3	24	—	5	3	24	—
$20\%\text{Yb}^{3+}, 1\%\text{Er}^{3+} @ 20\%\text{Yb}^{3+}, 10\%\text{Nd}^{3+}$ (24 h/12 h)	2	3	24	—	2	3	12	—
$20\%\text{Yb}^{3+}, 1\%\text{Er}^{3+} @ 20\%\text{Yb}^{3+}, 20\%\text{Nd}^{3+}$ ($2 \times \text{NH}_4\text{F}/2 \times \text{NH}_4\text{F}$)	2	2	24	—	2	2	24	20% Nd^{3+}
$20\%\text{Yb}^{3+}, 1\%\text{Er}^{3+} @ 20\%\text{Yb}^{3+}, 10\%\text{Nd}^{3+}$ (12 h/24 h)	2	3	12	—	2	3	24	—
$20\%\text{Yb}^{3+}, 1\%\text{Er}^{3+}, 10\%\text{Nd}^{3+}$	2	3	24	—	—	—	—	—

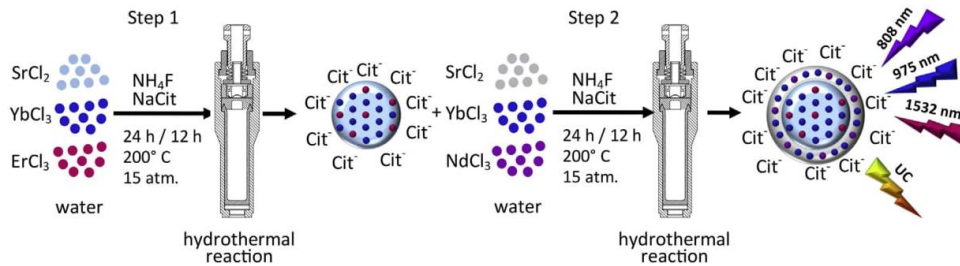


Fig. 1. Schematic representation of the synthesis procedure of $\text{SrF}_2:\text{Yb}^{3+},\text{Er}^{3+}@\text{SrF}_2:\text{Yb}^{3+},\text{Nd}^{3+}$ core/shell NPs via a hydrothermal method.

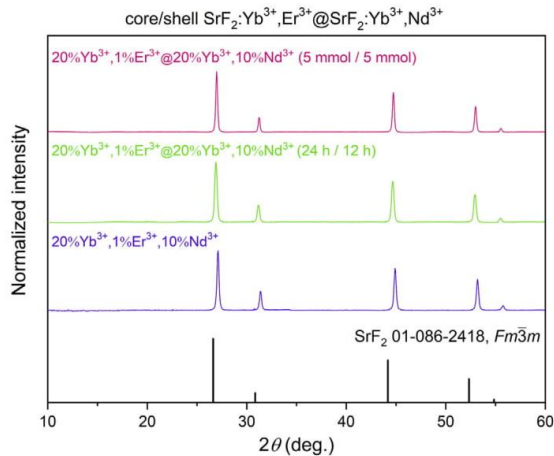


Fig. 2. XRD patterns of SrF_2 core/shell samples synthesized by hydrothermal method.

The DLS measurements confirmed the particle growth and revealed an additional tendency of the agglomeration of NPs.

The size of the presented NPs was also confirmed by analysis of TEM pictures for the core samples as well as for the core/shells (Figs. 3 and S5). The structure obtained from synthesis for 5 mmol of the product shows an irregular shape for both the core and core/shells, with sizes of 47 and 61 nm respectively. A reduction of the precursors' concentration and time of the 2nd step resulted in NPs with a more regular spherical shape and a lower size distribution (27 and 45 nm for core and core/shell, respectively).

To examine the surface of the particles, FT-IR spectra and zeta potentials were measured (for details see Fig. S6 and Table S3). The presence of citrate groups on the NPs surface was detected from the appearance of the signals assigned to the following types of vibrations: $-\text{OH}$ stretching vibration (3457 cm^{-1}), $-\text{CH}$ asymmetric

and symmetric stretching vibrations (2962 and 2840 cm^{-1}), $-\text{C}=\text{O}$ stretching vibrations (1622 cm^{-1}) and $-\text{CH}$ scissoring (1400 cm^{-1}). Furthermore, there was no significant shift in signals between the core and core/shell samples which indicates the lack of impact of the second step of synthesis on the surface of the nanoparticles. Moreover, samples exhibited a negative charge on the surface and usually, the cores had a higher negative charge than the core/shells, from -28.6 mV to -20.7 mV , and from -20.6 mV to -16.7 mV , respectively. The small difference between the presented values confirms similar stability in water of the prepared cores and core/shells structures and their tendency to agglomerate due to a not very high potential. Furthermore, an additional amount of Ln^{3+} ions in the structure of NPs can reduce the negative charge of NPs. Also, the growth of NPs can influence their charge, which may be responsible for observed differences between core and core/shells as electrostatic interaction between NPs decrease [71]. However, for a few samples differences between zeta potentials for core and core/shell are within the margin of measurement error.

It is very important to properly determine the elemental composition of the obtained products and confirm the core/shell structure. The existence of a core/shell structure can be assumed by the observed increase in the size of NPs after 2nd step of the synthesis, which is shown in Table 2 and S2. However, quantitative elemental analysis of the core/shell structures is difficult [27]. In this work, the ICP-MS technique was used for this purpose (see Table S4 for details). This method confirmed the coexistence of Sr^{2+} , Nd^{3+} , Er^{3+} , Yb^{3+} , and F^- ions in all the core/shell samples with only a slight difference between them.

3.2. Spectroscopic properties

To investigate the spectroscopic properties of the synthesized NPs, their excitation and emission spectra, as well as chromaticity diagrams, decay times and dependence of luminescence intensity on laser power were measured. Analysis of UC and DC properties is the most reliable method to confirm the successful doping with Ln^{3+} ions and the formation of the core/shell structure. In Fig. 4a excitation spectra of two the best emitting samples are presented together with the triple-doped core sample. In the spectra, several

Table 2

Sizes of obtained NPs, calculated from the Scherrer's equation based on XRD analysis [70], hydrodynamic diameters determined by DLS measurements, and NPs diameters taken from TEM images.

Sample	Scherrer equation (nm)		Hydrodynamic diameter (nm)		TEM images (nm)	
	Core	Core/shell	Core	Core/shell	Core	Core/shell
$20\%\text{Yb}^{3+}, 1\%\text{Er}^{3+}@\text{20}\%\text{Yb}^{3+}, 10\%\text{Nd}^{3+}$ (5 mmol/5 mmol)	49.2 ± 0.6	59.3 ± 0.9	76.9 ± 27.3	230.4 ± 93.0	47.1 ± 9.8	60.5 ± 12.3
$20\%\text{Yb}^{3+}, 1\%\text{Er}^{3+}@\text{20}\%\text{Yb}^{3+}, 10\%\text{Nd}^{3+}$ (24 h/12 h)	30.9 ± 0.9	41.9 ± 0.4	68.6 ± 20.3	158.7 ± 59.2	26.6 ± 4.3	45.3 ± 8.5
$20\%\text{Yb}^{3+}, 1\%\text{Er}^{3+}, 10\%\text{Nd}^{3+}$	35.6 ± 0.3	—	84.2 ± 29.5	—	34.7 ± 8.4	—

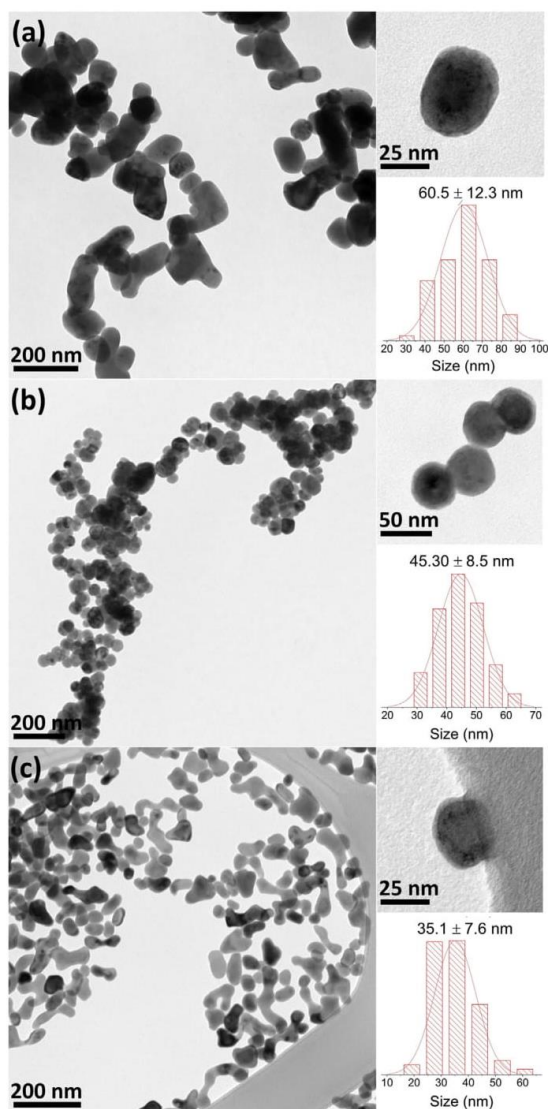


Fig. 3. TEM pictures and NPs size distributions of hydrothermally synthesized (a) $\text{SrF}_2:20\%\text{Yb}^{3+}, 1\%\text{Er}^{3+}@20\%\text{Yb}^{3+}, 10\%\text{Nd}^{3+}$ (5 mmol/5 mmol), (b) $\text{SrF}_2:20\%\text{Yb}^{3+}, 1\%\text{Er}^{3+}@20\%\text{Yb}^{3+}, 10\%\text{Nd}^{3+}$ (24 h/12 h), and (c) $\text{SrF}_2:20\%\text{Yb}^{3+}, 1\%\text{Er}^{3+}, 10\%\text{Nd}^{3+}$.

excitation bands are visible as a result of the presence of Yb^{3+} and Nd^{3+} ions. Four possible wavelengths can be used for the sample's excitation, i.e. 796, 802, and 866 nm, connected with Nd^{3+} transitions: $^2\text{H}_{9/2} \rightarrow ^4\text{I}_{9/2}$, $^4\text{F}_{5/2} \rightarrow ^4\text{I}_{9/2}$ and $^4\text{F}_{3/2} \rightarrow ^4\text{I}_{9/2}$ respectively, or 976 nm as a result of $^4\text{F}_{5/2} \rightarrow ^4\text{F}_{7/2}$ transition of Yb^{3+} ions. The sample $\text{SrF}_2:20\%\text{Yb}^{3+}, 1\%\text{Er}^{3+}@20\%\text{Yb}^{3+}, 10\%\text{Nd}^{3+}$ prepared from 5 mmol of product, with $3 \times$ excess of NH_4F during 24 h synthesis (1st and 2nd step), shows a higher emission and excitation intensity than the others. What is more, the strongest excitation band was registered for $^4\text{F}_{5/2} \rightarrow ^4\text{F}_{7/2}$ transition of Yb^{3+} ions, which is consistent with the highest emission intensity under

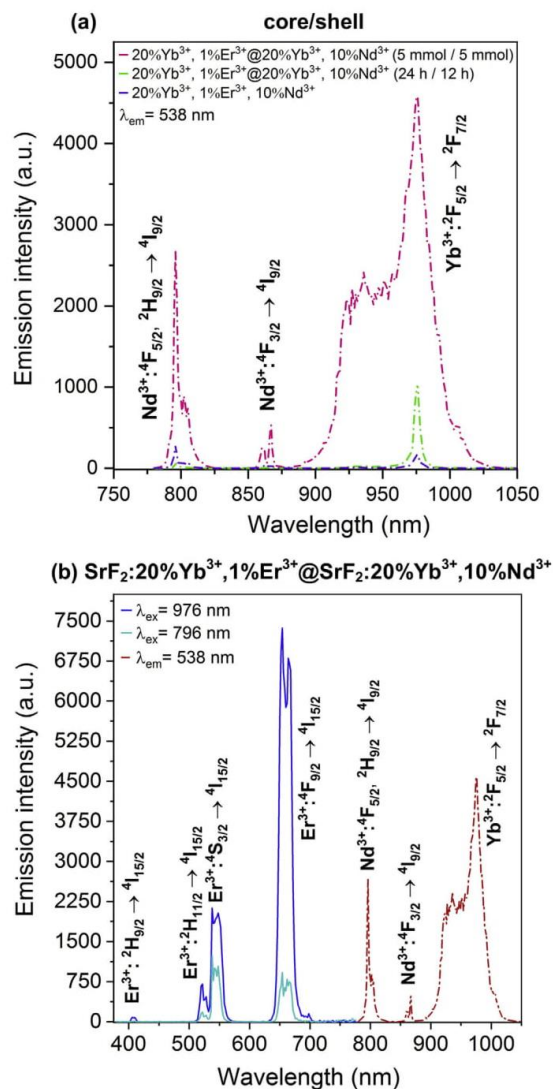


Fig. 4. (a) Excitation spectra of prepared samples and (b) emission spectra under different excitation wavelengths of $\text{SrF}_2:20\%\text{Yb}^{3+}, 1\%\text{Er}^{3+}@20\%\text{Yb}^{3+}, 10\%\text{Nd}^{3+}$, (5 mmol/5 mmol) sample. Spectra were obtained under pulsed excitation source (at 25 mJ cm^{-2}).

976 nm excitation (Fig. 4b). However, the emission under 796 nm excitation is also relatively intense. The difference between the emission intensities through excitation by Yb^{3+} ions and Nd^{3+} can be as a result of the quenching of Er^{3+} ions due to back energy transfer ($\text{Nd}^{3+} \rightarrow \text{Yb}^{3+} \rightarrow \text{Er}^{3+} \rightarrow \text{Nd}^{3+}$) [72]. It is worth noting that after the 2nd step of the synthesis, a significant enhancement of luminescence was obtained (see Figs. S7 and S8) due to the protective shell covering, which is characteristic for core/shell structures.

Emission spectra were also measured using a continuous laser as an excitation source (808, 975, and 1532 nm wavelengths) which

are presented in Fig. 5 and S9. From all excitation wavelengths, the highest UC emission was measured under 975 nm excitation. Furthermore, from the core, as well as core/shell samples, the sample prepared for 5 mmol of product in the 1st and 2nd step of synthesis showed the brightest emission when 975 nm wavelength was used, which results from the largest NPs and hence, a lower surface-related quenching.

The most visible difference between the core and core/shell NPs is shown in Fig. 5c where the separation of Nd^{3+} ions from the core allowed for an almost 15 times higher emission intensity under 808 nm excitation than that for the bare analogs, in which all dopant ions are in the same phase. The registered quenching effect in the triple-doped NPs is very strong and can be as a result of the high concentration of Nd^{3+} ions. Hence, the shortened distance between the sensitizer and luminescent ions leads to cross-relaxation between lanthanide ions. The unfavorable effect of triple-doping is visible in all the measured spectra presented in Fig. 5a–c. These results confirmed the sense and advantages of the synthesis of core/shell structures for applications in 808 nm sensitized UC.

Based on the collected emission spectra, the better emission properties under 975 nm excitation can be obtained during the synthesis of 5 mmol of the reaction product, 3 × excess of NH_4F , and 24 h of reaction for the core and core/shell NPs. However, under 808 nm excitation wavelength, the sample obtained from 2 mmol

of product and 2 × excess of NH_4F for the core and core/shell synthesis, where the time of 1st step is 24 h and 2nd is 12 h, shows a more effective emission in the visible region than the above-mentioned sample.

The prepared samples also showed a DC phenomenon under 808 nm or 975 nm excitation wavelengths (Fig. 5d and e, S10). As a result, the emission of Yb^{3+} and Er^{3+} in the NIR region (second, 1000–1400 nm, and third biological window, 1500–1700 nm) [33,73] was detected. What is interesting, the strongest luminescence of Er^{3+} ions under 975 nm excitation was observed for core samples, ($^4\text{I}_{13/2} \rightarrow ^4\text{I}_{15/2}$ transition). A lower luminescence of Er^{3+} ions in the NIR range for core/shell NPs indicates two effects: a more probable radiative relaxation of Er^{3+} ions from higher energy levels ($^2\text{H}_{9/2}$, $^2\text{H}_{11/2}$, $^4\text{S}_{3/2}$, $^4\text{F}_{9/2}$), and a lower concentration of Er^{3+} ions in the volume of measured powdered sample as a result of the addition of shell to core NPs. The emission of Yb^{3+} ions under 975 nm excitation is very similar for both the core as well as the core/shell sample. Excitation with 808 nm also resulted in the emission of Er^{3+} as an effect of the energy migration process. Because Er^{3+} ions can also absorb light at 808 nm due to $^4\text{I}_{15/2} \rightarrow ^4\text{I}_{9/2}$ transition, core NPs, doped only with Yb^{3+} and Er^{3+} , showed weak emission under 808 nm laser radiation. However, the presence of Nd^{3+} ions in the shell significantly increased the emission at around 1525 nm associated with Er^{3+} ions (Fig. 5d). When all of the Ln^{3+} ions are in the same phase, a weak emission

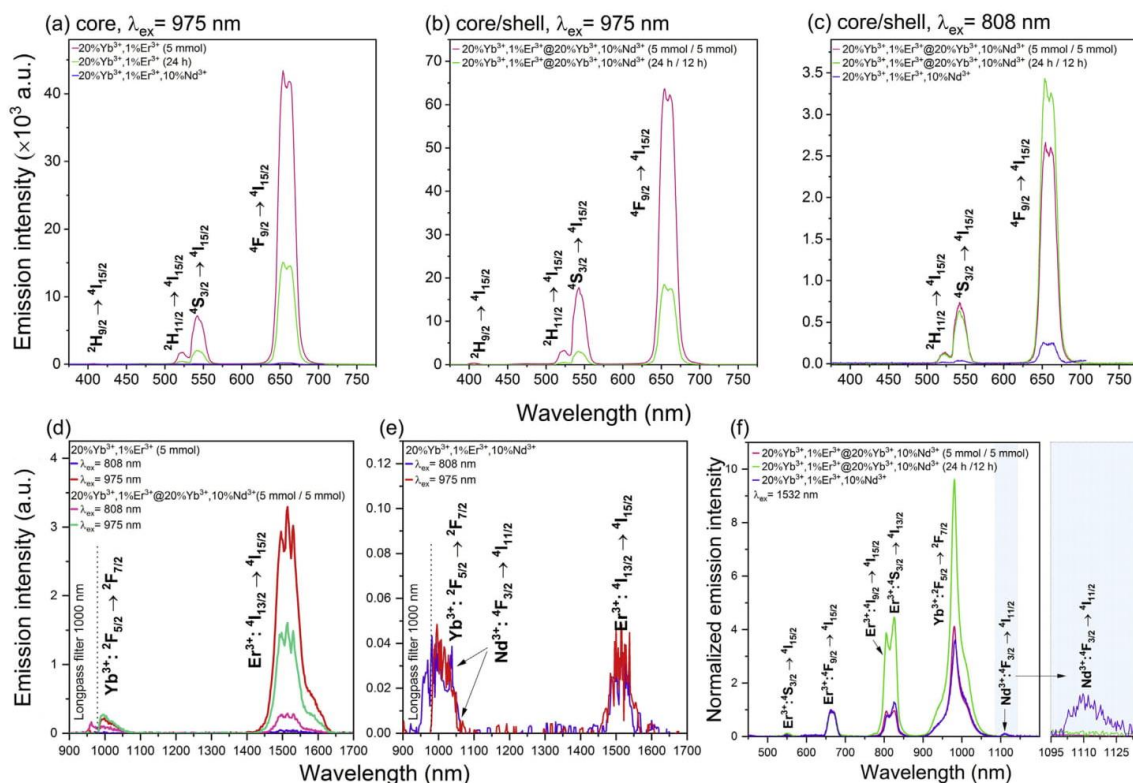


Fig. 5. (a–c) Up-conversion and (d,e) down-conversion emission of selected NPs ($\text{SrF}_2:20\%\text{Yb}^{3+},1\%\text{Er}^{3+}@/\text{SrF}_2:20\%\text{Yb}^{3+},10\%\text{Nd}^{3+}$, (5 mmol/5 mmol) and $\text{SrF}_2:20\%\text{Yb}^{3+},1\%\text{Er}^{3+},10\%\text{Nd}^{3+}$) sample in the Vis and NIR range under excitation with 808 or 975 nm CW laser light; (f) up-conversion luminescence of selected samples under excitation with 1532 nm CW laser light, normalized to $^4\text{F}_{9/2} \rightarrow ^4\text{I}_{15/2}$ emission band of Er^{3+} ions. Laser powers: (a–c) 15 W cm^{-2} for 808 and 975 nm, (d, e) 22, 27, or 61 W cm^{-2} for 808, 975, and 1532 nm respectively.

from Nd^{3+} ions (${}^4\text{F}_{3/2} \rightarrow {}^4\text{I}_{11/2}$) is also observed when 808 nm excitation is applied (Fig. 5e). The reason for such a result is the ineffective energy transfer to Er^{3+} ions resulting in a higher number of Nd^{3+} remaining in their excited state. The lack of energy migration to Er^{3+} ions through Yb^{3+} ions caused the radiative relaxation of Nd^{3+} ions with an associated luminescence (see Fig. 5e). In the core/shell structures, the back-energy transfer to Nd^{3+} ions is ineffective due to the separation of Nd^{3+} ions from Er^{3+} ions.

Up-conversion luminescence of prepared NPs was also observed under 1532 nm excitation (Fig. 5f). However, we utilized this excitation wavelength mainly to confirm the formation of core/shell structures. The applied laser wavelength is absorbed only by Er^{3+} ions through the ${}^4\text{I}_{15/2} \rightarrow {}^4\text{I}_{12/2}$ transition. Therefore, if cross-relaxation between Er^{3+} and Nd^{3+} occurs, emission from the latter one is observed. This process involves excitation of Er^{3+} to at least the ${}^4\text{I}_{9/2}$ level (absorption of two 1532 nm photons) and the energy transfer to ${}^2\text{H}_{9/2}$ excited state of the Nd^{3+} ions what is not possible through Yb^{3+} ions bridging the core and shell phases in core/shell NPs. The emission from Nd^{3+} ions around 1100 nm was only detected when all three Ln^{3+} dopants were present in a single core NPs (20% Yb^{3+} , 1% Er^{3+} and 10% Nd^{3+}). In the core/shell structures, the emission of Nd^{3+} was not observed which confirms the assumed structures.

The luminescence color of the prepared samples was dependent upon the excitation laser type (for chromaticity diagrams see Fig. S11 and ratios between luminescence bands in Fig. S12). Under a continuous excitation source with 808 and 975 nm, all samples exhibited a yellowish-orange emission with a small shift into the red region after covering core NPs with a shell. The use of pulsed laser as an excitation source resulted in green to orange emission of samples, depending on the synthesis conditions and concentration of dopant ions. Moreover, the use of 796 nm excitation light resulted in a green emission, whereas at 975 nm, this was yellowish-green as seen by the human eye. The result may indicate a different mechanism of Er^{3+} ion's excitation.

More information about the synthesized core/shell structures can be established based on emission lifetimes, calculated from decay time measurements (Fig. 6 and S13, Table 3, S4). It can be clearly seen that after shell covering, the lifetimes are longer than for the core particles. Extension of lifetimes is connected with the surface protective effect, minimizing quenching and decreasing the cross-relaxation processes between ions because of longer distances between them [49,74,75]. $\text{SrF}_2:20\%\text{Yb}^{3+},1\%\text{Er}^{3+},10\%\text{Nd}^{3+}$ NPs had a very short decay time which indicates, similar to the luminescence measurements, the quenching effect of Nd^{3+} ions due to the cross-relaxation process. Additionally, a higher concentration of Nd^{3+} in a shell (20%) quenches the luminescence intensity as well as decreases the lifetimes ($\text{SrF}_2:20\%\text{Yb}^{3+},1\%\text{Er}^{3+}@ \text{SrF}_2:20\%\text{Yb}^{3+},20\%\text{Nd}^{3+}$, $2 \times \text{NH}_4\text{F}/2 \times \text{NH}_4\text{F}$, Fig. S13, Table S4). Analogous lifetimes for prepared NPs were calculated for 808 nm excitation, confirming effective transfer between $\text{Nd}^{3+} \rightarrow \text{Yb}^{3+} \rightarrow \text{Yb}^{3+} \rightarrow \text{Er}^{3+}$ ions.

Important information about UC mechanism under 808 nm and 975 nm excitation, and the difference between them for prepared NPs, can be obtained from measurements of dependences of the luminescence intensity on the laser power. The number of photons can be estimated from the equation [76]:

$$I \propto P^n \quad (1)$$

where I is the UC intensity, P the pumping excitation power density, and n is the number of photons required to populate the excited state. The results of the calculations are collected in Table 4 (additionally Table S5 and for measurement results see Fig. S14).

Measurements have been distinguished by core and core/shell samples as well as the length of excitation wavelength (808 or 975 nm) and observed transitions. When we consider the two-photon excitation process of ${}^2\text{H}_{11/2}$, ${}^4\text{S}_{3/2}$, ${}^4\text{F}_{9/2}$, energy level, for samples doped with Yb^{3+} and Er^{3+} , the slope values are higher than one, which agrees with theoretical assumptions. An increase of slope value is especially observed for core/shell samples prepared from 5 mmol of precursors, under 975 nm excitation, in comparison to core ones. However, under 808 nm excitation, the slope coefficients have a lower value than under 975 nm excitation (from 0.81 to 1.89). The reason for this could be connected with energy transfer through intermediate Yb^{3+} ions, which has an influence on increasing the possibility of cross-relaxation occurring between ions, and the saturation effect, which is especially visible for the ${}^4\text{F}_{9/2} \rightarrow {}^4\text{I}_{15/2}$ transition. Furthermore, the triple-doped core sample has a significantly lower slope value than the other two samples. Additionally, for the sample prepared from 5 mmol of Ln^{3+} precursor (1st and 2nd step), the slope coefficient was also calculated for a three-photon process- ${}^2\text{H}_{9/2} \rightarrow {}^4\text{I}_{15/2}$ transition.

Based on the spectroscopic studies of synthesized NPs, the UC as well DC mechanisms are proposed for core/shell NPs in Fig. 7 (see Fig. S15 for a scheme of energy processes in core NPs). To observe UC emission, three different excitation wavelengths may be used. The first possibility of Er^{3+} ions excitation is the energy transfer from Yb^{3+} ions being excited by 975 nm laser radiation. This process is known as energy transfer up-conversion (ETU). All of the Yb^{3+} ions incorporated into the core, as well as the shell, can effectively absorb exciting radiation. When sensitizer ions are placed in the core, after excitation of Yb^{3+} ions to the ${}^2\text{F}_{5/2}$ energy level, energy is transferred directly to the ${}^4\text{I}_{11/2}$ excited state of Er^{3+} ions. Another possibility is the migration of energy between the core and shell phases among Yb^{3+} ions [77,78]. The second excitation pathway is possibly due to doping with Nd^{3+} ions which are capable of absorption of the 808 nm excitation radiation. After absorption of photons by Nd^{3+} ions and their excitation to the ${}^4\text{F}_{5/2}$ level, relaxation to ${}^4\text{F}_{3/2}$ occurs at the first step. Then, energy transfer to Er^{3+} ions is possible via Yb^{3+} ions, i.e. $\text{Nd}^{3+}(\text{shell}) \rightarrow \text{Yb}^{3+}(\text{shell}) \rightarrow \text{Yb}^{3+}(\text{core}) \rightarrow \text{Er}^{3+}(\text{core})$. This process is known as energy migration up-conversion (EMU).

Another possibility is the direct excitation of Er^{3+} ions under 1532 nm laser light. As a result of photons absorption, excitation from the ${}^4\text{I}_{15/2}$ ground state of Er^{3+} ions to their ${}^4\text{I}_{13/2}$ excited state occurs (ground state absorption, GSA) and next, to higher excited states, yielding Er^{3+} in their ${}^2\text{H}_{11/2}$ excited state (excited state absorption, ESA). Furthermore, energy transfer from Er^{3+} to Yb^{3+} ions is possible resulting in the emission at around 980 nm.

Moreover, under 975 nm and 808 nm excitations, DC in the NIR region was registered for the core as well as for the core/shell structures. Similar to the UC, energy transfer between Yb^{3+} and Er^{3+} ions was responsible for the emission of Er^{3+} at around 1525 nm. Additionally, a partial back energy transfer from Yb^{3+} in the core, to Yb^{3+} in the shell, can be observed with the occurred luminescence ($\text{Yb}^{3+}; {}^2\text{F}_{5/2} \rightarrow {}^2\text{F}_{7/2}$). A similar process, through excitation under 808 nm by Nd^{3+} ions with mediated energy transfer ($\text{Nd}^{3+} \rightarrow \text{Yb}^{3+} \rightarrow \text{Yb}^{3+} \rightarrow \text{Er}^{3+}$), was also observed.

Additionally, for the prepared triple-doped core sample, (Nd^{3+} , Er^{3+} , Yb^{3+}) a mechanism for the energetic processes is proposed (Fig. S15). Hence, UC emission of Er^{3+} can be obtained under 808 nm, 975 nm, and 1532 nm excitation wavelengths. However, in this sample, a different mechanism of excitation via Nd^{3+} ions can occur. Energy can be directly transferred from Nd^{3+} to activator ions ($\text{Nd}^{3+}; {}^4\text{F}_{5/2} \rightarrow \text{Er}^{3+}; {}^4\text{I}_{11/2}$) or by energy migration transfer ($\text{Nd}^{3+} \rightarrow \text{Yb}^{3+} \rightarrow \text{Er}^{3+}$). Also, under direct excitation of Er^{3+} ions ($\lambda_{\text{ex}} = 1532 \text{ nm}$), an additional emission from Nd^{3+} ions can be observed ($\text{Nd}^{3+}; {}^4\text{F}_{3/2} \rightarrow {}^4\text{I}_{11/2}$) as the result of energy transfer from

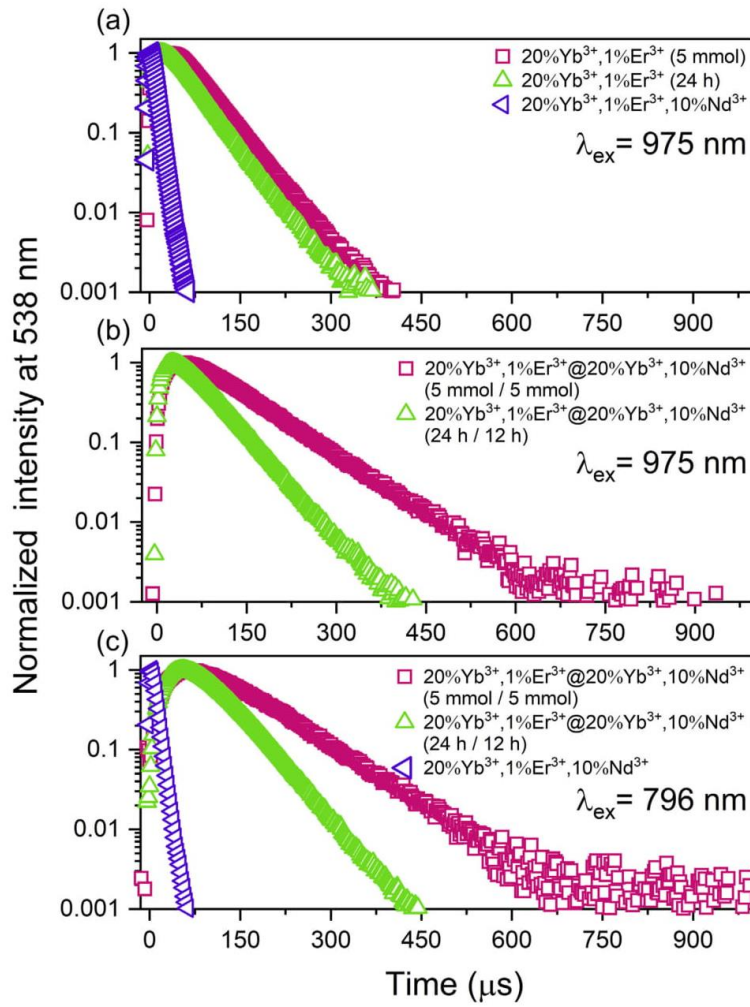


Fig. 6. Decay times of the two best emitting core/shell NPs, and the triple-doped sample for comparison, measured at 538 nm for the $^4S_{3/2} \rightarrow ^4I_{15/2}$ transition of Er^{3+} ions, under pulsed excitation source (at 25 mJ cm^{-2}).

Table 3

Emission lifetimes calculated from the measured luminescence decays of core and core/shell samples under 796 nm or 976 nm pulsed laser excitations (at 25 mJ cm^{-2}) (for decays see Fig. S13, err <1.1 μs).

Sample	Lifetimes (μs)								
	core			core/shell					
	$\lambda_{\text{ex}} = 975 \text{ nm}$			$\lambda_{\text{ex}} = 975 \text{ nm}$			$\lambda_{\text{ex}} = 796 \text{ nm}$		
	$^2H_{11/2}$ 2 \rightarrow $^4I_{15/2}$	$^4S_{3/2}$ 2 \rightarrow $^4I_{15/2}$	$^4F_{9/2}$ 2 \rightarrow $^4I_{15/2}$	$^2H_{11/2}$ 2 \rightarrow $^4I_{15/2}$	$^4S_{3/2}$ 2 \rightarrow $^4I_{15/2}$	$^4F_{9/2}$ 2 \rightarrow $^4I_{15/2}$	$^2H_{11/2}$ 2 \rightarrow $^4I_{15/2}$	$^4S_{3/2}$ 2 \rightarrow $^4I_{15/2}$	$^4F_{9/2}$ 2 \rightarrow $^4I_{15/2}$
20%Yb $^{3+}$, 1%Er $^{3+}$ @20%Yb $^{3+}$, 10%Nd $^{3+}$ (5 mmol / 5 mmol)	53	48	256	98	99	376	113	110	306
20%Yb $^{3+}$, 1%Er $^{3+}$ @20%Yb $^{3+}$, 10%Nd $^{3+}$ (24 h / 12 h)	47	49	245	60	64	250	66	67	217
20%Yb $^{3+}$, 1%Er $^{3+}$, 10%Nd $^{3+}$	9	9	52	—	—	—	9	9	56

Table 4

The number of photons involved in the UC mechanism, determined from the dependences of luminescence intensity on laser power for core and core/shell NPs under 808 nm and 975 nm continuous laser excitation wavelengths (for experimental results see Fig. S14, err < 0.05).

Sample	Number of photons											
	core				core/shell							
	$\lambda_{\text{ex}} = 975 \text{ nm}$				$\lambda_{\text{ex}} = 975 \text{ nm}$				$\lambda_{\text{ex}} = 808 \text{ nm}$			
	$^2\text{H}_{9/2} \rightarrow ^4\text{I}_{15/2}$	$^2\text{H}_{11/2} \rightarrow ^4\text{I}_{15/2}$	$^4\text{S}_{3/2} \rightarrow ^4\text{I}_{15/2}$	$^4\text{F}_{9/2} \rightarrow ^4\text{I}_{15/2}$	$^2\text{H}_{9/2} \rightarrow ^4\text{I}_{15/2}$	$^2\text{H}_{11/2} \rightarrow ^4\text{I}_{15/2}$	$^4\text{S}_{3/2} \rightarrow ^4\text{I}_{15/2}$	$^4\text{F}_{9/2} \rightarrow ^4\text{I}_{15/2}$	$^2\text{H}_{9/2} \rightarrow ^4\text{I}_{15/2}$	$^2\text{H}_{11/2} \rightarrow ^4\text{I}_{15/2}$	$^4\text{S}_{3/2} \rightarrow ^4\text{I}_{15/2}$	$^4\text{F}_{9/2} \rightarrow ^4\text{I}_{15/2}$
20%Yb ³⁺ , 1%Er ³⁺ @20%Yb ³⁺ , 10%Nd ³⁺ (5 mmol/5 mmol)	0.96	1.64	1.29	1.35	2.41	2.12	1.88	2.89	0.81	1.60	1.37	1.89
20%Yb ³⁺ , 1%Er ³⁺ @20%Yb ³⁺ , 10%Nd ³⁺ (24 h/12 h)	—	2.21	2.08	2.08	1.96	2.22	2.05	2.02	—	1.64	1.35	1.52
20%Yb ³⁺ , 1%Er ³⁺ , 10%Nd ³⁺	—	0.62	0.72	1.48	—	—	—	—	—	1.14	0.84	1.03

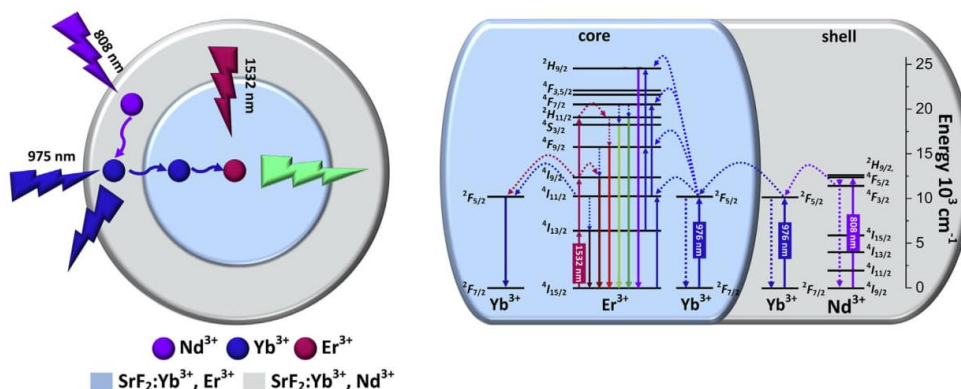


Fig. 7. Scheme of energetic processes taking place in for SrF₂:Yb³⁺, Er³⁺@SrF₂:Yb³⁺, Nd³⁺ core/shell systems, under NIR excitation ($\lambda_{\text{ex}} = 808, 975, \text{ or } 1532 \text{ nm}$).

Er³⁺ to Nd³⁺ ions, which is neglected in the core/shell structures. However, due to the shortened distance between the sensitizer and activator, significant emission quenching and a strong cross-relaxation process were observed.

4. Conclusions

We have successfully synthesized SrF₂:Yb³⁺, Er³⁺@SrF₂:Yb³⁺, Nd³⁺ core/shell NPs, by a two-step hydrothermal method. The synthesis procedure was optimized considering the spectroscopic properties as well as the morphology of NPs. The effects of different variables, such as the amount of precursors or time of reaction, were investigated. The developed procedure allowed for the synthesis of small, single-phase NPs with sizes between 30 and 60 nm, depending on the synthesis conditions. NPs formed stable water colloids with negatively charged surfaces, and hydrodynamic diameters between 80 and 230 nm. Intense emission under 808, 975, and 1532 nm was observed in the visible as well as NIR range (up- and down-conversion). The processes taking place in the core/shell structures were investigated by measuring excitation and emission spectra, power dependences, and luminescence decays under continuous or pulsed excitation sources. We have proved the existence of core/shell structures by selectively exciting Er³⁺ ions and the observation of cross-relaxation effects with Nd³⁺ emissions as a result. The lack of such process in the core/shell NPs, where Er³⁺ and Nd³⁺ were separated in two phases, and, at the same time, detected emission of Nd³⁺ ions when Er³⁺, Yb³⁺ and Nd³⁺ ions were in one phase, confirmed the successful formation of core/shell NPs via the hydrothermal process. The spectroscopic properties of the synthesized NPs are promising for

biomedical applications for deep tissue imaging as the emission can be obtained via excitation within biological windows (808 and 1532 nm), as well as for energy conversion in solar cells where all three excitation wavelengths fall in the range not absorbed by Si-based cells.

Declaration of competing interest

The authors declare that they have no known competing financial interests or personal relationships that could have appeared to influence the work reported in this paper.

CRediT authorship contribution statement

Dominika Przybylska: Conceptualization, Investigation, Writing - original draft, Visualization. **Tomasz Grzyb:** Conceptualization, Resources, Writing - review & editing, Visualization, Supervision.

Acknowledgements

Funding for this research was provided by the National Science Centre, Poland, under grants 2016/21/B/ST8/00477, 2016/22/E/ST5/00016 and 2017/27/N/ST5/02149.

Appendix A. Supplementary data

Supplementary data to this article can be found online at <https://doi.org/10.1016/j.jallcom.2020.154797>.

References

- [1] N. Bloembergen, Solid state infrared quantum counters, *Phys. Rev. Lett.* 2 (1959) 84–85, <https://doi.org/10.1103/PhysRevLett.2.84>.
- [2] F. Auzel, Compteur quantique par transfert d'énergie entre de Yb^{3+} a Tm^{3+} dans un tungstate mixte et dans verre germanate, *C. R. Acad. Sci. Paris B.* 263 (1966) 819–821.
- [3] F. Wang, D. Banerjee, Y. Liu, X. Chen, X. Liu, Upconversion nanoparticles in biological labeling, imaging, and therapy, *Analyst* 135 (2010) 1839–1854, <https://doi.org/10.1039/c0an00144a>.
- [4] Y. Il Park, H.M. Kim, J.H. Kim, K.C. Moon, B. Yoo, K.T. Lee, N. Lee, Y. Choi, W. Park, D. Ling, K. Na, W.K. Moon, S.H. Choi, H.S. Park, S.-Y. Yoon, Y.D. Suh, S.H. Lee, T. Hyeon, Theranostic probe based on lanthanide-doped nanoparticles for simultaneous in vivo dual-modal imaging and photodynamic therapy, *Adv. Mater.* 24 (2012) 5755–5761, <https://doi.org/10.1002/adma.201202433>.
- [5] S. Wang, J. Feng, S. Song, H. Zhang, Rare earth fluorides upconversion nanophosphors: from synthesis to applications in bioimaging, *CrystEngComm* 15 (2013) 7142, <https://doi.org/10.1039/c3ce40679b>.
- [6] D. Tu, Y. Liu, H. Zhu, X. Chen, Optical/magnetic multimodal bioprobes based on lanthanide-doped inorganic nanocrystals, *Chem. Eur. J.* 19 (2013) 5516–5527, <https://doi.org/10.1002/chem.201204640>.
- [7] G. Chen, H. Qiu, P.N. Prasad, X. Chen, Upconversion nanoparticles: design, nanochemistry, and applications in theranostics, *Chem. Rev.* 114 (2014) 5161–5214, <https://doi.org/10.1021/cr400425h>.
- [8] L.-D. Sun, Y.-F. Wang, C.-H. Yan, Paradigms and challenges for bioapplication of rare earth upconversion luminescent nanoparticles: small size and tunable emission/excitation spectra, *Acc. Chem. Res.* 47 (2014) 1001–1009, <https://doi.org/10.1021/ar400218t>.
- [9] A. Rapaport, J. Milliez, M. Bass, A. Cassanho, H. Janssen, Review of the properties of Up-conversion phosphors for new emissive displays, *IEEE/OSA J. Disp. Technol.* 2 (2006) 68–78, <https://doi.org/10.1109/JDT.2005.863781>.
- [10] T.R. Hinklin, S.C. Rand, R.M. Laine, Transparent, polycrystalline upconverting nanoceramics: towards 3-D displays, *Adv. Mater.* 20 (2008) 1270–1273, <https://doi.org/10.1002/adma.200701235>.
- [11] W.G. van Sark, J. de Wild, J.K. Rath, A. Meijerink, R.E. Schropp, Upconversion in solar cells, *Nanoscale Res. Lett.* 8 (2013) 81, <https://doi.org/10.1186/1556-276X-8-81>.
- [12] B.M. van der Ende, L. Aarts, A. Meijerink, Lanthanide ions as spectral converters for solar cells, *Phys. Chem. Chem. Phys.* 11 (2009) 11081, <https://doi.org/10.1039/b913877c>.
- [13] R. Ma, R. Shimmom, A. McDonagh, P. Maynard, C. Lennard, C. Roux, Fingerprint detection on non-porous and semi-porous surfaces using $\text{YVO}_4:\text{Er}, \text{Yb}$ luminescent upconverting particles, *Forensic Sci. Int.* 217 (2012) e23–e26, <https://doi.org/10.1016/j.forsciint.2011.10.033>.
- [14] C.M. Liu, L.Y. Zhang, L. Li, B.Y. Li, C.G. Wang, T.T. Wang, Specific detection of latent human blood fingerprints using antibody modified $\text{NaYF}_4:\text{Yb}, \text{Er}, \text{Cd}$ fluorescent upconversion nanorods, *Dyes Pigments* 149 (2018) 822–829, <https://doi.org/10.1016/j.dyepig.2017.11.050>.
- [15] M. Runowski, J.J. Marciniak, T. Grzyb, D. Przybylska, A. Shyichuk, B. Barszcz, A. Katrusiak, S. Lis, Lifetime nanomanometry - high-pressure luminescence of up-converting lanthanide nanocrystals - $\text{SrF}_2:\text{Yb}^{3+}, \text{Er}^{3+}$, *Nanoscale* 9 (2017) 16030–16037, <https://doi.org/10.1039/c7nr04353h>.
- [16] F. Auzel, Upconversion and anti-Stokes processes with f and d ions in solids, *Chem. Rev.* 104 (2004) 139–173, <https://doi.org/10.1021/cr020357g>.
- [17] J. Chen, J.X. Zhao, Upconversion nanomaterials: synthesis, mechanism, and applications in sensing, *Sensors* 12 (2012) 2414–2435, <https://doi.org/10.3390/s120302414>.
- [18] V. Mahalingam, J. Thirumalai, R. Krishnan, S. Mantha, Up/down conversion luminescence and charge compensation investigation of $\text{Ca}_{0.5}\text{Y}_{1-x}(\text{WO}_4)_2:\text{xLn}^{3+}$ ($\text{Ln} = \text{Pr}, \text{Sm}, \text{Eu}, \text{Tb}, \text{Dy}, \text{Yb}, \text{Er}$) phosphors, *Spectrochim. Acta Part A Mol. Biomol. Spectrosc.* 152 (2016) 172–180, <https://doi.org/10.1016/j.saa.2015.06.129>.
- [19] J.-C.G. Bünzli, C. Piguet, Taking advantage of luminescent lanthanide ions, *Chem. Soc. Rev.* 34 (2005) 1048–1077, <https://doi.org/10.1039/b406082m>.
- [20] L. Cheng, C. Wang, Z. Liu, Upconversion nanoparticles and their composite nanostructures for biomedical imaging and cancer therapy, *Nanoscale* 5 (2013) 23–37, <https://doi.org/10.1039/c2nr32311g>.
- [21] M.Z. Huang, B. Yuan, L. Dai, M.L. Fu, Toward NIR driven photocatalyst: fabrication, characterization, and photocatalytic activity of $\beta\text{-NaYF}_4:\text{Yb}^{3+}, \text{Tm}^{3+}/\text{g-C}_3\text{N}_4$ nanocomposite, *J. Colloid Interface Sci.* 460 (2015) 264–272, <https://doi.org/10.1016/j.jcis.2015.08.063>.
- [22] Z. Xue, X. Li, Y. Li, M. Jiang, G. Ren, H. Liu, S. Zeng, J. Hao, A 980 nm laser-activated upconverted persistent probe for NIR-to-NIR rechargeable in vivo bioimaging, *Nanoscale* 9 (2017) 7276–7283, <https://doi.org/10.1039/c6nr09716b>.
- [23] M.V. DaCosta, S. Doughan, Y. Han, U.J. Krull, Lanthanide upconversion nanoparticles and applications in bioassays and bioimaging: a review, *Anal. Chim. Acta* 832 (2014) 1–33, <https://doi.org/10.1016/j.aca.2014.04.030>.
- [24] M.H. Alkahtani, C.L. Gomes, P.R. Hemmer, Engineering water-tolerant core/shell upconversion nanoparticles for optical temperature sensing, *Opt. Lett.* 42 (2017) 2451, <https://doi.org/10.1364/OL.42.002451>.
- [25] Y.-F. Wang, G.-Y. Liu, L.-D. Sun, J.-W. Xiao, J.-C. Zhou, C.-H. Yan, Nd^{3+} -sensitized upconversion nanophosphors: efficient in vivo bioimaging probes with minimized heating effect, *ACS Nano* 7 (2013) 7200–7206, <https://doi.org/10.1021/nn402601d>.
- [26] B. Liu, C. Li, P. Yang, Z. Hou, J. Lin, 808-nm-Light-Excited lanthanide-doped nanoparticles: rational design, luminescence control and theranostic applications, *Adv. Mater.* 29 (2017), <https://doi.org/10.1002/adma.201605434>.
- [27] A. Hong, Y. Kim, T.S. Lee, S. Kim, K. Lee, G. Kim, H.S. Jang, Intense red-emitting upconversion nanophosphors (800 nm-driven) with a core/double-shell structure for dual-modal upconversion luminescence and magnetic resonance in vivo imaging applications, *ACS Appl. Mater. Interfaces* 10 (2018) 12331–12340, <https://doi.org/10.1021/acsami.7b18078>.
- [28] X. Li, R. Wang, F. Zhang, L. Zhou, D. Shen, C. Yao, D. Zhao, Nd^{3+} sensitized up/down converting dual-mode nanomaterials for efficient in-vitro and in-vivo bioimaging excited at 800 nm, *Sci. Rep.* 3 (2013) 3536, <https://doi.org/10.1038/srep03536>.
- [29] K. Prorok, M. Pawlyta, W. Stręk, A. Bednarkiewicz, Energy migration up-conversion of Tb^{3+} in Yb^{3+} and Nd^{3+} codoped active-core/active-shell colloidal nanoparticles, *Chem. Mater.* 28 (2016) 2295–2300, <https://doi.org/10.1021/acs.chemmater.6b00353>.
- [30] X. Xie, N. Gao, R. Deng, Q. Sun, Q. Xu, X. Liu, Mechanistic investigation of photon upconversion in Nd^{3+} -sensitized core-shell nanoparticles, *J. Am. Chem. Soc.* 135 (2013) 12608–12611, <https://doi.org/10.1021/ja4075002>.
- [31] S. Wen, J. Zhou, K. Zheng, A. Bednarkiewicz, X. Liu, D. Jin, Advances in highly doped upconversion nanoparticles, *Nat. Commun.* 9 (2018), <https://doi.org/10.1038/s41467-018-04813-5>.
- [32] L. Zeng, D. Wu, G. Lu, Y. Pan, J. Zhang, A. Wu, Y. Tian, Recent progress in 808 nm excited upconversion nanomaterials as multifunctional nanoprobes for visualized theranostics in cancers, *Curr. Med. Chem.* 25 (2017) 2954–2969, <https://doi.org/10.2174/0929867324666170320115959>.
- [33] X. Zhang, Z. Zhao, X. Zhang, D.B. Cordes, B. Weeks, B. Qiu, K. Madanan, D. Sardar, J. Chaudhuri, Magnetic and optical properties of $\text{NaGdF}_4:\text{Nd}^{3+}, \text{Yb}^{3+}, \text{Tm}^{3+}$ nanocrystals with upconversion/downconversion luminescence from visible to the near-infrared second window, *Nano Res* 8 (2015) 636–648, <https://doi.org/10.1007/s12274-014-0548-2>.
- [34] K. Wang, W. Qincheng, Y. Zhang, R. Qiao, S. Li, Z. Li, Synthesis of $\text{Nd}^{3+}/\text{Yb}^{3+}$ sensitized upconversion core-shell nanocrystals with optimized hosts and doping concentrations, *RSC Adv.* 5 (2015) 62899–62904, <https://doi.org/10.1039/C5RA09873D>.
- [35] M. Pokhrel, C. Valdes, Y. Mao, Ultraviolet upconversion enhancement in triply doped $\text{NaYF}_4:\text{Tm}^{3+}, \text{Yb}^{3+}$ particles: the role of Nd^{3+} or Gd^{3+} Co-doping, *Opt. Mater.* 58 (2016) 67–75, <https://doi.org/10.1016/j.optmat.2016.05.020>.
- [36] L. Tian, Z. Xu, S. Zhao, Y. Cui, Z. Liang, J. Zhang, X. Xu, The upconversion luminescence of $\text{Er}^{3+}/\text{Yb}^{3+}/\text{Nd}^{3+}$ triply-doped $\beta\text{-NaYF}_4$ nanocrystals under 808-nm excitation, *Materials* 7 (2014) 7289–7303, <https://doi.org/10.3390/ma7117289>.
- [37] J. Xu, M. Sun, Y. Kuang, H. Bi, B. Liu, D. Yang, R. Lv, S. Gai, F. He, P. Yang, Markedly enhanced up-conversion luminescence by combining IR-808 dye sensitization and core-shell-shell structures, *Dalton Trans.* 46 (2017) 1495–1501, <https://doi.org/10.1039/C6DT04529D>.
- [38] Y. Qin, Z. Dong, D. Zhou, Y. Yang, X. Xu, J. Qiu, Modification on populating paths of $\beta\text{-NaYF}_4:\text{Nd}/\text{Yb}/\text{Ho}/\text{SiO}_2/\text{Ag}$ core/double-shell nanocomposites with plasmon enhanced upconversion emission, *Opt. Mater. Express* 6 (2016) 1942, <https://doi.org/10.1364/ome.6.001942>.
- [39] S. Fischer, N.D. Bronstein, J.K. Swabeck, E.M. Chan, A.P. Alivisatos, Precise tuning of surface quenching for luminescence enhancement in core-shell lanthanide-doped nanocrystals, *Nano Lett.* 16 (2016) 7241–7247, <https://doi.org/10.1021/acs.nanolett.6b03683>.
- [40] X. Yin, H. Wang, Y. Tian, M. Xing, Y. Fu, X. Luo, Three primary color emissions from single multilayered nanocrystals, *Nanoscale* 10 (2018) 9673–9678, <https://doi.org/10.1039/c8nr01752b>.
- [41] Y. Zhang, X. Liu, Y. Lang, Z. Yuan, D. Zhao, G. Qin, W. Qin, Synthesis of ultra-small $\text{BaLuF}_5:\text{Yb}^{3+}, \text{Er}^{3+}/\text{BaLuF}_5:\text{Yb}^{3+}$ active-core-active-shell nanoparticles with enhanced up-conversion and down-conversion luminescence by a layer-by-layer strategy, *J. Mater. Chem. C* 3 (2015) 2045–2053, <https://doi.org/10.1039/C4TC02541E>.
- [42] X. Wang, J. Zhuang, Q. Peng, Y. Li, A general strategy for nanocrystal synthesis, *Nature* 437 (2005) 121–124, <https://doi.org/10.1038/nature03968>.
- [43] Y. Chen, B. Liu, X. Deng, S. Huang, Z. Hou, C. Li, J. Lin, Multifunctional Nd^{3+} -sensitized upconversion nanomaterials for synchronous tumor diagnosis and treatment, *Nanoscale* 7 (2015) 8574–8583, <https://doi.org/10.1039/C5NR00829H>.
- [44] M. Xia, D. Zhou, Y. Yang, Z. Yang, J. Qiu, Synthesis of ultrasmall hexagonal $\text{NaGdF}_4:\text{Yb}^{3+}, \text{Er}^{3+}/\text{NaGdF}_4:\text{Yb}^{3+}/\text{NaGdF}_4:\text{Nd}^{3+}$ active-core/active-shell/active-shell nanoparticles with enhanced upconversion luminescence, *ECS J. Solid State Sci. Technol.* 6 (2017) R41–R46, <https://doi.org/10.1149/2.0031704jss>.
- [45] B. Liu, Y. Chen, C. Li, F. He, Z. Hou, S. Huang, H. Zhu, X. Chen, J. Lin, Poly(Acrylic acid) modification of Nd^{3+} -sensitized upconversion nanophosphors for highly efficient UCL imaging and pH-responsive drug delivery, *Adv. Funct. Mater.* 25 (2015) 4717–4729, <https://doi.org/10.1002/adfm.201501582>.
- [46] B. Chen, F. Wang, $\text{NaYbF}_4/\text{CaF}_2$ core-satellite upconversion nanoparticles: one-pot synthesis and sensitive detection of glutathione, *Nanoscale* 10 (2018) 19898–19905, <https://doi.org/10.1039/c8nr05552a>.
- [47] X. Chen, D. Peng, Q. Ju, F. Wang, Photon upconversion in core-shell nanoparticles, *Chem. Soc. Rev.* 44 (2014) 1318–1330, <https://doi.org/10.1039/c4cs00151f>.
- [48] L. Lei, S. Xu, J. Yang, H.W.H. Lee, Power-dependent optical property of Yb/Er :

- NaGdF₄@Yb:NaGdF₄@Yb:NaNdF₄ nanocrystals, *Nano* 12 (2017) 1750086, <https://doi.org/10.1142/S1793292017500862>.
- [49] D. Wang, B. Xue, J. Song, J. Qu, Compressed energy transfer distance for remarkable enhancement of the luminescence of Nd³⁺-sensitized upconversion nanoparticles, *J. Mater. Chem. C* 6 (2018) 6597–6604, <https://doi.org/10.1039/c8tc00936h>.
- [50] Z. Xia, P. Du, L. Liao, Facile hydrothermal synthesis and upconversion luminescence of tetragonal Sr₂LnF₇:Yb³⁺/Er³⁺ (Ln = Y, Gd) nanocrystals, *Phys. Status Solidi Appl. Mater. Sci.* 210 (2013) 1734–1737, <https://doi.org/10.1002/pssa.201329114>.
- [51] J. Sun, J. Xian, H. Du, Hydrothermal synthesis of BaYF₅:Yb³⁺/Er³⁺ upconversion luminescence submicrospheres by a surfactant-free aqueous solution route, *J. Phys. Chem. Solid.* 72 (2011) 207–213, <https://doi.org/10.1016/j.jpcs.2010.12.013>.
- [52] A. Szczeszak, T. Grzyb, B. Barszcz, V. Nagirnyi, A. Kotlov, S. Lis, Hydrothermal synthesis and structural and spectroscopic properties of the new triclinic form of GdBO₃:Eu³⁺ nanocrystals, *Inorg. Chem.* 52 (2013) 4934–4940, <https://doi.org/10.1021/ic302525k>.
- [53] T. Grzyb, D. Przybylska, Formation mechanism, structural, and upconversion properties of alkaline rare-earth fluoride nanocrystals doped with Yb³⁺/Er³⁺ ions, *Inorg. Chem.* 57 (2018) 6410–6420, <https://doi.org/10.1021/acs.inorgchem.8b00484>.
- [54] M. Wang, G. Abbineni, A. Clevenger, C. Mao, S. Xu, Upconversion nanoparticles: synthesis, surface modification and biological applications, *Nanomaterials* 7 (2011) 710–729, <https://doi.org/10.1016/j.nano.2011.02.013>.
- [55] T. Jiang, W. Qin, J. Zhou, Citric acid-assisted phase controlled synthesis of NaYF₄:Yb³⁺, Tm³⁺ crystals and their intense ultraviolet upconversion emissions, *J. Fluor. Chem.* 156 (2013) 177–182, <https://doi.org/10.1016/j.jfluchem.2013.10.007>.
- [56] T. Grzyb, S. Balabhadra, D. Przybylska, M. Węclawiak, Upconversion luminescence in BaYF₅, BaGdF₅ and BaLuF₅ nanocrystals doped with Yb³⁺/Ho³⁺, Yb³⁺/Er³⁺ or Yb³⁺/Tm³⁺ ions, *J. Alloys Compd.* 649 (2015) 606–616, <https://doi.org/10.1016/j.jallcom.2015.07.151>.
- [57] S. Zanzoni, M. Pedroni, M. D'Onofrio, A. Speghini, M. Assfalg, Paramagnetic nanoparticles leave their mark on nuclear spins of transiently adsorbed proteins, *J. Am. Chem. Soc.* 138 (2016) 72–75, <https://doi.org/10.1021/jacs.5b11582>.
- [58] A.-H.H. Li, M. Lü, J. Yang, L. Chen, X. Cui, Z. Sun, Upconversion-luminescent/magnetic dual-functional sub-20 nm core-shell SrF₂:Yb,Tm@CaF₂:Gd heteronanoparticles, *Dalton Trans.* 45 (2016) 5800–5807, <https://doi.org/10.1039/c6dt00237d>.
- [59] P. Cortelletti, A. Skripka, C. Facciotti, M. Pedroni, G. Caputo, N. Pinna, M. Quintanilla, A. Benayas, F. Vetrone, A. Speghini, Tuning the sensitivity of lanthanide-activated NIR nanothermometers in the biological windows, *Nanoscale* 10 (2018) 2568–2576, <https://doi.org/10.1039/c7nr06141b>.
- [60] A.M. Pak, J.A. Ermakova, S.V. Kuznetsov, A.V. Ryabova, D.V. Pominova, V.V. Voronov, Efficient visible range SrF₂:Yb:Er- and SrF₂:Yb:Tm-based upconversion luminophores, *J. Fluor. Chem.* 194 (2017) 16–22, <https://doi.org/10.1016/j.jfluchem.2016.12.002>.
- [61] Z. Zhou, W. Li, J. Song, G. Yi, B. Mei, L. Su, Synthesis and characterization of Nd³⁺ doped SrF₂ nanoparticles prepared by precipitation method, *Ceram. Int.* 44 (2018) 4344–4350, <https://doi.org/10.1016/j.ceramint.2017.12.028>.
- [62] M. Pedroni, F. Piccinelli, T. Passuello, S. Polizzi, J. Ueda, P. Haro-González, L. Martínez Maestro, D. Jaque, J. García-Solé, M. Bettinelli, A. Speghini, Water (H₂O and D₂O) dispersible NIR-to-NIR upconverting Yb³⁺/Tm³⁺ doped MF₂ (M = Ca, Sr) colloids: influence of the host crystal, *Cryst. Growth Des.* 13 (2013) 4906–4913, <https://doi.org/10.1021/cg401077v>.
- [63] S. Kuznetsov, Y. Ermakova, V. Voronov, P. Fedorov, D. Busko, I.A. Howard, B.S. Richards, A. Turshatov, Up-conversion quantum yields of SrF₂:Yb³⁺, Er³⁺ sub-micron particles prepared by precipitation from aqueous solution, *J. Mater. Chem. C* 6 (2018) 598–604, <https://doi.org/10.1039/c7tc04913g>.
- [64] Z. Huang, H. Gao, Y. Mao, Understanding the effect of Mn²⁺ on Yb³⁺/Er³⁺ upconversion and obtaining a maximum upconversion fluorescence enhancement in inert-core/active-shell/inert-shell structures, *RSC Adv.* 6 (2016) 83321–83327, <https://doi.org/10.1039/c6ra10969a>.
- [65] S. Yu, Z. Wang, R. Cao, L. Meng, Microwave-assisted synthesis of water-disperse and biocompatible NaGdF₄:Yb,Ln@NaGdF₄ nanocrystals for UCL/CT/MR multimodal imaging, *J. Fluor. Chem.* 200 (2017) 77–83, <https://doi.org/10.1016/j.jfluchem.2017.06.002>.
- [66] T. Jiang, W. Qin, W. Di, R. Yang, D. Liu, X. Zhai, G. Qin, Citric acid-assisted hydrothermal synthesis of α-NaYF₄:Yb³⁺, Tm³⁺ nanocrystals and their enhanced ultraviolet upconversion emissions, *CrystEngComm* 14 (2012) 2302, <https://doi.org/10.1039/c2ce06311e>.
- [67] F. He, P. Yang, D. Wang, N. Niu, S. Gai, X. Li, Self-assembled β-NaGdF₄ microcrystals: hydrothermal synthesis, morphology evolution, and luminescence properties, *Inorg. Chem.* 50 (2011) 4116–4124, <https://doi.org/10.1021/ic200155q>.
- [68] A. Bartkowiak, A. Siejka, K. Borkowski, S. Lis, T. Grzyb, Up-converting LuF₃ and NaLuF₄ fluorides doped with Yb³⁺/Er³⁺ or Yb³⁺/Tm³⁺ ions for latent fingerprints detection, *J. Alloys Compd.* 784 (2019) 641–652, <https://doi.org/10.1016/j.jallcom.2018.12.344>.
- [69] R.D. Shannon, Revised effective ionic radii and systematic studies of interatomic distances in halides and chalcogenides, *Acta Crystallogr. A* 32 (1976) 751–767, <https://doi.org/10.1107/S0567739476001551>.
- [70] P. Scherrer, Bestimmung der Größe und der inneren Struktur von Kolloidteilchen mittels Röntgenstrahlen, *Nachr. Ges. Wiss. Göttingen* 26 (1918) 98–100.
- [71] Y. Wang, L. Ji, B. Zhang, P. Yin, Y. Qiu, D. Song, J. Zhou, Q. Li, Upconverting rare-earth nanoparticles with a paramagnetic lanthanide complex shell for upconversion fluorescent and magnetic resonance dual-modality imaging, *Nanotechnology* 24 (2013), <https://doi.org/10.1088/0957-4484/24/17/175101>.
- [72] K. Prorok, M. Pawlyta, W. Stręk, A. Bednarkiewicz, Energy migration up-conversion of Tb³⁺ in Yb³⁺ and Nd³⁺ codoped active-core/active-shell colloidal nanoparticles, *Chem. Mater.* 28 (2016) 2295–2300, <https://doi.org/10.1021/acs.chemmater.6b00353>.
- [73] I. Villa, A. Vedda, I.X. Cantarelli, M. Pedroni, F. Piccinelli, M. Bettinelli, A. Speghini, M. Quintanilla, F. Vetrone, U. Rocha, C. Jacinto, E. Carrasco, F.S. Rodríguez, Á. Juarranz, B. del Rosal, D.H. Ortigies, P.H. Gonzalez, J.G. Solé, D.J. García, 1.3 μm emitting SrF₂:Nd³⁺ nanoparticles for high contrast in vivo imaging in the second biological window, *Nano Res* 8 (2015) 649–665, <https://doi.org/10.1007/s12274-014-0549-1>.
- [74] Y. Zhang, F. Wang, Y. Lang, J. Yin, M. Zhang, X. Liu, D. Zhang, D. Zhao, G. Qin, W. Qin, KMnF₃:Yb³⁺, Er³⁺@KMnF₃:Yb³⁺ active-core-active-shell nanoparticles with enhanced red up-conversion fluorescence for polymer-based waveguide amplifiers operating at 650 nm, *J. Mater. Chem. C* 3 (2015) 9827–9832, <https://doi.org/10.1039/c5tc01838b>.
- [75] Q. Luo, X. Deng, W. Chen, H. Guo, W. Ou-Yang, X. Chen, S. Huang, Enhancing upconversion from NaYF₄:Yb,Er@NaYF₄ core-shell nanoparticles assembled on metallic nanostructures, *J. Nanosci. Nanotechnol.* 18 (2017) 5063–5073, <https://doi.org/10.1166/jnn.2018.15355>.
- [76] M. Pollnau, D. Gamelin, S. Lüthi, H. Güdel, M. Mehlen, Power dependence of upconversion luminescence in lanthanide and transition-metal-ion systems, *Phys. Rev. B* 61 (2000) 3337–3346, <https://doi.org/10.1103/PhysRevB.61.3337>.
- [77] Y. Zhong, G. Tian, Z. Gu, Y. Yang, L. Gu, Y. Zhao, Y. Ma, J. Yao, Elimination of photon quenching by a transition layer to fabricate a quenching-shield sandwich structure for 800 nm excited upconversion luminescence of Nd³⁺-sensitized nanoparticles, *Adv. Mater.* 26 (2014) 2831–2837.
- [78] F. Wang, R. Deng, J. Wang, Q. Wang, Y. Han, H. Zhu, X. Chen, X. Liu, Tuning upconversion through energy migration in core-shell nanoparticles, *Nat. Mater.* 10 (2011) 968–973, <https://doi.org/10.1038/nmat3149>.

Synthesis and up-conversion of core/shell
SrF₂:Yb³⁺,Er³⁺@SrF₂:Yb³⁺,Nd³⁺ nanoparticles
under 808, 975, and 1532 nm excitation
wavelengths

*Dominika Przybylska, Tomasz Grzyb**

Adam Mickiewicz University, Faculty of Chemistry, Department of Rare Earths,
Uniwersytetu Poznańskiego 8, 61-614 Poznań, Poland

*Corresponding e-mail: tgrzyb@amu.edu.pl

Supplementary data

Table S1 List of published articles regarding solvothermal synthesis of core/shell structures.

Material	Size	Synthesis method	Solvents and additives	Novelty	Ref.
BaF₂:Tm³⁺,Yb³⁺@Ln³⁺:SrF₂	3 nm C 7 nm CS	C -solvothermal S- thermal decomp. CS - thermal decomp.	1 st ethanol / oleic acid, 2 nd oleic acid / octadecene, thioglycolic acid (TGA)	NIR-to-NIR dual-modal luminescence based on colloid in non-polar solvent, conversion to hydrophilic NPs due to modification with thioglycolic acid (TGA).	[1]
Ba(Na)LaF₅:Tm³⁺,Yb³⁺@Ba(Na)LaF₃ (Na)LaF₃:Tm³⁺,Yb³⁺@(Na)LaF₃	1 st 9.6 ± 2.3 nm 2 nd 22.7 ± 4.5 nm	two-step solvothermal	ethanol, oleic acid, 1 st and 2 nd 200°C, 20 h	Synthesis and characterization of sub-10 nm, UV emissive, Na-co-doped LaF ₃ and BaLaF ₅ NPs and their core/shell derivatives, generated via a one-pot solvothermal approach.	[2]
KMnF₃:Yb³⁺,Er³⁺@KMnF₃:Yb³⁺	23 ± 5 nm C, 65 ± 20 nm CS 65 ± 20 nm CS	two-step solvothermal	oleic acid, ethanol, 1 st 200°C 1 h, 2 nd 200°C 12 h PMMA	Construction of polymer-based waveguide amplifiers using active-core–active-shell NPs doped with polymers as gain media, obtaining a relative optical gain in the polymer waveguides pumped by a 976 nm laser diode.	[3]
SrF₂:Yb³⁺,Tm³⁺@SrF₂:Yb³⁺,Er³⁺	10-12 nm	two-step hydrothermal	water, 1 st and 2 nd 190°C, 3 h, 2.5× NH ₄ F sodium citrate, ubiquitin	Investigation of interactions between Ln-doped fluoride NPs and biomolecules (ubiquitin).	[4]
SrF₂:Yb³⁺,Tm³⁺@CaF₂:Gd³⁺ CaF₂:Yb³⁺,Tm³⁺@CaF₂:Gd³⁺	9.1 and 9.7 nm C 12.9-17.1 nm CS	two- step hydrothermal	water, 1 st 190°C, 6 h, 2 nd 190°C, 6 h and then 200°C 6 h, sodium citrate	Analysis of core/shell UC properties, magnetic characterization.	[5]
NaYF₄@NaYF₄:Er³⁺/Yb³⁺/Mn²⁺@NaYF₄	8 nm C 11 nm CS 18 nm CS _s ,S	three-step solvothermal	deionized water, oleic acid, ethanol, 1 st - 3 rd 180°C for 0.5 h	Investigation of energy transfer mechanism of Yb ³⁺ /Mn ²⁺ /Er ³⁺ tri-doped cubic NaYF ₄ , designed a novel C/S _s /S nanostructure with Yb ³⁺ /Mn ²⁺ /Er ³⁺ ions in the middle two-dimensional layer.	[6]
YVO₄:Er³⁺,Yb³⁺,Nd³⁺ YVO₄:Er³⁺,Yb³⁺@YVO₄:Yb³⁺,Nd³⁺	17 nm C 20 nm CS	two-step hydrothermal	water, sodium oleate, 1 st and 2 nd 200°C, 6 h	Water-based, biocompatible, high-efficiency UC fluorescent core/shell NPs, optical temperature sensing investigation with high thermal sensitivity.	[7]
NaGdF₄:Yb³⁺,Ln³⁺@NaGdF₄ (Ln = Er, Tm, Ho)	45 nm C 75 nm CS	two-step solvothermal microwaves assisted	ethylene glycol, 1 st and 2 nd 240°C, 1 h at 800 W, EDTA–2Na	Design a monodisperse, water–dispersible and biocompatible UCNCs, with greatly enhanced UCL in water in comparison with core NPs, contrast agent for MRI and CT imaging, cytotoxicity study.	[8]
α-NaGdF₄@β-NaYF₄:Yb³⁺,Er³⁺	23 nm C 28 nm CS 33 nm CS 38 nm CS 115 × 125 nm CS	two-step solvothermal	ethylene glycol, 1 st and 2 nd 180°C, 0.5 h, PVP	Synthesis of α-NaGdF ₄ /β-NaYF ₄ :Yb ³⁺ ,Er ³⁺ core/shell particles by varying the shell growth time from 2 to 24 h	[9]
KMnF₃:Yb³⁺,Er³⁺,Nd³⁺@KMnF₃:Yb³⁺,Nd³⁺	32 nm C 55 nm CS	two-step solvothermal	water, ethanol, oleic acid, 1 st 220°C, 3 h / 2 nd 220°C, 12h	Synthesis new type of NPs with excitation (~808 nm) and emission (~668 nm), based energy transfer between Mn ²⁺ and Er ³⁺ , the active-core/active-shell nanostructured design.	[10]
SrF₂:Yb³⁺,Tm³⁺@SrF₂:Y³⁺@ @SrF₂:Yb³⁺,Er³⁺,Nd³⁺@SrF₂:Nd³⁺	8.5 nm C 10.1 nm CS 17.1 nm CSS 26.6 nm CSSS	four-step hydrothermal	water, 1 st -4 th 2.5× NH ₄ F, 190°C, 3 h, potassium citrate	Optimization of thermal relative sensitivity by changing Er ³⁺ content in 20–50°C temperature range, measured in water colloid, possibility of a multicolor UC emission.	[11]
SrF₂:Yb³⁺,Er³⁺@SrF₂:Yb³⁺,Nd³⁺	27/47 nm C 40/61 nm CS	two-step hydrothermal	water, 1 st 200°C, 12/24 h; 2 nd 200°C, 12/24 h, trisodium citrate	Optimization of synthesis of DC and UC core/shell with good dispersibility in water, investigation of energy transfer between Nd ³⁺ -Yb ³⁺ -Er ³⁺ ions, up-conversion from II to I optical transparency window, studies of Nd ³⁺ to Er ³⁺ energy transfer for confirmation of the core/shell structure formation.	This article

*C-core, CS- core/ shell, CSS- core/shell/shell, CS_sS- core/doped-shell/shell

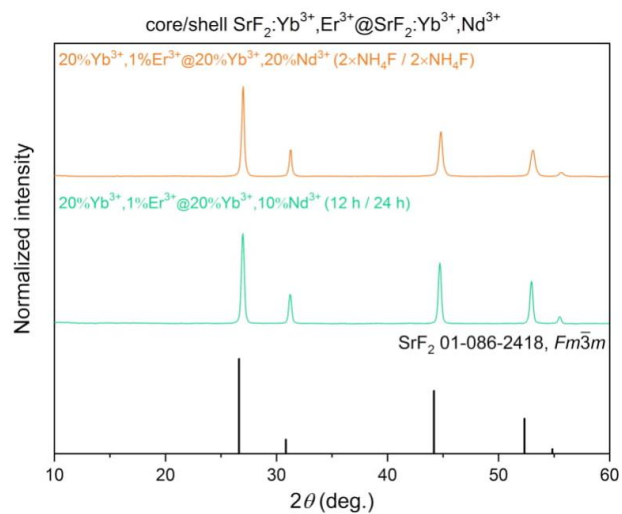


Fig. S1. XRD patterns of additional SrF₂ core NPs synthesized by hydrothermal method doped with Yb³⁺ and Er³⁺ ions.

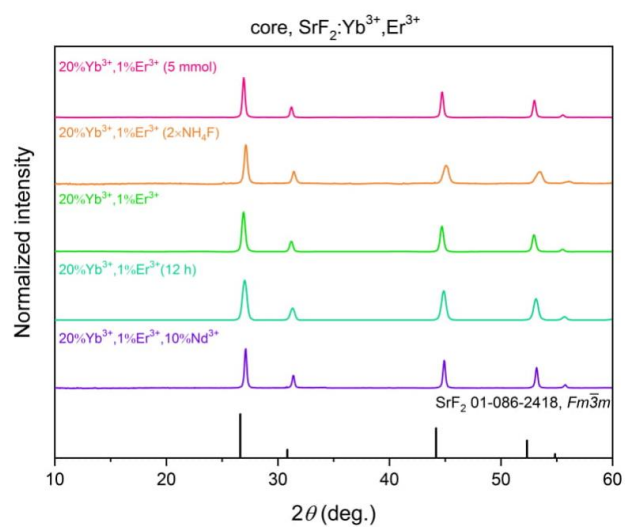


Fig. S2. XRD patterns of additional SrF₂ core/shell NPs synthesized by hydrothermal method doped with Yb³⁺ and Er³⁺ ions.

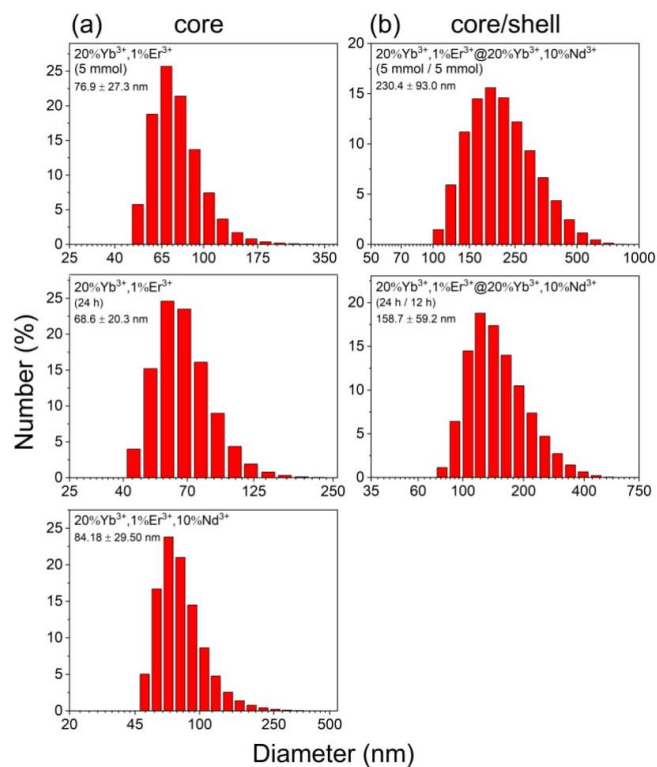


Fig. S3. Hydrodynamic diameters of the synthesized core and core/shell NPs obtained by DLS measurements. The presented results concern samples discussed in the main article.

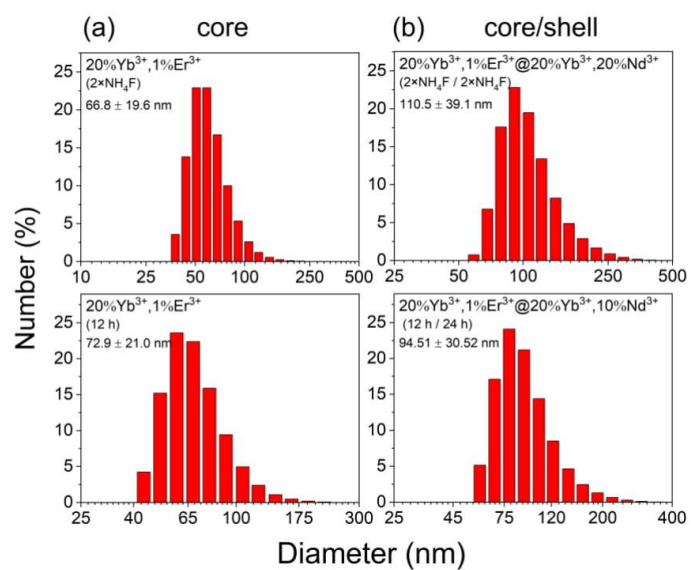


Fig. S4. Hydrodynamic diameters of the synthesized core and core/shell NPs obtained by DLS measurements. The presented results concern additional samples not discussed in the main article.

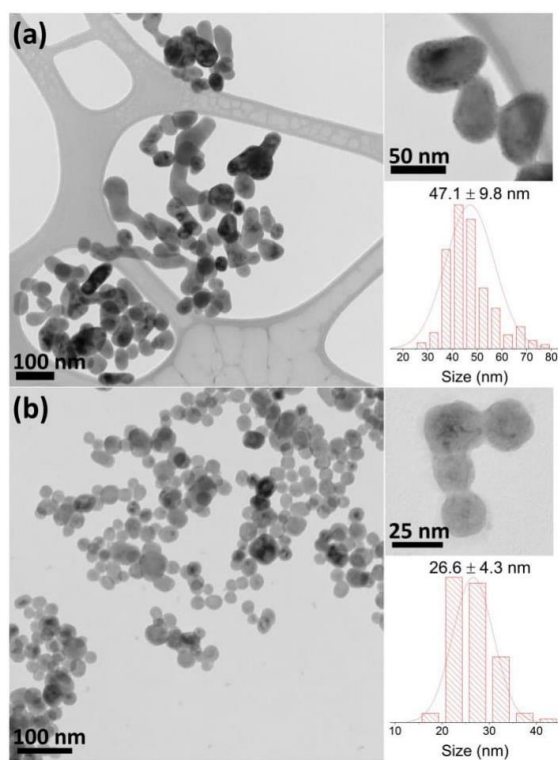


Fig. S5. TEM images and NPs sizes' distribution of hydrothermally synthesized cores
a) $\text{SrF}_2:20\% \text{Yb}^{3+}, 1\% \text{Er}^{3+}$ (5 mmol), b) $\text{SrF}_2:20\% \text{Yb}^{3+}, 1\% \text{Er}^{3+}$ (24 h).

Table S2 Average sizes of NPs, calculated from the Scherrer equation (based on XRD analysis)¹² and their hydrodynamic diameters determined by DLS measurements.

Samples	Scherrer's equation (nm)		Hydrodynamic diameter (nm)	
	Core	Core/shell	Core	Core/shell
20%Yb ³⁺ ,1%Er ³⁺ @20%Yb ³⁺ ,20%Nd ³⁺ (2× NH ₄ F / 2× NH ₄ F)	21.4 ± 2.9 nm	27.1 ± 2.1 nm	66.8 ± 19.6 nm	110.5 ± 39.1 nm
20%Yb ³⁺ ,1%Er ³⁺ @20%Yb ³⁺ ,10%Nd ³⁺ (12 h / 24 h)	20.9 ± 0.4 nm	37.7 ± 0.2 nm	72.9 ± 21.0 nm	94.5 ± 30.5 nm

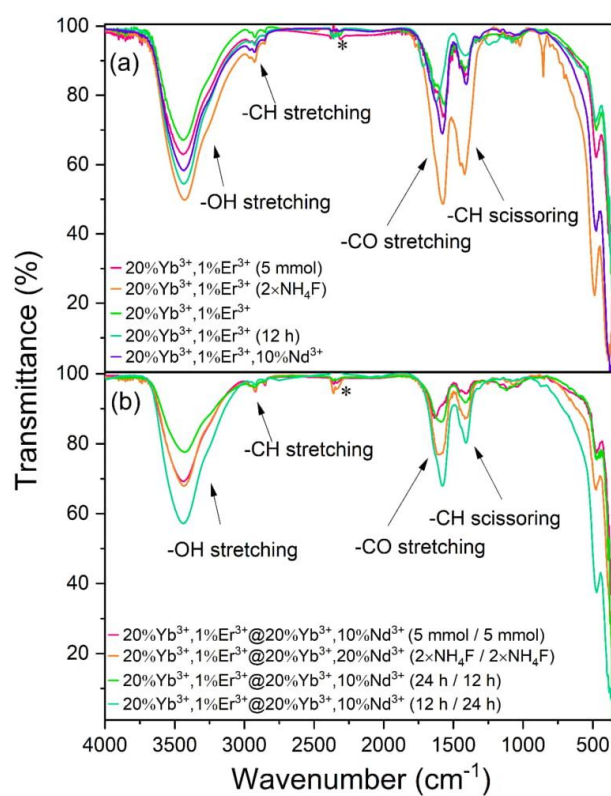


Fig. S6. FT-IR spectra of obtained samples (*peaks connected with impurities).

Table S3 Summary of zeta potential measurements for obtained NPs at physiological pH value.

Samples	Core		Core/shell	
	pH	Zeta potential (mV)	pH	Zeta potential (mV)
20% Yb ³⁺ , 1% Er ³⁺ @20% Yb ³⁺ , 10% Nd ³⁺ (5 mmol / 5 mmol)	7.38	-23.4 ± 3.9	7.37	- 19.6 ± 4.4
20% Yb ³⁺ , 1% Er ³⁺ @20% Yb ³⁺ , 10% Nd ³⁺ (24 h / 12 h)	7.40	-20.7 ± 6.9	7.38	- 20.6 ± 6.2
20% Yb ³⁺ , 1% Er ³⁺ @20% Yb ³⁺ , 20% Nd ³⁺ (2× NH ₄ F / 2× NH ₄ F)	7.45	-28.6 ± 6.1	7.35	- 16.7 ± 3.5
20% Yb ³⁺ , 1% Er ³⁺ @20% Yb ³⁺ , 10% Nd ³⁺ (12 h / 24 h)	7.40	-26.3 ± 6.2	7.48	- 17.4 ± 4.0
20% Yb ³⁺ , 1% Er ³⁺ , 10% Nd ³⁺	7.39	- 22.6 ± 3.7	-	-

Table S4 Composition of the synthesized NPs obtained by ICP-MS analysis.

Sample	Molar percentage (%)			
	Sr ²⁺	Yb ³⁺	Er ³⁺	Nd ³⁺
SrF ₂ :20%Yb ³⁺ , 1%Er ³⁺ @SrF ₂ :20Yb ³⁺ , 10%Nd ³⁺ (5 mmol / 5 mmol)	79.01	17.74	0.53	2.72
SrF ₂ :20%Yb ³⁺ , 1%Er ³⁺ @SrF ₂ :20%Yb ³⁺ , 10%Nd ³⁺ (3× NH ₄ F 24 h / 3× NH ₄ F 12 h)	70.66	22.88	0.34	6.12
SrF ₂ :20%Yb ³⁺ , 1%Er ³⁺ @SrF ₂ :20%Yb ³⁺ , 20%Nd ³⁺ (2× NH ₄ F 24 h / 2× NH ₄ F 24 h)	66.97	26.34	1.31	5.37
SrF ₂ :20%Yb ³⁺ , 1%Er ³⁺ @SrF ₂ :20%Yb ³⁺ , 10%Nd ³⁺ (3× NH ₄ F 12 h / 3× NH ₄ F 24 h)	73.96	23.98	0.07	1.99
SrF ₂ :20%Yb ³⁺ , 1%Er ³⁺ , 10%Nd ³⁺	64.74	24.43	1.11	9.72

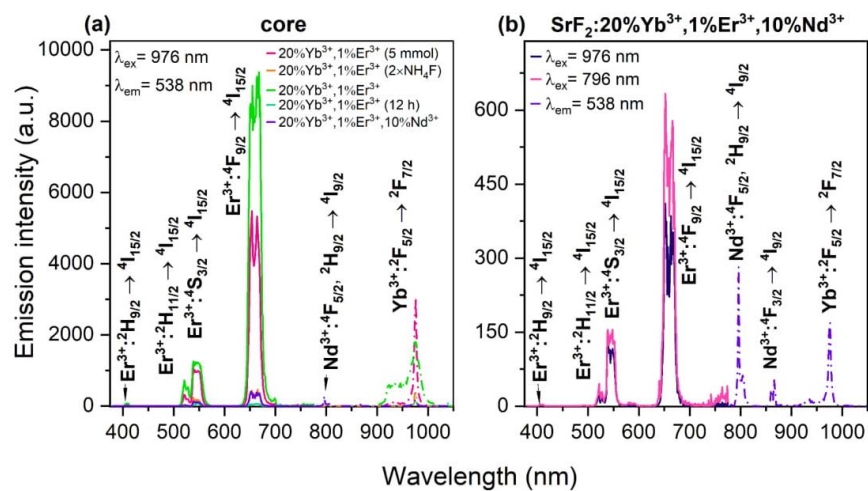


Fig. S7. Emission and excitation spectra of core NPs (a) measured for all obtained samples and (b) comparison of emission spectra received by excitation with 796, 802, 866, and 976 nm for triple-doped core NPs. Spectra were obtained under pulsed excitation source (at 25 mJ·cm⁻²).

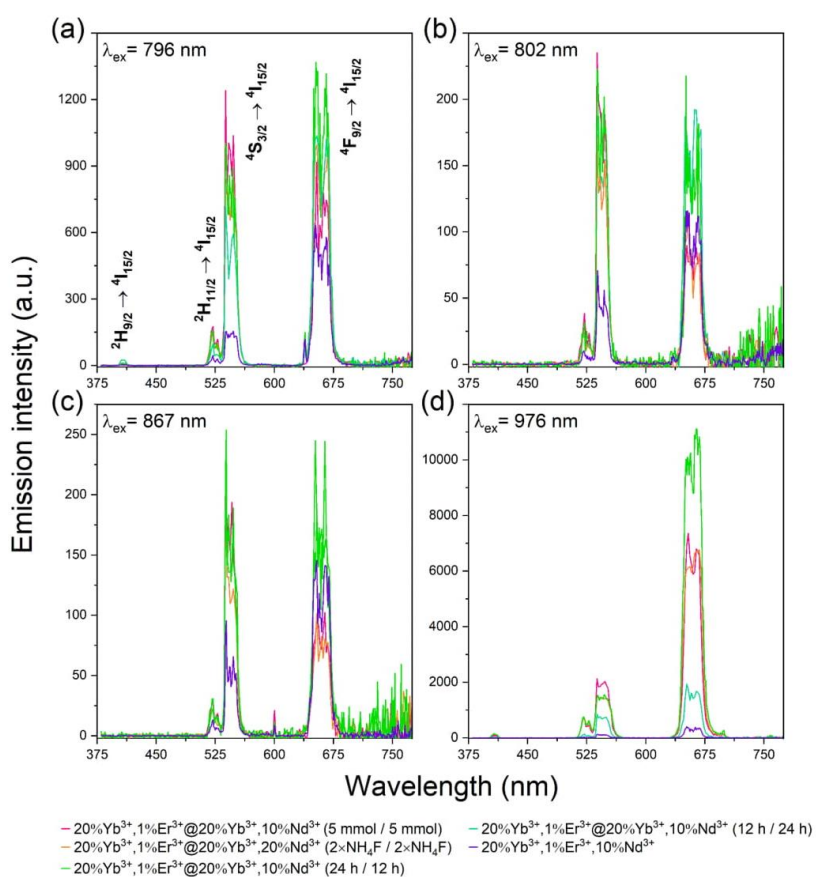


Fig. S8. Emission spectra of core/shell samples received under excitation with different wavelengths. Spectra were obtained under pulsed excitation source (at $25 \text{ mJ} \cdot \text{cm}^{-2}$).

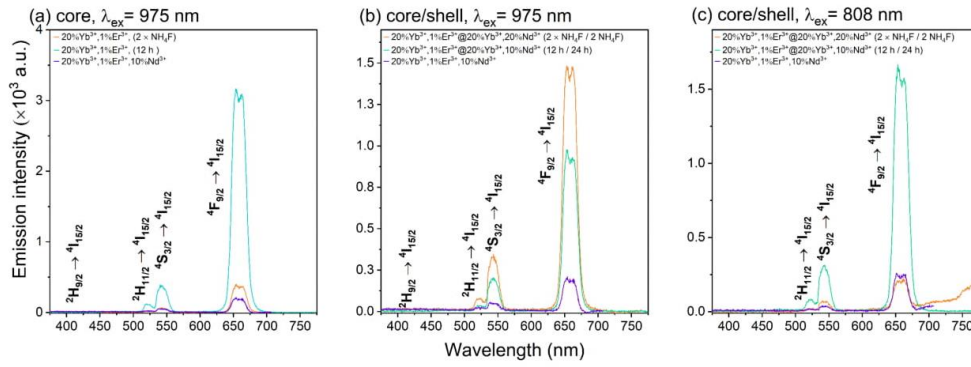


Figure S9. Up-conversion emission spectra of additional samples under excitation with 808 or 975 nm CW laser light. Laser powers $15 \text{ W} \cdot \text{cm}^{-2}$ for 808 and 975 nm.

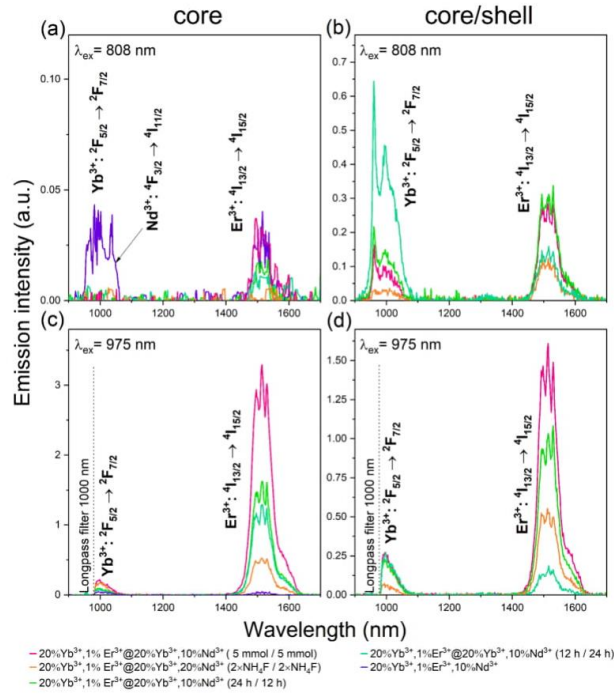


Fig. S10. Downconversion emission spectra of (a, c) core, and (b, d) core/shell samples, obtained under continuous excitation with different wavelengths. Laser powers: 22 or $27 \text{ W} \cdot \text{cm}^{-2}$ for 808 and 975 nm respectively.

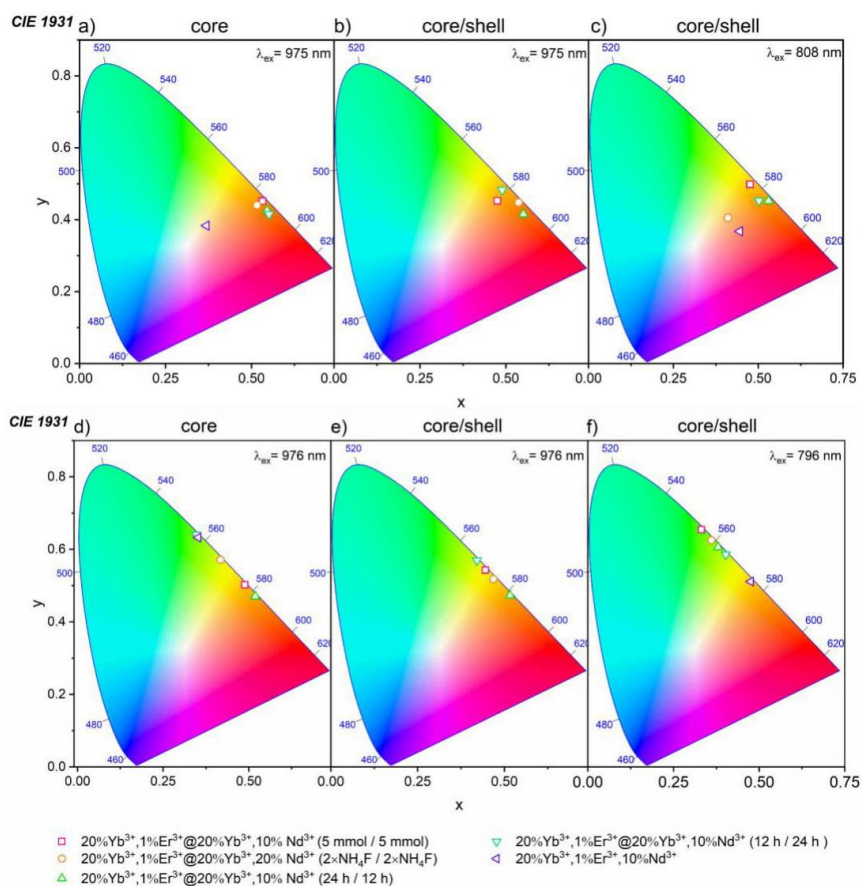


Fig. S11. CIE chromaticity diagrams of synthesized NPs, calculated from the emission spectra measured under 808 and 975 (CW) or 796 and 976 nm wavelengths (pulsed) where (a-c) were measured under continuous excitation source (at $15 \text{ W}\cdot\text{cm}^{-2}$) and (e-g) under pulsed excitation source (at $25 \text{ mJ}\cdot\text{cm}^{-2}$).

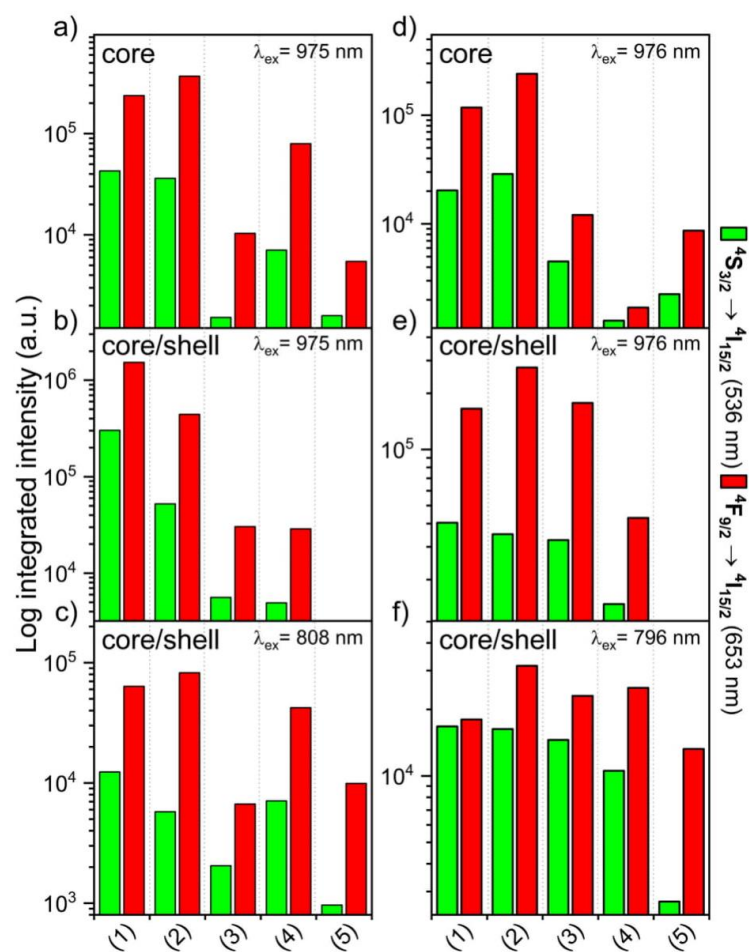


Fig. S12. Integrated luminescence intensities of a, d) SrF₂ core samples and b-c, e-f) SrF₂@SrF₂ core/shell samples, calculated from the spectra measured under $\lambda_{\text{ex}} = 975/808$ nm a-c) continuous excitation source (at 15 W·cm⁻²) and $\lambda_{\text{ex}} = 976/796$ nm d-e) pulsed excitation source (at 25 mJ·cm⁻²), where (1) 20%Yb³⁺,1%Er³⁺@20%Yb³⁺,10%Nd³⁺ (5 mmol / 5 mmol), (2) 20%Yb³⁺,1%Er³⁺@20%Yb³⁺,10%Nd³⁺ (24 h / 12 h), (3) 20%Yb³⁺,1%Er³⁺@20%Yb³⁺,20%Nd³⁺ (2× NH₄F / 2× NH₄F), (4) 20%Yb³⁺,1%Er³⁺@20%Yb³⁺,10%Nd³⁺ (12 h / 24 h), (5) 20%Yb³⁺,1%Er³⁺,10%Nd³⁺.

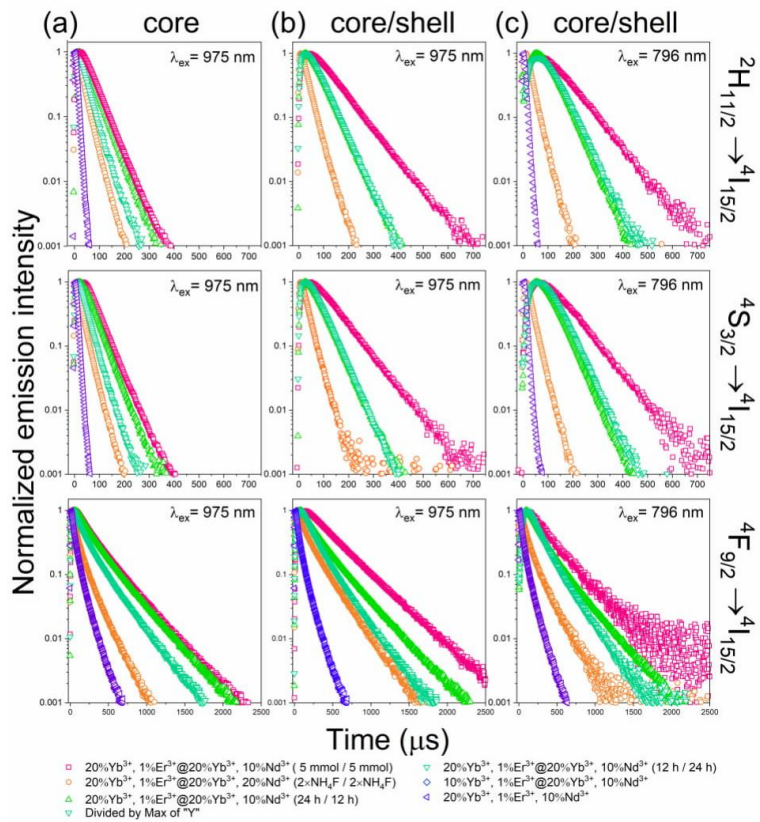


Fig. S13. Emission decays measured for synthesized core and core/shell NPs under 796 and 976 nm wavelengths and pulsed excitation source (at 25 mJ·cm⁻²).

Table S4 Emission lifetimes calculated from the measured luminescence decays of core and core/shell additional samples, under 796 nm or 976 nm pulsed laser excitation (at 25 mJ·cm⁻²) (for decays see Figure S14, err < 1.1 μs).

Sample	Lifetimes (μs)								
	core			core/shell					
	λ _{ex} = 976 nm			λ _{ex} = 976 nm			λ _{ex} = 796 nm		
	² H _{11/2} → ⁴ I _{15/2}	⁴ S _{3/2} → ⁴ I _{15/2}	⁴ F _{9/2} → ⁴ I _{15/2}	² H _{11/2} → ⁴ I _{15/2}	⁴ S _{3/2} → ⁴ I _{15/2}	⁴ F _{9/2} → ⁴ I _{15/2}	² H _{11/2} → ⁴ I _{15/2}	⁴ S _{3/2} → ⁴ I _{15/2}	⁴ F _{9/2} → ⁴ I _{15/2}
20% Yb ³⁺ , 1% Er ³⁺ @ 20% Yb ³⁺ , 20% Nd ³⁺ (2× NH ₄ F / 2× NH ₄ F)	25	24	89	28	28	169	25	26	102
20% Yb ³⁺ , 1% Er ³⁺ @ 20% Yb ³⁺ , 10% Nd ³⁺ (12 h / 24 h)	34	33	174	61	60	193	72	70	187

Table S5 Number of photons involved in the UC mechanism, determined from the dependences of luminescence intensity on laser power for core and core/shell NPs prepared in different synthesis conditions, under 808 nm and 975 nm continuous laser excitation wavelengths (for experimental results see Figure S14, err < 0.05).

Sample	Number of photons											
	core				core/shell							
	λ _{ex} = 975 nm				λ _{ex} = 975 nm				λ _{ex} = 808 nm			
	² H _{9/2} → ⁴ I _{15/2}	² H _{11/2} → ⁴ I _{15/2}	⁴ S _{3/2} → ⁴ I _{15/2}	⁴ F _{9/2} → ⁴ I _{15/2}	² H _{9/2} → ⁴ I _{15/2}	² H _{11/2} → ⁴ I _{15/2}	⁴ S _{3/2} → ⁴ I _{15/2}	⁴ F _{9/2} → ⁴ I _{15/2}	² H _{9/2} → ⁴ I _{15/2}	² H _{11/2} → ⁴ I _{15/2}	⁴ S _{3/2} → ⁴ I _{15/2}	⁴ F _{9/2} → ⁴ I _{15/2}
20% Yb ³⁺ , 1% Er ³⁺ @ 20% Yb ³⁺ , 20% Nd ³⁺ (2× NH ₄ F / 2× NH ₄ F)	-	0.92	1.32	1.88	-	1.15	1.65	2.15	-	0.99	0.94	1.37
20% Yb ³⁺ , 1% Er ³⁺ @ 20% Yb ³⁺ , 10% Nd ³⁺ (12 h / 24 h)	-	1.91	1.71	2.02	-	2.09	2.06	2.14	-	1.03	0.42	1.61

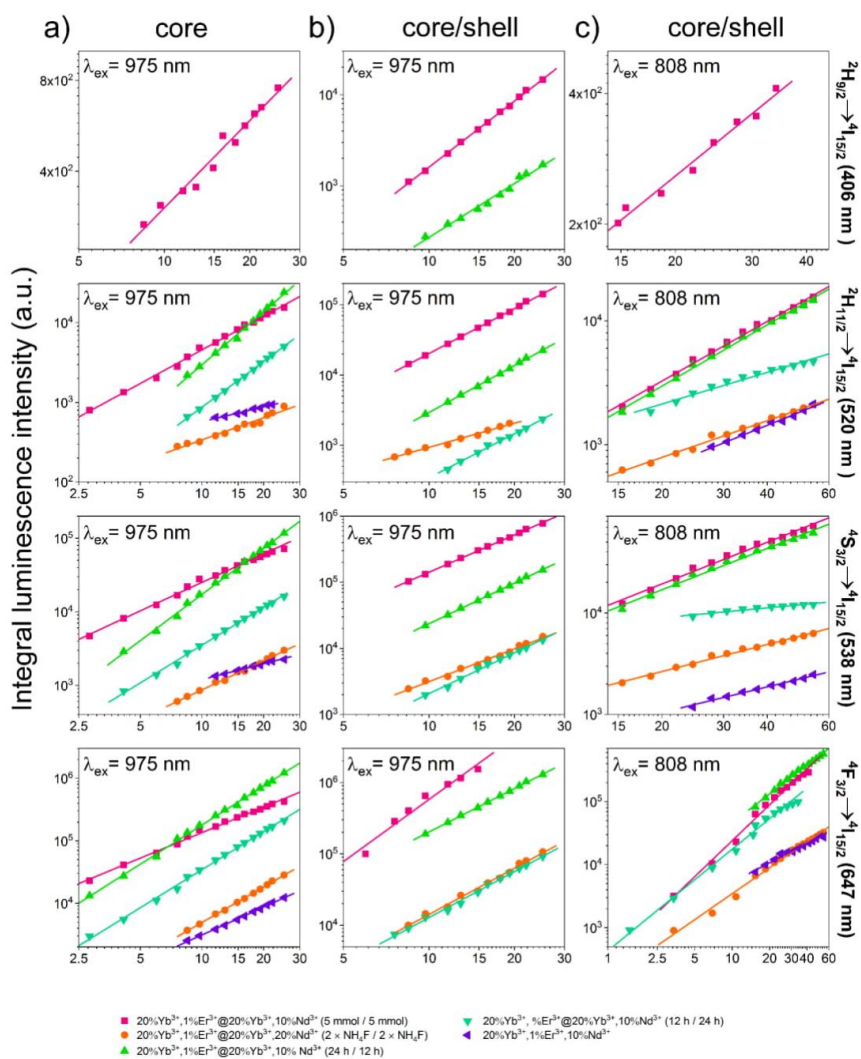


Fig. S14. Dependences of integral emission intensities on laser powers determined for prepared core and core/shell NPs under 808 and 975 nm wavelengths and continuous excitation source (at 25 mJ·cm⁻²).

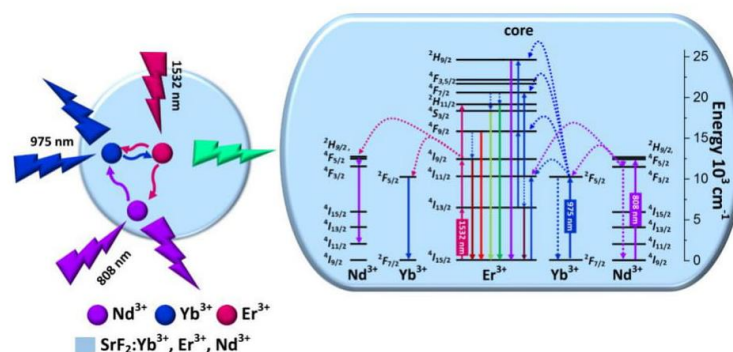


Fig. S15. Scheme of up- and down-conversion mechanisms for $\text{SrF}_2:\text{Yb}^{3+},\text{Er}^{3+},\text{Nd}^{3+}$ NPs under different NIR excitation wavelengths.

References

- [1] D.Q. Chen, Y.L. Yu, F. Huang, H. Lin, P. Huang, A.P. Yang, Z.X. Wang, Y.S. Wang, Lanthanide dopant-induced formation of uniform sub-10 nm active-core/active-shell nanocrystals with near-infrared to near-infrared dual-modal luminescence, *J. Mater. Chem.* 22 (2012) 2632–2640. <https://doi.org/10.1039/C1JM14589D>.
- [2] J. Stecher, A. Rohlfing, M. Therien, One-Pot Solvothermal Synthesis of Highly Emissive, Sodium-Codoped, LaF_3 and BaLaF_5 Core-Shell Upconverting Nanocrystals, *Nanomaterials*. 4 (2014) 69–86. <https://doi.org/10.3390/nano4010069>.
- [3] Y. Zhang, F. Wang, Y. Lang, J. Yin, M. Zhang, X. Liu, D. Zhang, D. Zhao, G. Qin, W. Qin, $\text{KMnF}_3:\text{Yb}^{3+},\text{Er}^{3+}@\text{KMnF}_3:\text{Yb}^{3+}$ active-core-active-shell nanoparticles with enhanced red up-conversion fluorescence for polymer-based waveguide amplifiers operating at 650 nm, *J. Mater. Chem. C*. 3 (2015) 9827–9832. <https://doi.org/10.1039/c5tc01838b>.
- [4] S. Zanzoni, M. Pedroni, M. D’Onofrio, A. Speghini, M. Assfalg, Paramagnetic

- Nanoparticles Leave Their Mark on Nuclear Spins of Transiently Adsorbed Proteins, *J. Am. Chem. Soc.* 138 (2016) 72–75. <https://doi.org/10.1021/jacs.5b11582>.
- [5] A.-H. Li, M. Lü, J. Yang, L. Chen, X. Cui, Z. Sun, Upconversion-luminescent/magnetic dual-functional sub-20 nm core-shell SrF₂:Yb,Tm@CaF₂:Gd heteronanoparticles, *Dalt. Trans.* 45 (2016) 5800–5807. <https://doi.org/10.1039/C6DT00237D>.
- [6] Z. Huang, H. Gao, Y. Mao, Understanding the effect of Mn²⁺ on Yb³⁺/Er³⁺ upconversion and obtaining a maximum upconversion fluorescence enhancement in inert-core/active-shell/inert-shell structures, *RSC Adv.* 6 (2016) 83321–83327. <https://doi.org/10.1039/c6ra10969a>.
- [7] M.H. Alkahtani, C.L. Gomes, P.R. Hemmer, Engineering water-tolerant core/shell upconversion nanoparticles for optical temperature sensing, *Opt. Lett.* 42 (2017) 2451. <https://doi.org/10.1364/ol.42.002451>.
- [8] S. Yu, Z. Wang, R. Cao, L. Meng, Microwave-assisted synthesis of water-disperse and biocompatible NaGdF₄:Yb,Ln@NaGdF₄ nanocrystals for UCL/CT/MR multimodal imaging, *J. Fluor. Chem.* 200 (2017) 77–83. <https://doi.org/10.1016/j.jfluchem.2017.06.002>.
- [9] H. Chen, P. Zhang, H. Cui, W. Qin, D. Zhao, Synthesis and Luminescence Properties of Water Soluble α-NaGdF₄/β-NaYF₄:Yb,Er Core-Shell Nanoparticles, *Nanoscale Res. Lett.* 12 (2017). <https://doi.org/10.1186/s11671-017-2306-3>.
- [10] P. Singh, P.K. Shahi, Z. Yi, T. Zeng, P.P. Sukul, Red Upconversion Emission in Active-Core / Active-Shell Nanocrystals, *Nanotechnology.* 29 (2018).

- [11] P. Cortelletti, A. Skripka, C. Facciotti, M. Pedroni, G. Caputo, N. Pinna, M. Quintanilla, A. Benayas, F. Vetrone, A. Speghini, Tuning the sensitivity of lanthanide-activated NIR nanothermometers in the biological windows, *Nanoscale*. 10 (2018) 2568–2576. <https://doi.org/10.1039/c7nr06141b>.

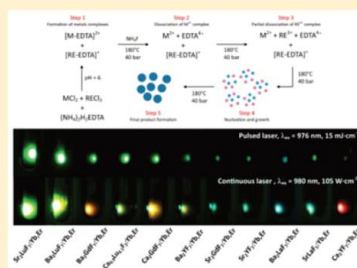
Formation Mechanism, Structural, and Upconversion Properties of Alkaline Rare-Earth Fluoride Nanocrystals Doped With Yb³⁺/Er³⁺ Ions

Tomasz Grzyb* and Dominika Przybylska

Department of Rare Earths, Faculty of Chemistry, Adam Mickiewicz University in Poznan, Umultowska 89b, 61-614 Poznan, Poland

Supporting Information

ABSTRACT: Ultrasmall (9–30 nm) Yb³⁺/Er³⁺-doped, upconverting alkaline rare-earth fluorides that are promising for future applications were synthesized by the microwave-assisted hydrothermal method. The formation mechanism was proposed, indicating the influence of the stability of metal ions complexes with ethylenediaminetetraacetic acid on the composition of the product and tendency to form M₂REF₇ (M_{0.67}RE_{0.33}F_{2.33}) cubic compounds in the M–RE–F systems. Their physicochemical properties (structure, morphology, and spectroscopic properties) are compared and discussed. The obtained nanoparticles exhibited emission of light in the visible spectra under excitation by 976 nm laser radiation. Excitation and emission spectra, luminescence decays, laser energy dependencies, and upconversion quantum yields were measured to determine the spectroscopic properties of prepared materials. The Yb³⁺/Er³⁺ pair of ions used as dopants was responsible for an intense yellowish-green emission. The upconversion quantum yields determined for the first time for M₂REF₇-based materials were 0.0192 ± 0.001% and 0.0176 ± 0.001% for Sr₂LuF₇:Yb³⁺,Er³⁺ and Ba₂LuF₇:Yb³⁺,Er³⁺ respectively, the two best emitting samples. These results indicated the prepared materials are good and promising alternatives for the most studied NaYF₄:Yb³⁺,Er³⁺ nanoparticles.



INTRODUCTION

In recent years, the properties of upconverting nanoparticles (UCNPs) have been investigated very intensively because of their potential applications. Particularly interesting are UCNPs based on lanthanide ions (Ln³⁺).^{1–3} Knowledge of the mechanisms responsible for the efficient upconversion process is increasing dynamically.^{4–6} Furthermore, methods of nanoparticles (NPs) production are continuously developing as the demand for smaller and more advanced NPs is growing.^{7,8}

Ln³⁺ ions feature narrow-band absorption and emission that are characteristic of these emitter ions, a large number of excited states, long luminescence lifetimes, large Stokes shift and upconversion (UC) phenomenon. The combination of these properties allows use of the materials doped with Ln³⁺ ions in solar cells, lasers and fiber amplifiers, persistent phosphors, and temperature/pressure sensors.^{9–16} Inorganic nanomaterials doped with Ln³⁺ ions, excited under near-infrared radiation (NIR), can be applied in bioimaging, cancer treatment, or drug delivery.^{17–20} The use of UCNPs for cell imaging ensures low autofluorescence and reduction of light scattering generated by tissue.^{21–24} Moreover, UCNPs are known to cause less photodamage to cells and usually have low cytotoxicity.^{25–27}

The morphology and composition of NPs are sometimes critical and often determine their applications. In nanomedicine, the important feature is the small average size of NPs, usually below 50 nm. Small NPs are noninvasive to cells and may be distributed in organism through blood vessels.^{25,26} Another fundamental property of the described compounds is

high photochemical stability and resistance to photobleaching. An additional advantage of inorganic NPs is also the fact that their surface can be very easily modified, e.g., by using silica, and further biologically functionalized.^{28–32}

The most popular and commonly used inorganic host materials for UC are fluorides. They have low phonon energy, which reduces the possibility of the occurrence of nonradiative relaxation, and high chemical stability. Nanomaterials based on fluorides are characterized by a relatively high quantum yield (QY) of luminescence.^{33–36} Nanocrystalline fluorides can be synthesized by several methods, of which the most common is the decomposition of product precursors (e.g., metal trifluoroacetates) in high-boiling solvents, such as oleic acid and octadecene.^{7,37,38} Other methods are based on the precipitation reaction, also carried out under solvo- or hydrothermal conditions.^{39–41}

Recently, the NaYF₄ matrix has been used most frequently in research concerning UC systems.^{42,43} UCNPs based on this compound are small, with high emission quantum yields (see Table S2).^{43–46} However, growing interest in the application of nanomaterials has created a need for new compounds with bright emissions and effective methods for their synthesis. Other fluorides, such as M₂RE₂F₇ systems (where M = Ca, Sr, Ba, and RE = Y, La, Gd, Lu) are relatively less studied. Only a few reports about Ca₂RE₂F₇ and Sr₂RE₂F₇ UCNPs are available.^{47–49} Similar compounds, like BaYF₅ or BaGdF₅,

Received: February 22, 2018

Published: May 14, 2018

have more often been the subject of studies revealing promising upconversion properties.^{50,51} The current state of knowledge about $M_2RE_7F_{21}$ -type compounds indicates that several of the UC materials presented in this article, such as Ca_2YF_7 , Ca_2GdF_7 , and Ba_2LuF_7 , have not been as yet subjects of literature reports. Other ones, such as Sr_2LuF_7 , Ba_2YF_7 , and Ba_2GdF_7 , have been more studied, but the upconversion quantum yields (UCQY) in these systems have not been reported to date.^{52–56}

Synthesis of nanocrystalline $M_xRE_yF_z$ fluorides is usually not an easy process because of the diversity of their stoichiometry and crystal structures.^{57–59} Very often, the resulting products have more than one crystal phase. Fedorov et al. analyzed BaF_2 – YF_3 systems proving a nonequilibrium character of these phases.⁶⁰ Therefore, there is not possible to obtain barium–yttrium fluorides with a specific composition, e.g., $BaYF_5$. Instead, these systems should be considered as $Ba_{1-x}RE_xF_{2+x}$ solid solutions.⁶⁰ Despite this, there are some articles using the $BaYF_5$ formula.^{51,61–63} Although some of the mixed M^{2+} and RE^{3+} fluorides have been investigated in recent years, their UC properties have not been compared. What is more, there is a high degree of uncertainty regarding the product composition in published articles. Therefore, it is important to carefully examine the properties of obtained M_xRE_{2x+3} compounds and determine their real stoichiometry. Our studies show that M – RE – F systems are complex and require deep investigation. Synthesis of NPs based on the compounds mentioned above and analysis of their properties can expand knowledge of these and similar systems, and also enlarge the base of inorganic nanomaterials for UC applications.

EXPERIMENTAL SECTION

Materials. Rare earth oxides: Y_2O_3 , La_2O_3 , Gd_2O_3 , Er_2O_3 , Yb_2O_3 , and Lu_2O_3 (99.99%, Stanford Materials, United States) were used as the source of RE^{3+} (and Ln^{3+}) ions. To obtain rare earth chloride solutions at a concentration of 1 or 0.5 M, the oxides were dissolved separately in hydrochloric acid (ultrapure, Sigma-Aldrich, 37%, Poland). Ammonium fluoride (98+%, Sigma-Aldrich, Poland) was used as the source of fluoride ions. Barium chloride dehydrate (Sigma-Aldrich, 99+%, Poland), calcium chloride dihydrate (Sigma-Aldrich, 99+%, Poland), strontium chloride hexahydrate (Sigma-Aldrich, 99+%, Poland), and ethylenediaminetetraacetic acid (EDTA) diammonium salt hydrate (Sigma-Aldrich, 97%, Poland) were used as received without further purification.

Synthesis. Nanoparticles showing UC based on M_2RE_7 matrices (where $M = Ca, Sr, Ba$, and $RE = Y, La, Gd, Lu$) doped with Yb^{3+} and Er^{3+} ions were synthesized using the microwave-assisted hydrothermal method (Magnum II, Ertec). To obtain $M_2RE_7:Yb^{3+},Er^{3+}$ (theoretical concentrations were set to 18% and 2% mol), 6 mmol of EDTA diammonium salt hydrate was dissolved in 20 mL of water, in a beaker which was placed on a magnetic stirrer. This substance was used to prevent precipitation of the product before applying the hydrothermal conditions. Then, an aqueous solution of MCl_2 (containing 3 mmol of reactant) mixed earlier in a beaker with $RECl_3$ and $LnCl_3$ ($Ln = Yb, Er$; total amount 3 mmol) with a specified concentration and stoichiometric ratio (1:1 metal ions) was added to dissolved EDTA. $NH_3(aq)$ (30%) was added dropwise upon vigorous stirring to obtain a transparent solution until pH = 6 was reached. NH_4F was used in the synthesis as a source of fluoride ions: metal and fluoride ions were mixed in a 1:5 ratio. During preparation of the solution, the pH was monitored and maintained at 6 using $NH_3(aq)$. The transparent solution with total volume of 70 mL was transferred into a Teflon-lined autoclave (100 mL) and treated under hydrothermal conditions for 4 h at 180 °C and 40 bar, with microwave heating. Afterward, the obtained white precipitate was purified by centrifugation with water

and ethanol several times. The final product was dried at 80 °C for 80 h.

Characterization. X-ray diffractograms (XRD) were recorded on a Bruker AXS D8 Advance diffractometer in the Bragg–Brentano geometry, with $Cu K_{\alpha 1}$ radiation, in the 2θ range from 6 to 60°. The reference data were taken from The International Centre for Diffraction Data (ICDD) database. Crystal cell volumes were calculated using the Maud 2.33 software.⁶⁴ The composition of the prepared materials was analyzed by inductively coupled plasma-optical emission spectrometer (Varian ICP-OES VISTA-MPX). Transmission-electron-microscopy (TEM) images were recorded on an FEI Tecnai G2 20 X-TWIN transmission electron microscope using an accelerating voltage of 200 kV.

The luminescence characteristics (excitation, emission spectra, luminescence decays, and power dependencies) of the prepared samples were measured on a Photon Technology International QuantaMaster 40 spectrofluorometer equipped with an Optronic Inc. Opolette 35SLD UVDM tunable laser, with a repetition rate of 20 Hz and pulse length of 7 ns; a Hamamatsu R928 photomultiplier was used as a detector and a Thorlabs FEL900 optical filter was used.

The absolute upconversion quantum yield (UCQY) measurements usually involve the use of integrating sphere.^{43,44,65–67} In our studies a barium sulfate-coated integrating sphere (80 mm diameter) from Photon Technology International was employed. The integrating sphere was mounted in a QuantaMaster 40 spectrofluorometer with the entry and output ports located at 90° to each other. A continuous Dragon Lasers DPSS 980 nm laser was used as the excitation source, coupled to a 200 μm optical fiber and collimator. A S305C Compact Thermal Power Sensor from Thorlabs was used to measure the power of the laser beam. As a detector, a Princeton Instruments PIXIS:256E Digital CCD Camera, equipped with an SP-2156 Imaging Spectrograph was applied, corrected for the instrumental response. All of the powder samples were held in a white Teflon cuvette with a quartz window, located in the center of the integrating sphere. Two filters, Thorlabs NENIR30B and NENIR40B, were used in order to measure the spectrum in the range covering the emission and excitation wavelengths (500–1050 nm) and to avoid saturation of the CCD camera. Measured spectra were corrected for the filters before the final calculations. For more details see Supporting Information.

Pictures of the samples were taken using a Canon EOS 550D camera under excitation by Opolette 35SLD UVDM ($\sim 10 \text{ mJ}\cdot\text{cm}^{-2}$) or a Dragon Lasers DPSS 980 nm laser ($\sim 20 \text{ W}\cdot\text{cm}^{-2}$) and with Thorlabs FEL900 and FGS900-A optical filters (exposure time 2.5 s, f/4, ISO-1600).

RESULTS AND DISCUSSION

Structure and Morphology. The $M_xRE_yF_z$ fluorides are known to crystallize as cubic, orthorhombic, hexagonal, or monoclinic structures depending on the composition.^{57,59,68–70} The synthesized compounds crystallized as disordered, fluorite-type, nonstoichiometric structures with a $M_{0.67}RE_{0.33}F_{2.33}$ composition per unit cell and $Fm\bar{3}m$ cubic space group.^{57,71} According to Sorokin et al., these type of compounds crystallize as solid solutions which remain metastable at low temperature.⁷¹ The article uses the M_2RE_7 formula containing the integer number of ions. Upon annealing, the fluorite structure may order with formation of tetragonal M_2RE_7 phase.⁷¹ The diffraction peaks of tetragonal phase are similar to those of the pure cubic structure, $Fm\bar{3}m$; however, according to literature, the compounds obtained by solid-state reaction may show very weak additional superstructure reflections.⁷² Also splitting of the main peaks of the fluorite-type lattice phase should be observed.⁷¹ These minor peaks as well as splitting of XRD peaks were not observed in the materials prepared, which confirms the cubic structure. However, there are some articles incorrectly reporting M_2RE_7 -type compounds as tetragonal

with similar XRD patterns to those presented in this article.^{52,53,56,73}

The crystal phases of all samples have been identified, and the results are presented in Figure 1. The diffraction peaks are

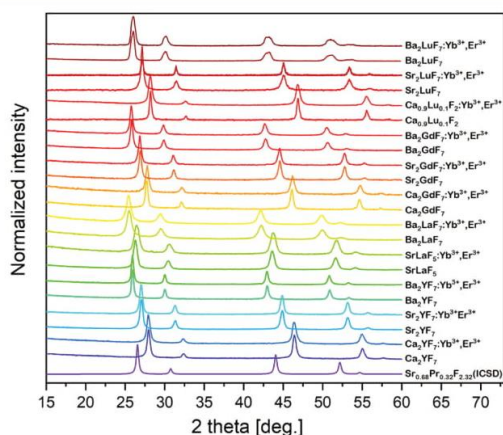


Figure 1. XRD patterns of the samples synthesized by hydrothermal method and the reference from the ICSD database (No. 190727).

broad, which indicates the small size of the nanocrystals (Table 1). The obtained patterns were compared to the standard data for cubic $\text{Sr}_{0.68}\text{Pr}_{0.32}\text{F}_{2.32}$ (ICSD No. 190727). The comparison confirmed the single-phase structure of all the compounds. Depending on the ions forming the material, crystal cell volume (Table 1) changed in comparison to that for the reference

compound, which resulted in a shift of the XRD peaks. Hence, when the host compound consists of Ba^{2+} ($r = 1.35 \text{ \AA}$), the calculated crystal cell volumes are the largest, and the shifts of the XRD peaks with respect to those in the reference pattern are the highest. Analogously, the materials including Ca^{2+} ions with the ionic radius smaller than that of the M^{2+} metal ions used ($r = 1.00 \text{ \AA}$) had the smallest cell volumes from all products obtained. In addition, differences between ionic radii of RE^{3+} ions caused similar changes, although to a smaller degree as the differences were also lower: Y^{3+} ($r = 0.9 \text{ \AA}$), La^{3+} ($r = 1.03 \text{ \AA}$), Gd^{3+} ($r = 0.94 \text{ \AA}$), and Lu^{3+} ($r = 0.86$) (ionic radius for the coordination number, $\text{CN} = 6$). The size of nanocrystals, calculated from the Scherrer equation, was independent of the crystal cell volume.

ICP-OES analysis was performed to confirm the obtained stoichiometry, and the results are presented in Table 1. Figure 1 presents the XRD patterns of the obtained compounds along with sample labels according to their elemental composition. On the basis of the elemental analysis, three different types of structures were obtained: MREF_5 (SrLaF_5), M_2REF_7 (Ca_2YF_7 , Sr_2YF_7 , Ba_2YF_7 , Ba_2LaF_7 , Ca_2GdF_7 , Sr_2GdF_7 , Ba_2GdF_7 , Sr_2LuF_7 , Ba_2LuF_7 , and $\text{M}_{1-x}\text{RE}_x\text{F}_{2+x}$ for a structure containing Ca^{2+} and Lu^{3+} ions with a very low content of lanthanide ions.

The complexity of the $\text{M}-\text{RE}-\text{F}$ systems results from the high capacity of the CaF_2 fluorite-type structure for ion exchange. The M^{2+} ions can be easily replaced by RE^{3+} ions, which additionally are similar in ionic radius to those they replace. The charge imbalance created after replacement can be compensated by highly mobile F^- ions. Hence, from the ideal fluorite-type CaF_2 structure, other structures can be delivered, such as tetragonal-type distortion.⁷⁴ However, in nanocrystalline materials in which a high proportion of ions are localized

Table 1. Results of ICP-OES Analysis, the Stoichiometric Ratio between Alkaline Metal (Ca, Sr, Ba) and Rare Earth Ions, Crystal Cell Volumes, and Nanocrystal Sizes Calculated Using the Scherrer Equation

metal ion		concentration (% mol)				$\text{M}^{2+}:\text{RE}^{3+}$ ratio	sample name	crystal cell volume (\AA^3)	nanocrystal size (nm)
M^{2+}	RE^{3+}	M^{2+}	RE^{3+}	Yb^{3+}	Er^{3+}				
Ca^{2+}	Y^{3+}	70.0	30.0			2:0.9	Ca_2YF_7	170.38	16.4 ± 1.6
		74.2	24.6	1.0	0.2	2:0.7	$\text{Ca}_2\text{YF}_7:3.9\%\text{Yb}^{3+},0.6\%\text{Er}^{3+}$	169.47	13.7 ± 1.6
Sr^{2+}	Y^{3+}	66.6	33.4			2:1.0	Sr_2YF_7	187.40	16.1 ± 0.6
		64.1	33.6	2.0	0.3	2:1.1	$\text{Sr}_2\text{YF}_7:5.6\%\text{Yb}^{3+},0.9\%\text{Er}^{3+}$	186.65	16.3 ± 0.8
Ba^{2+}	Y^{3+}	66.4	33.6			2:1.0	Ba_2YF_7	210.78	19.7 ± 1.7
		69.3	28.9	1.6	0.3	2:0.9	$\text{Ba}_2\text{YF}_7:5.1\%\text{Yb}^{3+},0.9\%\text{Er}^{3+}$	211.15	19.7 ± 1.8
Ca^{2+}	La^{3+}	52.6	47.4			2:1.8	SrLaF_5	202.35	13.2 ± 1.2
		55.3	44.2	0.4	0.1	2:1.6	$\text{SrLaF}_5:0.8\%\text{Yb}^{3+},0.2\%\text{Er}^{3+}$	200.40	10.7 ± 1.0
Ba^{2+}	La^{3+}	67.1	32.9			2:1.0	Ba_2LaF_7	221.78	9.4 ± 0.6
		63.3	36.2	0.4	0.1	2:1.2	$\text{Ba}_2\text{LaF}_7:1.1\%\text{Yb}^{3+},0.2\%\text{Er}^{3+}$	223.21	10.3 ± 0.9
Ca^{2+}	Gd^{3+}	67.0	33.0			2:1.0	Ca_2GdF_7	172.87	20.8 ± 4.4
		73.3	25.6	1.0	0.2	2:0.7	$\text{Ca}_2\text{GdF}_7:3.7\%\text{Yb}^{3+},0.7\%\text{Er}^{3+}$	171.90	15.5 ± 1.1
Sr^{2+}	Gd^{3+}	71.7	28.3			2:0.8	Sr_2GdF_7	189.90	20.8 ± 6.0
		60.4	37.1	2.2	0.3	2:1.3	$\text{Sr}_2\text{GdF}_7:5.5\%\text{Yb}^{3+},0.9\%\text{Er}^{3+}$	190.90	18.0 ± 2.9
Ba^{2+}	Gd^{3+}	74.0	26.0			2:0.7	Ba_2GdF_7	213.72	14.7 ± 1.7
		72.6	25.1	2.1	0.3	2:0.8	$\text{Ba}_2\text{GdF}_7:7.5\%\text{Yb}^{3+},1.1\%\text{Er}^{3+}$	214.77	15.4 ± 1.9
Ca^{2+}	Lu^{3+}	89.6	10.4			2:0.2	$\text{Ca}_{0.9}\text{Lu}_{0.1}\text{F}_2$	164.57	20.0 ± 2.2
		86.4	9.6	3.5	0.5	2:0.3	$\text{Ca}_{0.9}\text{Lu}_{0.1}\text{F}_2:3.5\%\text{Yb}^{3+},0.5\%\text{Er}^{3+}$	164.96	14.6 ± 1.7
Sr^{2+}	Lu^{3+}	72.3	27.7			2:0.8	Sr_2LuF_7	185.78	12.9 ± 1.6
		67.8	25.1	6.2	1.0	2:1.0	$\text{Sr}_2\text{LuF}_7:19.3\%\text{Yb}^{3+},3.0\%\text{Er}^{3+}$	184.17	20.5 ± 1.9
Ba^{2+}	Lu^{3+}	66.4	33.6			2:1.0	Ba_2LuF_7	210.16	10.6 ± 2.6
		66.1	25.1	7.7	1.1	2:1.0	$\text{Ba}_2\text{LuF}_7:22.8\%\text{Yb}^{3+},3.1\%\text{Er}^{3+}$	208.77	9.8 ± 2.6
		ICSD No. 190727					$\text{Sr}_{0.68}\text{Pr}_{0.32}\text{F}_{2.32}$	196.53	

with similar XRD patterns to those presented in this article.^{52,53,56,73}

The crystal phases of all samples have been identified, and the results are presented in Figure 1. The diffraction peaks are

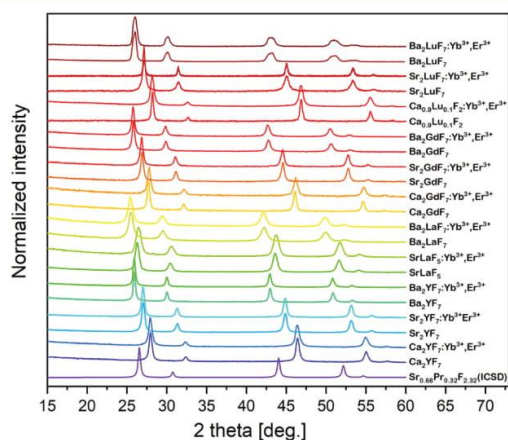


Figure 1. XRD patterns of the samples synthesized by hydrothermal method and the reference from the ICSD database (No. 190727).

broad, which indicates the small size of the nanocrystals (Table 1). The obtained patterns were compared to the standard data for cubic $\text{Sr}_{0.68}\text{Pr}_{0.32}\text{F}_{2.32}$ (ICSD No. 190727). The comparison confirmed the single-phase structure of all the compounds. Depending on the ions forming the material, crystal cell volume (Table 1) changed in comparison to that for the reference

compound, which resulted in a shift of the XRD peaks. Hence, when the host compound consists of Ba^{2+} ($r = 1.35 \text{ \AA}$), the calculated crystal cell volumes are the largest, and the shifts of the XRD peaks with respect to those in the reference pattern are the highest. Analogously, the materials including Ca^{2+} ions with the ionic radius smaller than that of the M^{2+} metal ions used ($r = 1.00 \text{ \AA}$) had the smallest cell volumes from all products obtained. In addition, differences between ionic radii of RE^{3+} ions caused similar changes, although to a smaller degree as the differences were also lower: Y^{3+} ($r = 0.9 \text{ \AA}$), La^{3+} ($r = 1.03 \text{ \AA}$), Gd^{3+} ($r = 0.94 \text{ \AA}$), and Lu^{3+} ($r = 0.86 \text{ \AA}$) (ionic radius for the coordination number, CN = 6). The size of nanocrystals, calculated from the Scherrer equation, was independent of the crystal cell volume.

ICP-OES analysis was performed to confirm the obtained stoichiometry, and the results are presented in Table 1. Figure 1 presents the XRD patterns of the obtained compounds along with sample labels according to their elemental composition. On the basis of the elemental analysis, three different types of structures were obtained: MREF₅ (SrLaF_5), M₂REF₇ (Ca_2YF_7 , Sr_2YF_7 , Ba_2YF_7 , Ba_2LaF_7 , Ca_2GdF_7 , Sr_2GdF_7 , Ba_2GdF_7 , Sr_2LuF_7 , Ba_2LuF_7 , and $\text{M}_{1-x}\text{RE}_x\text{F}_{2+x}$ for a structure containing Ca^{2+} and Lu^{3+} ions with a very low content of lanthanide ions.

The complexity of the M-RE-F systems results from the high capacity of the CaF_2 fluorite-type structure for ion exchange. The M^{2+} ions can be easily replaced by RE^{3+} ions, which additionally are similar in ionic radius to those they replace. The charge imbalance created after replacement can be compensated by highly mobile F^- ions. Hence, from the ideal fluorite-type CaF_2 structure, other structures can be delivered, such as tetragonal-type distortion.⁷⁴ However, in nanocrystalline materials in which a high proportion of ions are localized

Table 1. Results of ICP-OES Analysis, the Stoichiometric Ratio between Alkaline Metal (Ca, Sr, Ba) and Rare Earth Ions, Crystal Cell Volumes, and Nanocrystal Sizes Calculated Using the Scherrer Equation

metal ion		concentration (% mol)				$\text{M}^{2+}:\text{RE}^{3+}$ ratio	sample name	crystal cell volume (\AA^3)	nanocrystal size (nm)
M^{2+}	RE^{3+}	M^{2+}	RE^{3+}	Yb^{3+}	Er^{3+}				
Ca^{2+}		70.0	30.0			2:0.9	Ca_2YF_7	170.38	16.4 ± 1.6
		74.2	24.6	1.0	0.2	2:0.7	$\text{Ca}_2\text{YF}_7:3.9\%\text{Yb}^{3+},0.6\%\text{Er}^{3+}$	169.47	13.7 ± 1.6
Sr^{2+}	Y^{3+}	66.6	33.4			2:1.0	Sr_2YF_7	187.40	16.1 ± 0.6
		64.1	33.6	2.0	0.3	2:1.1	$\text{Sr}_2\text{YF}_7:5.6\%\text{Yb}^{3+},0.9\%\text{Er}^{3+}$	186.65	16.3 ± 0.8
Ba^{2+}		66.4	33.6			2:1.0	Ba_2YF_7	210.78	19.7 ± 1.7
		69.3	28.9	1.6	0.3	2:0.9	$\text{Ba}_2\text{YF}_7:5.1\%\text{Yb}^{3+},0.9\%\text{Er}^{3+}$	211.15	19.7 ± 1.8
Ca^{2+}		52.6	47.4			2:1.8	SrLaF_5	202.35	13.2 ± 1.2
		55.3	44.2	0.4	0.1	2:1.6	$\text{SrLaF}_5:0.8\%\text{Yb}^{3+},0.2\%\text{Er}^{3+}$	200.40	10.7 ± 1.0
Ba^{2+}	La^{3+}	67.1	32.9			2:1.0	Ba_2LaF_7	221.78	9.4 ± 0.6
		63.3	36.2	0.4	0.1	2:1.2	$\text{Ba}_2\text{LaF}_7:1.1\%\text{Yb}^{3+},0.2\%\text{Er}^{3+}$	223.21	10.3 ± 0.9
Ca^{2+}		67.0	33.0			2:1.0	Ca_2GdF_7	172.87	20.8 ± 4.4
		73.3	25.6	1.0	0.2	2:0.7	$\text{Ca}_2\text{GdF}_7:3.7\%\text{Yb}^{3+},0.7\%\text{Er}^{3+}$	171.90	15.5 ± 1.1
Sr^{2+}	Gd^{3+}	71.7	28.3			2:0.8	Sr_2GdF_7	189.90	20.8 ± 6.0
		60.4	37.1	2.2	0.3	2:1.3	$\text{Sr}_2\text{GdF}_7:5.5\%\text{Yb}^{3+},0.9\%\text{Er}^{3+}$	190.90	18.0 ± 2.9
Ba^{2+}		74.0	26.0			2:0.7	Ba_2GdF_7	213.72	14.7 ± 1.7
		72.6	25.1	2.1	0.3	2:0.8	$\text{Ba}_2\text{GdF}_7:7.5\%\text{Yb}^{3+},1.1\%\text{Er}^{3+}$	214.77	15.4 ± 1.9
Ca^{2+}		89.6	10.4			2:0.2	$\text{Ca}_{0.9}\text{Lu}_{0.1}\text{F}_2$	164.57	20.0 ± 2.2
		86.4	9.6	3.5	0.5	2:0.3	$\text{Ca}_{0.9}\text{Lu}_{0.1}\text{F}_2:3.5\%\text{Yb}^{3+},0.5\%\text{Er}^{3+}$	164.96	14.6 ± 1.7
Sr^{2+}	Lu^{3+}	72.3	27.7			2:0.8	Sr_2LuF_7	185.78	12.9 ± 1.6
		67.8	25.1	6.2	1.0	2:1.0	$\text{Sr}_2\text{LuF}_7:19.3\%\text{Yb}^{3+},3.0\%\text{Er}^{3+}$	184.17	20.5 ± 1.9
Ba^{2+}		66.4	33.6			2:1.0	Ba_2LuF_7	210.16	10.6 ± 2.6
		66.1	25.1	7.7	1.1	2:1.0	$\text{Ba}_2\text{LuF}_7:22.8\%\text{Yb}^{3+},3.1\%\text{Er}^{3+}$	208.77	9.8 ± 2.6
							$\text{Sr}_{0.68}\text{Pr}_{0.32}\text{F}_{2.32}$	196.53	

ICSD No. 190727

on the surface (~20% in nanocrystals with size around 8 nm),⁷⁵ where the crystal structure is highly distorted and XRD peaks are wide, the boundary between cubic and tetragonal structure may be not clear.

The results of ICP-OES analysis typically indicated different composition of products and lower dopant concentrations than expected from stoichiometric calculations. Most of the products were obtained with M^{2+} to RE^{3+} molar ratios of around 2:1, despite the fact that MCl_2 and $RECl_3$ chlorides were added to the solution at the 1:1 molar ratio. Also the ratios of RE^{3+} ions forming host (Yb^{3+} , La^{3+} , Gd^{3+} , or Lu^{3+}) to those used as dopants (Yb^{3+} and Er^{3+}) was not as expected from the concentrations of the reagents. The data presented in Table 1 show that the highest percentage amount of Yb^{3+} and Er^{3+} ions was found in the Ba_2LuF_7 -based sample (22.8% and 3.04%, respectively). The lowest efficiency of doping was observed for $SrLaF_7:Yb^{3+},Er^{3+}$ sample in which the dopant concentrations were 0.8% of Yb^{3+} and 0.2% of Er^{3+} ions.

As the reaction conditions and reagent compositions were the same for each synthesis, the final product stoichiometry and composition were determined by other factors. The differences in ionic radii between metal ions,⁷⁶ solubilities of metal fluorides,^{77,78} and, the most important factor, stability of the complexes with EDTA are known to influence the properties of the materials obtained (see Table S1 in Supporting Information for appropriate data).⁷⁹ The proposed product formation mechanism is presented in Figure 2. Alkaline metals, M^{2+} , form

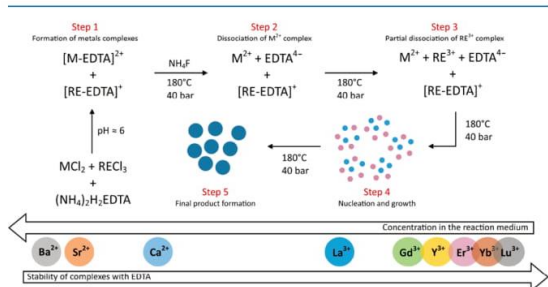


Figure 2. Proposition of mechanism of nanocrystal growth in hydrothermal conditions.

complexes with EDTA that are less stable than the complexes of RE^{3+} ions. An equilibrium between $[M-EDTA]^{2+}$, $[RE-EDTA]^+$, M^{2+} , RE^{3+} , and $EDTA^{4-}$ individuals is established after mixing all of the reagents. The RE^{3+} ions are in larger fraction complexed in $[RE-EDTA]^+$ than M^{2+} in $[M-EDTA]^{2+}$; therefore, the ratio between these ions is higher than expected. Additionally, after the reaction starts, $[M-EDTA]^{2+}$ complexes first dissociate (Step 2 in the mechanism) as they are less stable and as the result of EDTA decomposition.⁸⁰ Afterward, $[RE-EDTA]^+$ begins to dissociate, which explains why the concentration of RE^{3+} ions in the prepared materials is much lower than expected from the amounts of reagent salts added. After these two stages, the equilibrium between M^{2+} , RE^{3+} , and their complexes is established, and precipitation of the products begins (Step 4). The final step is nucleation followed by growth of nanoparticles (Step 5). This simplified mechanism is the only proposition not verified experimentally.

The proposed mechanism explains why most of the synthesized materials contained lower concentrations of Yb^{3+} and Er^{3+} dopants than expected (20% of Yb^{3+} and 2% of Er^{3+}

ions) and why the fraction of precipitated Er^{3+} ions is always larger than that of Yb^{3+} ions (Table 1). The dopant ions precipitate, the last one during the reaction, first Er^{3+} and next Yb^{3+} ions, except for syntheses of NPs containing Lu^{3+} ions. This also explains the difference between Sr_2LuF_7 - or Ba_2LuF_7 -based materials and the rest of products.

In the group of synthesized materials, three exceptions were observed: in Ca^{2+} - and La^{3+} -containing mixtures, the product was not formed in the applied conditions; Sr^{2+} and La^{3+} ions precipitated as a $SrLaF_5$ compound; Ca^{2+} and Lu^{3+} formed a $Ca_{0.9}Lu_{0.1}F_2$ compound. The explanation of these results is unclear. It is worth noting that the difference between the ionic radii of Ca^{2+} and La^{3+} is the smallest of the all used metal ions as well as the difference in stability constant of EDTA complexes. In addition, the differences in the size of M^{2+} and RE^{3+} ions in the remaining two cases are one of the smallest. This may be associated with the tendency to form the structure closest to cubic CaF_2 .

In our opinion, the information mentioned above is critical in designing the properties of fluoride nanocrystals and planning their syntheses. A similar mechanism can be extended to systems containing other chelating agents, such as citric acid or polyethylene glycol.

Morphology of the products was determined by analyzing XRD patterns and TEM images. The characteristics of the XRD patterns indicate the nanocrystallinity of the products. Average nanocrystal sizes, calculated using the Scherrer equation,⁸¹ vary in the range 9–21 nm and are displayed in Table 1. The TEM images together with size distribution histograms are presented in Figure 3. They show a very similar, quasi-spherical shape of the nanocrystals as well as their tendency to agglomerate. However, some single nanocrystals can still be observed, proving that they are not strongly connected. The $Ba_2LaF_7:Yb^{3+},Er^{3+}$ sample (Figure 3f) presented the smallest average particle size, estimated at approximately 9 nm, but the nanocrystal sizes of the other products were also small. The sample was composed of Ba_2LaF_7 nanocrystals making small clusters of several nanocrystals. Such behavior was not observed in other materials. The determined nanocrystal dimensions are comparable with those calculated from the Scherrer equation except for $Ba_2YF_7:Yb^{3+},Er^{3+}$. All nanocrystals exhibited a high degree of crystallinity.

Spectroscopic Properties. Upconversion properties were studied under excitation by a pulsed laser ($\lambda_{ex} = 976$ nm). Emission and excitation spectra are presented in Figure 4. Luminescence decays were also recorded for each transition band as well as the dependencies of the emission intensity on laser energy were obtained. The calculated emission lifetimes and the number of photons involved in the upconversion process are presented in Table 2. Experimental data (luminescence decays and dependencies of emission intensities on laser energy) are presented in the Supporting Information (Figures S3 and S4).

Figure 4 shows that the spectra of all samples show similar emission and excitation peaks with quite different intensities. The highest emission intensities were recorded for $Sr_2LuF_7:Yb^{3+},Er^{3+}$ and $Ba_2LuF_7:Yb^{3+},Er^{3+}$ samples. Also the emission intensity of $Ba_2GdF_7:Yb^{3+},Er^{3+}$ was relatively high. The other materials showed low emission or their emission was even almost quenched, like, e.g., for $Ca_2YF_7:Yb^{3+},Er^{3+}$.

The excitation spectra observed in Figure 4 show a narrow band with the maximum at 976 nm, characteristic of the ${}^2F_{7/2} \rightarrow {}^2F_{5/2}$ transition of Yb^{3+} ions. These ions participate in the

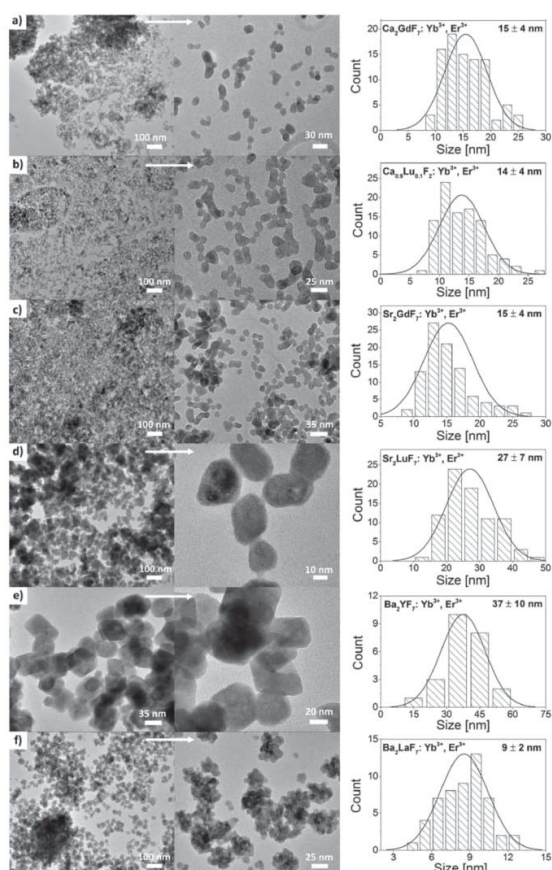


Figure 3. TEM images and nanocrystal size distributions of hydrothermally synthesized samples: (a) $\text{Ca}_2\text{GdF}_7:\text{Yb}^{3+},\text{Er}^{3+}$, (b) $\text{Ca}_{0.9}\text{Lu}_{0.1}\text{F}_2:\text{Yb}^{3+},\text{Er}^{3+}$, (c) $\text{Sr}_2\text{GdF}_7:\text{Yb}^{3+},\text{Er}^{3+}$, (d) $\text{Sr}_2\text{LuF}_7:\text{Yb}^{3+},\text{Er}^{3+}$, (e) $\text{Ba}_2\text{YF}_7:\text{Yb}^{3+},\text{Er}^{3+}$, (f) $\text{Ba}_2\text{LaF}_7:\text{Yb}^{3+},\text{Er}^{3+}$.

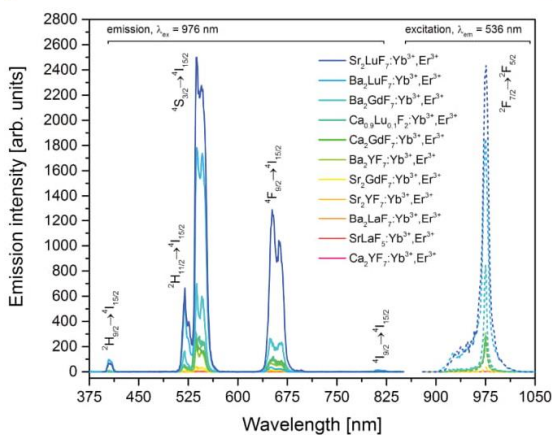


Figure 4. Upconversion luminescence (solid line) and excitation spectra of synthesized materials under pulsed excitation source (at $15 \text{ mJ}\cdot\text{cm}^{-2}$).

energy transfer process (as sensitizers) to Er^{3+} ions, which results in photon upconversion.

The intensity of UC is connected with the concentration of Yb^{3+} ions. The samples in which the Yb^{3+} ion concentration is high also show intense emission, which may be expected as Yb^{3+} ions absorb exciting radiation. Analysis of the sample composition is crucial for the appropriate interpretation of spectroscopic results. The presented results indicate that preparation of a series of samples, keeping the same conditions in the synthesis, does not necessarily lead to the desired composition of each product.

In the emission spectra, the $^4\text{S}_{3/2} \rightarrow ^4\text{I}_{15/2}$ transition (with a maximum at 536 nm) was observed as the most intense for all samples. Therefore, the color of the samples luminescence was green. The ratio between the intensities of transitions for the obtained nanopowders was very similar (see Figure S2). Four characteristic transitions of Er^{3+} ions: $^2\text{H}_{9/2} \rightarrow ^4\text{I}_{15/2}$ (~406 nm), $^2\text{H}_{11/2} \rightarrow ^4\text{I}_{15/2}$ (~520 nm), $^4\text{S}_{3/2} \rightarrow ^4\text{I}_{15/2}$ (~540 nm), and $^4\text{F}_{9/2} \rightarrow ^4\text{I}_{15/2}$ (~650 nm) were recorded only for some of the materials obtained: $\text{Sr}_2\text{LuF}_7:\text{Yb}^{3+},\text{Er}^{3+}$, $\text{Ba}_2\text{LuF}_7:\text{Yb}^{3+},\text{Er}^{3+}$, $\text{Ba}_2\text{GdF}_7:\text{Yb}^{3+},\text{Er}^{3+}$, $\text{Ca}_{0.9}\text{Lu}_{0.1}\text{F}_2:\text{Yb}^{3+},\text{Er}^{3+}$, and $\text{Ca}_2\text{GdF}_7:\text{Yb}^{3+},\text{Er}^{3+}$, which is related to the tendency of the $^2\text{H}_{9/2} \rightarrow ^4\text{I}_{15/2}$ level to be quenched by a cross-relaxation process, or a noneffective, multiphonon de-excitation process.⁸²

The upconversion quantum yields determined for the best emitting samples are presented in Figure 5. The calculated values were the highest for $\text{Sr}_2\text{LuF}_7:\text{Yb}^{3+},\text{Er}^{3+}$ and $\text{Ba}_2\text{LuF}_7:\text{Yb}^{3+},\text{Er}^{3+}$ the two best emitting samples (see also Table S2 and Figure 4). In these samples a saturation effect was observed, visible as a plateau-like region at higher power densities. The observed saturation may be explained by excitation trapping into intermediate state involved in UC mechanism. For Er^{3+} it is long-lived (bottleneck) $^4\text{I}_{13/2}$ excited state being unavailable for further excitation transfer at higher power densities.^{10,83}

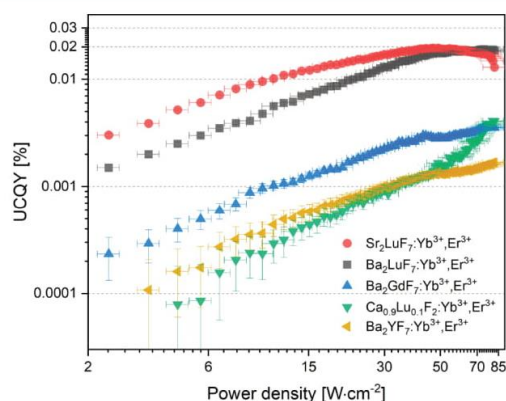
UCQYs are rarely published owing to the difficulties in their determination.^{36,43,66,83–89} The obtained values are usually low, in comparison to those for downshifting phosphors. The highest published values do not exceed several percent, and they were determined only for the core/shell samples, prepared by the thermal decomposition method.^{43,89,90} UCQY for a sample prepared by the hydrothermal method had been reported previously only once by Balabhadra et al.⁶⁶

The most often studied $\text{NaYF}_4:\text{Yb}^{3+},\text{Er}^{3+}$ nanoparticles, which showed one of the brightest emissions, revealed UCQY from 0.0022% to 0.32% under 980 nm laser irradiation, depending on the concentration of dopant ions, synthesis procedure, and particle size.^{36,44,65,67,90} Comparison of UCQYs determined for samples doped with Yb^{3+} and Er^{3+} presented in Supporting Information (Table S2) shows that Sr_2LuF_7 and Ba_2LuF_7 -based samples are capable of efficient emission, in some cases with higher quantum yield than for the most studied and best known $\text{NaYF}_4:\text{Yb}^{3+},\text{Er}^{3+}$ nanoparticles. It should be emphasized that the materials prepared by us were obtained by the hydrothermal method based on water solution, in contrast to most of the other reports. UCQY values measured in nonwater solutions are usually higher.⁴⁶ Also reported power densities, used for UCQYs measurements, were usually higher than applied in this article.

Because of the nonlinear nature of UC, the QYs of this process are strongly dependent on the excitation density.^{12,66,46,91} Furthermore, properties such as laser beam shape can also influence UCQYs.⁴³ Therefore, UC properties

Table 2. Emission Lifetimes Calculated on the Basis of Luminescence Decays and the Number of Photons Determined from Dependencies of Luminescence Intensity on Laser Energy^a

sample name	emission lifetimes (μs)					number of photons			
	$^2\text{H}_{9/2} \rightarrow ^4\text{I}_{15/2}$	$^2\text{H}_{11/2} \rightarrow ^4\text{I}_{15/2}$	$^4\text{S}_{3/2} \rightarrow ^4\text{I}_{15/2}$	$^4\text{F}_{9/2} \rightarrow ^4\text{I}_{15/2}$	$^2\text{H}_{11/2} \rightarrow ^4\text{I}_{15/2}$	$^2\text{H}_{11/2} \rightarrow ^4\text{I}_{15/2}$	$^4\text{S}_{3/2} \rightarrow ^4\text{I}_{15/2}$	$^4\text{F}_{9/2} \rightarrow ^4\text{I}_{15/2}$	$^4\text{F}_{9/2} \rightarrow ^4\text{I}_{15/2}$
$\text{Ca}_2\text{YF}_7:3.9\%\text{Yb}^{3+},0.6\%\text{Er}^{3+}$		7.5	8.4	10.9		1.6	1.6		
$\text{Sr}_2\text{YF}_7:5.6\%\text{Yb}^{3+},0.9\%\text{Er}^{3+}$		20.1	20.3	65.6		1.1	1.5	1.2	
$\text{Ba}_2\text{YF}_7:5.1\%\text{Yb}^{3+},0.9\%\text{Er}^{3+}$	74.4	73.4	107.7	336.7		1.8	2.3	1.9	
$\text{SrLaF}_3:0.8\%\text{Yb}^{3+},0.2\%\text{Er}^{3+}$		22.4	35.5	95.2		1.2	0.75		
$\text{Ba}_2\text{LuF}_7:1.1\%\text{Yb}^{3+},0.2\%\text{Er}^{3+}$		27.7	28.8	144.9		1.6	1.5	1.3	
$\text{Ca}_2\text{GdF}_7:3.7\%\text{Yb}^{3+},0.7\%\text{Er}^{3+}$	142.7	285.5	271.5	521.2	1.6	1.5	1.8	1.6	
$\text{Sr}_2\text{GdF}_7:5.5\%\text{Yb}^{3+},0.9\%\text{Er}^{3+}$		18.1	19.9	48.1		1.1	1.5	1.4	
$\text{Ba}_2\text{GdF}_7:7.5\%\text{Yb}^{3+},1.1\%\text{Er}^{3+}$	80.1	104.1	108.9	334.0	1.1	1.9	1.8	1.8	
$\text{Ca}_{0.9}\text{Lu}_{0.1}\text{F}_2:3.5\%\text{Yb}^{3+},0.5\%\text{Er}^{3+}$	20.4	28.3	27.2	61.7	1.5	1.3	1.6	1.4	
$\text{Sr}_2\text{LuF}_7:19.3\%\text{Yb}^{3+},3.0\%\text{Er}^{3+}$	65.6	103.2	106.9	225.2	2.5	1.5	1.6	1.7	
$\text{Ba}_2\text{LuF}_7:22.8\%\text{Yb}^{3+},3.1\%\text{Er}^{3+}$	63.5	91.1	93.2	202.4		1.8	1.9	1.9	

^aExperimental data in Supporting Information, Figures S3 and S4.**Figure 5.** Upconversion quantum yields calculated for the best emitting samples.

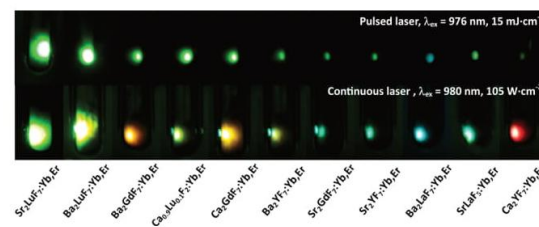
are sensitive to instrumentation, which makes it difficult to compare properties of the same materials in different setups.⁹⁰

The determined UCQYs were lower than for the best-known emitters. However, the emissions QY of $\text{Sr}_2\text{LuF}_7:\text{Yb}^{3+},\text{Er}^{3+}$ and $\text{Ba}_2\text{LuF}_7:\text{Yb}^{3+},\text{Er}^{3+}$ NPs are still at a satisfactory level, comparable with some of the reports for NaREF_4 -type materials. This makes the obtained materials look promising for upconversion applications. Moreover, the M_2REF_7 -type materials seem to be excellent candidates for synthesis by the thermal decomposition method.

The small difference in UCQY values between the two the best emitting materials results from different nanocrystals size, which are smaller in $\text{Ba}_2\text{LuF}_7:\text{Yb}^{3+},\text{Er}^{3+}$ (see Table 1). The relatively low QY values of the remaining $\text{M}^{2+}\text{-RE}^{3+}$ systems resulted from the low dopant concentrations. Also the synthesis method used, which requires the presence of water, may be responsible for low UCQY as the $-\text{OH}$ oscillators quench the higher excited states of Ln^{3+} ions.⁹² Other factors affecting UCQY are nonradiative processes between Ln^{3+} dopants, such as cross-relaxation and down-shifting emission of Yb^{3+} and Er^{3+} ions (above 1000 nm).⁹⁰ The dependence of QYs on the type of host used was similar as that presented in Figure 4.

The upconversion properties of the prepared materials were highly dependent on the excitation source, as shown in Figure

6. The pulsed excitation results mostly in a two-photon process (Table 2 and Figure S4), populating green- and red-emitting

**Figure 6.** Upconversion luminescence images under NIR excitation (pulsed and continuous lasers).

Er^{3+} energy levels similarly, whereas continuous laser excitation may lead to a saturation effect, which was most noticeable for the green emission band at higher power densities.^{4,3}

Luminescence decays measured for the obtained samples were used for calculation of luminescence lifetimes and are collected in Table 2 (for emission decays see Figure S3). From among all obtained matrices doped with $\text{Yb}^{3+}/\text{Er}^{3+}$ ions, the longest emission was found for Ca_2GdF_7 (between 142.7 and 521.2 μs , depending on the transition band). Long lifetimes were also calculated for Ba_2YF_7 (74.4–336.7 μs) and Ba_2GdF_7 -based materials (80.1–334.0 μs). The shortest (7.5–10.9 μs) emission was recorded for $\text{Ca}_2\text{YF}_7:\text{Yb}^{3+},\text{Er}^{3+}$, which may be connected to the very low content of dopant ions in this matrix. It is worth mentioning that for samples $\text{Sr}_2\text{LuF}_7:\text{Yb}^{3+},\text{Er}^{3+}$ and $\text{Ba}_2\text{LuF}_7:\text{Yb}^{3+},\text{Er}^{3+}$, which exhibited the strongest emission of light from all samples, the lifetimes were relatively short ($\text{Sr}_2\text{LuF}_7:\text{Yb}^{3+},\text{Er}^{3+}$ $\tau = 225.25$ μs , $\text{Ba}_2\text{LuF}_7:\text{Yb}^{3+},\text{Er}^{3+}$ $\tau = 202.41$ μs for the $^4\text{F}_{9/2} \rightarrow ^4\text{I}_{15/2}$ transition). The observed spectroscopic properties lead us to assume that the differences between samples are not only a result of their composition but also other factors. The EDTA adsorbed during the synthesis as well as the inhomogeneous distribution of dopant ions may also influence the upconversion process and luminescence decays.⁹³ This effect is especially visible in host materials in which alkaline M^{2+} ions are replaced by rare earth ions, RE^{3+} , requiring different charge compensation.

For all samples, the longest decay times were measured for the $^4\text{F}_{9/2} \rightarrow ^4\text{I}_{15/2}$ transition. It may be caused by the necessity

of the cross-relaxation process preceding the feeding of the $^4F_{9/2}$ excited state or even a different excitation mechanism.⁶ According to Xiang et al.,^{94,95} if the decay time of the transition $^4F_{9/2} \rightarrow ^4I_{15/2}$ is almost twice as long (or even more) than the $^4S_{3/2} \rightarrow ^4I_{15/2}$ transition, the excitation to the $^4F_{9/2}$ level may occur from the $^4I_{13/2}$ excited state, which is directly populated by energy transfer from Yb^{3+} ions: $^4I_{13/2} (Er^{3+}) + ^2F_{5/2} (Yb^{3+})$ to $^4F_{9/2} (Er^{3+}) + ^2F_{7/2} (Yb^{3+})$. The long rise time for samples that exhibited good emission (Yb^{3+} - and Er^{3+} -doped: Ca_2GdF_7 , $Ca_{0.9}Lu_{0.1}F_2$, Sr_2GdF_7 , Sr_2LuF_7 , Ba_2YF_7 , Ba_2GdF_7 , Ba_2LuF_7 hosts) can also be explained by this mechanism. If the excitation pathway occurs by multiphonon relaxation from $^2H_{11/2}$ to $^4F_{9/2}$, emission lifetime related to $^4F_{9/2} \rightarrow ^4I_{15/2}$ transition should be similar to $^4S_{3/2} \rightarrow ^4I_{15/2}$, which is true only for Ca_2YF_7 sample.

Dependencies of the luminescence intensity on the laser energy were also measured to better understand the mechanism of the UC process. They are presented in Supporting Information, Figure S4. At low power densities, the number of photons involved in the upconversion phenomena is equal to the slope coefficient in linear regressions obtained from excitation power dependencies. The determined numbers of photons involved in the upconversion mechanism are collected in Table 2.

The numbers of photons determined from the experimental data suggest that at least three photons are required to excite Er^{3+} ions to the $^2H_{9/2}$ level, and two photons to achieve $^2H_{11/2}$, $^4S_{3/2}$, and $^4F_{9/2}$ excited states. The schematic energy diagram presented in Figure 7 describes the proposed energy transfer

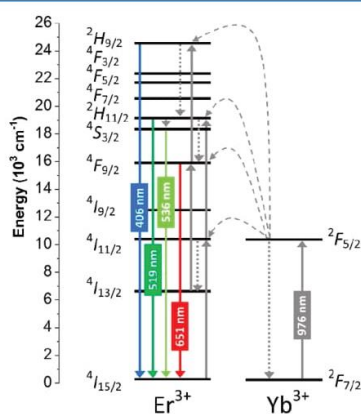


Figure 7. Schematic energy levels diagram for Yb^{3+} and Er^{3+} ion-doped samples.

processes occurring in the obtained materials. The $^4H_{9/2} \rightarrow ^4I_{15/2}$ transition was recorded only for four obtained samples, but, unfortunately, the determined slope values were much lower than the theoretical ones. It is caused by nonradiative deactivation processes, such as cross-relaxation between Er^{3+} ions, and the saturation effect,^{96–98} which appear at high laser energies. For Ba_2GdF_7 , Ba_2YF_7 , and Ca_2GdF_7 -based materials, the calculated slope values are close to two for the $^2H_{11/2} \rightarrow ^4I_{15/2}$, $^4S_{3/2} \rightarrow ^4I_{15/2}$, and $^4F_{9/2} \rightarrow ^4I_{15/2}$ transitions (preceded by two-photon excitation).⁵¹ Interestingly, for the $Ba_2YF_7:Yb^{3+},Er^{3+}$ sample, the $^4S_{3/2}$ excited state can also be

achieved by three-photon absorption followed by relaxation from higher excited states.

On the basis of the obtained values of the slopes, which are greater than 1, it can be concluded that for the other matrices a two-photon process also occurred to excite Er^{3+} ions into their $^2H_{11/2}$, $^4S_{3/2}$, and $^4F_{9/2}$ levels. For the $SrLaF_5$ sample, only two transitions were measured: $^2H_{11/2} \rightarrow ^4I_{15/2}$ and $^4S_{3/2} \rightarrow ^4I_{15/2}$ for which the slope values were 1.22 and 0.75. This confirmed the occurrence of highly quenching processes in this sample and explained the very low emission.

Figure 7 shows the UC mechanism occurring in the obtained alkaline rare-earth fluoride matrices doped with Yb^{3+} and Er^{3+} ions. In these materials, the Yb^{3+} ions acted as sensitizers because of their simple energy level structure and high absorption coefficient in the NIR region. In turn, Er^{3+} ions acted as energy acceptors and luminescence activators. Yb^{3+} ions can be excited by radiation with a wavelength of around 976 nm, which provides a transition from the $^2F_{7/2}$ ground state to the $^2F_{5/2}$ excitation state, having similar energy to the $^4I_{11/2}$ excited state of Er^{3+} ions.⁵³ Therefore, energy can be relatively easily transferred to the neighboring Er^{3+} ions, raising them to the $^4I_{11/2}$ excited state level or, owing to the relaxation processes, to the $^4I_{13/2}$ excited state. Depending on the energy of Er^{3+} ions, two or three photons are required to observe green emission from the $^2H_{11/2}$ and $^4S_{3/2}$ levels. Er^{3+} ions, in their $^4I_{11/2}$ excited state, can absorb the second photon from Yb^{3+} ions, which promotes them to the $^2H_{11/2}$ excited state. Furthermore, neighboring Er^{3+} ions may act as sensitizers, transferring their energy to the Er^{3+} emitter.⁹⁷ From the $^2H_{11/2}$ excited state, green emission may occur, or relaxation to the $^4S_{3/2}$ excited state and finally green emission ($^4S_{3/2} \rightarrow ^4I_{15/2}$ transition).

Excitation into the $^4F_{9/2}$ level of Er^{3+} ions may be realized in several different ways. The first possible pathway is a simple absorption of two photons as a result of energy transfer from Yb^{3+} ions, forming Er^{3+} ions in their $^2H_{11/2}$ excited state. Then, relaxation to the $^4F_{9/2}$ state takes place followed by red emission. However, at this point it needs to be mentioned that the proposed pathway is not always realized. Other mechanisms may also be proposed to explain the origin of the red emission, including cross-relaxation between Er^{3+} ions, which depends on the Er^{3+} concentration.⁶ Another possible pathway requires absorption of a photon from an excited Yb^{3+} ion to the $^4I_{11/2}$ level of the Er^{3+} ion, then relaxation to the $^4I_{13/2}$ state, from which the second absorbed photon results in the Er^{3+} ion in its $^4F_{9/2}$ excited state. Then the emission of red light can be observed.

Another explanation of the origin of the red emission and, in general, the UC mechanism at low Er^{3+} concentrations has been given by Berry et al.⁶ In the proposed mechanism, they proved that red ($^4F_{9/2} \rightarrow ^4I_{15/2}$) UC is preceded by a three-photon excitation process to $^4G/2K$ states through the green emitting $^4S_{3/2}$ and $^2H_{11/2}$ states. Multiphonon relaxation from the Er^{3+} higher-excited states may lead to the blue-emitting state, $^2H_{9/2}$, or by back energy transfer to Yb^{3+} ions to red emitting $^4F_{9/2}$.⁶ The long rise and decay time of the $^4F_{9/2} \rightarrow ^4I_{15/2}$ transition are explained by the fact that the $^4S_{3/2}$ and $^2H_{11/2}$ states are the initial states for the energy transfer from Yb^{3+} ions, leading to excitation of the Er^{3+} ions to their $^4G/2K$ states.⁶

The $^2H_{9/2} \rightarrow ^4I_{15/2}$ transition must be preceded by three-photon absorption. The third photon may be absorbed by Er^{3+}

ions in their $^4F_{9/2}$ excited state achieved by two pathways mentioned above. However, absorption from the $^2H_{11/2}$ excited state is also possible, as mentioned above. Both possible mechanisms lead to the emission of blue light.

CONCLUSIONS

Alkaline, M^{2+} , and rare earth, RE^{3+} , fluorides as well as their Yb^{3+}/Er^{3+} -doped counterparts were synthesized by the hydrothermal method. Three different M^{2+} ions, Ca^{2+} , Sr^{2+} and Ba^{2+} , and four RE^{3+} ions, Y^{3+} , La^{3+} , Gd^{3+} , and Lu^{3+} were used in order to obtain upconverting materials. The synthesized compounds crystallized with $M_{0.67}RE_{0.33}F_{2.33}$ composition in a cubic crystal cell. The mechanism of material formation was studied, indicating the influence of the stability of the metal ion EDTA complexes on the final product composition. The tendency to getting lower than expected concentrations of RE^{3+} metal ions forming complexes with EDTA of high stability was observed. Comparison of the XRD patterns to the references confirmed the formation of nanocrystals of cubic structure. Nanocrystal sizes determined from XRD patterns were in the range of 10–21 nm. Similar results were obtained by analyzing TEM images, which revealed sizes in the range of 9–37 nm.

All of the Yb^{3+} - and Er^{3+} -doped materials exhibited UC phenomenon. The most intense emission under 976 nm excitation was observed for $Sr_2LuF_7:Yb^{3+},Er^{3+}$, $Ba_2LuF_7:Yb^{3+},Er^{3+}$, and $Ba_2GdF_7:Yb^{3+},Er^{3+}$ samples. Luminescence lifetimes were in the range of 7.5–521 μs , depending on the sample, and indicating the complexity of the obtained systems and energy processes occurred. Energy transfer between Yb^{3+} and Er^{3+} ions was also analyzed by measuring the dependence of the integral luminescence intensity on the excitation laser energy. Analysis of experimental data revealed the occurrence of the two- and three-photon processes, preceding the observed upconversion luminescence. In addition, the presence of quenching phenomena was noticed.

The UCQY measured for the two the best emitting samples $Sr_2LuF_7:Yb^{3+},Er^{3+}$, $Ba_2LuF_7:Yb^{3+},Er^{3+}$ ($0.0192 \pm 0.001\%$ and $0.0176 \pm 0.001\%$ respectively) prove good properties of used fluoride compounds as hosts for upconverting Yb^{3+} and Er^{3+} ions. The obtained values were similar to those reported for $NaYF_4$ and $NaGdF_4$, known as the best hosts for UC applications.^{36,44,67,99,100} This result proves the effectiveness of the hydrothermal method which is also easier and more ecofriendly than the thermal decomposition method, as the synthesis conditions do not require inert atmosphere or a vacuum as well as organic solvents. The hydrothermal method may be considered as a good alternative and complementary method for the synthesis of UCNPs.

This study has also shown the importance of such factors as the stability of the precursors in the hydrothermal conditions and the difference between the ionic radii of metal ions forming the host compound, on the spectroscopic properties of the final product. In addition, the necessity of composition determination by a highly accurate technique (ICP-OES) was emphasized. From the series of studied materials, the most promising for further research and applications are $Sr_2LuF_7:Yb^{3+},Er^{3+}$ and $Ba_2LuF_7:Yb^{3+},Er^{3+}$. They can be obtained in hydrothermal conditions as nanomaterials with minimal risk of lower than expected concentrations of Yb^{3+} and Er^{3+} dopant ions.

ASSOCIATED CONTENT

Supporting Information

The Supporting Information is available free of charge on the ACS Publications website at DOI: 10.1021/acs.inorgchem.8b00484.

Table S1: Solubility of metal ions fluorides and stability constants of M^{2+} and RE^{3+} complexes with EDTA; Table S2: Upconversion quantum yields of noncore/shell nanoparticles with similar size to the described in the article products; Figure S1: Schematic representation of system setup used to measure upconversion quantum yields; Figure S2: Integral emission intensities of the red and the green bands, and the ratio between them calculated for the obtained samples; Figure S3: Upconversion luminescence decays; Figure S4: Comparison of upconversion luminescence dependencies on laser energy) (PDF)

AUTHOR INFORMATION

Corresponding Author

*E-mail: tgrzyb@amu.edu.pl.

ORCID

Tomasz Grzyb: 0000-0002-2947-6366

Notes

The authors declare no competing financial interest.

ACKNOWLEDGMENTS

Funding for this research was provided by the National Science Centre, Poland (Grant No. DEC-2011/03/D/ST5/05701 and DEC-2016/22/E/ST5/00016).

REFERENCES

- (1) Chuai, X.; Guo, X.; Liu, X.; He, G.; Zheng, K.; He, C.; Qin, W. Bifunctional $NaGdF_4:Yb,Er,Fe$ Nanocrystals with the Enhanced Upconversion Fluorescence. *Opt. Mater.* **2015**, *44*, 13–17.
- (2) Zhang, Y.; Liu, X.; Lang, Y.; Yuan, Z.; Zhao, D.; Qin, G.; Qin, W. Synthesis of Ultra-Small $BaLuF_5:Yb^{3+},Er^{3+}$ @ $BaLuF_5:Yb^{3+}$ Active-Core-active-Shell Nanoparticles with Enhanced. *J. Mater. Chem. C* **2015**, *3*, 2045–2053.
- (3) Rao, L.; Lu, W.; Zeng, T.; Yi, Z.; Wang, H.; Liu, H.; Zeng, S. One-Pot Synthesis of PEG Modified $BaLuF_5:Gd/Yb/Er$ Nanoparticles for Dual-Modal in Vivo Upconversion Luminescence and X-Ray Bioimaging. *Dalton Trans.* **2014**, *43*, 13343–13348.
- (4) Dong, H.; Sun, L.-D.; Yan, C.-H. Energy Transfer in Lanthanide Upconversion Studies for Extended Optical Applications. *Chem. Soc. Rev.* **2015**, *44*, 1608–1634.
- (5) Liu, G. Advances in the Theoretical Understanding of Photon Upconversion in Rare-Earth Activated Nanophosphors. *Chem. Soc. Rev.* **2015**, *44*, 1635–1652.
- (6) Berry, M. T.; May, P. S. Disputed Mechanism for NIR-to-Red Upconversion Luminescence in $NaYF_4:Yb^{3+},Er^{3+}$. *J. Phys. Chem. A* **2015**, *119*, 9805–9811.
- (7) Li, X.; Gai, S.; Li, C.; Wang, D.; Niu, N.; He, F.; Yang, P. Monodisperse Lanthanide Fluoride Nanocrystals: Synthesis and Luminescent Properties. *Inorg. Chem.* **2012**, *51*, 3963–3971.
- (8) Wang, F.; Banerjee, D.; Liu, Y.; Chen, X.; Liu, X. Upconversion Nanoparticles in Biological Labeling, Imaging, and Therapy. *Analyst* **2010**, *135*, 1839–1854.
- (9) Auzel, F. Compteur Quantique Par Transfert D'energie Entre de Yb^{3+} a Tm^{3+} Dans Un Tungstate Mixte et Dans Verre Germanate. *C. R. Acad. Sci. Paris B* **1966**, *263*, 819–821.
- (10) Auzel, F. Upconversion and Anti-Stokes Processes with f and d Ions in Solids. *Chem. Rev.* **2004**, *104*, 139–173.

- (11) Brites, C. D. S.; Millán, A.; Carlos, L. D. Lanthanides in Luminescent Thermometry. In *Handbook on the Physics and Chemistry of Rare Earths*; Bünzli, J.-C., Pecharsky, V., Eds.; Elsevier, 2016; Vol. 49, pp 339–427.
- (12) Chen, G.; Qiu, H.; Prasad, P. N.; Chen, X. Upconversion Nanoparticles: Design, Nanochemistry, and Applications in Theranostics. *Chem. Rev.* **2014**, *114*, 5161–5214.
- (13) DaCosta, M. V.; Doughan, S.; Han, Y.; Krull, U. J. Lanthanide Upconversion Nanoparticles and Applications in Bioassays and Bioimaging: A Review. *Anal. Chim. Acta* **2014**, *832*, 1–33.
- (14) Smet, P. F.; Van den Eeckhout, K.; De Clercq, O. Q.; Poelman, D. *Persistent Phosphors*; 1st ed.; Elsevier B.V., 2015; Vol. 48.
- (15) Reszczyńska, J.; Grzyb, T.; Wei, Z.; Klein, M.; Kowalska, E.; Ohtani, B.; Zaleska-Medynska, A. Photocatalytic Activity and Luminescence Properties of RE³⁺-TiO₂ Nanocrystals Prepared by Sol-gel and Hydrothermal Methods. *Appl. Catal., B* **2016**, *181*, 825–837.
- (16) van der Ende, B. M.; Aarts, L.; Meijerink, A. Lanthanide Ions as Spectral Converters for Solar Cells. *Phys. Chem. Chem. Phys.* **2009**, *11*, 11081–11095.
- (17) Yang, D.; Dai, Y.; Liu, J.; Zhou, Y.; Chen, Y.; Li, C.; Ma, P.; Lin, J. Ultra-Small BaGdF₅-Based Upconversion Nanoparticles as Drug Carriers and Multimodal Imaging Probes. *Biomaterials* **2014**, *35*, 2011–2023.
- (18) Feng, L.; Gai, S.; He, F.; Dai, Y.; Zhong, C.; Yang, P.; Lin, J. Multifunctional Mesoporous ZrO₂ encapsulated Upconversion Nanoparticles for Mild NIR Light Activated Synergistic Cancer Therapy. *Biomaterials* **2017**, *147*, 39–52.
- (19) Xu, J.; Gulzar, A.; Liu, Y.; Bi, H.; Gai, S.; Liu, B.; Yang, D.; He, F.; Yang, P. Integration of IR-808 Sensitized Upconversion Nanostructure and MoS₂ Nanosheet for 808 Nm NIR Light Triggered Phototherapy and Bioimaging. *Small* **2017**, *13*, 1701841.
- (20) Xu, J.; Yang, P.; Sun, M.; Bi, H.; Liu, B.; Yang, D.; Gai, S.; He, F.; Lin, J. Highly Emissive Dye-Sensitized Upconversion Nanostructure for Dual-Photosensitizer Photodynamic Therapy and Bioimaging. *ACS Nano* **2017**, *11*, 4133–4144.
- (21) Cheng, Z.; Lin, J. Synthesis and Application of Nanohybrids Based on Upconverting Nanoparticles and Polymers. *Macromol. Rapid Commun.* **2015**, *36*, 790–827.
- (22) Chen, D. Q.; Yu, Y. L.; Huang, F.; Lin, H.; Huang, P.; Yang, A. P.; Wang, Z. X.; Wang, Y. S. Lanthanide Dopant-Induced Formation of Uniform Sub-10 Nm Active-Core/active-Shell Nanocrystals with near-Infrared to near-Infrared Dual-Modal Luminescence. *J. Mater. Chem.* **2012**, *22*, 2632–2640.
- (23) Wang, C.; Cheng, L.; Liu, Z. Upconversion Nanoparticles for Photodynamic Therapy and Other Cancer Therapeutics. *Theranostics* **2013**, *3*, 317–330.
- (24) Villa, I.; Vedda, A.; Cantarelli, I. X.; Pedroni, M.; Piccinelli, F.; Bettinelli, M.; Speghini, A.; Quintanilla, M.; Vetrone, F.; Rocha, U.; Jacinto, C.; Carrasco, E.; Rodríguez, F.; Juarranz, A.; del Rosal, B.; Ortgies, D. H.; Gonzalez, P. H.; Solé, J. G.; Garcia, D. J. 1.3 Mm Emitting SrF₂:Nd³⁺ Nanoparticles for High Contrast in Vivo Imaging in the Second Biological Window. *Nano Res.* **2015**, *8*, 649–665.
- (25) Runowski, M.; Ekner-Grzyb, A.; Mrówczyńska, L.; Balabhadra, S.; Grzyb, T.; Paczesny, J.; Zep, A.; Lis, S. Synthesis and Organic Surface Modification of Luminescent, Lanthanide-Doped Core/Shell Nanomaterials (LnF₃@SiO₂@NH₂@Organic Acid) for Potential Bioapplications: Spectroscopic, Structural, and in Vitro Cytotoxicity Evaluation. *Langmuir* **2014**, *30*, 9533–9543.
- (26) Dou, Q. Q.; Guo, H. C.; Ye, E. Near-Infrared Upconversion Nanoparticles for Bio-Applications. *Mater. Sci. Eng., C* **2014**, *45*, 635–643.
- (27) Grzyb, T.; Runowski, M.; Dąbrowska, K.; Giersig, M.; Lis, S. Structural, Spectroscopic and Cytotoxicity Studies of TbF₃@CeF₃ and TbF₃@CeF₃@SiO₂ Nanocrystals. *J. Nanopart. Res.* **2013**, *15*, 1958.
- (28) Runowski, M.; Goderski, S.; Paczesny, J.; Książkowska-Gocalska, M.; Ekner-Grzyb, A.; Grzyb, T.; Rybka, J. D.; Giersig, M.; Lis, S. Preparation of Biocompatible, Luminescent-Plasmonic Core/Shell Nanomaterials Based on Lanthanide and Gold Nanoparticles Exhibiting SERS Effects. *J. Phys. Chem. C* **2016**, *120*, 23788–23798.
- (29) Chen, J.; Zhao, J. X. Upconversion Nanomaterials: Synthesis, Mechanism, and Applications in Sensing. *Sensors* **2012**, *12*, 2414–2435.
- (30) Muhr, V.; Wilhelm, S.; Hirsch, T.; Wolfbeis, O. S. Upconversion Nanoparticles: From Hydrophobic to Hydrophilic Surfaces. *Acc. Chem. Res.* **2014**, *47*, 3481–3493.
- (31) Sperling, R. a.; Parak, W. J. Surface Modification, Functionalization and Bioconjugation of Colloidal Inorganic Nanoparticles. *Philos. Trans. R. Soc., A* **2010**, *368*, 1333–1383.
- (32) Gnach, A.; Lipinski, T.; Bednarkiewicz, A.; Rybka, J.; Capobianco, J. a. Upconverting Nanoparticles: Assessing the Toxicity. *Chem. Soc. Rev.* **2015**, *44*, 1561–1584.
- (33) De, G.; Qin, W.; Wang, W.; Gui, B. Infrared-to-Ultraviolet Upconversion Luminescence of La_{0.95}Yb_{0.49}Tm_{0.01}F₃ Nanostructures. *Opt. Commun.* **2009**, *282*, 2950–2953.
- (34) Xu, C.; Ma, M.; Yang, L.; Zeng, S.; Yang, Q. Upconversion Luminescence and Magnetic Properties of Ligand-Free Monodisperse Lanthanide Doped BaGdF₅ Nanocrystals. *J. Lumin.* **2011**, *131*, 2544–2549.
- (35) Jiang, T.; Qin, W.; Di, W.; Yang, R.; Liu, D.; Zhai, X.; Qin, G. Citric Acid-Assisted Hydrothermal Synthesis of α-NaYF₄:Yb³⁺,Tm³⁺ Nanocrystals and Their Enhanced Ultraviolet Upconversion Emissions. *CrystEngComm* **2012**, *14*, 2302.
- (36) Brites, C. D. S.; Xie, X.; Debasu, M. L.; Qin, X.; Chen, R.; Huang, W.; Rocha, J.; Liu, X.; Carlos, L. D. Instantaneous Ballistic Velocity of Suspended Brownian Nanocrystals Measured by Upconversion Nanothermometry. *Nat. Nanotechnol.* **2016**, *11*, 851.
- (37) Voß, B.; Nordmann, J.; Uhl, A.; Komban, R.; Haase, M. Effect of the Crystal Structure of Small Precursor Particles on the Growth of β-NaREF₄ (RE = Sm, Eu, Gd, Tb) Nanocrystals. *Nanoscale* **2013**, *5*, 806–812.
- (38) Yan, C.-H.; Yan, Z.-G.; Du, Y.-P.; Shen, J.; Zhang, C.; Feng, W. Controlled Synthesis and Properties of Rare Earth Nanomaterials. In *Handbook on the Physics and Chemistry of Rare Earths*; Gschneidner, K. A., Bünzli, J.-C., Pecharsky, V., Eds.; Elsevier, 2011; Vol. 41, pp 275–472.
- (39) Fedorov, P. P.; Luginina, A. A.; Ermakova, J. A.; Kuznetsov, S. V.; Voronov, V. V.; Uvarov, O. V.; Pynenkov, A. A.; Nishchev, K. N. Preparation of Nanodispersed Fluorite-Type Sr_{1-x}R_xF_{2+2x} (R = Er, Yb, Ho) Phases from Citrate Solutions. *J. Fluorine Chem.* **2017**, *194*, 8–15.
- (40) Grzyb, T.; Runowski, M.; Szczeszak, A.; Lis, S. Influence of Matrix on the Luminescent and Structural Properties of Glycerine-Capped, Tb³⁺-Doped Fluoride Nanocrystals. *J. Phys. Chem. C* **2012**, *116*, 17188–17196.
- (41) Mayakova, M. N.; Luginina, A. A.; Kuznetsov, S. V.; Voronov, V. V.; Ermakov, R. P.; Baranchikov, A. E.; Ivanov, V. K.; Karban, O. V.; Fedorov, P. P. Synthesis of SrF₂-YF₃ nanopowders by Co-Precipitation from Aqueous Solutions. *Mendeleev Commun.* **2014**, *24*, 360–362.
- (42) Shi, F.; Zhao, Y. Sub-10 Nm and Monodisperse β-NaYF₄:Yb,Tm,Gd Nanocrystals with Intense Ultraviolet Upconversion Luminescence. *J. Mater. Chem. C* **2014**, *2*, 2198–2203.
- (43) Kaiser, M.; Würth, C.; Kraft, M.; Hyppänen, I.; Soukka, T.; Resch-Genger, U. Power-Dependent Upconversion Quantum Yield of NaYF₄:Yb³⁺,Er³⁺ Nano- and Micrometer-Sized Particles – Measurements and Simulations. *Nanoscale* **2017**, *9*, 10051–10058.
- (44) Boyer, J.-C.; van Veggel, F. C. J. M. Absolute Quantum Yield Measurements of Colloidal NaYF₄:Er³⁺,Yb³⁺ Upconverting Nanoparticles. *Nanoscale* **2010**, *2*, 1417.
- (45) Nadort, A.; Sreenivasan, V. K. A.; Song, Z.; Grebenik, E. A.; Nechaev, A. V.; Semchishen, V. A.; Panchenko, V. Y.; Zvyagin, A. V. Quantitative Imaging of Single Upconversion Nanoparticles in Biological Tissue. *PLoS One* **2013**, *8*, e63292.
- (46) Würth, C.; Kaiser, M.; Wilhelm, S.; Grauel, B.; Hirsch, T.; Resch-Genger, U. Excitation Power Dependent Population Pathways and Absolute Quantum Yields of Upconversion Nanoparticles in Different Solvents. *Nanoscale* **2017**, *9*, 4283–4294.

- (47) Mao, Y.; Ma, M.; Gong, L.; Xu, C.; Ren, G.; Yang, Q. Controllable Synthesis and Upconversion Emission of Ultrasmall near-Monodisperse Lanthanide-Doped Sr_2LaF_7 Nanocrystals. *J. Alloys Compd.* **2014**, *609*, 262–267.
- (48) Liu, Q.; Yan, X.; Chen, Y.; Wang, X. Upconversion Emission of $\text{SrYbF}_5\text{:Er}^{3+}$ Nanosheets Modified by Tm^{3+} Ions. *J. Rare Earths* **2013**, *31*, 1053–1058.
- (49) Ma, M.; Xu, C.; Yang, L.; Yang, Q.; Lin, J. Solvothermal Synthesis and Tailored Upconversion Emission of Monodisperse Ultrasmall Face-Centered Cubic Sr_2YF_7 Nanocrystals. *J. Alloys Compd.* **2012**, *525*, 97–102.
- (50) Guo, L.; Wang, Y.; Zhang, J.; Dong, P.; Wang, Y. Crystal Structure and up- and down-Conversion Properties of Yb^{3+} , Ho^{3+} Codoped BaGdF_5 Solid-Solution with Different Morphologies. *CrystEngComm* **2012**, *14*, 3131.
- (51) Du, H.; Zhang, W.; Sun, J. Structure and Upconversion Luminescence Properties of $\text{BaYF}_5\text{:Yb}^{3+}, \text{Er}^{3+}$ Nanoparticles Prepared by Different Methods. *J. Alloys Compd.* **2011**, *509*, 3413–3418.
- (52) Chen, C.; Liu, J.; Chen, Y.; Li, C.; Liu, X.; Huang, H.; Liang, C.; Lou, Y.; Shi, Z.; Feng, S. Sub-10 Nm $\text{Sr}_2\text{LuF}_7\text{:Yb/Er@Sr}_2\text{GdF}_7\text{:@SrF}_2$ Up-Conversion Nanocrystals for Up-Conversion Luminescence–Magnetic Resonance—Computed Tomography Trimodal Bioimaging. *ACS Appl. Mater. Interfaces* **2017**, *9*, 5748–5756.
- (53) Gong, L.; Ma, M.; Xu, C.; Li, X.; Wang, S.; Lin, J.; Yang, Q. Multicolor Upconversion Emission of Dispersed Ultrasmall Cubic Sr_2LuF_7 Nanocrystals Synthesized by a Solvothermal Process. *J. Lumin.* **2013**, *134*, 718–723.
- (54) Chuai, X.; Zhang, D.; Zhao, D.; Zheng, K.; He, C.; Shi, F.; Wang, L.; Chen, H.; Qin, W. Synthesis and Characterization of $\text{Yb}^{3+}, \text{Tm}^{3+}\text{:Ba}_2\text{YF}_7$ Nanocrystalline with Efficient Upconversion Fluorescence. *Mater. Lett.* **2011**, *65*, 2368–2370.
- (55) Chuai, X.; Yin, F.; Liu, Z.; Shi, F.; Wang, J.; Wang, L.; Zheng, K.; He, C.; Qin, W. Tunable Upconversion Emission in $\text{Ba}_2\text{YF}_7\text{:Yb}^{3+}/\text{Er}^{3+}$ Nanocrystals with Different Yb^{3+} Concentration. *Mater. Res. Bull.* **2013**, *48*, 2361–2364.
- (56) Li, H.; Liu, G.; Wang, J.; Dong, X.; Yu, W. Hydrothermal Synthesis, down-/enhanced up-Conversion, Color Tuning Luminescence, Energy Transfer and Paramagnetic Properties of Ln^{3+} ($\text{Ln} = \text{Eu/Dy, Yb/Ho}$)-Doped Ba_2GdF_7 Multifunctional Nanophosphors. *New J. Chem.* **2017**, *41*, 1609–1617.
- (57) Greis, O.; Haschke, J. M. Chapter 45: Rare Earth Fluorides. *Handbook on the Physics and Chemistry of Rare Earths* **1982**, *5*, 387–460.
- (58) Golubev, A. M.; Simonov, V. I. Superlattice Structures Based on Fluorite. *Kristallografiya* **1986**, *31*, 478.
- (59) Sobolev, B. P. Part I. The High Temperature Chemistry of the Rare Earth Trifluorides. In *The Rare Earth Trifluorides*; Institut d'Estudis Catalans: Barcelona, 2000; p 520.
- (60) Fedorov, P. P.; Mayakova, M. N.; Kuznetsov, S. V.; Voronov, V. V.; Ermakov, R. P.; Samarina, K. S.; Popov, A. I.; Osiko, V. V. Co-Precipitation of Yttrium and Barium Fluorides from Aqueous Solutions. *Mater. Res. Bull.* **2012**, *47*, 1794–1799.
- (61) Sun, J.; Xian, J.; Du, H. Hydrothermal Synthesis of $\text{BaYF}_5\text{:Yb}^{3+}/\text{Er}^{3+}$ Upconversion Luminescence Submicrospheres by a Surfactant-Free Aqueous Solution Route. *J. Phys. Chem. Solids* **2011**, *72*, 207–213.
- (62) Yan, Z.-Y.; Yan, B. Luminescent Hybrid Ionogels Functionalized with Rare Earth Fluoride up-Conversion Nanocrystals Dispersing in Ionic Liquid. *Photochem. Photobiol.* **2013**, *89*, 1262–1268.
- (63) Huang, S.; Gao, Q.; Gu, M. Enhanced Luminescence in Transparent Glass Ceramics Containing $\text{BaYF}_5\text{:Ce}^{3+}$ Nanocrystals. *J. Lumin.* **2012**, *132*, 750–754.
- (64) Lutterotti, L.; Bortolotti, M. Object Oriented Programming and Fast Computation Techniques in Maud, a Program for Powder Diffraction Analysis Written in Java. *Compcomm. Newsl.* **2003**, *1*, 43–50.
- (65) Wang, J.; Deng, R.; MacDonald, M. A.; Chen, B.; Yuan, J.; Wang, F.; Chi, D.; Hor, T. S. A.; Zhang, P.; Liu, G.; Han, Y.; Liu, X. Enhancing Multiphoton Upconversion through Energy Clustering at Sublattice Level. *Nat. Mater.* **2014**, *13*, 157–162.
- (66) Balabhadra, S.; Debasu, M. L.; Brites, C. D. S.; Ferreira, R. A. S.; Carlos, L. D. A Cost-Effective Quantum Yield Measurement Setup for Upconverting Nanoparticles. *J. Lumin.* **2017**, *189*, 64–70.
- (67) Li, X.; Shen, D.; Yang, J.; Yao, C.; Che, R.; Zhang, F.; Zhao, D. Successive Layer-by-Layer Strategy for Multi-Shell Epitaxial Growth: Shell Thickness and Doping Position Dependence in Upconverting Optical Properties. *Chem. Mater.* **2013**, *25*, 106–112.
- (68) Wang, G.; Peng, Q.; Li, Y. Synthesis and Upconversion Luminescence of $\text{Ba}_2\text{F}_8\text{:Yb}^{3+}/\text{Er}^{3+}$ Nanobelts. *Chem. Commun.* **2010**, *46*, 7528–7529.
- (69) Xingren, L.; Gang, X.; Powell, R. C. Fluorescence and Energy-Transfer Characteristics of Rare Earth Ions in BaYF_5 Crystals. *J. Solid State Chem.* **1986**, *62*, 83–91.
- (70) Sobolev, B. P.; Golubev, A. M.; Otroshchenko, L. P.; Molchanov, V. N.; Zakalyukin, R. M.; Ryzhova, E. A.; Herrero, P. $\text{Ba}_{1-x}\text{R}_x\text{F}_{2+x}$ Phases ($\text{R} = \text{Gd-Lu}$) with Distorted Fluorite-Type Structures—products of Crystallization of Incongruent Melts in the $\text{BaF}_2\text{-RF}_3$ Systems ($\text{R} = \text{Gd-Lu}$). III. Defect $\text{Ba}_{0.75}\text{Lu}_{0.25}\text{F}_{2.25}$ Structure. A New $\{\text{Lu}_8[\text{Ba}_6\text{F}_{71}]\}$ Supercluster of Defects. *Crystallogr. Rep.* **2003**, *48*, 944–952.
- (71) Sorokin, N. I.; Karimov, D. N.; Sul'yanova, E. A.; Sobolev, B. P. Nanostructured Crystals of Fluorite Phases $\text{Sr}_{1-x}\text{R}_x\text{F}_{2+x}$ and Their Ordering: 12. Influence of Structural Ordering on the Fluorine-Ion Conductivity of $\text{Sr}_{0.667}\text{R}_{0.333}\text{F}_{2.333}$ Alloys ($\text{R} = \text{Tb}$ or Tm) at Their Annealing. *Crystallogr. Rep.* **2018**, *63*, 121–126.
- (72) Greis, O.; Cader, M. S. R. Preparation and Characterization of Fluorite-Related Superstructure Phases Sr_2RF_7 , with $\text{R} = \text{Sm-Lu}$ and Y . *Chem. Informationsdienst* **1986**, *17*, 1754–1758.
- (73) Xiang, L.; Ren, G.; Mao, Y.; He, J.; Su, R. Controllable Synthesis and Upconversion Emission of Ultrasmall Lanthanide-Doped Sr_2GdF_7 Nanocrystals. *Opt. Mater.* **2015**, *49*, 6–14.
- (74) Sobolev, B. P.; Golubev, A. M.; Krivandina, E. A.; Marychev, M. O.; Chuprunov, E. V.; Alcobe, X.; Gali, S.; Pascual, L.; Rojas, R.-M.; Herrero, P. $\text{Ba}_{1-x}\text{R}_x\text{F}_{2+x}$ Phases ($\text{R} = \text{Gd-Lu}$) with Distorted Fluorite-Type Structure— Products of Crystallization of Incongruent Melts in the $\text{BaF}_2\text{-RF}_3$ Systems. I. $\text{Ba}_{0.75}\text{R}_{0.25}\text{F}_{2.25}$ Crystals (Synthesis and Some Characteristics). *Crystallogr. Rep.* **2002**, *47*, 201–212.
- (75) Rosenthal, S. J.; McBride, J.; Pennycook, S. J.; Feldman, L. C. Synthesis, Surface Studies, Composition and Structural Characterization of CdSe, Core/shell and Biologically Active Nanocrystals. *Surf. Sci. Rep.* **2007**, *62*, 111–157.
- (76) Shannon, R. D. Revised Effective Ionic Radii and Systematic Studies of Interatomic Distances in Halides and Chalcogenides. *Acta Crystallogr., Sect. A: Cryst. Phys., Diffr., Theor. Gen. Crystallogr.* **1976**, *32*, 751–767.
- (77) *CRC Handbook of Chemistry and Physics*, 84th ed.; Lide, D. R., Ed.; CRC Press, 2004.
- (78) Menon, M. P.; James, J. Solubilities, Solubility Products and Solution Chemistry of Lanthanone Trifluoride-Water Systems. *J. Chem. Soc., Faraday Trans. 1* **1989**, *85*, 2683.
- (79) *The Rare Earths in Modern Science and Technology*; McCarthy, G. J.; Rhyne, J. J.; Silber, H. B., Eds.; Springer US: Boston, MA, 1980; Vol. 2.
- (80) Martell, A. E.; Motekaitis, R. J.; Fried, A. R.; Wilson, J. S.; MacMillan, D. T. Thermal Decomposition of EDTA, NTA, and Nitrilotrimethylenephosphonic Acid in Aqueous Solution. *Can. J. Chem.* **1975**, *53*, 3471–3476.
- (81) Scherrer, P. Bestimmung Der Grösse Und Der Inneren Struktur von Kolloidteilchen Mittels Röntgenstrahlen. *Nachr. Ges. Wiss. Göttingen* **1918**, *26*, 98–100.
- (82) Grzyb, T.; Balabhadra, S.; Przybylska, D.; Węclawiak, M. Upconversion Luminescence in BaYF_5 , BaGdF_5 and BaLuF_5 Nanocrystals Doped with $\text{Yb}^{3+}/\text{Ho}^{3+}$, $\text{Yb}^{3+}/\text{Er}^{3+}$ or $\text{Yb}^{3+}/\text{Tm}^{3+}$ Ions. *J. Alloys Compd.* **2015**, *649*, 606–616.
- (83) Page, R. H.; Schaffers, K. I.; Waide, P. A.; Tassano, J. B.; Payne, S. A.; Krupke, W. F.; Bishel, W. K. Upconversion-Pumped

Luminescence Efficiency of Rare-Earth-Doped Hosts Sensitized with Trivalent Ytterbium. *J. Opt. Soc. Am. B* **1998**, *15*, 996.

(84) Fischer, S.; Johnson, N. J. J.; Pichaandi, J.; Goldschmidt, J. C.; Van Veggel, F. C. J. M. Upconverting Core-Shell Nanocrystals with High Quantum Yield under Low Irradiance: On the Role of Isotropic and Thick Shells. *J. Appl. Phys.* **2015**, *118*, 193105.

(85) Pokhrel, M.; Gangadharan, A. K.; Sardar, D. K. High Upconversion Quantum Yield at Low Pump Threshold in Er³⁺/Yb³⁺ Doped La₂O₃S Phosphor. *Mater. Lett.* **2013**, *99*, 86–89.

(86) Chen, G.; Ohulchanskyy, T. Y.; Kachynski, A.; Ågren, H.; Prasad, P. N. Intense Visible and near-Infrared Upconversion Photoluminescence in Colloidal LiYF₄:Er³⁺ Nanocrystals under Excitation at 1490 Nm. *ACS Nano* **2011**, *5*, 4981–4986.

(87) Macdougall, S. K. W.; Ivaturi, A.; Marques-Hueso, J.; Richards, B. S. Measurement Procedure for Absolute Broadband Infrared up-Conversion Photoluminescent Quantum Yields: Correcting for Absorption/re-Emission. *Rev. Sci. Instrum.* **2014**, *85*, 063109.

(88) Wrighton, M. S.; Ginley, D. S.; Morse, D. L. Technique for the Determination of Absolute Emission Quantum Yields of Powdered Samples. *J. Phys. Chem.* **1974**, *78*, 2229–2233.

(89) Huang, P.; Zheng, W.; Zhou, S.; Tu, D.; Chen, Z.; Zhu, H.; Li, R.; Ma, E.; Huang, M.; Chen, X. Lanthanide-Doped LiLuF₄ Upconversion Nanoprobes for the Detection of Disease Biomarkers. *Angew. Chem., Int. Ed.* **2014**, *53*, 1252–1257.

(90) Liu, X.; Deng, R.; Zhang, Y.; Wang, Y.; Chang, H.; Huang, L.; Liu, X. Probing the Nature of Upconversion Nanocrystals: Instrumentation Matters. *Chem. Soc. Rev.* **2015**, *44*, 1479–1508.

(91) Liu, H.; Xu, C. T.; Lindgren, D.; Xie, H.; Thomas, D.; Gundlach, C.; Andersson-Engels, S. Balancing Power Density Based Quantum Yield Characterization of Upconverting Nanoparticles for Arbitrary Excitation Intensities. *Nanoscale* **2013**, *5*, 4770.

(92) Beeby, A.; Clarkson, I. M.; Dickens, R. S.; Faulkner, S.; Parker, D.; Royle, L.; de Sousa, A. S.; Williams, J. a. G.; Woods, M. Non-Radiative Deactivation of the Excited States of Europium, Terbium and Ytterbium Complexes by Proximate Energy-Matched OH, NH and CH Oscillators: An Improved Luminescence Method for Establishing Solution Hydration States. *J. Chem. Soc., Perkin Trans. 2* **1999**, *2*, 493–504.

(93) Pedroni, M.; Piccinelli, F.; Passuello, T.; Polizzi, S.; Ueda, J.; Haro-González, P.; Martínez Maestro, L.; Jaque, D.; García-Solé, J.; Bettinelli, M.; Speghini, A. Water (H₂O and D₂O) Dispersible NIR-to-NIR Upconverting Yb³⁺/Tm³⁺ Doped MF₂ (M = Ca, Sr) Colloids: Influence of the Host Crystal. *Cryst. Growth Des.* **2013**, *13*, 4906–4913.

(94) Xiang, G.; Zhang, J.; Hao, Z.; Zhang, X.; Pan, G. H.; Chen, L.; Luo, Y.; Lü, S.; Zhao, H. Solvothermal Synthesis and Upconversion Properties of about 10nm Orthorhombic LuF₃:Yb³⁺, Er³⁺ Rectangular Nanocrystals. *J. Colloid Interface Sci.* **2015**, *459*, 224–229.

(95) Xiang, G.; Zhang, J.; Hao, Z.; Zhang, X.; Luo, Y.; Lü, S.; Zhao, H. Transition to Cubic Phase and Enhancement of Green Upconversion Emission by Adding La³⁺ Ions in Hexagonal NaLuF₄:Yb³⁺/Er³⁺ Nanocrystals. *CrystEngComm* **2014**, *16*, 2499.

(96) Hu, S.; Wu, X.; Chen, Z.; Hu, P.; Yan, H.; Tang, Z.; Xi, Z.; Liu, Y. Uniform NaLuF₄ Nanoparticles with Strong Upconversion Luminescence for Background-Free Imaging of Plant Cells and Ultralow Power Detecting of Trace Organic Dyes. *Mater. Res. Bull.* **2016**, *73*, 6–13.

(97) Grzyb, T.; Gruszczyk, A.; Lis, S. Up-Conversion Luminescence of Yb³⁺ and Er³⁺ Doped YPO₄, LaPO₄ and GdPO₄ Nanocrystals. *J. Lumin.* **2016**, *175*, 21–27.

(98) Wawrzyńczyk, D. Surface Functionalization of up-Converting NaYF₄ Nanocrystals with Chiral Molecules. *RSC Adv.* **2016**, *6*, 5558–5565.

(99) Ostrowski, A. D.; Chan, E. M.; Gargas, D. J.; Katz, E. M.; Han, G.; Schuck, P. J.; Milliron, D. J.; Cohen, B. E. Controlled Synthesis and Single-Particle Imaging of Bright, Sub-10 Nm Lanthanide-Doped Upconverting Nanocrystals. *ACS Nano* **2012**, *6*, 2686–2692.

(100) Wisser, M. D.; Fischer, S.; Maurer, P. C.; Bronstein, N. D.; Chu, S.; Alivisatos, A. P.; Sallee, A.; Dionne, J. A. Enhancing Quantum

Yield via Local Symmetry Distortion in Lanthanide-Based Upconverting Nanoparticles. *ACS Photonics* **2016**, *3*, 1523–1530.

Supporting Materials

Formation Mechanism, Structural and Upconversion Properties of Alkaline Rare-Earth Fluoride Nanocrystals Doped With Yb³⁺/Er³⁺ Ions

Tomasz Grzyb*, Dominika Przybylska

Department of Rare Earths, Faculty of Chemistry, Adam Mickiewicz University in Poznan, Umultowska 89b,
61-614 Poznan, Poland

E-mail: tgrzyb@amu.edu.pl

Table S1. Solubility of metal ions fluorides and stability constants of M²⁺ and RE³⁺ complexes with EDTA.

Ion	Ionic radius (Å)	Solubility of fluoride (pK _{so})	EDTA complex stability constant (logK ₁)
Ca ²⁺	1.00	10.7	10.70
Sr ²⁺	1.18	8.4	8.63
Ba ²⁺	1.35	6.7	7.78
Y ³⁺	0.90	20.1	18.09
La ³⁺	1.03	15.3	15.50
Gd ³⁺	0.94	17.2	17.37
Er ³⁺	0.89	14.7	18.85
Yb ³⁺	0.87	15.3	19.51
Lu ³⁺	0.86	13.5	19.83

Table S2. Upconversion quantum yields of non-core/shell nanoparticles with similar size to the described in the article products, under excitation with a laser at around 980 nm. (* OA = oleic acid, OD = octadecene, OM = oleylamine).

Material	Average particle size (nm)	Sample form	Power density (W·cm ⁻²)	UCQY (%)	Synthesis method*	Ref.
Sr ₂ LuF ₇ :19%Yb ³⁺ ,3%Er ³⁺	20.5 ± 1.9	powder	50	0.0192 ± 0.001	hydrothermal method in water at 180 °C	-
Ba ₂ LuF ₇ :23%Yb ³⁺ ,3%Er ³⁺	9.8 ± 2.6			0.0176 ± 0.001		
NaYF ₄ :20%Yb ³⁺ ,2%Er ³⁺	~30	dispersion in hexane	150	0.1 ± 0.05	thermal decomposition in OA/OD at 310 °C	1
	8 - 10	dispersion in hexane	150	0.005 ± 0.005	thermal decomposition in OM at 300 °C	
NaYF ₄ :20%Yb ³⁺ ,2%Er ³⁺	68 ± 16	powder	150	~2	thermal decomposition in OA/OD at 290 °C	2
NaYF ₄ :20%Yb ³⁺ ,2%Er ³⁺	5.4	dispersion in hexane	1000	0.0022 ± 0.0001	thermal decomposition in OA/OD at 310 °C	3
NaGdF ₄ :18%Yb ³⁺ ,2%Er ³⁺	~5	dispersion in cyclohexane	100	0.016 ± 0.08	thermal decomposition in OA/OD at 270 °C	4
LiLuF ₄ : 20%Yb ³⁺ ,1%Er ³⁺	~28	dispersion in cyclohexane	127	0.11	thermal decomposition in OA/OD at 320 °C	5
NaYF ₄ :20%Yb ³⁺ ,2%Er ³⁺	~17.5	dispersion in cyclohexane	63	0.045	thermal decomposition in OA/OD at 315 °C	6
NaGdF ₄ :18%Yb ³⁺ ,2%Er ³⁺	~23	dispersion in water	5	0.26	thermal decomposition in OA/OD at 290 °C	7
		dispersion in chloroform		0.048		
SrF ₂ :20%Yb ³⁺ ,2%Er ³⁺	~40	powder	388	0.00577 ± 0.0002	hydrothermal method in water at 190 °C	8
NaYF ₄ :20%Yb ³⁺ ,2%Er ³⁺	22.7 ± 0.7	dispersion in water (citrate stabilized)	100	~0.1	thermal decomposition in OA/OD at 320 °C	9
		dispersion in cyclohexane		~0.25		
NaYF ₄ :17%Yb ³⁺ ,3%Er ³⁺	~25	dispersion in toluene	20	0.098	thermal decomposition in OA/OD at 300 °C	10
		Powder		0.32		

S2

Upconversion quantum yields

The upconversion quantum yields were calculated using the following equation:¹¹⁻¹³

$$\phi = \frac{\text{number of photons emitted}}{\text{number of photons absorbed}} = \frac{E_{\text{sample}}}{R_{\text{reference}} - R_{\text{sample}}} \quad (1)$$

where ϕ is the quantum yield, E_{sample} is the area under the corrected emission curve of the sample, and $R_{\text{reference}}$ and R_{sample} are the corrected areas under the diffuse reflectance curves of the non-absorbing standard and samples, respectively, at the excitation wavelength. As the white standard we used spectrally pure Y_2O_3 powder (from Alfa Aesar, 99.99%). This compound of spectral purity shows no absorption in the visible or NIR range and cannot be excited by used 980 nm laser light.¹⁴

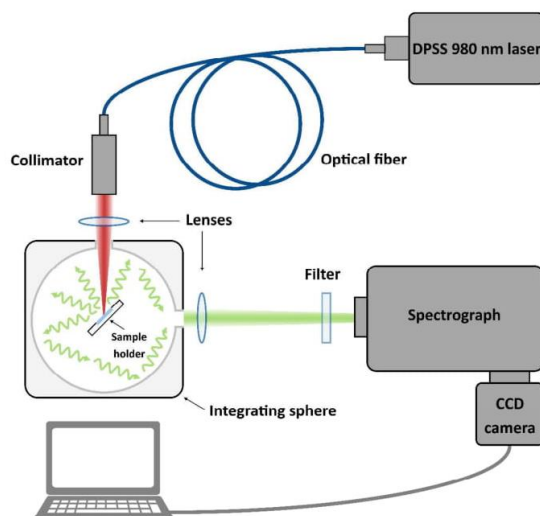


Figure S1. Schematic representation of system setup used to measure upconversion quantum yields.

Luminescence properties

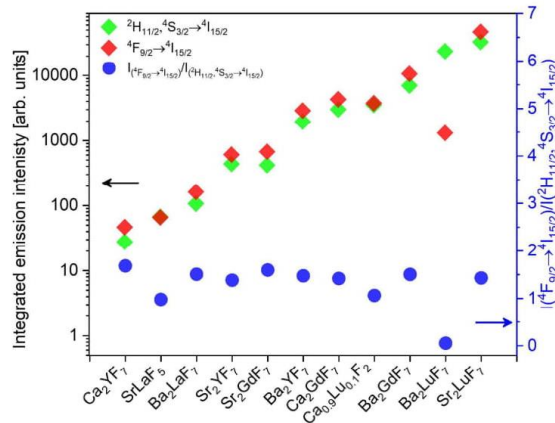


Figure S2. Integral emission intensities of the red (${}^4F_{9/2} \rightarrow {}^4I_{15/2}$) and the green (${}^2H_{11/2}, {}^4S_{3/2} \rightarrow {}^4I_{15/2}$) bands, and the ratio between them calculated for the obtained samples.

Luminescence decays

Since the luminescence kinetics in measured emission decays was non-exponential, effective lifetimes were used for calculations by applying the equation below:

$$\tau_{eff} = \frac{\int_0^{\infty} tI(t)dt}{\int_0^{\infty} I(t)dt} \quad (2)$$

where τ_{eff} is the effective decay time and $I(t)$ is the intensity at time t .¹⁵

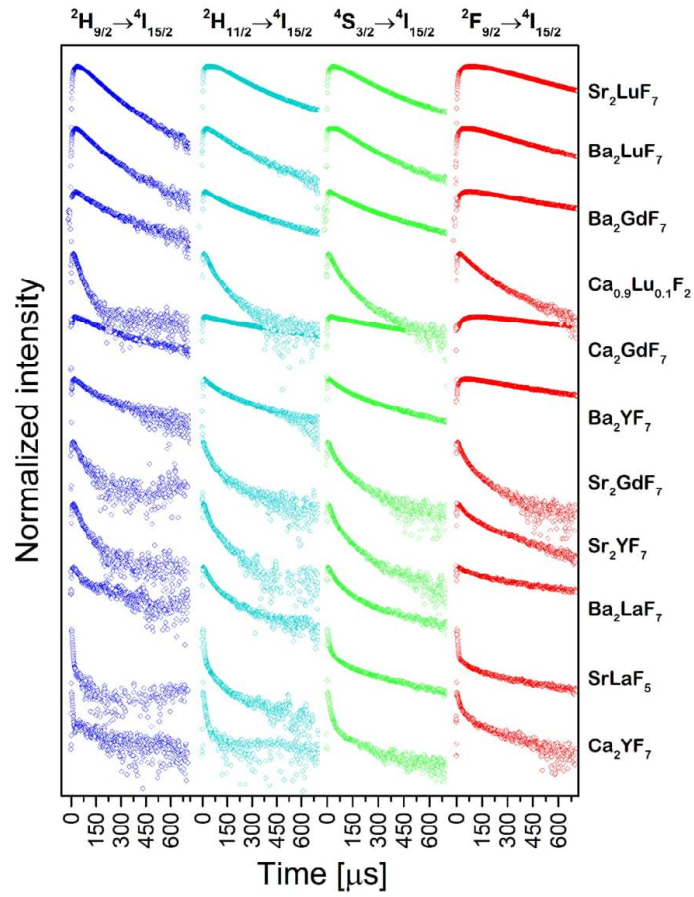


Figure S3. Upconversion luminescence decays measured for the synthesised materials ($\lambda_{exc} = 976$ nm).

Upconversion luminescence dependencies on laser energy

The relation between the UC intensity I and the pumping excitation power density, P_{exc} is given by the following equation:¹⁶

$$I \propto P_{exc}^n \quad (3)$$

where the exponent n represents the number of photons involved in the UC process.^{17,18,19}

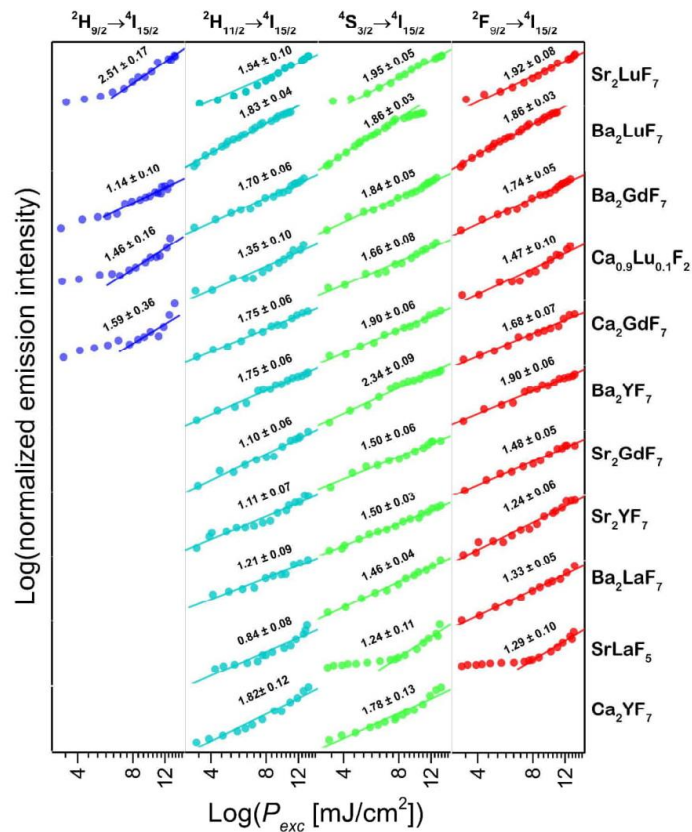


Figure S4. Comparison of upconversion luminescence dependencies on laser energy ($\lambda_{\text{ex}} = 976 \text{ nm}$, calculated slope values are presented in Table 2).

References

- (1) Boyer, J.-C.; van Veggel, F. C. J. M. Absolute Quantum Yield Measurements of Colloidal $\text{NaYF}_4:\text{Er}^{3+}, \text{Yb}^{3+}$ Upconverting Nanoparticles. *Nanoscale* **2010**, *2*, 1417.
- (2) Nadort, A.; Sreenivasan, V. K. A.; Song, Z.; Grebenik, E. A.; Nechaev, A. V.; Semchishen, V. A.; Panchenko, V. Y.; Zvyagin, A. V. Quantitative Imaging of Single Upconversion Nanoparticles in Biological Tissue. *PLoS One* **2013**, *8*, e63292.
- (3) Ostrowski, A. D.; Chan, E. M.; Gargas, D. J.; Katz, E. M.; Han, G.; Schuck, P. J.; Milliron, D. J.; Cohen, B. E. Controlled Synthesis and Single-Particle Imaging of Bright, Sub-10 Nm Lanthanide-Doped Upconverting Nanocrystals. *ACS Nano* **2012**, *6*, 2686–2692.
- (4) Li, X.; Shen, D.; Yang, J.; Yao, C.; Che, R.; Zhang, F.; Zhao, D. Successive Layer-by-Layer Strategy for Multi-Shell Epitaxial Growth: Shell Thickness and Doping Position Dependence in Upconverting Optical Properties. *Chem. Mater.* **2013**, *25*, 106–112.

- (5) Huang, P.; Zheng, W.; Zhou, S.; Tu, D.; Chen, Z.; Zhu, H.; Li, R.; Ma, E.; Huang, M.; Chen, X. Lanthanide-Doped LiLuF₄ Upconversion Nanoprobes for the Detection of Disease Biomarkers. *Angew. Chemie - Int. Ed.* **2014**, *53*, 1252–1257.
- (6) Wisser, M. D.; Fischer, S.; Maurer, P. C.; Bronstein, N. D.; Chu, S.; Alivisatos, A. P.; Salleo, A.; Dionne, J. A. Enhancing Quantum Yield via Local Symmetry Distortion in Lanthanide-Based Upconverting Nanoparticles. *ACS Photonics* **2016**, *3*, 1523–1530.
- (7) Brites, C. D. S.; Xie, X.; Debasu, M. L.; Qin, X.; Chen, R.; Huang, W.; Rocha, J.; Liu, X.; Carlos, L. D. Instantaneous Ballistic Velocity of Suspended Brownian Nanocrystals Measured by Upconversion Nanothermometry. *Nat. Nanotechnol.* **2016**, 1–7.
- (8) Balabhadra, S.; Debasu, M. L.; Brites, C. D. S.; Ferreira, R. A. S.; Carlos, L. D. A Cost-Effective Quantum Yield Measurement Setup for Upconverting Nanoparticles. *J. Lumin.* **2017**, *189*, 64–70.
- (9) Würth, C.; Kaiser, M.; Wilhelm, S.; Grauel, B.; Hirsch, T.; Resch-Genger, U. Excitation Power Dependent Population Pathways and Absolute Quantum Yields of Upconversion Nanoparticles in Different Solvents. *Nanoscale* **2017**, *9*, 4283–4294.
- (10) Kaiser, M.; Würth, C.; Kraft, M.; Hyppänen, I.; Soukka, T.; Resch-Genger, U. Power-Dependent Upconversion Quantum Yield of NaYF₄:Yb³⁺,Er³⁺ Nano- and Micrometer-Sized Particles – Measurements and Simulations. *Nanoscale* **2017**, *9*, 10051–10058.
- (11) Wrighton, M. S.; Ginley, D. S.; Morse, D. L. Technique for the Determination of Absolute Emission Quantum Yields of Powdered Samples. *J. Phys. Chem.* **1974**, *78*, 2229–2233.
- (12) Grzyb, T.; Runowski, M.; Szczeszak, A.; Lis, S. Influence of Matrix on the Luminescent and Structural Properties of Glycerine-Capped, Tb³⁺-Doped Fluoride Nanocrystals. *J. Phys. Chem. C* **2012**, *116*, 17188–17196.
- (13) Chen, G.; Ohulchanskyy, T. Y.; Kachynski, A.; Ågren, H.; Prasad, P. N. Intense Visible and near-Infrared Upconversion Photoluminescence in Colloidal LiYF₄:Er³⁺ Nanocrystals under Excitation at 1490 Nm. *ACS Nano* **2011**, *5*, 4981–4986.
- (14) Wang, J.; Tanner, P. A. Upconversion for White Light Generation by a Single Compound. *J. Am. Chem. Soc.* **2010**, *132*, 947–949.
- (15) Lakowicz, J. R. *Principles of Fluorescence Spectroscopy*; third edition; Springer: Baltimore, 2006.
- (16) Berry, M. T.; May, P. S. Disputed Mechanism for NIR-to-Red Upconversion Luminescence in NaYF₄:Yb³⁺,Er³⁺. *J. Phys. Chem. A* **2015**, *119*, 9805–9811.
- (17) Scheps, R. Upconversion Laser Processes. *Ptog. Quant. Electron.* **1996**, *20*, 271–358.
- (18) Pollnau, M.; Gamelin, D.; Lüthi, S.; Güdel, H.; Hehlen, M. Power Dependence of Upconversion Luminescence in Lanthanide and Transition-Metal-Ion Systems. *Phys. Rev. B* **2000**, *61*, 3337–3346.
- (19) Lei, Y.; Song, H.; Yang, L.; Yu, L.; Liu, Z.; Pan, G.; Bai, X.; Fan, L. Upconversion Luminescence, Intensity Saturation Effect, and Thermal Effect in Gd₂O₃:Er³⁺,Yb³⁺ Nanowires. *J. Chem. Phys.* **2005**, *123*, 174710.